
**UV femtosecond laser ablation applied to Fe and Si
isotope variations in Precambrian iron formations**

Von der Naturwissenschaftlichen Fakultät
der Gottfried Wilhelm Leibniz Universität Hannover

zur Erlangung des Grades

DOKTORIN DER NATURWISSENSCHAFTEN

Dr. rer. nat.

genehmigte Dissertation

von

Dipl.-Geol. Grit Steinhöfel

geboren am 30.09.1977 in München

2009

Referent: Prof. Dr. Friedhelm von Blanckenburg (Leibniz Universität Hannover)

Koreferent: Prof. Dr. Kurt Konhauser (University of Alberta, Canada)

Mitglieder der Prüfungskommission:

Prof. Dr. Carla Vogt (Vorsitzende)

Prof. Dr. Friedhelm von Blanckenburg

PD Dr. Axel Schippers

Tag der Promotion: 13.02.2009

Erklärung zur Dissertation

Hierdurch erkläre ich, dass die Dissertation „UV femtosecond laser ablation applied to Fe and Si isotope variations in Precambrian iron formations“ selbstständig verfasst und alle benutzten Hilfsmittel sowie evtl. zur Hilfeleistung herangezogene Institutionen vollständig angegeben wurden.

Die Dissertation wurde nicht schon als Diplom- oder ähnliche Prüfungsarbeit verwendet.

Hannover, den 18. Dezember 2008

Grit Steinhöfel

Danksagung

An dieser Stelle möchte ich mich bei allen Leuten bedanken, die zum Gelingen dieser Arbeit beigetragen haben. Insbesondere danke ich Ingo Horn und Friedhelm von Blanckenburg, die dieses Projekt initiiert haben und mir ermöglicht haben, mich mit neuer faszinierender Lasertechnik und alten geologischen Fragestellungen zu beschäftigen. Zahlreiche intensive Diskussionen und Hilfe bei allen analytischen Schwierigkeiten haben maßgebend zum Gelingen dieser Arbeit beitragen. Anregungen von Kurt Konhauser, Nic Beukes und Jens Gutzmer haben geholfen die Genese gebänderter Eisenerze besser zu verstehen.

Probenmaterial wurde von Thomas Oberthür, Frank Melcher, Kurt Konhauser, Nic Beukes und Igor Villa zur Verfügung gestellt. Paul Königer vom Leibniz Institut für Geowissenschaftliche Gemeinschaftsaufgaben, Hannover, hat freundlicherweise die C Isotopenmessungen durchgeführt. Mikrobeprobungen konnte ich an der Georg-August Universität Göttingen bei Andreas Konz durchführen. Bei Otto Diedrich bedanke ich mich für die exzellente und schnelle Probenpräparation. Die Mitarbeiter der Werkstatt, insbesondere Willi Hurkuck und Bettina Aichinger, waren immer hilfreich bei technischen Belangen. Außerdem möchte ich mich bei Wanja Dziony, Kirsten Möller und Alexandra Tangen für die Hilfe bei Laborarbeiten in letzter Minute sehr bedanken. Kevin Norton und Jan Schüssler sei gedankt für das umsichtige Durchlesen dieser Arbeit.

Meine Büromädels Monika Gülke und Sonja Zink haben dafür gesorgt, dass das Leben nicht auf der Strecke bleibt. Sie haben mich auch immer auf dem Laufenden gehalten und kleine und größere organisatorische Dinge für mich erledigt, wenn ich nicht in Hannover sein konnte – besten Dank dafür!

Außerdem möchte ich mich bei der ganzen ehemaligen ‚Isotopen‘ Gruppe der Uni Hannover bedanken für die anregenden Diskussionen, analytischen Hilfestellungen und anderweitigen Aktivitäten. Es hat mir immer großen Spaß gemacht, in Hannover zu arbeiten.

Zu Allerletzt möchte ich mich noch bei meiner Familie bedanken, die mich immer unterstützt hat und gerne mal auf die kleine Helena aufgepasst hat.

Contents

Danksagung	5
Zusammenfassung	11
Abstract	14
1 Introduction	17
1.1. Overview and Fundamentals	17
1.1.1. Theory of stable isotope fractionation	18
1.1.2. Natural Fe isotope variation	24
1.1.3. Natural Si isotope variation	29
1.2. Laser Ablation	33
1.2.1. Comparison between femtosecond and nanosecond laser ablation	34
1.2.2. Elemental and isotope fractionation during laser ablation ICP-MS	41
1.2.3. Laser ablation instrumentation	45
1.3. Precambrian Iron Formation	51
1.3.1. Nature and depositional environment of iron formations	51
1.3.2. Geochemical Si cycle during iron formation deposition and the Precambrian Si isotope record	52
1.3.3. Geochemical Fe cycle during iron formation deposition	54
1.3.4. The Precambrian Fe isotope record	58

2	Matrix-independent stable Fe isotope ratio determination using UV femtosecond laser ablation ICP-MS	65
2.1.	Introduction	66
2.2.	Methods	67
2.3.	Results	71
2.4.	Discussion	73
2.4.1.	Isobaric Cr interference	74
2.4.2.	Variable mass load in the ICP-MS	75
2.4.3.	Precision and accuracy	75
2.5.	Conclusions	77
3	Micro-scale tracing of Fe and Si isotope signatures in banded iron formation using femtosecond laser ablation	79
3.1.	Introduction	80
3.2.	Investigated BIF	81
3.3.	Methods	87
3.3.1.	<i>In situ</i> LA-ICP-MS	88
3.3.2.	Solution ICP-MS	91
3.4.	Results	92
3.4.1.	Fe isotope composition	92
3.4.2.	Si isotope composition	94
3.5.	Discussion	98
3.5.1.	Significance of bulk Fe and Si isotope composition in the Old Wanderer Iron Formation	98
3.5.2.	Diagenesis and the formation of magnetite and iron carbonate	103
3.5.3.	The significance of zoned magnetite crystals	106
3.6.	Conclusions	107

4	Deciphering formation processes of banded iron formations from the Transvaal and the Hamersley successions by combined Si and Fe isotope analysis using UV femtosecond laser ablation	109
4.1.	Introduction	110
4.2.	Geological Background	112
4.3.	Sample Description	113
4.4.	Methods	116
4.5.	Results	117
4.5.1.	Fe isotope composition	117
4.5.2.	Si isotope composition	119
4.5.3.	C isotope composition	119
4.6.	Discussion	125
4.6.1.	Seawater to sediment cycling of Si and Fe	125
4.6.2.	Formation of Fe-bearing minerals	132
4.7.	Conclusions	136
	References	139
	Curriculum Vitae.....	167
	Publications	169

Zusammenfassung

Eisen und Silicium sind die viert- und zweithäufigsten chemischen Elemente in der Erdkruste. Grosses Interesse an der Fraktionierung ihrer Isotope in rezenten und fossilen Systemen kam durch die Einführung der Multikollektor induktiv gekoppelten Plasma Massenspektrometrie (MC-ICP-MS) vor *ca.* 10 Jahren auf. Diese ermöglicht es, die Isotopenverhältnisse schwerer Elemente präzise zu messen. Diese Arbeit beschäftigt sich mit einer Weiterentwicklung dieser Technik. UV Femtosekunden Laserablation, gekoppelt mit MC-ICP-MS, stellt eine ausgezeichnete Methode dar, Verhältnisse der stabilen Fe und Si Isotope *in situ* bei hoher räumlicher Auflösung (30 μm) in Festkörpern zu bestimmen. Mit dieser neuen Mikrostrahltechnik können Fe und Si Isotopenzusammensetzungen in einzelnen Mineralkörnern gemessen werden. Eine wissenschaftlich attraktive erste Anwendung ist die Untersuchung der Genese Präkambrischer gebänderter Eisenerze, deren Bildung mit großen Veränderungen in der Erdgeschichte, wie dem Anstieg atmosphärischen Sauerstoffs und der Entwicklung einfacher Formen des Lebens einherging.

Femtosekunden Laserablation ICP-MS bietet große Vorteile gegenüber herkömmlich verwendeten Nanosekunden Laserablationssystemen. Die durch Laser induzierte und von der Partikelgröße abhängige Element- und Isotopenfraktionierung ist weitestgehend unterbunden, so dass eine Kalibration mit Referenzmaterialien unabhängig ihrer Matrix möglich ist. Um das Potential dieser Methode für die Analyse stabiler Isotopenverhältnisse zu untersuchen, wurde die Fe Isotopenzusammensetzung von Biotit, Hornblende, Olivin (Fayalit und Forsterit), Granat und einer ozeanischen Fe-Mn Kruste bestimmt, wobei das Metallreferenzmaterial IRMM-014 zur Kalibrierung verwendet worden ist. Die Genauigkeit der Laserablationsdaten wurde durch Lösungs-ICP-MS Daten überprüft, die von einem Teil der Proben nach Auflösen und chromatographischer Fe Abtrennung mit Lösungs-ICP gemessen worden sind. Alle Probenmaterialien ergeben $\delta^{56}\text{Fe}$ und $\delta^{57}\text{Fe}$ Werte, die mit den Lösungs-ICP-MS Werten übereinstimmen. Bei hohen Cr Gehalten ($^{54}\text{Cr}/^{54}\text{Fe} > 0.1\%$) jedoch, z.B. in Granat und Forsterit, wurden die $\delta^{56}\text{Fe}$ und $\delta^{57}\text{Fe}$ Werte aus $^{57}\text{Fe}/^{56}\text{Fe}$ Verhältnissen errechnet, da bei solchen Cr Gehalten das Verfahren zur Korrektur der isobaren Interferenz von ^{54}Cr auf ^{54}Fe unzureichend ist. Die externe Reproduzierbarkeit für homogene Materialien ist 0.1‰ (2 SD) für $\delta^{56}\text{Fe}$ und 0.2‰ (2 SD) für $\delta^{57}\text{Fe}$; diese Reproduzierbarkeit hängt nicht von der Probenmatrix ab. Damit wurde gezeigt, dass Femtosekunden Laserablation ICP-MS eine weitestgehend matrixunabhängige Methode ist, was in Betracht des vielfältigen Probenmaterials einen bedeutenden Vorteil für geologische Anwendungen darstellt.

Variationen stabiler Isotopeverhältnisse der Hauptelemente in gebänderten Eisenerzen, Fe und Si, in koexistierenden Mineralphasen zu messen ist eine neue Herangehensweise, die Genese dieser fossilen chemischen Sedimente zu rekonstruieren. Der Vergleich von gemessenen Unterschieden im Isotopenverhältnis koexistierender Mineralphasen mit publizierten Isotopenfraktionierungsfaktoren ermöglicht die Identifikation von Ablagerungsmechanismen und diagenetischen Prozessen. In der Archaischen Old Wanderer Iron Formation im Shurugwi Grünsteingürtel (Zimbabwe) weist Magnetit gleichbleibende $\delta^{56}\text{Fe}$ Werte von $\sim 0.9\%$ auf, wobei die Kristalle allerdings intern zoniert sind. Für Eisenkarbonatlagen wurden ebenfalls relativ einheitliche $\delta^{56}\text{Fe}$ Werte um 0% ermittelt. Die Isotopenverhältnisse einzelner Karbonatkristalle sind jedoch stark von der chemischen Zusammensetzung abhängig und ergeben $\delta^{56}\text{Fe}$ Werte von bis zu 0.4% für Siderit und -0.7% für Ankerit. Der Unterschied in der Fraktionierung zwischen Eisenkarbonate und Magnetit deutet auf eine gekoppelte Magnetit-Eisenkarbonat Bildung während der Diagenese durch biotische oder abiotische Reduktion eines Eisen(III)(hydr)oxid Präkursors bei gleichzeitiger Oxidation organischer Kohlenwasserstoffe hin. Die Si Isotopenzusammensetzung in kieseligen Lagen weist deutliche Variationen von Lage zu Lage auf und ergibt $\delta^{30}\text{Si}$ Werte zwischen -2.6 bis -1.0% . Dies deutet auf Silica Ausfällung aus Meerwasser hin, das mit hydrothermalen Lösungen angereichert wurde. Die Fe und Si Isotopenzusammensetzungen variieren gleichförmig von Lage zu Lage. Dies belegt die Erhaltung primärer Signaturen, welche die Auftriebsdynamik hydrothermal dominierter Tiefenwässer widerspiegelt. Demzufolge hat die hydrothermale Aktivität im marinen Becken die Fe und Si Ausfällungsraten bestimmt und somit auch die Ausbildung der Lagen.

Die Proterozoischen gebänderten Eisenerze der Hamersley Group (Australien) und der Transvaal Supergroup (Südafrika) zeigen eine andere Isotopenverteilung. Die untersuchten Kernabschnitte zeigen Variationen in der Fe Isotopenzusammensetzung, während die Si Isotopensignaturen gleich bleiben. Der Fe und Si Eintrag in die Ablagerungen scheint also auf getrennten Pfaden stattgefunden zu haben. Die Fe Isotopenzusammensetzung der Minerale wurde durch die Zusammensetzung des Meerwassers, die Fraktionierung bei der Ausfällung primärer Mineralphasen und der Eisenumverteilung nach der Ablagerung beeinflusst. Magnetit zeigt negative $\delta^{56}\text{Fe}$ Werte, die vom Eisen(III)(hydr)oxid Präkursor ererbt und durch diagenetische Eisenumverteilung bedingt worden sind. Primärer Siderit liegt vor, wenn ein isotopisches Ungleichgewicht zu koexistierendem Magnetit besteht, wohingegen Siderit und Magnetit, die den Gleichgewichtfraktionierungsfaktor widerspiegeln, als diagenetische Phasen interpretiert werden. Primäre Isotopensignaturen in Hämatit und Siderit implizieren eine variable Meerwasserzusammensetzung mit $\delta^{56}\text{Fe}$ Werten zwischen -0.8 bis 0% . Die Si

Isotopenzusammensetzung kieseliger Lagen wird als primäre Signatur interpretiert und ergibt $\delta^{30}\text{Si}$ Werte zwischen -1.2 und -0.8% . Die Ergebnisse sprechen für konstante Fe und Si Isotopenzusammensetzungen des Meerwassers während der Ablagerung der untersuchten Kernabschnitte, was im Einklang mit der langen Verweilzeit von Fe und Si und dem typischen Ablagerungsmilieu Proterozoischer gebänderter Eisenerze an kontinentalen Schelfgebieten entfernt von hydrothermalen und kontinentalen Einfluss steht. Die für längere Zeiträume als die der hier untersuchten Dünnschliffe publizierte Fe Isotopenzusammensetzung gebänderter Eisenerze aus dem Hamersley und Transvaal Becken von ungefähr 0% wird durch ein stationäres Gleichgewichtsmodell im Ozeanbecken erklärt, in dem der hydrothermale Eintrag des Fe isotopisch dem der in gebänderten Eisenerzen gefundenen entspricht. Da die hier untersuchten Abschnitte jedoch überwiegend Fe mit negativen $\delta^{56}\text{Fe}$ Werten enthalten, muss dies leichte Fe durch Ablagerung isotopisch schwerer gebänderter Eisenerze an anderer Stelle oder Zeit ausgeglichen worden sein. Die Si Isotopensignaturen in diesen Kernabschnitten und in gebänderten Eisenerzen im Allgemeinen erscheinen im Vergleich zur angenommenen Zusammensetzung hydrothermalen und kontinentaler Zuflüsse als zu leicht. Dies impliziert entweder eine komplementäre Senke für isotopisch schweres Si im Ozeanbecken bei stationärem Gleichgewicht oder nicht-stationäre Bedingungen. Diese könnten etwa durch erhöhte hydrothermale Aktivität oder Verwitterung zur Zeit der Ablagerung gebänderter Eisenerze bedingt worden sein.

Die Resultate dieser Doktorarbeit zeigen das Potential von UV Femtosekunden Laser Ablation ICP-MS in der Analyse stabiler Isotopenverhältnisse in hoher räumlicher Auflösung für geologische Fragestellungen. Diese Methode stellt ein gänzlich neues Werkzeug in der Untersuchung der Mikrostratigraphie chemischer Ablagerungen auf der Längenskala eines Dünnschliffes dar.

Schlagwörter: UV Femtosekunden Laserablation, stabile Eisenisotope, stabile Siliciumisotope, gebänderte Eisenerze

Abstract

Iron and silicon are the fourth and second most elements in the Earth's crust. Immense interest in the fractionation of their isotopes in recent and ancient environments began *ca.* 10 years ago with the ability to measure their isotope ratios precisely by multiple collector inductively coupled plasma mass spectrometry (MC-ICP-MS). The topic of this thesis is a further development of this technique. UV femtosecond laser ablation in conjunction with MC-ICP-MS provides an excellent tool to analyse stable Fe and Si isotope ratios in solid samples *in situ* at high-spatial resolution (30 μm). This new microbeam tool allows the determination of Fe and Si isotope compositions on the mineral grain scale. An obvious first application is to explore the genesis of Precambrian iron formations whose deposition is associated with major changes in the Earth's history as the rise of atmospheric oxygen and the evolution of early forms of life.

Femtosecond laser ablation ICP-MS provides significant advantages over commonly employed nanosecond laser ablation systems. Laser-induced and particle size-controlled elemental and isotope fractionation is suppressed to such an extent that non-matrix matched calibration is feasible. To explore the capability of this system for stable isotope ratio analysis, the Fe isotope composition of biotite, hornblende, olivine (fayalite and forsterite), garnet and an oceanic Fe-Mn crust has been determined using the metal reference material IRMM-014 for calibration. The accuracy of the laser ablation measurements was verified by solution ICP-MS data, measured after chromatographic Fe separation from aliquots. For all investigated sample materials, $\delta^{56}\text{Fe}$ and $\delta^{57}\text{Fe}$ values from laser ablation ICP-MS agree with those measured by solution ICP-MS. At high Cr content ($^{54}\text{Cr}/^{54}\text{Fe} > 0.1\%$), i.e. garnet and forsterite, $\delta^{56}\text{Fe}$ and $\delta^{57}\text{Fe}$ values were derived from $^{57}\text{Fe}/^{56}\text{Fe}$ ratios, as the correction mode of isobaric interference of ^{54}Cr on ^{54}Fe is unsatisfactory. An external reproducibility for homogeneous materials of 0.1‰ (2 SD) for $\delta^{56}\text{Fe}$ and 0.2‰ (2 SD) for $\delta^{57}\text{Fe}$ is achieved regardless of the sample matrix. These results demonstrate that femtosecond laser ablation ICP-MS is a largely matrix-independent method, which is a substantial advantage for geological applications considering the large spectrum of sample materials of interest.

The determination of stable isotope variations of the major chemical constituents of Precambrian iron formations, Fe and Si, in coexisting mineral phases is a new approach to reconstructing their genesis. Depositional and diagenetic processes in Precambrian ocean basins are disclosed by comparison of isotope differences of coexisting minerals with published isotope fractionation factors. In the Archean Old Wanderer Iron Formation in the Shurugwi Greenstone Belt (Zimbabwe), magnetite shows an overall uniform $\delta^{56}\text{Fe}$ value of $\sim 0.9\%$ on

crystals despite internal zonation. Bulk iron carbonates are also relatively uniform with $\delta^{56}\text{Fe}$ values of near-zero, however individual $\delta^{56}\text{Fe}$ values are highly composition-dependent with end member compositions of 0.4‰ for siderite and -0.7‰ for ankerite. These results are best explained by coupled magnetite-iron carbonate formation during diagenesis due to biotic or abiotic reduction of a ferric (hydr)oxide precursor by organic matter oxidation. The Si isotope composition of chert shows significant inter-layer variations ranging between -2.6 and -1.0‰ in $\delta^{30}\text{Si}$, which is indicative of silica precipitation from seawater with a hydrothermal signature. Fe and Si isotope compositions of bulk layers covary, indicating that primary signatures, which reflect the upwelling dynamics of hydrothermal-rich water, are preserved. Hence, hydrothermal activity seems to have governed the rates of Fe and Si precipitation and therefore also the development of layering.

Proterozoic iron formations from the Hamersley Group (Australia) and Transvaal Supergroup (South Africa) record a very different isotope pattern from that of the Archean iron formation. The investigated core sections show variations in Fe isotope composition, but Si isotope signatures are uniform, implying independent pathways for Si and Fe. The Fe isotope composition was governed by that of seawater, the fractionation during precipitation of initial mineral phases, and post-depositional Fe redistribution. Magnetite exhibits negative $\delta^{56}\text{Fe}$ values, which are inherited from the ferric (hydr)oxide precursor and caused by diagenetic Fe redistribution. Primary siderite is identified by isotopic disequilibrium to coexisting magnetite, whereas siderite and magnetite, which reflect the equilibrium fractionation factor, are interpreted to be diagenetic phases. Primary isotope signatures in hematite and siderite imply a range in $\delta^{56}\text{Fe}$ between -0.8 and 0‰ for ancient seawater. The Si isotope composition of chert is interpreted as primary signature ranging between -1.2 and -0.8‰ in $\delta^{30}\text{Si}$. The results imply steady Fe and Si compositions of seawater during deposition of individual samples, which is consistent with the long residence times of Fe and Si as well as with the typical depositional settings of Proterozoic iron formations on continental shelf areas far from hydrothermal and continental influences. The published long-term Fe isotope composition of near-zero in the Hamersley and Transvaal iron formations is explained with a steady state ocean model in which the hydrothermal flux is isotopically balanced by deposition of Fe into iron formations. Hence, the isotopically light Fe in the iron formations investigated here has to be balanced by deposition of isotopically heavy iron formations elsewhere, or in a different period. The Si isotope signatures in these core sections and in iron formations in general appear to be too light as compared to the assumed hydrothermal and continental influx composition. This indicates either a complementary sink for isotopically heavy Si for a steady state ocean basin or non-

steady state conditions due to extraordinary hydrothermal activity or weathering at the time of iron formation deposition.

The results of this thesis demonstrate the capability of UV femtosecond laser ablation ICP-MS for analysing stable isotope ratios at high-spatial resolution in geological applications. Furthermore, it provides a novel tool to investigate microstratigraphy of chemical sediments at the thin section scale.

Keywords: UV femtosecond laser ablation, stable iron isotopes, stable silicon isotopes, banded iron formations

1

Introduction

1.1. Overview and Fundamentals

The employment of ultra-short pulses in laser ablation ICP mass spectrometry provides significant advantages for *in situ* elemental and isotope ratio analysis in solids, which open up applications in the field of heavy stable isotope geochemistry. In this thesis, a UV femtosecond laser ablation system coupled to a multiple-collector inductively coupled plasma mass spectrometer (MC-ICP-MS) was used to investigate the capability of precise Fe and Si isotope ratio analysis exploring the formation processes of Precambrian iron formations. To demonstrate the feasibility of this new approach, Fe isotope ratios were analysed in various matrices in order to investigate potential matrix effects for femtosecond laser ablation. The ability to determine stable isotope variations of the major chemical constituents of iron formations, Fe and Si, on the mineral grain scale offers the opportunity to reconstruct depositional and diagenetic mechanisms in Precambrian ocean basins.

This thesis is subdivided into four chapters. The first chapter gives an introduction to the methods and theory used in following chapters, which comprise comprehensive manuscripts with separate introductions and conclusions and have been submitted for publication in international journals.

Chapter 1 provides an overview of stable isotope fractionation with a focus on the stable Fe and Si isotope systems. Recent developments in laser ablation with respect to the advantages of ultra-short pulses are discussed, and the UV femtosecond laser ablation system at the Leibniz Universität Hannover is described. An overview is given on Precambrian iron formations with respect to the Si and Fe isotope records based on a concise survey of the literature.

Chapter 2 investigates potential matrix-effects for femtosecond laser ablation by determining stable Fe isotope ratios in silicate matrices including olivine, biotite, hornblende, garnet and an oceanic Fe-Mn crust. This chapter has been submitted for publication in *Chemical Geology* (Steinheffel, G., Horn, I. and von Blanckenburg, F.: Matrix-independent stable Fe isotope ratio determination using UV femtosecond laser ablation ICP-MS. *Chemical Geology* – in review).

Chapter 3 includes a study of Fe and Si isotope micro-tracing in the Archean Old Wanderer Iron formation from the Shurugwi Greenstone Belt (Zimbabwe) using UV femtosecond laser ablation. In this iron formation, covariant bulk Fe and Si isotope compositions of layers reflect the dynamics of hydrothermal activity, whereas the Fe isotope composition of specific minerals discloses diagenetic processes. The results of this study highlight the potential of micro-analytical techniques for investigating heavy stable isotope variations. This chapter has been submitted for publication to *Geochimica et Cosmochimica Acta* (Steinheffel, G., Horn, I. and von Blanckenburg, F.: Micro-scale tracing of Fe and Si isotope signatures in banded iron formation using femtosecond laser ablation. *Geochimica et Cosmochimica Acta* – in review).

Chapter 4 presents a study of Fe and Si isotope composition in Proterozoic iron formations from the Hamersley Basin (Australia) and the Transvaal Basin (South Africa) determined by UV femtosecond laser ablation. Uniform Si compositions in these formations are consistent with continuous silica precipitation on continental shelf areas, a typical depositional setting for Proterozoic iron formations. Variations in Fe isotope composition of the major Fe-bearing minerals can be attributed to various processes including the isotope fractionation between seawater and the initially precipitated phases, variable degrees of partial Fe(II) oxidation in the upper water column and diagenetic Fe redistribution. The determination of stable isotope variations in the major chemical constituents of iron formation on the mineral grain scale provides a significant advantage in reconstructing the temporal evolution of Proterozoic seawater and post-depositional diagenetic processes. This chapter is considered for publication in *Geochimica et Cosmochimica Acta* (Steinheffel, G., von Blanckenburg, F., Horn, I., Konhauser, K. O., Beukes, N. and Gutzmer, J.: Deciphering formation processes of banded iron formation from the Transvaal and the Hamersley successions by combined Si and Fe isotope analysis using UV femtosecond laser ablation. *Geochimica et Cosmochimica Acta* – in review).

1.1.1. Theory of stable isotope fractionation

In recent years, ‘non-traditional’ isotope geochemistry has become a research field of immense interest driven by advances in mass spectrometry, and in particular by the introduction of MC-

ICP-MS. Besides the ‘traditional’ stable isotope systems of H, C, N, O and S, commonly measured by gas source mass spectrometry, and Li, B, Cl, Sr and Br, commonly measured by thermal ionization mass spectrometry (TIMS), mass-dependent isotope fractionation has now been measured by MC-ICP-MS for many further elements including Mg, Si, Ca, Ti, Cr, Fe, Cu, Zn, Ge, Sr, Mo, Ag, Cd, Sb, Te, Hg and Tl. These isotope systems are called ‘non-traditional’ stable isotope systems. Especially the stable isotopes of transition metals show pronounced mass-dependent isotope fractionation (see review of Anbar and Rouxel (2007)).

Since natural isotope variations are typically in the range of parts per thousand to parts per hundred, a stable isotope ratio, R ($R = \frac{\text{heavy } X}{\text{light } X}$), of an element X in a sample is commonly reported as permil deviation from a reference material, described as the δ notation:

$$\frac{\delta}{\text{‰}} = \frac{R_{\text{sample}} - R_{\text{standard}}}{R_{\text{standard}}} * 1000 . \quad (1.1)$$

Isotope fractionation between two substances, A and B , is described by the fractionation factor, α , which is defined as

$$\alpha_{A-B} = \frac{R_A}{R_B} . \quad (1.2)$$

Because isotope fractionation is relatively small, especially for heavy stable isotope systems, fractionation of isotopes between two phases are often reported as

$$\Delta_{A-B} = \delta_A - \delta_B , \quad (1.3)$$

where α is related to Δ by

$$\Delta \approx 10^3 \ln \alpha . \quad (1.4)$$

Below, the theory of stable isotope fractionation is briefly summarized based on recent reviews by Chacko et al. (2001), Hoefs (2004) and Schauble (2004). Basically, mass-dependent isotope fractionation can be caused by two different processes – equilibrium isotope fractionation and kinetic isotope fractionation.

Equilibrium isotope fractionation

Mass-dependent equilibrium isotope fractionation during chemical reactions is a fundamental quantum mechanical phenomenon mainly caused by shifts in the vibrational energies of molecules on isotopic substitution, associated with a change in the zero-point energy of the bond (ZPE) and therefore a change in bond strength (Bigeleisen, 1965; Urey, 1947). The ZPE

is predominately determined by the vibrational frequency of a bond, whereas rotational and translational frequencies have subordinate effects, particularly for solid phases such as minerals. An exception is hydrogen. This can be illustrated for a simple diatomic gas molecule, AB , where the ZPE can be described by

$$ZPE = \frac{1}{2} h\nu, \quad (1.5)$$

where ν is the vibrational frequency of the bond and h is the Planck's constant.

For a simple diatomic molecule, AB , the vibrational frequency of the bond can be approximated by a harmonic oscillator:

$$\nu = \frac{1}{2\pi\sqrt{k/\mu}}, \quad (1.6)$$

where k is the effective spring constant, which depends on the electronic configuration of the molecule, and μ is the reduced mass of the molecule AB defined as

$$\mu = \frac{m_A m_B}{m_A + m_B}, \quad (1.7)$$

with m_A and m_B being the masses of the atoms A and B , respectively.

Therefore, the ZPE is a function of the masses of A and B . The lower the ZPE the greater the energy difference between the bonded and dissociated atoms. Bond strength increases when a heavier isotope substitutes for a lighter isotope; e.g. for two isotopes of A , $^{heavy}A$ and $^{light}A$, the bond of $^{heavy}AB$ is stronger than that of $^{light}AB$. Hence, shifts in the ZPE control equilibrium isotope fractionation.

For a simple isotope exchange reaction: $^{light}AB + ^{heavy}A \rightleftharpoons ^{heavy}AB + ^{light}A$, the equilibrium constant k_{eq} is defined as the quotient of the activities of the products and reactants:

$$k_{eq} = \frac{\{^{heavy}AB\}\{^{light}A\}}{\{^{light}AB\}\{^{heavy}A\}}. \quad (1.8)$$

Assuming an ideal mixing of isotopes in both phases, AB and A , the equilibrium constant in this simple example is equivalent to the equilibrium isotope fractionation factor α_{AB-A} :

$$k_{eq} = \alpha_{AB-A} = \frac{R_{AB}}{R_A}. \quad (1.9)$$

The equilibrium constant is related to the free energies of the reactants and products:

$$\Delta G^0 = -RT \ln(k_{eq}) \text{ giving } k_{eq} = \exp\left(\frac{-\Delta G^0}{RT}\right), \quad (1.10)$$

where ΔG^0 is the Gibbs free energy change of the reaction, R is the molar gas constant, and T is the absolute temperature.

The bond structure, and therefore the potential energy, of each molecule is unaffected by equilibrium isotope exchange reactions. Hence, only the kinetic energy of the bond resulting from atomic motion has to be considered. Changes in pressure P and volume V are negligible, except for some light stable isotope systems, such as hydrogen. Under these conditions, the Gibbs free energy, G , is equivalent to the Helmholtz free energy F :

$$G = F + PV \text{ and } \Delta G \approx \Delta F, \quad (1.11)$$

giving the following expression for the equilibrium constant:

$$k_{eq} = \alpha = \exp\left(\frac{-\Delta F}{RT}\right). \quad (1.12)$$

Approximating the atomic motion by a harmonic oscillator, the energy difference, ΔF , equals approximately the difference in the zero-point energy, ΔZPE , which can be calculated using *Equation (1.5)*:

$$\Delta F \approx \Delta ZPE = \sum_{Products} \left(\frac{1}{2}h\nu\right) - \sum_{Reactants} \left(\frac{1}{2}h\nu\right) = \frac{1}{2}h\Delta\nu, \quad (1.13)$$

where ν is the vibrational frequency and h is the Plank's constant.

Therefore, equilibrium isotope fractionation between two substances is driven by the difference in vibrational frequency, $\Delta\nu$, which is related to the masses (see *Equation 1.6*).

More accurately, the total energy of motion of a molecule including vibrational, rotational and translational energies can be described by statistical mechanics using partition functions, Q . Partition functions consider all energy states of a molecule and the probability to occupy particular states. It is related to the Helmholtz free energy according to

$$F = -RT \ln Q. \quad (1.14)$$

The vibrational partition function, Q_{vib} , for harmonic vibrations describes the sum over all vibrational energies, E_n , in a molecule:

$$Q_{vib} = \sum_n \exp(-E_n / kT) \text{ with } E_n = \left(n + \frac{1}{2}\right)h\nu, \quad (1.15)$$

where k is the Boltzmann's constant and n ($n = 0, 1, 2, \dots$) describes the energy state, i.e. the quantum number, of the vibrational degree of freedom. For a molecule in the ground state, $n = 0$, which defines the zero-point energy.

The partition functions for rotation and translation in a molecule, Q_{rot} and Q_{trans} , can be approximated by:

$$Q_{rot} = \frac{8\pi^2 I kT}{h^2} \text{ and} \quad (1.16)$$

$$Q_{trans} = V \left(\frac{2\pi m kT}{h^2} \right)^{\frac{3}{2}}, \quad (1.17)$$

where I is the moment of inertia of the molecule, V is the volume of the molecule, and m is its mass. Therefore, the total energy of atomic motion is

$$\begin{aligned} F &= -RT(\ln Q_{trans} + \ln Q_{rot} + \ln Q_{vib}) \\ &= -RT \ln(Q_{trans} * Q_{rot} * Q_{vib}) \end{aligned} \quad (1.18)$$

resulting in the following expression for the equilibrium constant, k_{eq} , and therefore for the equilibrium isotope fractionation factor, α :

$$\begin{aligned} k_{eq} = \alpha &= \exp\left(\frac{-\Delta F}{RT}\right) = \exp\left[\frac{-(F_{Products} - F_{Reactants})}{RT}\right] \\ &= \exp\left\{\sum_{Products} \ln(Q_{trans} * Q_{rot} * Q_{vib}) - \sum_{Reactants} \ln(Q_{trans} * Q_{rot} * Q_{vib})\right\} \\ &= \frac{\prod_{Products} (Q_{trans} * Q_{rot} * Q_{vib})}{\prod_{Reactants} (Q_{trans} * Q_{rot} * Q_{vib})}. \end{aligned} \quad (1.19)$$

Inserting the partition functions in the equation above, the equilibrium fractionation factor, α_{AB-A} , for the isotope exchange reaction: $^{light}AB + ^{heavy}A \Leftrightarrow ^{heavy}AB + ^{light}A$ is

$$\begin{aligned} \alpha_{AB-A} = k_{eq} &= \frac{Q_{trans} (^{light}A)}{Q_{trans} (^{heavy}A)} * \frac{Q_{trans} * Q_{rot} * Q_{vib} (^{heavy}AB)}{Q_{trans} * Q_{rot} * Q_{vib} (^{light}AB)} \\ &= \left(\frac{m_{light A}}{m_{heavy A}}\right)^{\frac{3}{2}} * \left(\frac{m_{heavy AB}}{m_{light AB}}\right)^{\frac{3}{2}} * \frac{I_{heavy AB}}{I_{light AB}} * \frac{\exp\left(-\frac{h\nu_{heavy AB}}{2kT}\right)}{1 - \exp\left(-\frac{h\nu_{heavy AB}}{kT}\right)} * \frac{1 - \exp\left(-\frac{h\nu_{light AB}}{kT}\right)}{\exp\left(-\frac{h\nu_{light AB}}{2kT}\right)}. \end{aligned} \quad (1.20)$$

Therefore, to calculate an equilibrium fractionation factor, the vibrational frequencies, ν , and the moment of inertia, I , have to be known, which can be determined by spectroscopic measurements (e.g. infrared, Raman, and inelastic neutron scattering measurements) or force field modeling (e.g. modified Urey-Bradley force field – MUBFF and density functional theory

– DFT) and from the molecular structure, respectively (e.g. Anbar et al., 2005; Georg et al., 2007; Hill and Schauble, 2008; Jarzecki et al., 2004; Méheut et al., in press; Schauble et al., 2001). Calculations based on Mössbauer spectroscopy data and inelastic nuclear resonant x-ray scattering (INRXS) are also used to predict inter-mineral stable isotope fractionation (e.g. Mineev et al., 2007; Polyakov and Mineev, 2000; Polyakov, 1997).

Analogous to *Equation 1.8*, the equilibrium constant of the isotope exchange reaction between substance A and B and therefore α can be expressed as partition function ratios:

$$\alpha_{A-B} = \frac{Q_{light\ A}/Q_{heavy\ A}}{Q_{light\ B}/Q_{heavy\ B}}. \quad (1.21)$$

Calculated partition function ratios are usually reported as reduced partition functions (β -factors), which ignore translational and rotational energies. From these β -factors, the equilibrium fractionation factor can be calculated according to:

$$\alpha_{A-B} = \frac{\beta_A}{\beta_B} \text{ or}$$

$$1000 \ln a_{A-B} = 1000 \ln \beta_A - 1000 \ln \beta_B. \quad (1.22)$$

The sign and magnitude of equilibrium isotope fractionation is governed by many aspects, which have been summarized in a few simplified qualitative rules by Schauble (2004). These rules predict large equilibrium isotope fractionation between substances at low temperatures, where marked differences in oxidation state, bond partners, electron configuration or coordination number exist.

- Equilibrium isotope fractionation decreases with increasing temperature roughly in the proportion $1/T^2$.
- Fractionation is largest for elements of low atomic mass and large relative mass differences between the isotopes of interest.
- Heavy isotopes of an element prefer the strongest bonds when incorporated into a substance. High bond stiffness correlates with the following properties: high oxidation state, bonding to elements near the top of the periodic table, highly covalent bonds, low-spin electronic configuration for transition elements and low coordination number.

Kinetic isotope fractionation

Kinetic isotope fractionation between different phases can occur during incomplete isotope exchange reactions. Such a non-equilibrium effect can be caused by differences in the reaction rate constants of different isotopes of an element as a result of the mass-dependence of bond strength, i.e. $^{heavy}AB$ reacts more slowly than $^{light}AB$. Kinetic isotope effects can occur during unidirectional reactions or incomplete processes, such as evaporation, diffusion or dissociation reactions. Many aspects drive kinetic isotope fractionation, however, one of the most common effects observed in nature and in laboratory experiments for various stable isotope systems are differences in the molecular and atomic velocity.

The mass of a molecule or atom affects its velocity, which can lead to isotope fractionation during unidirectional reactions. This can be illustrated for an ideal gas, where the translational kinetic energy E_{kin} is equivalent for all molecules or atoms:

$$E_{kin} = \frac{3}{2}kT = \frac{1}{2}mv^2, \quad (1.23)$$

where k is the Boltzmann's constant, T is the absolute temperature, m is the mass of the molecule or the atom, and v is its velocity. For molecules or atoms of different isotope composition, the velocities differ according to:

$$\frac{m_{light}}{m_{heavy}} = \frac{v_{heavy}^2}{v_{light}^2}. \quad (1.24)$$

Therefore, the isotope fractionation process is governed by the molecular or atomic velocity giving a translational isotope fractionation factor $\alpha_{translational}$:

$$\alpha_{translational} = \sqrt{\frac{m_{heavy}}{m_{light}}}. \quad (1.25)$$

1.1.2. Natural Fe isotope variation

The field of stable Fe isotope research emerged about 10 years ago when Fe isotope variations were discovered in many geobiological systems. In the last few years, research has been accelerated with over 200 articles being published on analytical methods, natural variation in Fe isotope ratios and experimental and theoretical investigations on mechanisms and degrees of isotope fractionation.

Fe is the most abundant element on Earth after O. As most of the Fe is concentrated in the Earth's core, it represents the fourth-most abundant element in the Earth's crust after O, Si and Al (Wedepohl, 1995). Fe is an important element in biogeochemical cycles on Earth, where it is a vital nutrient for organisms, and is a major element in many rock-forming minerals, including economically interesting Fe ore deposits. Fe participates in many abiotic and biotic mediated redox processes and has a variety of bonding partners and ligands, which mainly control equilibrium isotope fractionation. Fe has four stable isotopes, ^{54}Fe , ^{56}Fe , ^{57}Fe and ^{58}Fe with approximate abundances of 5.85%, 91.75%, 2.12% and 0.28% of total Fe, respectively (De Laeter et al., 2003). Fe isotope compositions are usually reported relative to the reference material IRMM-014 as followed:

$$\frac{\delta^{56}\text{Fe}}{\text{‰}} = \frac{\left(\frac{^{56}\text{Fe}}{^{54}\text{Fe}}\right)_{\text{sample}} - \left(\frac{^{56}\text{Fe}}{^{54}\text{Fe}}\right)_{\text{IRMM-014}}}{\left(\frac{^{56}\text{Fe}}{^{54}\text{Fe}}\right)_{\text{IRMM-014}}} * 1000 \quad (1.25)$$

$$\frac{\delta^{57}\text{Fe}}{\text{‰}} = \frac{\left(\frac{^{57}\text{Fe}}{^{54}\text{Fe}}\right)_{\text{sample}} - \left(\frac{^{57}\text{Fe}}{^{54}\text{Fe}}\right)_{\text{IRMM-014}}}{\left(\frac{^{57}\text{Fe}}{^{54}\text{Fe}}\right)_{\text{IRMM-014}}} * 1000 \quad (1.26)$$

The first attempts to measure stable Fe isotope compositions were carried out using thermal ionization mass spectrometry (TIMS) (e.g. Dixon et al., 1993; Walczyk, 1997). Significant analytical difficulties, for example high ionization potential of Fe and variable instrumental mass discrimination, are associated with this method. Nowadays, Fe isotopes are analyzed routinely in many laboratories using MC-ICP-MS, (e.g. see review of Dauphas and Rouxel (2006) and references therein). In addition, *in situ* techniques as laser ablation coupled to MC-ICP-MS (e.g. Graham et al., 2004; Horn et al., 2006; this study), secondary ionization mass spectrometry (SIMS) (e.g. Whitehouse and Fedo, 2007) and time of flight resonant ionization mass spectrometry (RIMS) (e.g. Tripa et al., 2002) have been applied to the determination of Fe isotope variations at high spatial resolution.

The overall variation in $\delta^{56}\text{Fe}$ observed in natural systems on Earth is about 5‰ (see overview in *Figure 1.1*). Mass-dependant fractionation up to several hundreds of permil and mass-independent fractionation have been reported for extraterrestrial materials such as cosmic spherules, presolar SiC grains and calcium-aluminum-rich inclusions (CAIs) in meteorites (e.g. Engrand et al., 2005; Tripa et al., 2002; Völkening and Papanastassiou, 1989). However, the limited range of $\delta^{56}\text{Fe}$ in chondrites, meteorites thought to originate from Mars and Vesta, lunar rocks, and igneous rocks from Earth suggest a largely homogeneous Fe isotope composition of

the solar system. Only small differences appear to exist between planetary bodies (e.g. Poitrasson, 2007; Schoenberg and von Blanckenburg, 2006). The Fe isotope composition of igneous rocks seems to be influenced slightly by magmatic processes, as more evolved rocks show slightly higher $\delta^{56}\text{Fe}$ values than less evolved rocks (e.g. Poitrasson and Freydier, 2005; Schuessler et al., in press; Teng et al., 2008). The bulk silicate Earth is estimated to have a $\delta^{56}\text{Fe}$ value of about 0.1‰ (Beard et al., 2003).

The degree of equilibrium isotope fractionation increases with decreasing temperature causing a larger variability in low temperature systems. In the biosphere, Fe is an important nutrient for plants and higher organisms. Investigations of plants, animals, and the human body, exhibit large fractionations with preferential incorporation of isotopically light Fe making Fe isotopes an attractive tracer for biological processes (e.g. Guelke and von Blanckenburg, 2007; Walczyk and von Blanckenburg, 2002; Walczyk and von Blanckenburg, 2005). Biological processes, redox changes and adsorption determine the variability of Fe isotope composition of modern aquatic systems, which exhibit largely negative $\delta^{56}\text{Fe}$ values (e.g. Bergquist and Boyle, 2006; Fantle and De Paolo, 2004; Teutsch et al., 2005). Considerable variations in the marine environment provide information on the biogeochemical Fe cycle of the modern and ancient ocean. Modern mid-ocean ridge (MOR) hydrothermal fluids exhibit a limited range of Fe isotope compositions and are slightly depleted in isotopically heavy Fe (e.g. Beard et al., 2003; Severmann et al., 2004; Sharma et al., 2001). Sulfide deposits around oceanic smokers are variable with tendency to low $\delta^{56}\text{Fe}$ values (Rouxel et al., 2004). Mobilized Fe in pore waters of sediments varies from strongly negative to slightly positive $\delta^{56}\text{Fe}$ values, depending whether microbial dissimilatory iron reduction (DIR) or sulfate reduction dominates organic matter degradation (e.g. Bergquist and Boyle, 2006; Severmann et al., 2006). Phanerozoic organic-rich sediments (black shales) exhibit variations of up to 1‰, which is interpreted as diagenetic Fe cycling through several pathways including: microbial organic matter degradation liberating Fe from ferric (hydr)oxides and the diagenetic formation of pyrites and Fe carbonates (e.g. Matthews et al., 2004; Rouxel et al., 2005). In contrast, sediments with low organic content such as grey shales, turbidites, suspended river load, and loess exhibit a more restricted range close to the average igneous rock composition (e.g. Beard et al., 2003). Fe-Mn crusts and nodules show negative but variable $\delta^{56}\text{Fe}$ values and may record recycled Fe from continental shelf sediments released by microbial activity (Chu, 2006; Levasseur et al., 2004; Zhu et al., 2000). Fe isotope studies on Precambrian sediments have revealed significant variations, providing insights into the ancient Fe cycle before the rise of oxygen in the atmosphere. Black shales and sedimentary pyrites show large Fe isotope fractionation ranging from positive to significant negative $\delta^{56}\text{Fe}$

values. A similar range is observed in iron formations. These variable Fe isotope compositions are interpreted to result from: partial Fe(II) oxidation in the upper ocean, variable seawater composition, diagenetic reduction of Fe oxides, and the formation of diverse Fe-bearing minerals (e.g. Dauphas et al., 2004; Johnson et al., 2003; Johnson et al., 2008a; Rouxel et al., 2005; Whitehouse and Fedo, 2007; Yamaguchi et al., 2005; this study). Stromatolitic limestones are variably depleted in isotopically heavy Fe and may serve as proxy of the ancient seawater composition (von Blanckenburg et al., 2008).

Fe ore deposits exhibit significant variations in Fe isotope composition, which are considered to result from partial Fe(II) oxidation and mineral-fluid fractionation during the formation of Fe ore mineral as sulfides, oxides and carbonates (e.g. Graham et al., 2004; Horn et al., 2006; Markl et al., 2005).

In order to interpret Fe isotope variations in nature, equilibrium and kinetic fractionation factors, ranging from near-zero to about 3‰ for distinct reactions, have been determined by experimental and theoretical approaches. Laboratory studies have investigated abiotically and biotically mediated reactions involving different aqueous Fe species, Fe redox changes, adsorption, and mineral precipitation and dissolution (e.g. Brantley et al., 2004; Bullen et al., 2001; Crosby et al., 2005; Crosby et al., 2007; Icopini et al., 2004; Johnson et al., 2002; Johnson et al., 2005; Matthews et al., 2001; Schuessler et al., 2006; Teutsch et al., 2005; Welch et al., 2003; Wiederhold et al., 2006; Wiesli et al., 2004). Besides experimental work, Fe isotope fractionation has been predicted from vibrational force field modeling and from vibrational spectroscopic data for Fe complexes in solution (Anbar et al., 2005; Hill and Schauble, 2008; Jarzecki et al., 2004; Schauble et al., 2001). Equilibrium fractionation factors between minerals have also been estimated using calculations based on Mössbauer spectroscopic data and inelastic nuclear resonant X-ray scattering (Mineev et al., 2007; Polyakov and Mineev, 2000; Polyakov, 1997). Relevant Fe isotope fractionation factors for the examination of Precambrian iron formation genesis are summarized in *Chapter 3* (see *Table 3.4*).

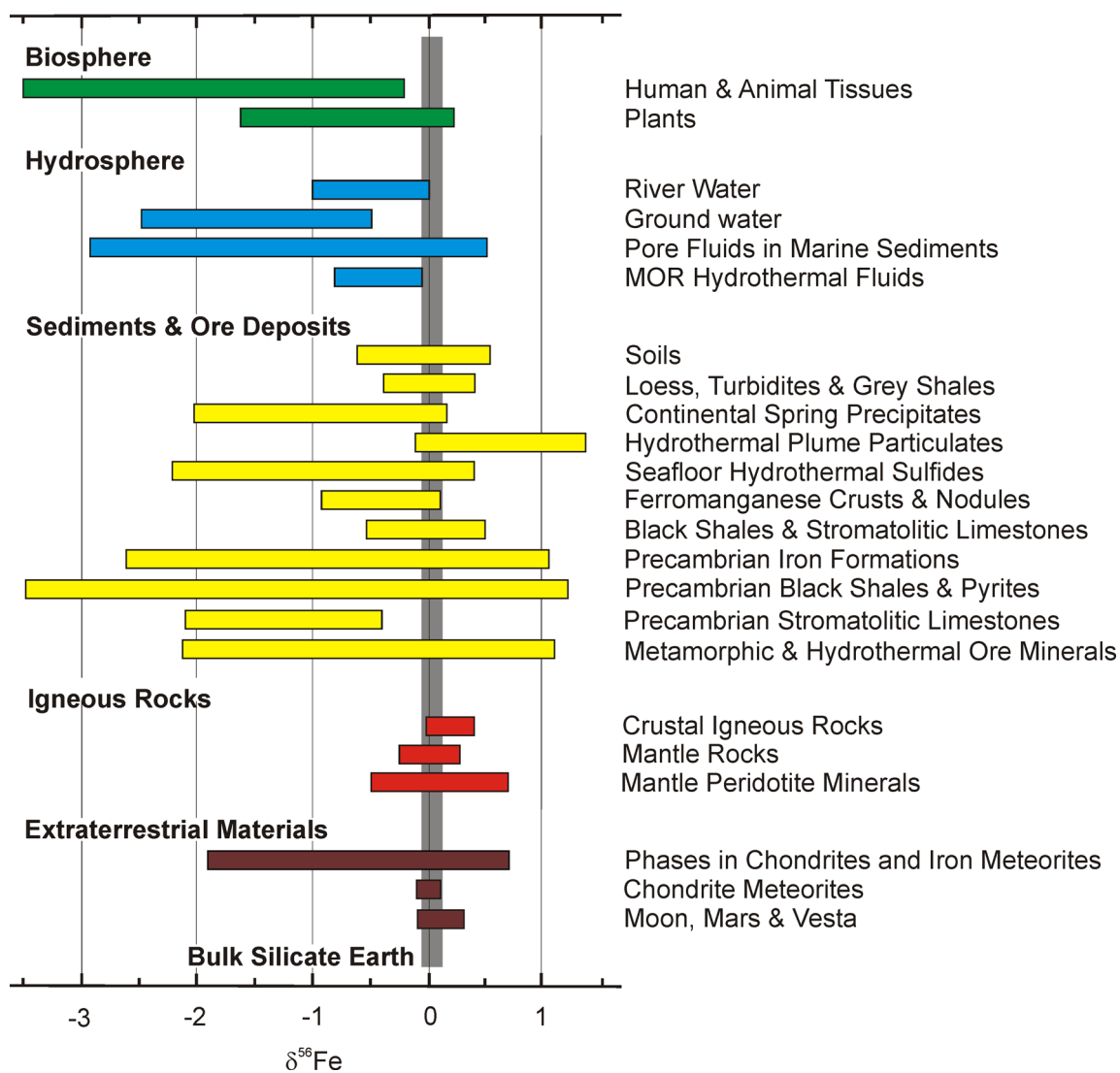


Figure 1.1 Overview of natural Fe isotope variations (for references see recent reviews of Anbar and Rouxel (2007), Beard and Johnson (2004) and Dauphas and Rouxel (2006)).

1.1.3. Natural Si isotope variation

Si is the second-most abundant element in the silicate earth after O. It possesses three stable isotopes, ^{28}Si , ^{29}Si and ^{30}Si , with approximate relative abundances of 92.22%, 4.69% and 3.09%, respectively (De Laeter et al., 2003). In recent years, Si isotope compositions are reported relative to the reference material NBS28 defined as:

$$\delta^{30}\text{Si} \text{‰} = \frac{\left(\frac{^{30}\text{Si}}{^{28}\text{Si}} \right)_{\text{sample}} - \left(\frac{^{30}\text{Si}}{^{28}\text{Si}} \right)_{\text{NBS28}}}{\left(\frac{^{30}\text{Si}}{^{28}\text{Si}} \right)_{\text{NBS28}}} * 1000 \quad (1.27)$$

$$\delta^{29}\text{Si} \text{‰} = \frac{\left(\frac{^{29}\text{Si}}{^{28}\text{Si}} \right)_{\text{sample}} - \left(\frac{^{29}\text{Si}}{^{28}\text{Si}} \right)_{\text{NBS28}}}{\left(\frac{^{29}\text{Si}}{^{28}\text{Si}} \right)_{\text{NBS28}}} * 1000 \quad (1.28)$$

Si is an important constituent in igneous and sedimentary rocks, soils, plants and biominerals. Si is utilized by diatoms, radiolaria and sponges and is present as a solute in aquatic systems. Continental weathering involves decomposition of silicates, resulting in the removal of CO_2 from the atmosphere (Berner, 1997). The formation of clay minerals and soils provides soluble Si for the terrestrial vegetation (Alexandre et al., 1997; Ma, 2003; Sommer et al., 2006). Continental drainage is the major source of dissolved Si entering the oceans (Elderfield and Schultz, 1996; Treguer et al., 1995). In the modern ocean, Si is one of the main nutrients for phytoplankton production and biomineralization, i.e. primary diatoms, which control Si removal from seawater (Ragueneau et al., 2000). In the absence of silica-secreting organisms in the Precambrian ocean, Si precipitation might have been promoted by reaching the saturation state of amorphous silica gel causing the formation of extensive chert deposits such as the Precambrian iron formations and other siliceous deposits (Maliva et al., 2005; Siever, 1992).

Up to 2008, nearly 100 articles on stable Si isotopes were published dealing with fractionation in natural systems and analytical methods. The majority of these articles have been released in the past 5 years demonstrating an immensely increased interest in this research field based on the new ability to routinely determine precise stable Si isotope ratios. Most studies have focused on the characterization of different Si isotope reservoirs, whereas investigations on processes causing Si isotope variations and quantification of the magnitude of isotope fractionation using theoretical or experimental methods are rare (e.g. Georg et al., 2007; Méheut et al., in press). The first investigations of stable Si isotopes in the 1950s (Allenby, 1954; Reynold and

Verhoogen, 1953) were compromised by the complexity of Si purification methods prior to analysis, as well as the poor analytical precision and accuracy achievable at that time. These early studies are only of historical interest as the large proposed variations in terrestrial samples could not be confirmed by later studies. In subsequent studies, more precise and accurate analysis of Si isotope ratios became possible by using isotope ratio mass spectrometry (IRMS), which combines laser fluorination with gas source mass spectrometry (De La Rocha et al., 1998; Douthitt, 1982; Molini-Velsko et al., 1986; Tilles, 1961). However, the utilization of dangerous gases, i.e. F₂ gas, has prevented a widespread application of this method. The introduction of MC-ICP-MS in the mid 1990s has opened a wide field of applications in the Earth Sciences including the analysis of stable Si isotopes (e.g. André et al., 2006; Cardinal et al., 2003; Cardinal et al., 2005; Cardinal et al., 2007; De La Rocha, 2002; Engström et al., 2006; Georg et al., 2006; van den Boorn et al., 2006). Prior to analysis using solution MC-ICP-MS, Si needs to be separated and purified by wet-chemical procedures after sample decomposition (e.g. Brzezinski et al., 2003; Cardinal et al., 2003; Georg et al., 2006; van den Boorn et al., 2006). *In situ* techniques such as laser ablation MC-ICP-MS (Chmeleff et al., 2008; Shahar and Young, 2007; this study) and SIMS (Basile-Doelsch et al., 2005; Hua et al., 2005; Robert and Chaussidon, 2006), now provide the possibility for high-spatial resolution analysis while maintaining sufficient accuracy and precision to resolve Si isotope variations in natural samples. The variation of $\delta^{30}\text{Si}$ found in nature covers a range of approximately 12‰, from -5.7‰ (siliceous cements in sandstones (Basile-Doelsch et al., 2005)) to 6.2‰ (rice grains (Ding et al., 2005)) (Figure 1.2). An exception are presolar SiC grains and early solar calcium-aluminium-rich inclusions (CAIs) in primitive meteorites which exhibit variations of several tens to hundreds of permil (Ding et al., 1996; Lugaro et al., 1999; Shahar and Young, 2007). The small range in $\delta^{30}\text{Si}$ for chondrites and achondrites from Mars and Vesta implies Si isotope homogeneity in the Solar system (e.g. Georg et al., 2007). Mantle and mantle-derived mafic magmatic rocks overlap with meteorite compositions suggesting that early Earth differentiation and later mantle processes have had no major impact on Si isotope fractionation (Ding et al., 1996; Douthitt, 1982; Georg et al., 2007). Crustal igneous rocks show a slight increase in $\delta^{30}\text{Si}$ with increasing SiO₂ content (Ding et al., 1996; Douthitt, 1982; Georg et al., 2007; Ziegler et al., 2005). The estimated Si isotope composition for the bulk silicate Earth is -0.4‰ (Douthitt, 1982; Georg et al., 2007). Quartzites and sandstones are in the same range as crustal igneous rocks as these are derived from the latter (Ding et al., 1996). Clays, slates, schists and soils exhibit variable low $\delta^{30}\text{Si}$ values (Ding et al., 1996; Ding et al., 2007; Ding et al., 2008; Street-Perrott et al., 2008; Wu et al., 1997; Ziegler et al., 2005). Degradation of silicate minerals in

igneous rocks by weathering produces clay minerals of low $\delta^{30}\text{Si}$ values and releases dissolved Si with high $\delta^{30}\text{Si}$ values that dominate river waters (Alleman et al., 2005; De La Rocha et al., 2000; Ding et al., 2004; Georg et al., 2006; Georg et al., 2007; Ziegler et al., 2005). Soluble Si is partially utilized by higher plants with preferential uptake of light Si isotopes and precipitated as biogenic opaline phytoliths (Ding et al., 1996; Ding et al., 2005; Ding et al., 2008; Douthitt, 1982; Hodson et al., 2008; Opfergelt et al., 2006a; Opfergelt et al., 2006b; Sun et al., 2008). Plants exhibit large $\delta^{30}\text{Si}$ variations caused by uptake of dissolved Si with variable Si isotope composition and intra-plant fractionation. Recycling of phytoliths by the degradation of organic matter has a major impact on the Si composition of soils (e.g. Opfergelt et al., 2006a). Siliceous cements in sandstone exhibit strongly negative $\delta^{30}\text{Si}$ values, which are attributed to quartz reprecipitation (Basile-Doelsch et al., 2005). The Si isotope budget of the ocean is mainly controlled by the supply of isotopically heavy river water (Alleman et al., 2005; De La Rocha et al., 2000; Ding et al., 2004; Georg et al., 2006; Georg et al., 2007) and the preferential removal of light Si isotopes by biomineralization (primary diatoms) (Alleman et al., 2005; Beucher et al., 2008; Cardinal et al., 2005; Cardinal et al., 2007; De La Rocha et al., 1998; De la Rocha, 2003; Douthitt, 1982; Fripiat et al., 2007; Milligan et al., 2004; Varela et al., 2004), which promote positive $\delta^{30}\text{Si}$ values in seawater (Beucher et al., 2008; Cardinal et al., 2005; Cardinal et al., 2007; De La Rocha et al., 2000; Reynolds et al., 2006; Varela et al., 2004). Another source of Si to the ocean is mid-ocean ridge hydrothermal fluids, which appear to have slightly negative $\delta^{30}\text{Si}$ values (De La Rocha et al., 2000). Seafloor siliceous deposits derived from those hydrothermal fluids show more negative $\delta^{30}\text{Si}$ values (Ding et al., 1996; Douthitt, 1982). The same trend is observed for continental hot springs and associated siliceous deposits (Ding et al., 1996; Douthitt, 1982; Pan et al., 2001; Xu, 2001). Precambrian marine siliceous deposits originated from abiotic Si precipitation. Chert within Precambrian iron formation exhibits negative $\delta^{30}\text{Si}$ values (André et al., 2006; Ding et al., 1996; Jiang et al., 1993; this study) in the range of modern seafloor siliceous deposits around oceanic smokers, whereas other Precambrian siliceous deposits show a wider range including positive $\delta^{30}\text{Si}$ values (Robert and Chaussidon, 2006; van den Boorn et al., 2007).

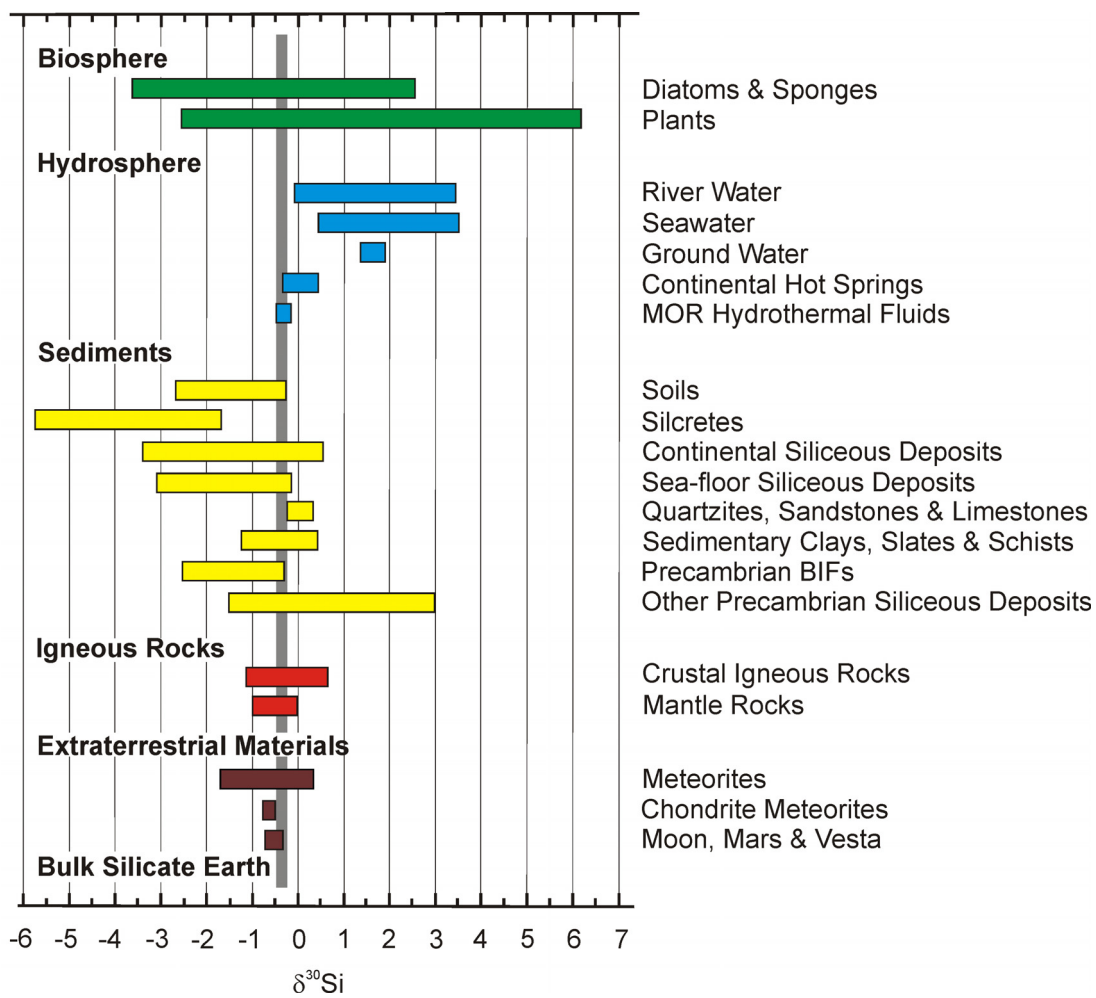


Figure 1.2 Overview of natural Si isotope variations (see text for references).

1.2. Laser Ablation

With the introduction of commercially available inductively coupled plasma mass spectrometers (ICP-MS) in the mid 1980s, laser ablation was immediately investigated for the direct analysis of solid samples (Gray, 1985). Today, laser ablation is a powerful and very sensitive micro-analytical technique for the determination of element and isotope compositions with wide applications in geosciences, chemistry and biosciences. Several advantages make laser ablation to an attractive alternative to solution analysis. There is no complicated sample preparation, which allows fast data acquisition while at the same time avoiding contamination. In addition, high-spatial resolution at high sensitivity is acquired with only small quantities of sample material consumed. However, major drawbacks of laser ablation are laser-related element and isotope fractionation and matrix-effects demanding a non-linear and matrix-matched calibration, which set limits on the obtainable precision and the applicability of the method. Nowadays, most laser ablation systems employ solid state Nd-YAG (Neodymium:Yttrium-Aluminum-Garnet) lasers operating in the ultraviolet (UV) range at wavelengths of 266 nm and 193 nm or ArF gas Excimer lasers with a typical wavelength of 193 nm. Both types of laser provide pulses width typically between 5 and 23 ns ($1 \text{ ns} = 10^{-9} \text{ s}$). These lasers have been successfully applied to the analysis of elemental compositions and isotope ratio determinations of various non-conducting materials such as silicate glasses and minerals (e.g. Gao et al., 2002; Jackson et al., 1992; Jackson et al., 2004; Jochum and Willbold, 2006; Jochum et al. 2007; Yuan et al., 2004). The analysis of semi-conductors and conductors remains challenging due to the heat-affected zone surrounding the laser ablated crater, leading to material redistribution (e.g. Bleiner and Graser, 2004; Košler et al., 2005). Many studies have investigated strategies to overcome these limitations for nanosecond laser ablation, with the conclusion that problems have to be solved individually for each specific application. Recent analytical developments in laser ablation favor the use of ultra-short pulses with a pulse width in the femtosecond range ($1 \text{ fs} = 10^{-15} \text{ s}$). fs pulses exhibit a different ablation behavior when compared to ns pulses having the potential to diminish many limitations previously observed during laser ablation. So far, only a few laboratories utilize femtosecond laser ablation systems either in conjunction with quadrupole ICP-MS for minor and trace element analysis or multiple collector ICP-MS (MC-ICP-MS) for the determination of isotope ratios. Recent studies illustrate the analytical potential of applying ultra-short pulses in the near infra-red (NIR) to UV range in laser ablation (see reviews of Fernández et al. (2007) and Horn (2008)).

1.2.1. Comparison between femtosecond and nanosecond laser ablation

Ablation encompasses a sequence of processes: the deposition of the laser energy onto the solid sample, phase transformation of the laser affected material, ejection of the material from the sample surface and expansion of the plasma plume. For ns pulses, these processes overlap in time and consequently influence one another, whereas for fs pulses, the energy deposition ends before the material starts to react to the incoming pulse. The differences in material removal using fs pulses and ns pulses can be understood by considering the interaction of laser irradiation and sample material, which has been reviewed by Hergenröder et al. (2006a) (see also for references). The deposition of laser energy into any material is always mediated by electrons. An incoming electromagnetic wave in the form of a short pulse of light with a wavelength in the UV to near IR range excites the electrons, which transfer the energy via collision to the lattice, attaining thermodynamic equilibrium after ~ 10 ps (10^{-12} to 10^{-11} s). This describes the boundary between thermal and non-thermal pathways and establishes the fundamental difference between ns and fs pulses for laser ablation, which is visible in crater morphology (*Figure 1.3*).

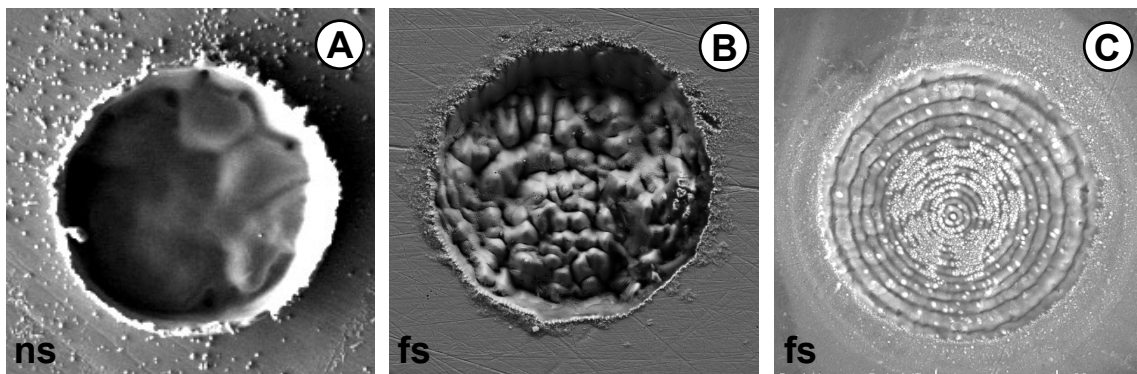


Figure 1.3 Laser spots in pure iron of about 35 μm diameter using ns and fs pulses. **A)** Laser spot using an Eximer laser with a wavelength of 193 nm and a pulse width of 12 ns (ETH Zürich). The molten bottom of the crater, the high crater rim and the spherical particles around the crater are evidence for significant melting during ablation. **B)** Laser spot using a Ti:Sapphire regenerative amplifier system with a wavelength of 196 nm and a pulse width of ~ 200 fs (Leibniz Universität Hannover). Evidence of melting is not observed. The heterogeneity of the crater bottom reflects the heterogeneous energy distribution of the laser beam. **C)** Spot after ~ 10 pulses using the same laser setup. The imprint of so-called Newton Rings reflects an interference pattern of the laser beam caused by apertures in the laser system.

Two-temperature model

The difference between ns and fs pulses in the pathway of energy deposition into the material can be described by the two-temperature model, considering electrons and lattice as separate systems (e.g. Nolte et al., 1997). The energy of the laser irradiation is absorbed by free electrons without affecting the lattice. The time-scale of energy relaxation within the electrons is much shorter ($\sim 10^{-15}$ s) than the time necessary to transfer the energy to the lattice (10^{-12} to 10^{-11} s). As a result electrons and lattice are ascribed to two different temperatures. This is significant when applying pulses with pulse width of ~ 100 fs, as the laser irradiation is over before electrons and lattice attain thermal equilibrium. Energy deposition using ns pulses is much slower, therefore electrons and lattice are considered to have reached their equilibrium temperature during laser irradiation, and thermal diffusion in the lattice is significant carrying the energy away from the irradiated volume into the bulk material.

Ablation mechanisms

The ablation mechanism for ns and fs pulses always includes more than one process (e.g. Lorazo et al., 2006). While thermal pathways dominate the ns ablation process, non-thermal pathways are considered to be significant during the fs ablation process. Based on modeling, the ns ablation process occurs in thermodynamic equilibrium as the energy deposition on the laser-irradiated spot is limited. Thermal diffusion distributes the energy to the bulk material. The incoming pulse interacts with the expanding plume as the onset of material removal takes places during the pulse after 1 to 100 ps. This phenomenon is known as plasma shielding and limits the energy transfer onto the sample surface (Mao and Russo, 1997; Mao et al., 1996). Both thermal diffusion and plasma shielding limit the attainable energy density on the sample surface. The ablation process for ns pulses follows pathways in thermodynamic equilibrium from solid through liquid into a plasma state (pathway 1 in *Figure 1.4*). The long duration of the pulse initiates melting of the material and affects the material around the ablation crater, known as ‘heat-affected’ zone, which in turn leads to non-stoichiometric ablation. For metals, this ‘heat-affected’ zone would be approximately $1 \mu\text{m}$ (Hergenröder et al., 2006).

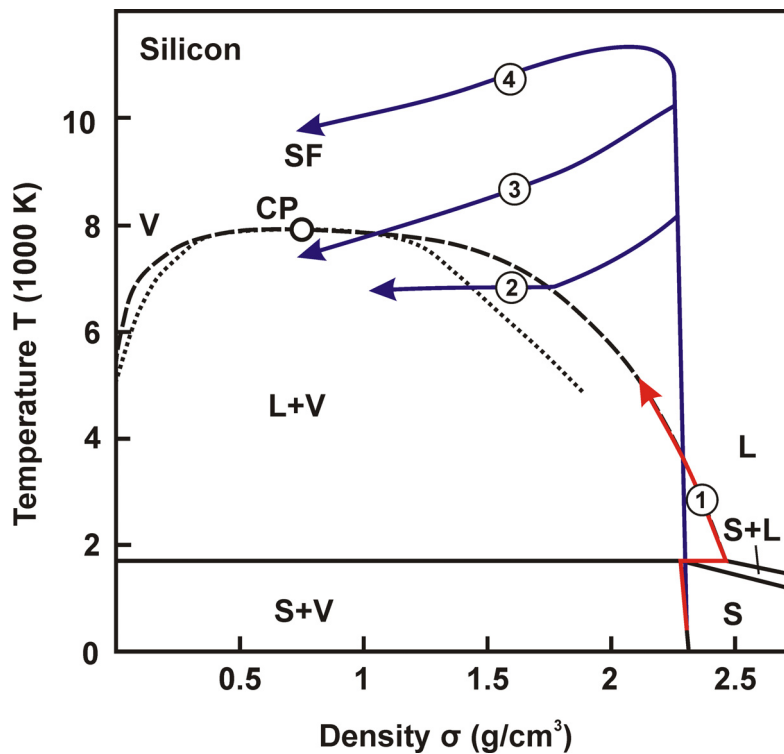


Figure 1.4 Schematic illustration of the dominant thermodynamic pathways for ns pulses (red) and fs pulses (blue) in a temperature-density phase diagram of silicon (modified after Lorazo et al. (2006)): 1) normal vaporization and boiling, 2) explosive phase separation/explosive boiling, 3) critical-point phase separation/spinodal decomposition and 4) ‘non-trivial’ fragmentation. The dashed line represents the binodal curve, which is the boundary between a one-phase and a two-phase regime. The dotted line is the spinodal curve, which describes the boundary to the absolute mechanical instability. The zone between the binodal and spinodal curve is the metastable zone. S = solid, L = liquid, V = vapour, CP = critical point, SF = supercritical fluid ($T > T_{\text{critical}}$, $\sigma > \sigma_{\text{critical}}$). See text for details.

The fs ablation process involves non-thermal pathways. The deposition of the laser energy ends before electron-lattice equilibrium is achieved and material removal occurs, therefore thermal diffusion and plasma shielding is considered to be negligible. This provides a high concentration of the energy onto the irradiated material turning the ablation processes away from thermal pathways. The material is heated isochorically to temperatures in the range of $\sim 10^4$ K within the supercritical regime generating a high internal pressure gradient. Subsequently, adiabatic cooling promotes homogeneous expansion of the material until the onset of the material removal (pathways 2 to 4 in *Figure 1.4*). The short pulse duration allows full energy deposition on the irradiated spot, which initiates material removal under thermodynamic disequilibrium promising a way to stoichiometric ablation. The laser-affected zone around the crater is less than several 10's of nm, even for metals with a high thermal diffusivity (Hergenröder et al., 2006).

Although, it is clear that material removal during fs pulses differs significantly from that of ns pulses, the underlying mechanisms are still subject of intensive investigation. As experimental measurements of transient parameters such as temperature and pressure during ns and fs pulses are highly challenging, most efforts have been concentrated on theoretical approaches using molecular dynamics simulations to explore the ablation mechanisms of semi-conductors and conductors (e.g. Bouilly et al., 2007; Cheng and Xu, 2005; Lorazo et al., 2006; Miotello and Kelly, 1999; Perez and Lewis, 2003; Zhigilei and Garrison, 2000; Zhigilei, 2003). In the following paragraph, the general mechanisms of material removal are summarized based on the aforementioned references. Depending on the laser fluence and pulse width, the following ablation mechanisms may take place (see *Figure 1.4*):

1. Normal vaporization and boiling
2. Explosive phase separation (explosive boiling)
3. Critical-point phase separation (spinodal decomposition)
4. "Non-trivial" fragmentation
5. Photomechanical spallation

Normal vaporization and boiling are dominant processes governing ns ablation (pathway 1 in *Figure 1.4*). The sample material is heated slowly, reaching thermodynamic equilibrium. Heating of the material follows therefore the solid-liquid and liquid-vapor phase boundaries along the binodal curve. Normal vaporization occurs on the outer surface of the sample material, where atoms of the outer layer pass into the vapor phase. Normal boiling involves the heterogeneous formation of vapor bubbles in the liquid phase at boiling temperature, which escape by diffusion. The material is removed by heterogeneous melting and vaporization.

Explosive phase separation or explosive boiling refers to the explosion-like relaxation of a supercritical liquid (pathway 2 in *Figure 1.4*). This process appears to be significant at high energy densities ($> 10^{11}$ W/cm²) either reached by high fluence (> 400 J/cm²) (Lu et al., 2002) or ultra-short pulses. As these extremely high fluences are not achievable by commercially available nanosecond laser ablation systems, this process seems to be only a dominant pathway for fs pulses with fluences between ~ 0.2 to 1.5 J/cm². It is predicted that the material undergoes a rapid transition from an overheated liquid to a mixture of vapor bubbles and liquid droplets. After heating of the surface region into the subcritical state by laser irradiation, the superheated liquid undergoes rapid adiabatic cooling by expansion into the liquid-vapor regime entering the metastable region. Highly localized thermal fluctuations cause density fluctuations, which causes homogeneous nucleation of a stable vapor phase in the metastable liquid phase.

Critical-point phase separation or spinodal decomposition (pathway 3 in *Figure 1.4*) is a principal ablation mechanism for fs pulses at high fluence (> 1.5 J/cm²). As a result of an extraordinary heating rate, the material exceeds the critical temperature and turns from the solid phase into a supercritical liquid. Phase separation occurs in the unstable zone, which is entered close to the critical point by adiabatically cooling.

“Nontrivial” fragmentation may occur at high fluence (> 1.5 J/cm²) for fs pulses. In this case, the onset of ablation occur in the supercritical regime above the critical point (temperature $T > T_{\text{critical}}$, density $\sigma > \sigma_{\text{critical}}$) and hence cannot be ascribed to any phase transition. The high pressure gradient that builds up in the material by rapid isochoric heating causes rapid expansion of the initially homogeneous material. This leads to a heterogeneous clustered fluid through a ‘nontrivial’ fragmentation process.

Photomechanical spallation might play a role at near-threshold fluence for ablation (for fs pulses: ~ 0.05 J/cm²) or in inhomogeneous materials, i.e. polycrystalline samples. The incoming laser irradiation generates tensile stress in the target, which can lead to subsurface cavitation and mechanical fracturing followed by ejection of large, irregular shaped particles.

Particle characteristics

The generation of particles by laser ablation, their size distribution and the chemical composition are of particular interest as the complexity of related elemental and isotope fractionation involving laser-, transport- and ICP-induced phenomena are common limitations for laser ablation analysis (e.g. Guillong and Guenther, 2002; Jackson and Guenther, 2003; Jeong et al., 1999; Koch et al., 2002; Koch et al., 2004; Kozlov et al., 2003; Outridge et al., 1997). Laser-induced fractionation refers to the formation of particles by laser ablation, which

differ in their bulk composition from the sample material. This means that the ablation mechanism is non-stoichiometric. Transport- and ICP-related fractionations are related because both types are significant if large particles contribute to the aerosol. During transport from the ablation site to the ICP, selective particle deposition occurs due to gravitational settling and inertial deposition. Diffusion into the wall-material of the transport tube might be a factor for very small particles (e.g. Koch et al., 2004). ICP-induced fractionation results from incomplete vaporization of particles. Therefore the specific characteristics of an aerosol have a significant impact on the accuracy and precision of the analytical method.

In general, aerosols consists of particles with a size roughly between 10 nm and 10 μm (see overview of Hergenröder (2006a) and references therein). Two types of particles can be distinguished: single solid, often spherical particles, and agglomerates of much finer nm-sized particulates (e.g. Perdian et al., 2008). Typically, particles generated by ns pulses show a bimodal size-distribution with the smaller fraction of ~ 10 nm in diameter and the larger fraction in the μm range. This indicates at least two distinct mechanisms of particle formation. Depending on the matrix, the overall composition of the aerosol can differ significantly from the bulk sample material, an effect, which is pronounced when analyzing conductors (Jackson and Guenther, 2003; Kuhn and Guenther, 2003; Liu et al., 2004; Outridge et al., 1996; Outridge et al., 1997). Using fs pulses, the generated particles are much smaller, largely between 10 and 100 nm, and of a monomodal size-distribution. Recently, the use of fs pulses for ablation has proven to be a way to generate stoichiometric aerosols (Koch et al., 2004; Koch et al., 2005; Koch et al., 2006; Perdian et al., 2008).

Generation of particles. The principle mechanisms of particle generation have been reviewed by Hergenröder (2006a) and include formation of particles from vapor, hydrodynamic sputtering, phase explosion and mechanical spallation. Particle formation processes are investigated by experimental studies and theoretical approaches, but actual the mechanisms are still not completely understood. Small particles (10 to 100 nm) appear to be formed from vapor in the expanding plume after ablation (Bäuerle, 2000; Hergenröder, 2006b; Noël et al., 2007). Rapid expansion promotes a decrease in pressure and temperature, which leads to nucleation and condensation in the supersaturated vapor state. Subsequent coagulation and coalescence of liquid droplets result in particles with a size of a few nm. This mechanism is considered to be the dominant process for the formation of particles with a diameter of less than 100 nm for nanosecond as well as for femtosecond laser ablation (Koch et al., 2004; Luk'yanchuk et al., 1998). The prevailing formation of large spherical particles (μm -size) is related to hydrodynamic sputtering (Hergenröder, 2006c; Webb et al., 1997). This process refers to the

interaction of the expanding plume after ablation with a molten layer in the crater. The lateral expansion of the ablated material causes a surface tension effect in the liquid layer, which result in splashing of large particles. Efficient melting of the sample material occurs during ns pulses but is minimized when using fs pulses, suppressing this effect. Other mechanisms may also produce large particles when using fs pulses. Phase explosion potentially generates both small and large particles due to explosion-like relaxation of a supercritical liquid, which produces a mixture of droplets and vapor (Koch et al., 2004). Such an aerosol is likely for fs pulses at high fluence (Koch et al., 2004; Perez and Lewis, 2003; Russo et al., 2002). Large, irregular shaped particles are contributed by mechanical spallation, which is especially pronounced when ablating inhomogeneous materials (e.g. Brailovsky et al., 1995; Webb et al., 1997).

Size distribution and chemical composition. Particle size distribution becomes relevant in light of particle size-dependent chemical compositions and the efficiency of transport and disintegration of large particles in ICP. The particle-size distribution and composition of the aerosol depends on many parameters including laser wavelength, fluence, pulse duration, sample material, carrier gas and the acquisition time and consequently the depth of the ablation crater (Amoruso et al., 2007; Eggins et al., 1998; Guillong and Guenther, 2002; Guillong et al., 2003; Horn and Guenther, 2003; Horn et al., 2001; Koch and Guenther, 2007; Koch et al., 2004; Koch et al., 2005; Koch et al., 2006; Kuhn and Guenther, 2004; Liu et al., 2004; Russo et al., 2000; Russo et al., 2002; Vadiillo and Laserna, 2004). Wavelength has a major impact on the particle size distribution using ns pulses. The change from IR to the UV range reduces particle size-related fractionation, which is attributed to the generation of smaller particles (Guillong et al., 2003; Horn et al., 2003; Telouk et al., 2003). For fs pulses however, the particle size distribution appears to be largely independent of wavelength (Koch et al., 2006).

Comparative studies have revealed significant differences in the aerosols produced by femtosecond and nanosecond laser ablation of brass (Koch et al., 2004; Liu et al., 2004; Margetic et al., 2000; Margetic et al., 2001; Saetveit et al., 2008). Brass alloys are commonly chosen to investigate the properties of an aerosol because of the different thermal properties of Zn and Cu. In the study by Koch et al. (2004), particle size distribution and chemical composition have been evaluated using low pressure impaction and total reflection X-ray fluorescence (TXRF), respectively. The most promising results for reducing particle size-related fractionation effects have been obtained with NIR femtosecond laser ablation at low fluence ($< 5 \text{ J/cm}^2$) using He as carrier gas. The ultra-fine aerosol shows a monomodal particle size distribution with a peak at 10 nm. The overall Cu/Zn ratio of this aerosol reflects the composition of the sample material, which indicates stoichiometric ablation. At high fluence ($>$

10 J/cm²), femtosecond laser ablation generates a bimodal aerosol with peaks at 20 nm and 1 μm and a total Cu/Zn ratio which slightly differs from the bulk material. Similar particle-size distributions and stoichiometric aerosol composition have been determined for brass alloys and silicate glass by Koch et al. (2005), Liu et al. (2004), Saetveit et al. (2008) and Wälle et al. (2008). In comparison, the study by Koch et al. (2004) shows that nanosecond laser ablation produces a typical bimodal aerosol, consisting of nano-size and μm-size spherical particles, with a significant portion of particles larger than 100 nm. The total Cu/Zn ratio diverges significantly from the sample material indicating non-stoichiometric ablation. Common to fs and ns pulsed ablation is that small particles tend to be enriched in volatile elements, while large particles are depleted in them (Koch et al., 2004; Liu et al., 2005). However, particle size-dependent variations in chemical composition are more pronounced in aerosols produced by ns pulses, as is to be expected considering the different mechanisms of particle generation discussed above. In general, fs pulses produce mostly particles and agglomerates ranging between 10 and 100 nm. This type of aerosol can be transported over long distances (Arrowsmith and Hughes, 1988). Experimental studies show, that the transport efficiency of ultra-fine aerosols released by femtosecond laser ablation is close to 100%, regardless of the ablation cell geometry and the carrier gas used, which enhances signal intensity and stability in ICP-MS (Garcia et al., 2008a; Garcia et al., 2008b; Gonzalez et al., 2006; Koch et al., 2004; Koch et al., 2008; Liu et al., 2004). All these features lead to a significant improvement in precision and accuracy for elemental and isotope analysis using femtosecond laser ablation over commonly employed nanosecond laser ablation systems.

1.2.2. Element and isotope fractionation during laser ablation ICP-MS

Non-stoichiometric effects, if present, are a severe drawback of laser ablation limiting the obtainable accuracy and precision. Elemental and isotope fractionation during laser ablation includes progressively changing elemental and isotope ratios in the course of an analysis, and matrix-dependent elemental or isotope ratios. Fractionation can occur during the ablation process, the transport of the aerosol to the ICP source and the excitation process in the ICP (Figg et al., 1998; Guillong and Guenther, 2002; Jackson and Guenther, 2003). Several processes have been associated with elemental and isotope fractionation during nanosecond laser ablation (see overview by Sylvester (2008)): redistribution of material within the heat-affected zone around the crater (e.g. Košler et al., 2005), preferential vaporation of volatile elements at the ablation site (e.g. Hergenröder, 2006d), preferential condensation of refractory

elements at the crater wall (e.g. Eggins et al., 1998), differential transport of particles with size-dependent composition from the ablation site to the ICP (e.g. Koch et al., 2002), non-congruent vaporization of large incompletely atomised particles in the ICP (e.g. Guillong et al., 2003), and ion-load-dependant mass discrimination in the ICP-MS (e.g. Kroslakova and Guenther, 2007). Recent investigations demonstrate that these laser-related fractionation processes are significantly reduced or even undetectable when using fs laser ablation.

Laser-induced elemental fractionation

The first type of fractionation results from different ablation characteristics of siderophile, chalcophile, lithophile and hydrophile elements (e.g. Longerich et al., 1996). Volatile elements evaporate preferentially into the carrier gas. This effects mainly siderophile elements, e.g. Zn, Pb, Au, Tl, while refractory elements, e.g. Ca, Th, U, the rare earth elements (REE) and high field strength elements (HFSE), are mobilized less efficiently. The different ablation behavior is related to the condensation temperatures derived from studies of meteorites. With increasing crater depth, the transport efficiency of refractory elements decreases due to condensation at high temperatures, whereas volatile elements remain preferentially in the gas phase and are transported more efficiently to the ICP. Therefore the ratio of a volatile element to a refractory element evolves from its true ratio to significant higher values during the course of a spot analysis. This fractionation effect has been studied extensively for the determination of the Pb/U ratio using nanosecond laser ablation as it limits the precision for applications in geochronology (e.g. Hirata and Nesbitt, 1995; Hirata, 2003; Horn et al., 2000; Jackson et al., 2004; Košler et al., 2001; Longerich et al., 1996). For a spot analysis, the Pb/U ratio increases up to 100% within an acquisition time of 100 s. Possible solutions to this problem are the use of short ablation times, the raster-mode or spot analysis, which are corrected by external calibration or mathematical approaches (e.g. Horn et al., 2000; Horstwood et al., 2003; Košler et al., 2001; Simonetti et al., 2005; Sláma et al., 2008). Laser-induced fractionation is significantly less prominent or even undetectable when using fs pulses in the NIR to UV range (Freydier et al., 2008; Hirata and Kon, 2008; Horn and von Blanckenburg, 2007; Koch et al., 2006; Poitrasson et al., 2003; Russo et al., 2002). Wavelength and repetition rate seem to have no effect on the precision but fluence appears to have a significant influence. Best results have been obtained by Horn and von Blanckenburg (2007) with a precision of 0.2% (2 SD) for the $^{206}\text{Pb}/^{238}\text{U}$ ratio. The authors used a 196 nm fs laser ablation system at a fluence of 1.5 J/cm² coupled to a MC-ICP-MS equipped with Faraday detector array (10¹¹ Ω resistor). The Zn/Cu ratio is also commonly used to characterize this type of fractionation as it behaves in the same way as the Pb/U ratios.

While the Zn/Cu ratio is increased over the true ratio of the sample using nanosecond laser ablation, it approaches the true ratio for femtosecond laser ablation (Cromwell and Arrowsmith, 1995; Koch et al., 2004; Liu et al., 2005; Mao et al., 1998; Saetveit et al., 2008). However, the obtainable precision for this ratio appears to be fluence-dependent. The best results were obtained at low fluences ($< 5 \text{ J/cm}^2$) (Koch et al., 2004).

Particle-size related elemental fractionation in the ICP

Particle-size fractionation is related to incomplete disintegration of the aerosol in the ICP. Ionisation efficiency and the degree of fractionation depends mainly on particle size and particle composition, but temperature and particle trajectory in the ICP have also an effect (Aeschliman et al., 2003; Guillong and Guenther, 2002; Olesik, 1997; Perdian et al., 2008; Wang et al., 2006). Fractionation occurs for the incongruent disintegration of a particle, which leads to continuous preferential vaporation of a certain element compared to another element. Although, the average residence time of an particle in the ICP is as short as 1 ms, there is evidence that particles obtain a time-dependent chemical- and isotope compositions when passing the ICP (e.g. Wang et al., 2006). This type of fractionation is commonly investigated by determining U/Th ratios as both elements possess very similar first ionisation potentials and atomic masses. During the course of a spot analysis, ns pulses generate an aerosol evolving from a wide range in particle size with large particles of up to several μm to a more confined distribution of significantly smaller particles, which strongly depends on the wavelength (Guillong and Guenther, 2002; Guillong et al., 2003). Incomplete ionisation in the ICP at the beginning of the analysis leads to a significant increase in the U/Th ratio of up to 200%, converging to the true ratio with continuing ablation (e.g. Gonzalez et al., 2008; Guillong and Guenther, 2002; Koch et al., 2004; Kuhn and Guenther, 2003; Kuhn et al., 2004). In contrast, fs pulses, independent of the wavelength, produce particles which are small enough to prevent this type of fractionation, resulting in a constant and accurate U/Th ratio over the acquisition time (Gonzalez et al., 2008; Hirata and Kon, 2008; Horn and von Blanckenburg, 2007; Koch et al., 2006).

Isotope Fractionation during laser ablation ICP-MS

Potential sources of artificial isotope fractionation using laser ablation coupled to ICP-MS have been discussed by Horn and von Blanckenburg (2007) and Horn (2008). Laser-induced isotope fractionation at the ablation site could be related to preferential vaporization of light isotopes, whereas heavy isotopes might preferentially condense within the laser crater (Jackson and Guenther, 2003; Norman et al., 2006). However, this effect seems unlikely, because the

formation of particles with a high mass prevents significant kinetic isotope effects. Particle size-related isotope fractionation in the ICP, a mechanism similar to elemental fractionation, is the most likely process. The incomplete ionization of large particles in the ICP might result in strong kinetic isotope fractionation, which lead to the preferential evaporation of light isotopes (Horn and von Blanckenburg, 2007; Jackson and Guenther, 2003; Norman et al., 2006). Continuous kinetic fractionation occurs at simultaneous vaporation of light isotopes from the particle surface and a resupply by diffusion maintaining isotopic homogeneity in the particle. If the redistribution of isotopes by diffusion is ineffective, kinetic effects dominate only initially and the particle remains unfractionated. Consequently the significance of kinetic fractionation depends on the diffusion coefficient, a material property and is therefore matrix-dependent. Aerosols generated by ns pulses are characterized by a particle size distribution with large particles shifting towards smaller particles in the course of a spot analysis. This predisposes ns pulses towards this type fractionation, resulting in a transient isotope ratio. In contrast, the ultra-fine aerosols generated by fs pulses likely prevent this type of fractionation. Another potential fractionation effect is related to the space charge effect in the ICP, which is influenced by the ion plasma load. A high ion plasma load forces the preferential extraction of heavy isotopes into the skimmer cone of the mass spectrometer (e.g. Krosiakova and Guenther, 2007). The quantity of ablated material decreases for both ns and fs spot analysis, which leads to a change in the ion plasma load and can result in changing isotope ratios. Variation in the fraction of particle ionisation for ns ablation might amplify this effect, whereas particles of fs ablation appear to be completely ionised. Heavy stable isotope ratios, i.e. Mg, Fe, Cu and Si have been determined by ns and fs laser ablation systems coupled to MC-ICP-MS, which provides insights into laser-related isotope fractionation (Chmeleff et al., 2008; Graham et al., 2004; Hirata and Kon, 2008; Horn and von Blanckenburg, 2007; Horn et al., 2006; Ikehata et al., 2008; Jackson and Guenther, 2003; Košler et al., 2005 ; Norman et al., 2006; Shahar and Young, 2007; Young et al., 2002). The determination of heavy stable isotope ratios are challenging because their natural variations are in the order of parts per thousand, which demands highly precise and accurate analysis.

A gradual increase of isotope ratios towards heavier compositions during ns spot analysis has been reported for the heavy stable isotope systems of Fe, Mg and Cu (Jackson and Guenther, 2003; Košler et al., 2005; Norman et al., 2006), which supports particle-size related isotope fractionation in the ICP. To diminish artificial isotope fractionation for nanosecond laser ablation, raster-mode or line scans, matrix-matched calibration, filtering of the large particle fraction and large spot sizes have been applied for the analysis of Fe, Mg, Cu and Si isotope

ratios (Graham et al., 2004; Jackson and Guenther, 2003; Košler et al., 2005; Shahar and Young, 2007; Young et al., 2002). Significant improvements have been reported for the determination of Cu, Fe and Si isotope ratios using fs pulses (Chmeleff et al., 2008; Horn and von Blanckenburg, 2007; Horn et al., 2006; Ikehata et al., 2008; this study). For instance, fs spot analysis reveal constant Fe isotope ratios at transient signal intensities (Horn and von Blanckenburg, 2007). Precision and accuracy of isotope determination using femtosecond laser ablation have been characterized for the Fe and Si isotope systems by analyses of a variety of matrices using non-matrix matched calibration (Chmeleff et al., 2008; Horn et al., 2006; this study). Achievable precisions are $\pm 0.1\%$ for $^{56}\text{Fe}/^{54}\text{Fe}$ and $\pm 0.2\%$ for $^{30}\text{Si}/^{28}\text{Si}$, which are close to those for solution ICP-MS.

1.2.3. Laser ablation instrumentation

The UV fs laser ablation system is described in detail by Horn et al. (2006) and Horn and von Blanckenburg (2007) and is reviewed in this section (*Figure 1.5*). It is based on a 100 fs Ti:Sapphire regenerative amplifier system (Hurricane I, Spectra-Physics, USA) providing ultra-short laser pulses in the IR spectrum. After frequency conversion into the UV spectrum the laser beam is steered into a New Wave Femto XP front end, which includes the sample stage with an 8x objective, the ablation cell, and a visualization system. The ablated material is then transported by a carrier gas, He or Ar, to either a ThermoFinnigan Neptune MC-ICP-MS for isotope ratio measurements or to a Varian Vista Pro inductively coupled plasma optical emission spectrometer (ICP-OES) for element analysis. Instrumental parameters for Fe and Si isotope ratio analysis are given in *Table 1.1*.

Femtosecond laser system

The 100 fs Ti:Sapphire regenerative amplifier system (Hurricane I, Spectra-Physics, USA) is a compact computer-controlled assembly, which comprises a mode-locked Ti-sapphire femtosecond seed laser, a pulse stretcher and compressor, a Ti-sapphire regenerative amplifier and its pump laser. The Ti-sapphire femtosecond seed source is internally pumped by a 5 W Nd:YLF laser (Neodymium:Yttrium-Lithium-Fluoride), which is frequency-doubled to produce a wavelength of 532 nm resulting in an output wavelength tuneable from 775 to 785 nm. This range has been chosen instead of the factory default setting with a center wavelength of 800 nm in order to generate a frequency-quadrupled wavelength close to 193 nm, the ArF Excimer laser wavelength. The output is a pulsed seed beam with a repetition rate of 40 MHz, a pulse width of

~80 fs and a pulse energy of few nJ. In order to reach a useable pulse energy, the seed beam is injected into a regenerative amplifier, a Q-switched Ti-sapphire cavity, which is excited by a 10 W internally frequency-doubled (532nm) Nd:YLF pump laser. The Ti-sapphire rod can be

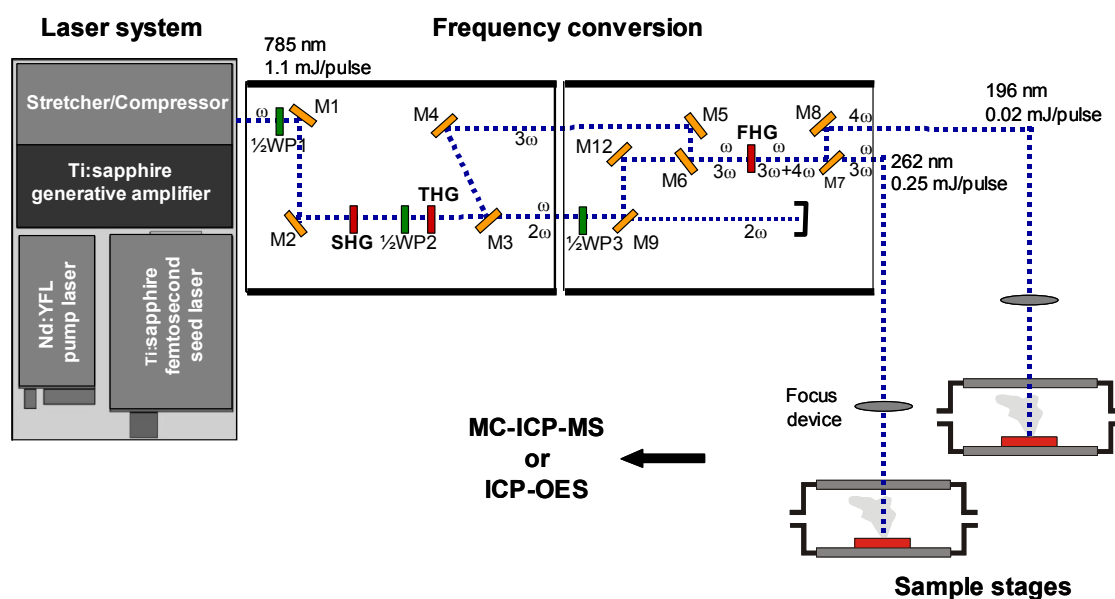


Figure 1.5 Schematic setup of the UV femtosecond laser ablation system at the Leibniz University of Hannover. The system consists of a compact 100 fs Ti:Sapphire regenerative amplifier system (Hurricane I, Spectra-Physics, USA), a frequency conversion setup, samples stages with visualisation units for the output beams with wavelength of 262 nm and 196 nm. The fundamental wavelength 1ω (785 nm) is partly frequency-doubled (2ω) and subsequently mixed with the second and third harmonics according to the schemes $1\omega + 2\omega \rightarrow 3\omega$ (262 nm) and $1\omega + 3\omega \rightarrow 4\omega$ (196 nm). The laser ablation system can be connected either to a MC-ICP-MS or ICP-OES. Abbreviations: WP = wave plate (adaption for type I frequency conversion); M = reflection coated mirrors; SHG, THG and FHG = second, third and fourth harmonic generators, respectively, which are type I BBO-crystals.

Table 1.1
Instrumental parameters of UV fs LA-ICP-MS
for Fe and Si isotope ratio analysis

Laser system

Laser type	Ti:Sapphire
Wavelength	196 nm
Pulse width	~200 fs
Pulse energy	0.02 mJ
Fluence	~1.6 J/cm ²
Power density	8000 GW/cm ²
Repetition rate	1-350 Hz
Crater Diameter	15-35 μm

ICP-MS

Type	ThermoFinnigan Neptune MC-ICP-MS
Cool gas	15 l/min (Argon)
Auxiliary gas	0.7-1.0 l/min (Argon)
Sample gas	0.7-0.8 l/min (Argon)
Additional gas (carrier gas)	0.9-1.0 l/min (Helium)
RF generator power	1200 W
Acceleration voltage	-10000 V
Extraction	-1200 V
Focus	-600 V
Sample cone	Ni, orifice 1.1 mm diameter
Skimmer cone	H-type, Ni, orifice 0.8 mm diameter
Mass resolution (5%)	~8000
Amplifiers	10 ¹¹ Ω

Faraday cup setup

Fe isotope analysis: ⁵²Cr (L4), ⁵⁴Fe (L2), ⁵⁶Fe (Central), ⁵⁷Fe (H1), ⁵⁸Fe (H2), ⁶⁰Ni (H4)

Si isotope analysis: ²⁸Si (L2), ²⁹Si (Central), ³⁰Si (H2)

Cycle integration time	2 s
Number of cycles	40-80

pumped at relative high power without danger of damage but cannot handle the high peak power of fs pulses. Therefore, the ultra-short seed pulse needs to be temporally stretched to reduce power prior to amplification and subsequently recompressed. The pulse stretcher makes use of the fundamental relationship between pulse width and bandwidth. An ultra-short pulse exhibits a relatively broad wavelength range of about 20 nm. The stretching device consists of diffraction gratings, which delay the shorter wavelength (blue part) to the longer wavelength (red part) of the spectrum stretching the pulse over a longer time, which goes in hand with a reduction in pulse energy. Amplification occurs by passing of the stretched pulse multiple times through the excited Ti:sapphire rod. By rotating the polarisation direction through switching of a pockels cell in the amplifier, the strongest pulse of the pulse train is sent towards the compressor, which operates like a reversed stretcher to restore the pulse width to nearly its initial duration. The output of this system is an ~1.1 mJ/pulse at a pulse width of 100 fs and a wavelength of 785 nm. The repetition rate can be regulated from 1 to 1000 Hz. The laser beam exhibits a Gaussian intensity distribution.

Frequency conversion

The laser system delivers a beam in the IR spectrum with a fundamental wavelength of 785 nm, which is subsequently converted into the UV spectrum. Frequency conversion occurs in nonlinear optical crystals by sum frequency generation, in which two low-frequency photons with ω_1 and ω_2 , respectively, are combined into a high-frequency photon with ω_3 :

$$\omega_1 + \omega_2 = \omega_3 \text{ or}$$

$$\frac{1}{\lambda_1} + \frac{1}{\lambda_2} = \frac{1}{\lambda_3} \quad (1.29)$$

according to the relationships between angular frequency ω , wavelength λ , frequency f and speed of light c of $c = \lambda * f$ and $\omega = 2\pi f$.

The implemented nonlinear optical crystals are type I BBO crystals (β -BaB₂O₄) (*Figure 1.6*). BBO crystals have the advantage of a broad phase-matching range, a large effective nonlinear coefficient and a high damage threshold. The relatively small acceptance angle and the large walk-off support high conversion efficiency. The acceptance angle defines the tolerance of the beam divergence relative to the phase-matching direction. The walk-off describes the divergence of the extraordinary wave relative to the ordinary wave in a nonlinear crystal. These conditions match the fundamental laser beam parameters as it has a very small divergence and needs not to be focused onto the crystal. In order to reach type I phase-matching on each single

BBO crystal, the polarization of input beams needs to be parallel within the phase-matching direction. Parallel polarization is maintained by wave plates, which are implemented in the beam path. These optical elements are used because the outgoing converted wavelength of a BBO crystal is tuned by 90° relative to the incoming wavelengths, which makes restoration of parallel polarization necessary for further frequency conversion by type I BBO crystals.

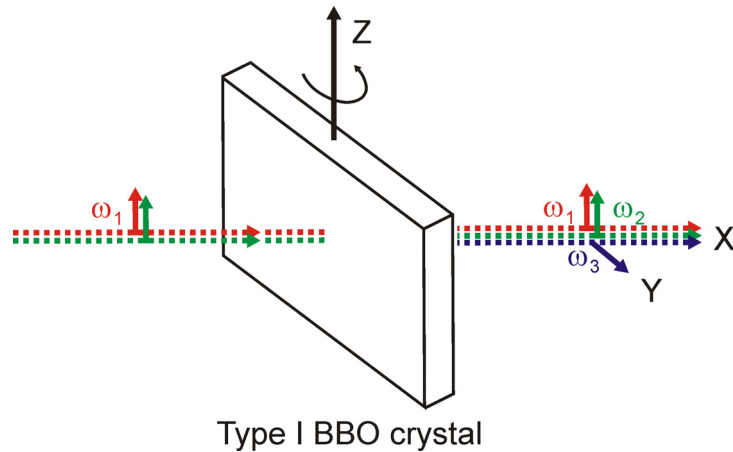


Figure 1.6 Frequency conversion by a type I BBO crystal. The polarization of the two input laser beams of ω_1 and ω_2 , respectively, is parallel, which is called type I phase-matching. The generated beam of ω_3 is polarized perpendicular (y-axis) to the incoming beams. In contrast, input beams with polarizations perpendicular to each other demands crystals for type II phase-matching. The BBO crystal can be rotated around its tilting axis (z-axis) to reach phase-matching direction in order to optimise conversion efficiency.

Within the first BBO crystal, the frequency is doubled resulting in a wavelength of 393 nm, with an efficiency of about 50%. By mixing of 393 nm and the fundamental wavelength of 785 nm within the second BBO crystal, the third harmonics is generated with a wavelength of 262 nm. The total efficiency for the third harmonics is about 20%. However, it is not optimized in order to keep enough energy of the 785 nm beam to convert efficiently to the fourth harmonics. Using a time delay arrangement, 785 nm is mixed with 262 nm in a third BBO crystal to produce the fourth harmonics in the deep UV at 196 nm. The total frequency conversion efficiency is about 3%. The high reflection coated mirrors, which steer the laser beams are designed for a center wavelength of 266 nm and 193 nm, but can be utilized for 262 and 196 nm without significant loss of energy, since their bandwidths are significantly larger. The spot size can be varied continuously from 35 down to 2 μm in diameter by an iris, which is placed at a distance of 2 m to sample surface to generate a 100 fold demagnification ratio. The system

provides two usable laser beams for ablation in the UV range, at 262 nm with a pulse energy of 0.25 mJ/pulse and at 196 nm with a pulse energy of 0.02 mJ/pulse. The pulse width is controlled by the intensity autocorrelation technique, which is a method to measure the pulse by itself. For this process, the 785 nm beam is split in two pulses and one is delayed with respect to the other. Then, the two pulses are recombined and spatially overlapped in a SHG crystal (SHG = second harmonic generation) resulting in a frequency converted symmetrical signal. By recording the delay versus the signal by means of a CCD array (Charge Coupled Device), the so-called autocorrelation length, which is defined as the full width at half maximum (FWHM) of the signal, can be determined using an oscilloscope. The approximate pulse width can then be calculated with the knowledge of the temporal shape of the pulse, which has a Gaussian distribution. Frequent measurements after frequency conversion to the fourth harmonics of the 785 nm beam have revealed pulse widths between 100 and 120 fs showing that the original pulse width measured at 100 fs using autocorrelation is preserved during frequency conversion. Because autocorrelation makes use of the second harmonic generation, which demands a high pulse energy and nonlinear optics availability, the pulse width of a beam in the UV spectra cannot be determined. Further optical elements, which deliver the beam to the sample surface include high reflection coated mirrors, an 8 x objective comprised of 5 lenses, and the fused silica window of the sample cell, which may stretch the pulse width slightly; it might be doubled to ~200 fs by this process. The working distance from the objective to the sample surface is about 20 mm.

Ablation cell

The ablation cell was designed to minimize volume while maintaining maximum area. This reduces wash-out times and allows mounting of a standard-size thin section together with calibration standards, which is essential when using the standard sample bracketing technique. The volume of the cell is 25 cm³. The cell is made of pyrex with a transparent bottom for transmitted light microscopy and an integrated fused silica window in the lid for beam delivery. This also permits the use of reflected light microscopy. To guarantee optimal transport of the aerosol the cell has three gas inlets with a nozzle size of 0.5 mm and one outlet of 6 mm in diameter.

1.3. Precambrian Iron Formation

1.3.1. Nature and depositional environment of iron formations

Precambrian iron formations are prominent chemical sediments consisting generally of alternating Fe-rich and Si-rich layers (see recent overviews of Beukes and Gutzmer (2008), Clout and Simonson (2005), Klein (2005) and Trendall (2002)). Their peak of deposition at around 2.4 Ga correlates with major changes in the Earth's history such as the rise of oxygen in the atmosphere, the change from anoxic to oxic conditions in the ocean and the evolution of life. Therefore, iron formations represent an extraordinary record of ancient environmental conditions and have been used as proxies to infer oceanic and atmospheric chemistry and their redox conditions, seafloor hydrothermal activity, and the activity of early microbes.

Iron formations are preserved within all major Precambrian shield areas and were deposited mainly from 3.8 through 1.8 Ga but reoccur from 0.8 to 0.6 Ga. Most Archean iron formations are associated with greenstone belts with close spatial and temporal relationship to volcanism (Simonson and Hassler, 1996) and are classified as 'Algoma-type' (Gross, 1973). Usually, these iron formations are small tectonically deformed deposits, which have been metamorphosed to various grades and dismembered. In the Proterozoic, laterally extensive iron formation sequences were deposited on partially isolated platforms on the continental shelf regions of Archean cratons representing the 'Superior-type' of Gross (1973). These deposits are usually well-preserved, and minimally deformed and metamorphosed. The reoccurrence of iron formations in the Neoproterozoic is considered to have occurred as a result of anoxic conditions resulting from an ice-covered ocean, referred to as 'Snowball Earth'. They are associated with glacio-marine deposits and represent the 'Rapitan-type' (Gross, 1973).

Iron formations exhibit a large spectrum of textural and mineralogical rock types with lateral and vertical facies variations. Many Precambrian iron formations, especially those of Archean age, are laminated and lack detrital components indicating a low-energy, basinal marine environment (< 200m) detached from terrigenous influence by some form of physical barrier (e.g. Garrels, 1987; Trendall and Blockley, 1970). These deposits are typical banded iron formation (BIF) deposited as orthochemical muds. Layering is observed on various scales from coarse macrobands (units of meters in thickness) through mesobands (several centimeter thick layers) to microbands (lamination in the order of millimeters) (Trendall and Blockley, 1970). Some of the Proterozoic iron formations feature a granular texture containing oolites, granules

and other fragments embedded in a matrix, which is associated with high-energy, subtidal environments on platform areas (e.g. Gross, 1972). Except for the Neoproterozoic iron formations, the chemical composition is relative uniform with total Fe of about 20 to 40 wt.%, SiO₂ of 43 to 56 wt.%, CaO of 1.75 to 9.0 wt.%, MgO of 1.20 to 6.7 wt.% and very low Al₂O₃ of 0.09 to 1.8 wt.% devoid of detrital material (Klein, 2005). In general, the organic carbon content is low ranging from 0.01 to 0.20 wt.% with oxide-rich iron formations having higher organic carbon concentrations than siderite-rich iron formations (Beukes et al., 1990; Kaufman et al., 1990; Klein and Beukes, 1989; Klein and Beukes, 1993; Klein and Ladeira, 2004). Major mineral phases in low-grade metamorphosed iron formations consist of chert (microcrystalline quartz), magnetite, hematite and carbonates including siderite and members of dolomite-ankerite series. Most common iron-silicates are greenalite, stipnomelane and minnesotaite, with pyrite occurring occasionally. Depending on the major Fe-bearing mineral phase, iron formations are classified as oxide, carbonate and silicate facies with several mixed facies.

Fe and Si are the most abundant elements in iron formations, making fractionation of their isotopes ideally suited to exploring ancient environmental conditions and reconstructing the Precambrian Fe and Si geochemical cycles. Although Fe and Si have been deposited simultaneously in iron formations, the question of to what extent they have followed common pathways is still open. In the following sections, the ancient Fe and Si cycles during iron formation genesis are roughly outlined together with the available Precambrian Si and Fe isotope record.

1.3.2. Geochemical Si cycle during iron formation deposition and the Precambrian Si isotope record

Although most iron formations contain more SiO₂ than total Fe, little attention has been paid to the Precambrian geochemical Si cycle (see reviews of Siever (1992), Perry and Lefticariu (2003) and Maliva et al. (2005)). Nevertheless, it clearly differed from that of the Phanerozoic given that silica-secreting organisms (i.e. primary diatoms) were absent in the Precambrian ocean. *Figure 1.7* shows a likely simplified Si cycle at the time of deposition of iron formation together with the Si isotope composition of main reservoirs as inferred from modern systems. The Si concentration likely reached saturation in Precambrian seawater. Depending on assumed temperature and pH conditions, estimates range between 60 and 120 ppm (e.g. Morris, 1993; Siever, 1992), which implies a long residence time on the order of 10⁵ years in the Precambrian ocean. In contrast, the efficient Si precipitation by diatoms promote very low Si concentrations

in the modern ocean of 1 ppm or less (e.g. Perry and Leticariu, 2003; Siever, 1992). The origin of Si in the Precambrian ocean is controversial. Seafloor hydrothermal fluids and/or continental drainage are considered as potential sources (see discussion in Maliva et al. (2005)). Investigations of modern seafloor hydrothermal fluids indicate slightly negative $\delta^{30}\text{Si}$ values (De La Rocha et al., 2000), however only two samples have been measured to date. The dissolved Si from continental drainage supply was controlled by weathering of igneous silicate minerals. Modern river systems, which are considered to reflect largely the weathering products of igneous rocks, reveal a mean $\delta^{30}\text{Si}$ value of $0.8 \pm 0.1\%$ (1 SD, 4 rivers) (Georg et al., 2006). Therefore depending on the relative proportion of hydrothermal and terrigenous input, the overall Si isotope signature of Si entering the Precambrian ocean might have been between 0 and 0.8‰ in $\delta^{30}\text{Si}$. In the absence of biologically-mediated precipitation, the most likely Si removal process is direct precipitation of amorphous silica gel from seawater due to saturation (Maliva et al., 2005; Siever, 1992). Sorption of silica on clay minerals, Fe oxides, or organic matter could have played a role in nucleation and/or precipitation (e.g. Perry and Leticariu, 2003; Siever, 1992). In contrast to the redox-sensitive element Fe, Si precipitation is independent from an oxidant and potentially occurred in the whole water column. While Fe-rich layers might reflect periods of intensive upwelling of Fe-rich water into the oxidizing upper water column, chert layers are thought to represent quiescent periods of Fe-poor background sedimentation (Morris, 1993). Chert within iron formations has negative $\delta^{30}\text{Si}$ values ranging from -2.6 to -0.3‰, whereas other Precambrian marine siliceous deposits indicate a wider range, with $\delta^{30}\text{Si}$ values up to 3‰ (André et al., 2006; Ding et al., 1996; Jiang et al., 1993; Robert and Chaussidon, 2006; van den Boorn et al., 2007; this study). Negative values are interpreted as hydrothermal signature, whereas positive $\delta^{30}\text{Si}$ values may indicate an elevated temperature of the seawater, the influence of a continental source or precipitation from isotopically heavy seawater. Although Si isotope geochemistry still lacks accurately determined fraction factors, there is consensus that silica precipitation from solution favours isotopically light Si (Basile-Doelsch, 2006; Ziegler et al., 2005). Therefore ongoing precipitation might have driven the seawater composition to significant positive $\delta^{30}\text{Si}$ values, which is estimated to be between 1.8 and 4.6‰ (De La Rocha and Bickle, 2005).

The Si cycle during iron formation deposition

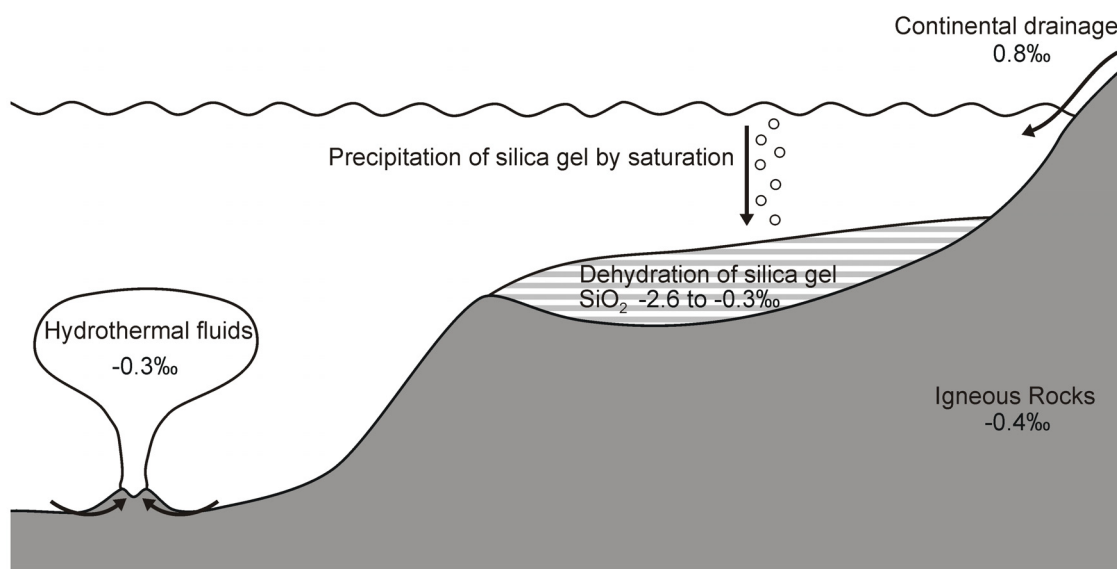


Figure 1.7 Simplified geochemical Si cycle during the deposition of iron formations and Si isotope compositions of the major reservoirs given as $\delta^{30}\text{Si}$ values (see text for details).

1.3.3. Geochemical Fe cycle during iron formation deposition

Figure 1.8 illustrates a simplified Fe cycle for the deposition of iron formations including the Fe isotope compositions of major iron reservoirs. Iron formations are thought to have been deposited within largely anoxic ocean basins containing a high concentration of dissolved Fe(II) (e.g. Holland, 1984), which is consistent with conditions of low atmospheric oxygen. The modern oxygenated ocean has a Fe concentration of ~ 0.05 ppb (Wu et al., 2001), which stands in marked contrast to estimated concentrations of 2 to 50 ppm for the Precambrian ocean (Canfield, 2005; Ewers, 1983; Sumner, 1997). The elevated Fe(II) inventory in the Precambrian ocean involves a long residence time in the order of between 10^5 to 10^6 years (Trendall, 2002) compared to about 70 to 140 years in the modern ocean (e.g. Bruland et al., 1994). Rare earth element patterns with pronounced positive Eu-anomalies and mantle-like Nd isotope signatures in iron formations indicate a seafloor hydrothermal Fe source (e.g. Bau and Dulski, 1996; Isley, 1995; Jacobsen and Pimentel-Klose, 1988), possibly supplemented by continental drainage (e.g. Canfield, 1998). Modern mid-ocean ridge hydrothermal fluids exhibit $\delta^{56}\text{Fe}$ values between -0.6 and -0.2‰ (Beard et al., 2003; Severmann et al., 2004; Sharma et al., 2001) with higher values

corresponding to high Fe concentrations (Johnson et al., 2008a). Presumably higher Precambrian hydrothermal and heat fluxes (Bau and Möller, 1993) together with minimal oxidation rate close to the vent site under anoxic conditions might have promoted hydrothermal fluids with an Fe isotope composition closer to that of bulk oceanic crust, i.e. near-zero (Johnson et al., 2008a). The modern continental drainage appears to supply dissolved and colloidal Fe, mainly leached from soils, with slightly negative $\delta^{56}\text{Fe}$ values between -1 and 0‰ (Bergquist and Boyle, 2006; Fantle and De Paolo, 2004). A higher proportion of Fe derived from weathering of igneous rocks and the absence of pronounced redox chemistry on Precambrian continents imply riverine supply with $\delta^{56}\text{Fe}$ values of near-zero (Johnson et al., 2008a; Yamaguchi et al., 2005). Therefore, the overall Fe source composition might have had an Fe isotope composition of near-zero, which is also assumed for the ancient seawater composition (e.g. Johnson et al., 2008a). The large inventory of Fe oxides in iron formations requires oxidation in a largely anoxic environment, which is generally explained with a stratified ocean model (e.g. Anbar and Knoll, 2002; Canfield, 1998; Klein and Beukes, 1989; Morris, 1993). Upwelling of Fe(II)-rich deep water in continental shelf regions (e.g. Klein and Beukes, 1989) or buoyancy of hydrothermal plumes (e.g. Isley, 1995) might transport Fe(II) to the upper ocean, where it is oxidized and subsequently precipitated as ferric oxyhydroxide. Three mechanisms are discussed in the literature for oxidation of Fe(II) to Fe(III): oxidation by free oxygen (e.g. Drever, 1974; Holland, 1973), by anaerobic photosynthesis (e.g. Konhauser et al., 2002; Widdel et al., 1993), and by UV photochemical oxidation (e.g. Cairns-Smith, 1978). Recently, experimental investigations of Konhauser et al. (2007) have excluded the latter as a process for efficient oxidation. The two proposed processes involve micro-organisms. During oxygenic photosynthesis, cyanobacteria or their predecessors use water as electron donor and release oxygen, which in turn oxidizes Fe(II) to Fe(III). Alternatively, during anaerobic photosynthesis, bacteria play a more active role by utilizing Fe(II) as electron donor generating Fe(III).

Fe(III) has a low solubility in water, which promotes precipitation of ferric oxyhydroxide. Besides ferric oxyhydroxide, siderite might be a primary phase (e.g. Klein and Beukes, 1989; Sumner and Grotzinger, 2004; Sumner, 1997; Tice and Lowe, 2004). The concentration of dissolved Fe(II) may increase with depth in a ocean basin, which slows down calcite precipitation and triggers supersaturation of siderite. Siderite might have precipitated directly from seawater or formed at the water-sediment interface.

After initial deposition of primary phases, diagenetic processes involve dehydration of the hydrous sediments, Fe mobilization and formation of diagenetic mineral phases. Microbial

dissimilatory Fe(III) reduction (DIR) coupled to organic carbon oxidation mobilizes Fe(II) during diagenesis. An estimated 70% of the Fe(III) precipitated initially might have been recycled to the seawater during this process (Konhauser et al., 2005). Investigations of modern marine sediments have revealed Fe isotope compositions of pore waters ranging between -3.0 and 0.4% depending on whether microbial dissimilatory Fe(III) or sulfate reduction dominates organic matter degradation (Bergquist and Boyle, 2006; Severmann et al., 2006).

The Fe isotope compositions of Fe-bearing mineral phases in iron formations reflect these processes. Investigations of early and late Archean iron formations, the voluminous ~ 2.5 Ga iron formations from the Hamersley and Transvaal successions and the 1.9 Ga Biwabik Iron Formation, have revealed an overall range in $\delta^{56}\text{Fe}$ for hematite from -0.9 and 0.8% , magnetite yields $\delta^{56}\text{Fe}$ values between -1.1 and 1.2% , Fe carbonate ranges from -2.2 to 1.1% , and pyrite exhibits $\delta^{56}\text{Fe}$ values between -2.4 and 1.1% (Figure 1.8) (Dauphas et al., 2004; Dauphas et al., 2007; Frost et al., 2007; Johnson et al., 2003; Johnson et al., 2008; Rouxel et al., 2005; Valaas Hyslop et al., 2008; Whitehouse and Fedo, 2007; this study). The reactions of possible formation pathways for hematite, magnetite and siderite are summarized in Figure 1.9 and are discussed in the light of these minerals' Fe isotope composition in Chapter 3 and 4.

The Fe cycle during iron formation deposition

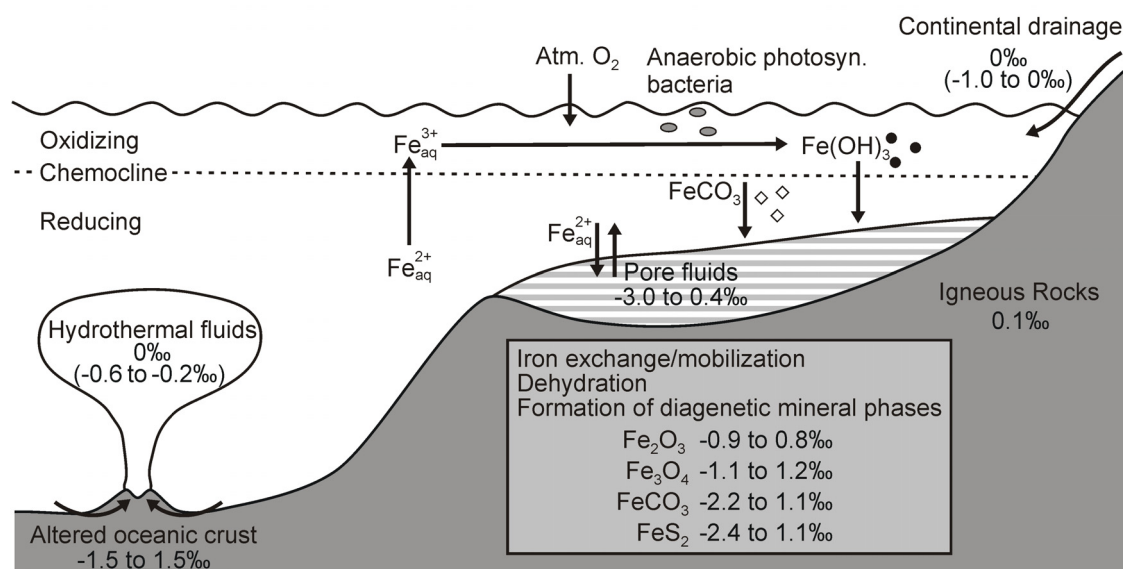


Figure 1.8 Simplified geochemical Fe cycle during the deposition of iron formations and the Fe isotope compositions of the major reservoirs expressed as $\delta^{56}\text{Fe}$ (see text for details).

Formation of mineral phases in iron formation and Fe isotope fractionation

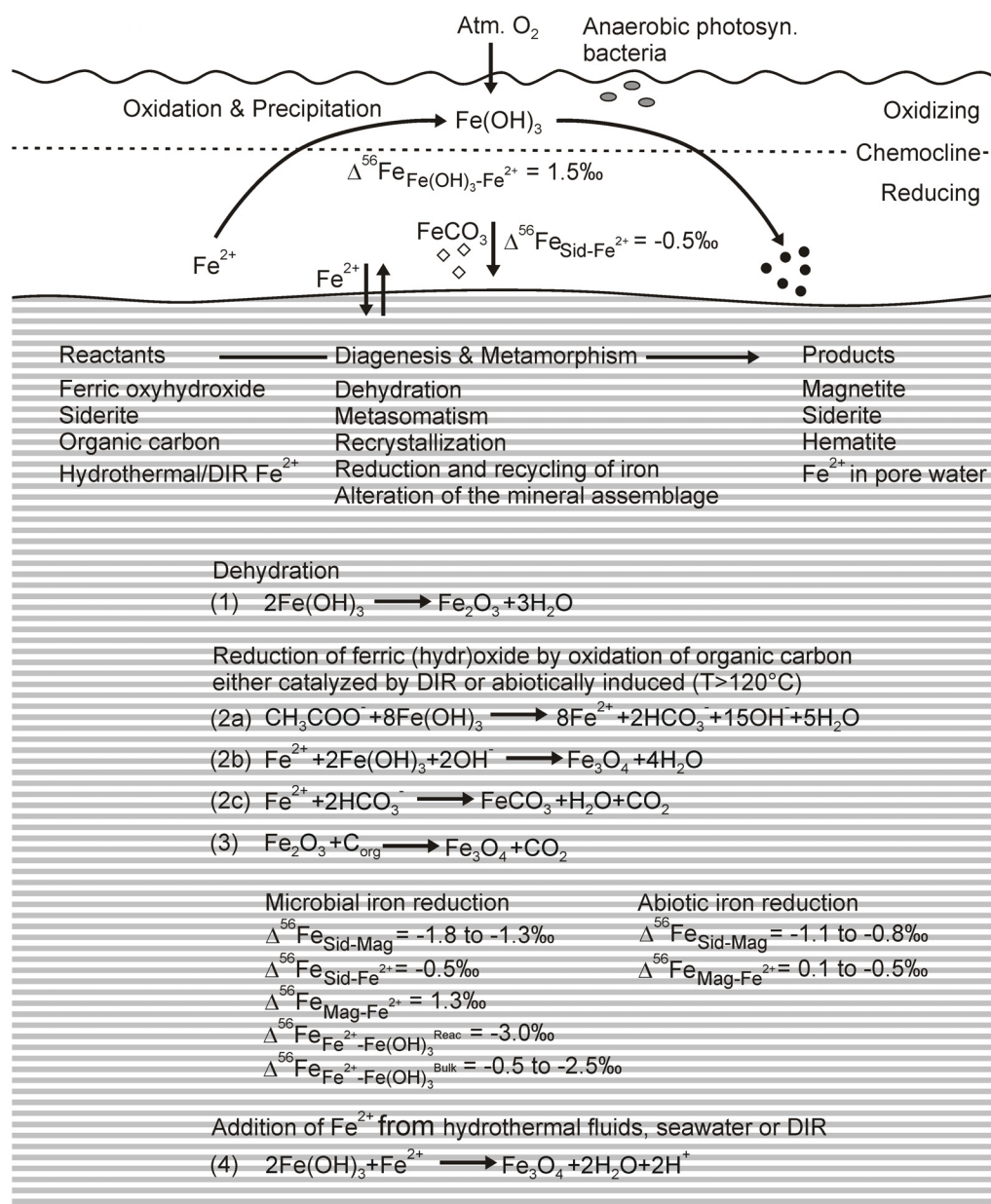


Figure 1.9 Summary of possible formation pathways of Fe-bearing mineral phases in iron formations and relevant fractionation factors discussed in *Chapter 3* and *4* in light of the Fe isotope record (for references see *Chapter 3* and *4*).

1.3.4. The Precambrian Fe isotope record

The largest variability in Fe isotope composition is recorded in Precambrian marine deposits encompassing shales, sedimentary sulfides buried in shales, microbial carbonates, and iron formations (see *Figure 1.1* and *1.10*). This variability suggests major recycling of Fe involving multiple pathways, which fractionated Fe isotopes prior to ultimate fixation in the sediment. The record includes different rock types, containing information on a variety of environments. While marine shales are derived from terrestrial weathering products, and modified by diagenetic processes, iron formations are chemical marine sediments that are the product of initial precipitates from seawater and subsequent diagenetic and metamorphic processes. Both deposits formed in moderately deep water. In contrast, microbial carbonates, i.e. primary stromatolites in the Precambrian formed within coastal areas by microbially-induced carbonate precipitation.

Precambrian organic carbon-poor shales exhibit a limited range in $\delta^{56}\text{Fe}$ from -0.6 to 0.2‰ , whereas organic carbon-rich sediments (black shales) reveal large variation with $\delta^{56}\text{Fe}$ values as low as -2.5‰ (Yamaguchi et al., 2005). The isotope composition of Precambrian Fe-poor shales with low organic carbon and carbonate content is indistinguishable from that of Phanerozoic low-C and low-S clastic sediments (Beard et al., 2003; Fehr et al., 2008), and is close to the average igneous rock composition of 0.1‰ (Beard et al., 2003). If these sediments have experienced limited diagenetic alteration they provide information on terrestrial weathering products. The restricted range in $\delta^{56}\text{Fe}$ suggests that chemical weathering produces no isotope fractionation in bulk sedimentary debris throughout Earth history (Yamaguchi et al., 2005). Weathering processes seem to be dominated by the congruent dissolution of minerals without redox changes preserving the isotope signature of igneous rocks. In contrast, carbon-rich sediments rich in siderite or magnetite experienced diagenetic Fe cycling through several pathways. This diagenesis resulted in a large variability of $\delta^{56}\text{Fe}$ with strong negative values, which is attributed to the incorporation of isotopically light Fe(II) released by DIR (Yamaguchi et al., 2005). DIR is considered as one of the earliest forms of microbial respiration (Vargas et al., 1998) and seems to be an important process during diagenesis since at least 2.9 Ga (Yamaguchi et al., 2005). Precambrian microbial carbonates are likewise characterized by negative $\delta^{56}\text{Fe}$ values between -0.5 and -2.1‰ , which might provide direct evidence for the Fe isotope composition of surface seawater as inferred from modern microbial carbonates (von Blanckenburg et al., 2008). However, systematic studies have to be carried out to evaluate this potential seawater proxy.

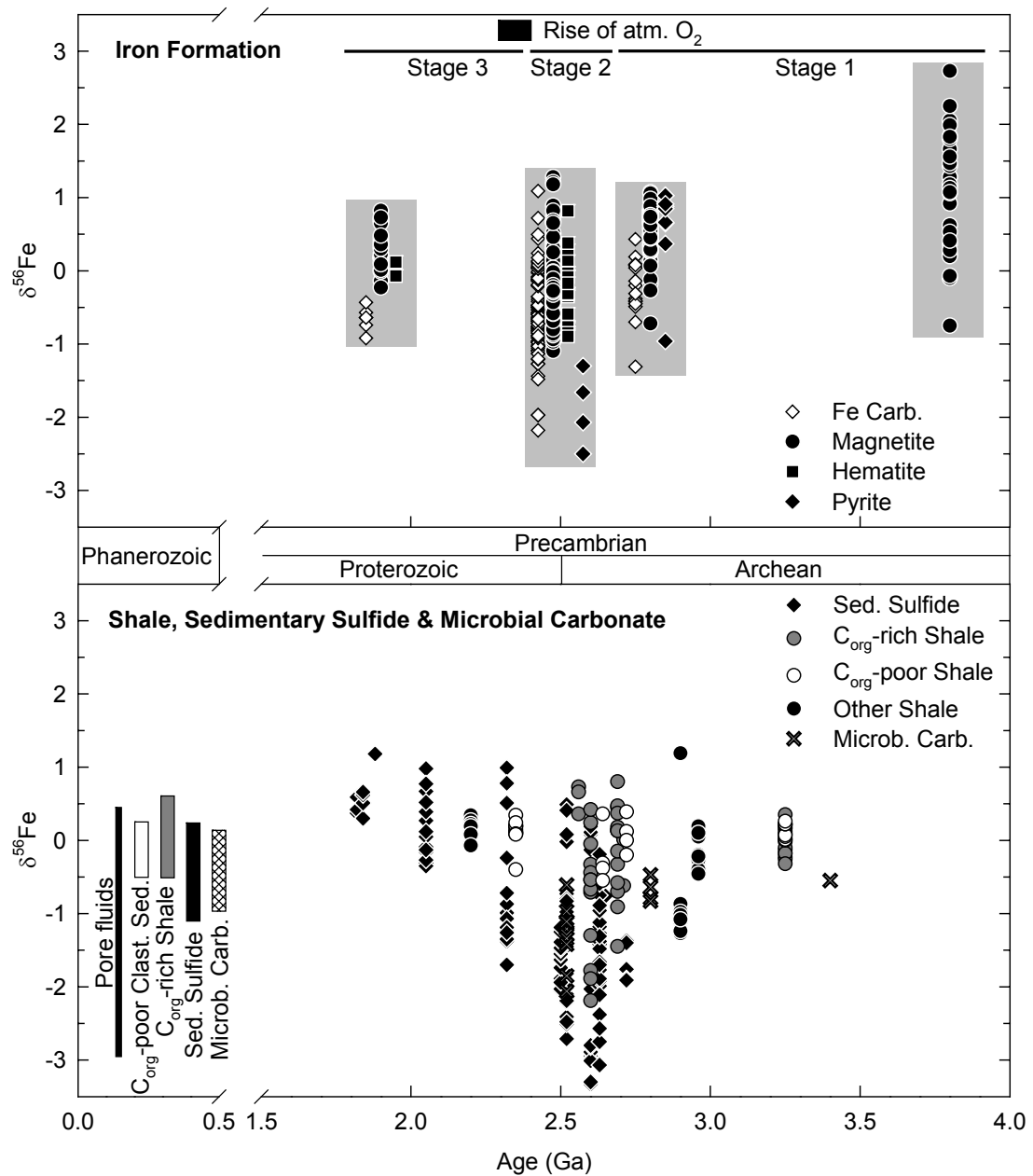


Figure 1.10 The Precambrian Fe isotope record. Fe isotope variations in Precambrian iron formation of different ages and grades of metamorphism including data of distinct mineral phases and bulk rock analysis (Dauphas et al., 2004; Dauphas et al., 2007; Rouxel et al., 2005; Frost et al., 2007; Valaas-Hyslop et al., 2008, Whitehouse and Fedo, 2007; Johnson et al., 2003; Johnson et al., 2008a; this study). The gray bars indicate the overall range in $\delta^{56}\text{Fe}$ for distinct periods. Early and late Archean iron formations (~3.8 Ga Isua, Akilia and Innersuatuut (Greenland), ~3.8 Ga Innuksuac (Canada), ~2.7 Ga Old Wanderer Iron Formation, Shurugwi Greenstone Belt and Manjeri Formation, Belingwe Belt (Zimbabwe)) show overall positive $\delta^{56}\text{Fe}$ values, whereas the voluminous ~2.5 Ga iron formations from the Hamersley and Transvaal Basins (Australia and South Africa, respectively) exhibit a more variable Fe isotope

composition ranging from negative to positive $\delta^{56}\text{Fe}$ values. Younger Proterozoic iron formations appear to return to more positive $\delta^{56}\text{Fe}$ values (~1.9 Ga Biwabik Iron Formation and Ironwood Iron Formation (USA)). Precambrian organic-rich shales, sedimentary pyrites and microbial carbonates are more variable with the tendency to very negative $\delta^{56}\text{Fe}$ values around 2.5 Ga compared to Phanerozoic samples (Rouxel et al., 2005; Yamaguchi et al., 2005; von Blanckenburg et al., 2008). Organic-poor shale exhibits little variations over time (Yamaguchi et al., 2005). Modern pore fluids of marine environments exhibit very negative to slightly positive $\delta^{56}\text{Fe}$ values depending whether microbial dissimilatory iron reduction (DIR) or sulfate reduction dominates organic matter degradation (Bergquist and Boyle, 2006; Severmann et al., 2006). The compositions of modern sediments and pore fluids are shown as bars on the left side of the diagram.

Fe isotope data of iron formations are available from three formation periods (Stage 1 to 3 in *Figure 1.10*), which are characterized by distinct Fe isotope variations and depositional environments. Sedimentary sulfides extracted from black shales exhibit a similar trend in Fe isotope systematic. These sulfides have been interpreted as direct proxy for the ancient seawater composition (Rouxel et al., 2005), but more likely represent a diagenetically altered signature (Yamaguchi and Ohmoto, 2006). Temporal variations in iron formation and sedimentary sulfide correlate roughly with other indicators of the redox state of the atmosphere and ocean as the S and C isotope record (see review of Dauphas and Rouxel (2006)) and seems to be related to the evolution of microbial metabolism.

Stage 1. In general, Archean iron formations formed within greenstone belts, probably in close relationship to hydrothermal systems (e.g. Simonson and Hassler, 1996), and are characterized by Fe mineral phases with positive Fe isotope signatures (Dauphas et al., 2004; Dauphas et al., 2007; Rouxel et al., 2005; Whitehouse and Fedo, 2007; this study). In contrast, sedimentary sulfides exhibit variably negative $\delta^{56}\text{Fe}$ values (Rouxel et al., 2005). The occurrence of mass-independent S isotope fractionation until about 2.45 Ga indicates low atmospheric oxygen for this period (Farquhar and Wing, 2003; Farquhar et al., 2001), although there is some evidence for early evolution of atmospheric oxygen in paleosols (Ohmoto, 1996). These low oxygen levels would have caused high Fe(II) and low sulfate concentrations in the ocean (e.g. Canfield 2000). The occurrence of Fe oxides in Archean iron formations requires oxidation in a largely anoxic environment, which was likely dominated by anaerobic photosynthesis (Canfield et al., 2006) prior to the widespread evolution of oxygen-producing cyanobacteria. Early Archean iron formation deposits are highly deformed and metamorphosed and contain magnetite with strongly positive $\delta^{56}\text{Fe}$ values up to ~2‰ (Dauphas et al., 2004; Dauphas et al., 2007; Rouxel et al., 2005; Whitehouse and Fedo, 2007). The high $\delta^{56}\text{Fe}$ values and a study of the Proterozoic contact-metamorphosed Biwabik Iron Formation by Frost et al. (2007) indicate that magnetite preserved its original Fe isotope composition during prograde metamorphism. Hence, the

positive $\delta^{56}\text{Fe}$ values appear to reflect a primary or early diagenetic signature, which is interpreted as inherited from a ferric oxyhydroxide precursor formed in the upper water column by partial Fe(II) oxidation. Consequently, the oxidant was the limiting factor for Fe(III) precipitation. Late Archean iron formations reveal a similar picture, showing moderately positive $\delta^{56}\text{Fe}$ values (Rouxel et al., 2005; this study), which might indicate a higher degree of partial Fe(II) oxidation. Fe isotope fractionation in Archean iron formations appears to be dominated by partial Fe(II) oxidation, while diagenetic redistribution of Fe is minor. In contrast, late Archean sedimentary sulfides are highly variable and are dominated by strong negative values as low as -3.5% , indicating multiple isotope fractionation processes. The combined effect of partial Fe(II) oxidation and Fe(III) reduction, Rayleigh distillation, and the apparent preferential incorporation of isotopically light Fe in pyrite might have resulted in variably negative $\delta^{56}\text{Fe}$ values. Partial reduction of ferric (hydr)oxide by oxidation of organic matter due to the activity of DIR releases large quantities of isotopically light Fe(II) (Crosby et al., 2005; Crosby et al., 2007; Johnson et al., 2008b), which could have caused very negative $\delta^{56}\text{Fe}$ in sulfides. The covariance of Fe and S isotope signatures in pyrites from Belingwe basin are interpreted as coupled microbial Fe and sulfate reduction via organic carbon oxidation (Archer and Vance, 2006). The organic origin of carbon in these sediments is supported by very low $\delta^{13}\text{C}$ values typical for carbon subjected to photosynthesis (Grassineau et al., 2001). In addition, low $\delta^{56}\text{Fe}$ values might have been promoted by reservoir effects in the ocean basin due to removal of isotopically heavy Fe recorded in iron formations (Rouxel et al., 2005).

Stage 2. The Fe isotope record between 2.4 and 1.6 Ga is characterized by highly variable $\delta^{56}\text{Fe}$ values in mineral phases of iron formations and a trend from very negative to unusually high $\delta^{56}\text{Fe}$ values in sedimentary sulfides. This period encompasses the rise of atmospheric oxygen at about 2.4 Ga (e.g. Holland, 1984) as indicated by the appearance of mass-dependent S isotope fractionation (Bekker et al., 2004), which induced a redox-related change in the global Fe cycle. Alternatively, atmospheric oxygen might have reached considerable levels much earlier as suggested by Ohmoto (1996). Free oxygen is the result of oxygenic photosynthesis by cyanobacteria or their ancestors, which were present in the environment at least since 2.7 Ga (e.g. Blankenship, 1998; Brocks et al., 1999). Multiple lines of evidence indicate a rather dynamic process with a progressively increasing oxygen level (see overview in Canfield (2005)). In response to rising oxygen levels, the Fe(II) concentration declined in the ocean, whereas the sulfate concentration increased due to oxidative weathering of pyrites in soils (e.g. Canfield, 2005). The peak of iron formation deposition overlaps the beginning rise of atmospheric oxygen. However, before oxygen could reach significant levels, all sinks for

atmospheric oxygen had to be consumed. The high concentration of Fe(II) in the seawater represented an important sink, which would enforce precipitation of Fe(III) before the rise of oxygen (Johnson et al., 2008b). Increased Fe(III) precipitation and organic carbon production in the ocean would have supported the activity of DIR, which appears to play an important role in the diagenesis of iron formation (Johnson et al., 2008a). The large well-preserved ~2.5 Ga iron formations of the Hamersley and Transvaal Basins are typical Proterozoic iron formations deposited on partially isolated platforms within continental shelf areas. The fine lamination of these rocks suggests deposition in low-energy, basinal environments (e.g. Trendall and Blockley, 1970). Their mineral phases exhibit a large variability in the Fe isotope composition but reveal an overall average of near-zero in $\delta^{56}\text{Fe}$, which is in balance with the Fe influx composition from hydrothermal and continental sources (Johnson et al., 2003; Johnson et al., 2008; this study). Contemporaneous sedimentary sulfides likewise exhibit a large range in the Fe isotope composition and reach strongly negative $\delta^{56}\text{Fe}$ values. These variations are interpreted as the fingerprint of the interaction of a series of processes including primary precipitation and subsequent diagenetic processes (Johnson et al., 2008a; Johnson et al., 2008b). Positive to near-zero $\delta^{56}\text{Fe}$ values of Fe oxides and carbonates might be inherited from variable degrees of partial Fe(II) oxidation in the upper water column. Alternatively, Fe oxides with a positive Fe isotope signature could represent the isotopically heavy residuum after partial Fe(III) reduction by DIR. Siderite with $\delta^{56}\text{Fe}$ values of about -0.5‰ seems to have formed in equilibrium with seawater and hence represents primary precipitates. Significant negative values of Fe(II)-bearing minerals are attributed to the contribution of isotopically light Fe(II) released by DIR. The variable but overall balanced Fe isotope signature of the Hamersley and Transvaal iron formations may indicate major diagenetic Fe redistribution on Proterozoic shelf areas similar to modern environments. Recent investigations in the Black Sea and the Baltic Sea suggest a flux of isotopically light Fe(II) released by DIR from oxic to euxinic environments (Fehr et al., 2008; Severmann et al., 2008). The expanded range in $\delta^{56}\text{Fe}$ for sedimentary sulfides are associated with large variations in the sulfur isotope record, which is interpreted as bacterial sulfate reduction (BSR) under sulfate excess conditions (e.g. Cameron, 1982). This analogy argues for concurrent activity of DIR and BSR, producing variable $\delta^{56}\text{Fe}$ values as measured in the Belingwe pyrites by Archer and Vance (2006).

Stage 3. With the exception of Neoproterozoic iron formations, the final episode of iron formation at ~1.8 Ga indicate an apparent return to low oxygen conditions before the definitive establishment of an oxygenated atmosphere (e.g. Canfield, 2005). The granular texture of the 1.9 Ga Biwawik BIF is characteristic for deposition in a high-energy environment near the

seashore (e.g. Lanier, 1989). Similar to Archean iron formations, this deposit yields mostly positive $\delta^{56}\text{Fe}$ values (Frost et al., 2007; Valaas Hyslop et al., 2008). Sedimentary pyrites from this period are characterized by unusually high $\delta^{56}\text{Fe}$ between -0.3 and 1.2% (Rouxel et al., 2005). Once the sulfate concentration is high in the ocean, BSR might dominates over DIR for organic matter degradation, which prevents the release of Fe with negative isotope signatures (Johnson et al., 2008b). Positive values might result from partial Fe(II) oxidation during initial precipitation or post-depositional Fe redistribution similar to modern environments in the Black Sea and the Baltic Sea (Fehr et al., 2008; Severmann et al., 2008). After 1.8 Ga, iron formations are no longer formed and sedimentary sulfides exhibit a limited range from -1 to 0% . By this time, free oxygen has reached considerable levels accompanied by high sulfate concentrations in the ocean (e.g. Canfield, 2005). Instead of oxygen (e.g. Holland, 2004), high sulfide concentrations produced by sulfate reduction could have removed dissolved Fe(II) from solution establishing a sulfidic deep ocean (Canfield, 1998). These euxinic conditions might have promoted near complete scavenging of dissolved Fe(II) by reaction with biogenic sulfide forming Fe sulfide minerals. Therefore mass balance may limit the Fe isotope variability in pyrites (Johnson et al., 2008b).

Matrix-independent stable Fe isotope ratio determination using UV femtosecond laser ablation ICP-MS

Abstract

UV femtosecond laser ablation coupled to MC-ICP-MS provides a promising *in situ* tool to investigate elemental and isotope ratios by non-matrix matched calibration. In this study, we investigate Fe isotope composition in siliceous matrices including biotite, hornblende, garnet, fayalite and forsterite (San Carlos Olivine), and an oceanic Fe-Mn crust using the iron reference material IRMM-014 for calibration. To test the accuracy of the laser ablation data, Fe isotope compositions were obtained independently by solution ICP-MS after chromatographic separation of Fe. Sample materials with low Cr content, i.e. biotite, hornblende, fayalite and the Fe-Mn crust, reveal $\delta^{56/54}\text{Fe}$ and $\delta^{57/54}\text{Fe}$ values that agree with those from solution ICP-MS data within the measured precision. For high Cr concentration ($^{54}\text{Cr}/^{54}\text{Fe} > 0.0001$), i.e. in the garnet and forsterite sample, $\delta^{56/54}\text{Fe}$ and $\delta^{57/54}\text{F}$ values were derived from $^{57}\text{Fe}/^{56}\text{Fe}$ ratios as correction of the isobaric interference of ^{54}Cr on ^{54}Fe is unsatisfactory. This approach provides accurate results for both minerals. Moreover, the garnet crystal exhibits isotopic zonation with differences of 0.3‰ in $\delta^{56/54}\text{Fe}$ showing that substantial heterogeneities exist in high-temperature metamorphic minerals. Multiple analyses of homogeneous sample materials reveal a repeatability of 0.1‰ (2 SD) for $\delta^{56/54}\text{Fe}$ and 0.2‰ (2 SD) for $\delta^{57/54}\text{Fe}$, respectively. This precision is obtained regardless of the sample matrix and is only twice as high as that obtained by solution ICP-MS. This study adds to the observations of Horn et al. (2006) who have shown that the determination of Fe isotope ratios in various matrices including iron alloys, iron oxides and hydroxides, iron sulfide and iron carbonates can be performed with high accuracy and precision at high spatial resolution using UV femtosecond laser ablation ICP-MS. These results

demonstrate that femtosecond laser ablation ICP-MS is a largely matrix-independent method, which provides a substantial advantage over commonly employed nanosecond laser ablation systems

2.1. Introduction

In the past two decades, laser ablation (LA) in conjunction with inductively coupled plasma mass spectrometry (ICP-MS) has become a powerful *in situ* micro-analytical technique with broad applications in elemental and isotope ratio analysis. Today, most laser ablation systems operate in the UV range with a pulse duration of several nanoseconds ($1 \text{ ns} = 10^{-9} \text{ s}$). However, a major drawback of this technique is laser-related elemental and isotope fractionation, which introduces a strong matrix-dependency into the results (e.g. Sylvester, 2008). To control this effect, matrix-matched calibration standards are required. For geological applications, this approach is not always practicable, because sample materials cover a large spectrum of matrices. Recent developments in LA employ lasers with shorter pulse durations ranging from ~60 to several hundreds of femtoseconds ($1 \text{ fs} = 10^{-15} \text{ s}$) (see reviews of Fernández et al. (2007) and Horn (2008)). The use of fs pulses for ablation provides significant improvements with respect to laser-induced and particle-size related fractionation so that non-matrix-matched calibration turns out to be feasible. fs LA-ICP-MS using non-matrix-matched calibration has been successfully applied to the analysis of element ratios, i.e. Zn/Cu, Pb/U and U/Th (Bian et al., 2005; 2006 ; González et al., 2004; Horn and von Blanckenburg, 2007; Koch et al., 2006; Mozna et al., 2006; Poitrasson et al., 2003) and of isotope ratios of heavy stable isotope systems, i.e. Cu, Fe and Si (Chmeleff et al., 2008; Horn and von Blanckenburg, 2007; Horn et al., 2006; Ikehata et al., 2008; Steinhoefel et al., submitted; Steinhoefel et al., submitted). The measurement of heavy stable isotope ratios is particularly challenging as the natural mass-dependent fractionation is very small, in the range of parts per thousand, which requires highly precise and accurate analysis. For instance, the natural variation in $\delta^{56/54}\text{Fe}$ is about 5‰ (e.g. Dauphas and Rouxel, 2006). The absence of matrix-effects has been demonstrated for Fe isotope ratio determinations by UV-fs-LA coupled to a multiple collector ICP-MS (MC-ICP-MS) for a variety of matrices including native iron, iron alloys, iron sulfides, Fe-carbonates, iron oxides and hydroxides using the isotopically certified iron reference material IRMM-014 for calibration (Horn et al., 2006). A similar approach demonstrates the matrix-independency for the determination of Si isotope ratios in siliceous materials including pure silicon, quartz, olivine and diopside by using the quartz reference standard NBS28 for calibration (Chmeleff et

al., 2008). Non-matrix matched calibration using near IR-fs-LA has also been successfully applied for the determination of Cu isotope ratios in Cu-rich minerals including cuprite, chalcocite and chalcopyrite by using the pure copper standard NIST-SRM 976 (Ikehata et al., 2008).

In this study, we show that accurate and precise Fe isotope ratios can be determined in silicate minerals using UV-fs-LA coupled to a MC-ICP-MS, which is a substantial advancement considering that 90% of the Earth's surface consists of silicates. Olivine (fayalite and forsterite), hornblende, biotite, garnet and complex matrices such as Fe-Mn crusts have been analysed using the iron reference material IRMM-014 for calibration. In these sample materials, the complexity of the matrix and the low Fe concentrations provide a formidable challenge.

2.2. Methods

The in-house built fs LA system at the Leibniz University of Hannover is based on a 100 fs Ti:sapphire regenerative amplifier system (Spectra Physics Hurricane I, USA) with a fundamental wavelength of 785 nm, which is consecutively frequency-quadrupled providing an output laser beam in the deep UV region at 196 nm with a pulse energy of 0.02 mJ. Sample and standard materials can be placed as thin sections or as polished sections in a sample cell with an integrated fused silica window, which has three gas inlets and one outlet and a volume of 30 cm³. The sample cell is mounted on a New Wave XP sample stage for visualization and precise positioning. The ablation rate for silicates is about 1.5 nm per pulse (Chmeleff et al., 2008). More details on the laser ablation system are given by Horn and von Blanckenburg (2007). The UV fs laser ablation system is coupled to a ThermoFinnigan Neptune MC-ICP-MS, which is equipped with conventional Ni skimmer and sampler cones running under standard conditions (*Table 2.1*). The aerosol is transported to the mass spectrometer using He as carrier gas and is mixed with Ar gas before entering the torch. Fe isotope ratios were determined following the analytical protocol of Horn et al. (2006). The ThermoFinnigan Neptune MC-ICP-MS provides high mass resolution, which is able to resolve all molecular interference on the Fe isotopes excluding isobaric isotope interferences. As well as the Fe isotopes ⁵⁴Fe, ⁵⁶Fe, ⁵⁷Fe and ⁵⁸Fe, ⁵²Cr and ⁶⁰Ni were measured by Faraday cups in static collection mode to correct for isobaric interferences of ⁵⁴Cr on ⁵⁴Fe and ⁵⁸Ni on ⁵⁸Fe. The correction modes for the LA data are identical to the method described and tested in detail for solution ICP-MS data by Schoenberg and von Blanckenburg (2005).

The analyses were performed using the standard-sample bracketing technique and the iron reference material IRMM-014. This external calibration technique involves the analysis of a reference standard of known isotope composition prior to and after the measurement of the sample material to correct for the instrumental mass discrimination and its temporal drift. The instrumental drift has to be less than 0.1‰ on the $^{56}\text{Fe}/^{54}\text{Fe}$ ratio between standard measurements to apply this method successfully to the analysis of stable Fe isotopes. To stabilize measurement conditions for the analysis of silicates, the siliceous sample material was continuously ablated for about one hour prior to analysis. This procedure conditions the interface region, which stabilizes the interaction of the ions with skimmer and sampler cones through a coating. Conditioning enables alternating analyses of silicate and Fe metal matrices, which is required for calibration by the sample-standard-bracketing method and therefore precise Fe isotope measurements.

Table 2.1
Instrumental parameters of the Neptune MC-ICP-MS
for fs LA

Cool gas: Ar [L min ⁻¹]	15.00
Auxiliary gas: Ar [L min ⁻¹]	0.7-1.0
Sample gas: Ar [L min ⁻¹]	0.7-0.8
Add gas: He [L min ⁻¹]	0.9-1.0
RF generator power [W]	1200
Acceleration voltage [V]	-10000
Extraction [V]	-1200
Focus [V]	-600
Sample cone	Ni, orifice 1.1 mm diameter
Skimmer cone	H-type, Ni, orifice 0.8 mm diameter
Mass resolution	~8000
Amplifiers [Ω]	10 ¹¹
Faraday cup setup:	
^{52}Cr (L4), ^{54}Fe (L2), ^{56}Fe (Central), ^{57}Fe (H1), ^{58}Fe (H2), ^{60}Ni (H4)	
Cycle integration time [s]	2
Number of cycles	40-80

To explore the behaviour of different siliceous matrices, we analysed the following sample materials: olivine (fayalite and forsterite), biotite, hornblende, garnet and a Fe-Mn crust. Olivine with fayalite composition is from the contact metamorphosed Biwabik Iron Formation (USA) (sample E in Frost et al. (2007)). San Carlos Olivine (SC Olivine), a well-established $\delta^{18}\text{O}$ mineral standard, is of forsterite composition and is often used in experimental petrology (e.g. Costa and Chakraborty, 2008; Galer and O'Nions, 1989; Holzheid and Grove, 2002). The biotite sample B-4B is a mineral standard for K-Ar dating (Flisch, 1982). The hornblende sample Siss 3 is from the Bergell tonalite in the southeast Central Alps (Villa and von Blanckenburg, 1991). The garnet sample is a piece from the rim of a large almandine crystal formed in schist. The Fe-Mn crust (cruise VA13/2, sample 327 KD) is from the Central Pacific (von Stackelberg et al., 1984) and was analysed at its surface. The in-house metal standard Puratronic (Johnson Matthey) is frequently analysed as control sample during our laser ablation sessions. The major element composition of the sample materials are reported in *Table 2.2*.

Table 2.2
Chemical composition in weight percent with anhydrous, F and Cl excluded

Sample	Olivine ^a (fayalite)	SC Olivine ^b (forsterite)	Garnet	Biotite	Hornblende ^c	Fe-Mn Crust ^d
SiO ₂	30.72	40.54	37.63	35.04	43.80	6.40
Al ₂ O ₃	-	0.03	21.21	18.10	9.22	-
TiO ₂	-	0.01	0.01	2.88	1.53	-
Cr ₂ O ₃	-	0.02	0.11	-	0.01	-
MgO	3.64	48.82	4.96	7.14	11.23	1.11
FeO	64.75	9.81	33.63	21.88	17.16	12.65
MnO	1.10	0.14	0.60	0.33	0.39	20.10
CaO	0.04	0.08	2.40	-	11.91	1.25
Na ₂ O	-	0.02	0.02	0.08	1.17	-
K ₂ O	-	-	-	9.40	1.16	-
Total	100.25	99.39	100.58	95.09	97.55	41.51

The chemical compositions are averages obtained from data published by ^aFrost et al. (2007), ^bGaler and O'Nions (1989), ^cVilla and von Blanckenburg (1991) and ^dvon Stackelberg et al. (1984). The compositions of biotite B-4B and garnet were obtained by electron microprobe.

Sample materials and iron reference material IRMM-014 were analysed in raster-mode using a spot diameter of ~ 30 μm . The acquisition parameters were set to acquire 50 to 80 cycles per analysis, with a cycle integration time of 2 s. On-peak-zero measurements were usually not subtracted as the background signal on mass ⁵⁶Fe was less than 1.5 mV compared to signal intensities of 8 to 12 V on a 10^{11} Ω resistor when analysing the sample material. Exceptions are biotite and forsterite, where signal intensities on mass ⁵⁶Fe of only 5 V could be achieved. In

theses cases, the background levels for all detected isotopes were measured for 30 cycles prior to each analysis by closing the laser shutter and were subtracted from each measured cycle. To compensate for different Fe concentrations and light absorption efficiencies between sample and standard materials, Fe signal intensities were matched by applying different laser repetition rates (Table 2.3). Multiple analyses were performed for each sample to investigate the external repeatability. Each sample was analysed in one to three measuring sessions within 12 months.

Table 2.3
Repetition rates and signal intensities for UV fs LA-ICP-MS

Sample	IRMM-014/ Puratronic	SC Olivine (forsterite)	Olivine (fayalite)	Biotite	Hornblende	Garnet	Fe-Mn Crust
Repetition rate [Hz]	2-5	90-350	60	50-70	60	100	20
Ion beam on $^{56}\text{Fe}^*$ [V]	5-10	5	10	5	9	12	8

*Faraday cups are equipped with 10^{11} resistors.

To prove the accuracy of the LA data, Fe isotope composition of the sample materials were obtained independently by solution nebulization ICP-MS following the procedure described in Schoenberg and von Blanckenburg (2005). Forsterite, biotite, garnet and hornblende were digested in HF-HNO₃. The Mn-Fe crust was dissolved in 6 mol/L HCl. Fe was separated by anion-exchange chromatography. For the Fe-Mn crust, Fe was additionally precipitated with NH₄(OH) after anion-exchange chromatography to remove residual transition metals. The Fe isotope compositions were then determined on a ThermoFinnigan Neptune MC-ICP-MS from solutions by the standard-sample bracketing method using the iron reference material IRMM-014. The external reproducibility at the 95% confidence level of solution nebulization ICP-MS for $\delta^{56/54}\text{Fe}$ and $\delta^{57/54}\text{Fe}$ are 0.049‰ and 0.071‰, respectively (Schoenberg and von Blanckenburg, 2005).

LA and solution data are reported as $\delta^{56/54}\text{Fe}$, $\delta^{57/54}\text{Fe}$ and $\delta^{57/56}\text{Fe}$ values relative to IRMM-014, e.g. for $\delta^{56/54}\text{Fe}$:

$$\frac{\delta^{56/54}\text{Fe}}{\text{‰}} = \left(\frac{{}^{56}\text{Fe}/{}^{54}\text{Fe}_{\text{Sample}}}{{}^{56}\text{Fe}/{}^{54}\text{Fe}_{\text{IRMM-014}}} - 1 \right) * 1000 \quad (2.1)$$

2.3. Results

All LA data of the individual samples are presented in three-isotope plots as $\delta^{56/54}\text{Fe}$ versus $\delta^{57/54}\text{Fe}$ together with the independently obtained solution ICP-MS data as reference values (*Figure 2.1*). Mean Fe isotope data of fs LA-ICP-MS and solution ICP-MS are summarized in *Table 2.4*. Accurate data have to plot along the mass-dependent fractionation line defined by the mass differences with a slope of 1.4881 and should agree with the solution ICP-MS values within their respective precision. Data that plots elsewhere in the diagram are affected by isobaric interferences.

The fayalite sample exhibits a mean LA $\delta^{56/54}\text{Fe}$ value of $-0.19 \pm 0.15\text{‰}$ (2 SD, $n = 8$) compared to -0.18‰ in $\delta^{56/54}\text{Fe}$ obtained by solution ICP-MS (*Figure 2.1a*). For the SC Olivine (fosterite) (*Figure 2.1b*), the LA data yielded lower $\delta^{56/54}\text{Fe}$ values than solution ICP-MS giving mean $\delta^{56/54}\text{Fe}$ values of $-0.32 \pm 0.13\text{‰}$ (2 SD, $n = 18$) and -0.04‰ , respectively. Moreover, not all LA data plot on the fractionation line giving evidence for isobaric interferences. Garnet revealed a mean LA $\delta^{56/54}\text{Fe}$ value of $-0.23 \pm 0.34\text{‰}$ (2 SD, $n = 44$) (*Figure 2.1c*). Isotopic difference exists within the garnet crystal when comparing the data of the outer rim ('top') with data obtained in 2 cm distance from it ('bottom') (see *Table 2.4*), although its chemical composition is homogeneous. Some of the data points for garnet do not plot on the fractionation line. Solution ICP-MS obtained a $\delta^{56/54}\text{Fe}$ value of -0.18‰ for garnet. Biotite revealed a mean LA $\delta^{56/54}\text{Fe}$ value of $0.22 \pm 0.15\text{‰}$ (2 SD, $n = 11$) and a solution ICP-MS $\delta^{56/54}\text{Fe}$ value of 0.09‰ (*Fig. 1d*). For hornblende (*Figure 2.1e*), the mean LA $\delta^{56/54}\text{Fe}$ value is $-0.01 \pm 0.11\text{‰}$ (2 SD, $n = 12$), and solution ICP-MS revealed a $\delta^{56/54}\text{Fe}$ value of 0.08‰ . LA-ICP-MS analyses of the surface of the Fe-Mn crust give a mean $\delta^{56/54}\text{Fe}$ value of $-0.23 \pm 0.10\text{‰}$ (2 SD, $n = 11$) as compared to -0.30‰ in $\delta^{56/54}\text{Fe}$ obtained by solution ICP-MS (*Fig. 1f*). All data obtained for fayalite, biotite, hornblende and the Fe-Mn crust plot on the mass-dependent fractionation line.

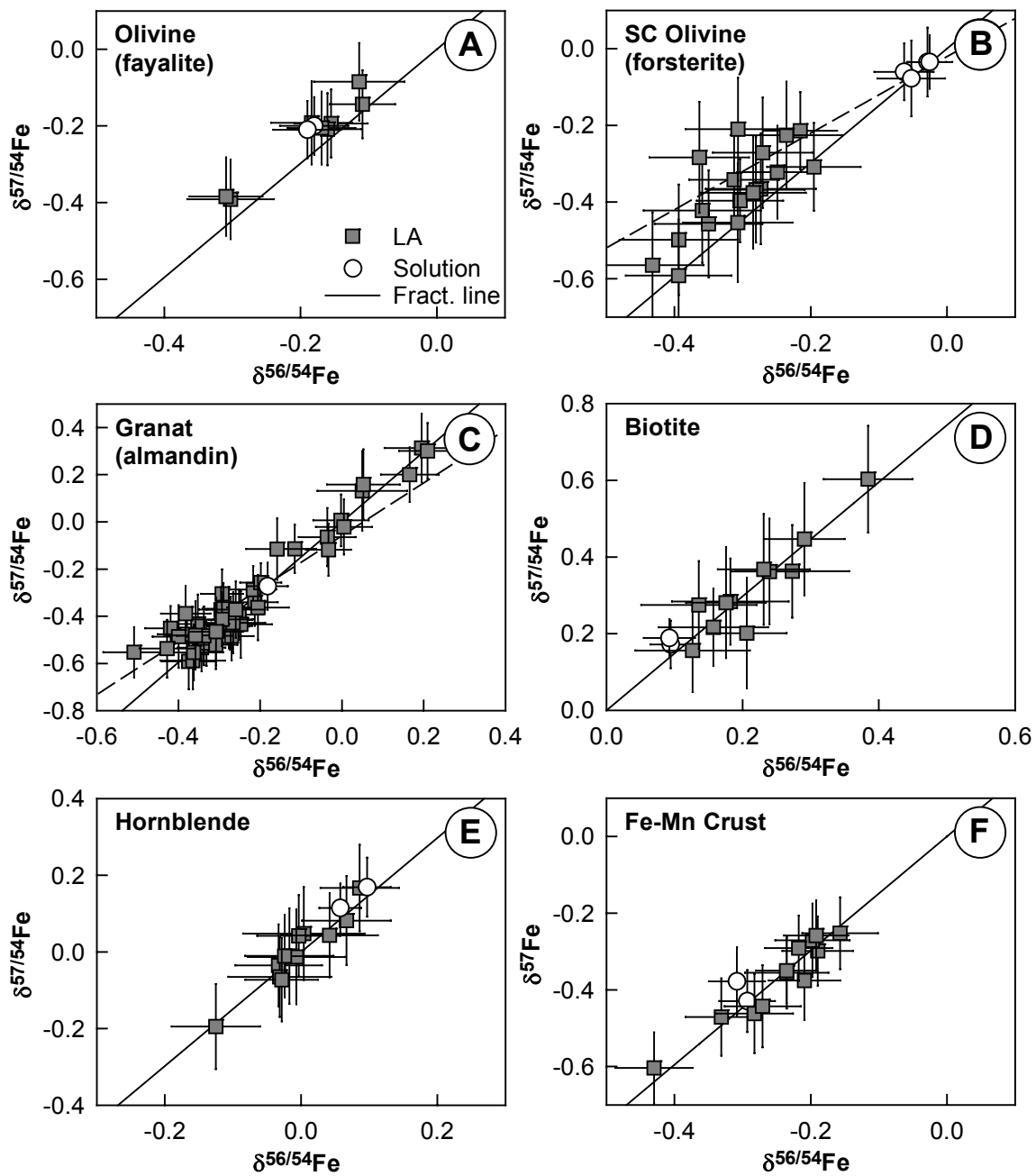


Figure 2.1 Three-isotope plots for the analysed sample materials showing normalized isotope ratios obtained by UV fs LA-ICP-MS using the raster-mode (closed squares) and conventional solution nebulization ICP-MS (open cycles). With the exception of forsterite (SC Olivine) and garnet, all data plot along the mass-dependent fractionation line demonstrating the absent of molecular or elemental interferences during UV fs LA-ICP-MS. The LA data of forsterite (SC Olivine) (**B**) are shifted towards lower values along a vector with the slope of ~ 1 (dashed line) indicating if compared to solution ICP-MS data a significant under-correction of the isobaric interference of ^{54}Cr on ^{54}Fe . The same effect is observable for garnet but to less extent.

Table 2.4

Mean Fe isotope data obtained by UV fs LA-ICP-MS and solution ICP-MS

Sample material	UV fs LA-ICP-MS						Solution ICP-MS		
	$\delta^{56/54}\text{Fe}_{\text{mean}}$	$\delta^{57/54}\text{Fe}_{\text{mean}}$	$\delta^{57/56}\text{Fe}_{\text{mean}}$	$\delta^{56/54}\text{Fe}^*_{\text{mean}}$	$^{54}\text{Cr}/^{54}\text{Fe}_{\text{mean}}$	n	$\delta^{56/54}\text{Fe}_{\text{mean}}$	$\delta^{57/54}\text{Fe}_{\text{mean}}$	n
Puratronic (pure iron)	0.08 ± 0.09	0.12 ± 0.14	0.04 ± 0.08	0.08 ± 0.17	0.0000035	83	0.09	0.13	4
Olivine (fayalite)	-0.19 ± 0.15	-0.23 ± 0.22	-0.04 ± 0.07	-0.08 ± 0.15	0.0000019	8	-0.18 ^a	-0.21 ^a	2
SC Olivine (forsterite)	-0.31 ± 0.13	-0.37 ± 0.23	-0.06 ± 0.15	-0.13 ± 0.30	0.0011	18	-0.04	-0.05	4
Garnet total	-0.23 ± 0.34	-0.32 ± 0.49	-0.09 ± 0.19	-0.17 ± 0.38	0.0010	44	-0.18	-0.27	1
top	-0.28 ± 0.13	-0.40 ± 0.20	-0.12 ± 0.13	-0.25 ± 0.25	0.0010	23			
bottom	0.01 ± 0.30	0.05 ± 0.37	0.04 ± 0.13	0.07 ± 0.25	0.0010	11			
Biotite	0.22 ± 0.15	0.32 ± 0.25	0.12 ± 0.13	0.24 ± 0.26	0.000017	11	0.09	0.18	2
Hornblende	-0.01 ± 0.11	0.00 ± 0.18	0.00 ± 0.08	0.01 ± 0.16	0.000082	12	0.08	0.14	2
Fe-Mn Crust	-0.23 ± 0.10	-0.35 ± 0.16	-0.12 ± 0.08	-0.24 ± 0.16	0.0000077	11	-0.30	-0.40	2

UV fs LA-ICP-MS and solution ICP-MS data are given as mean values in permil [‰], though all data are plotted in *Figure 2.1*. Uncertainties give the external reproducibility as 2 standard deviations yielded by multiple analyses (n). $\delta^{56/54}\text{Fe}^*_{\text{mean}}$ values are calculated from $\delta^{57/56}\text{Fe}$ values by multiplying with a factor of 1.9944, which corresponds to the mass difference between ^{56}Fe and ^{54}Fe relative to the mass difference between ^{57}Fe and ^{56}Fe . $\delta^{56/54}\text{Fe}^*$ and $\delta^{57/56}\text{Fe}$ values are preferred if $^{54}\text{Cr}/^{54}\text{Fe} > 0.0001$ as the Cr correction becomes unsatisfactory (Schoenberg and von Blanckenburg, 2005). ^apublished by Frost et al. (2007).

2.4. Discussion

Matrix effects during LA-ICP-MS cause deviation from the assumed true Fe isotope composition, i.e. solution ICP-MS values. Well-known matrix-dependent processes for ns LA are 1) fractionation at the ablation site, which leads to non-stoichiometric aerosols (e.g. Eggins et al., 1998; Hergenröder, 2006; Košler et al., 2005) and 2) particle size-related fractionation due to incomplete transport and ionisation of large particles in the ICP (e.g. Koch et al., 2002; Guillong et al., 2003). These effects, however, appear to be largely absent for fs LA (Garcia et al., 2008a, b; Horn and von Blanckenburg, 2007; Koch et al., 2004; 2005; Liu et al., 2004; Margetic et al., 2000; Saetveit et al., 2008; Wälle et al., 2008). Other matrix effects can be relevant for both ns and fs LA. For instance, variable plasma-loads can affect the instrumental mass discrimination (e.g. Kroslakova and Guenther, 2007), which might arise from the requirement to match the intensities of Fe ion beams by adjusting the laser repetition rates between sample and standard material, thereby introducing a higher load of non-Fe ions for the sample.

Other effects are isobaric interferences, which can compromise the results. At high Cr concentration of the sample material, the isobaric interference of ^{54}Cr on ^{54}Fe limits the accurate determination of $^{56}\text{Fe}/^{54}\text{Fe}$ and $^{57}\text{Fe}/^{54}\text{Fe}$ ratios for the MC-ICP-MS measurements.

2.4.1. Isobaric Cr interference

The isobaric interference of ^{54}Cr on ^{54}Fe is corrected using the method described in Schoenberg and von Blanckenburg (2005) but can become unsatisfactory at high Cr concentration. ^{52}Cr is measured to calculate ^{54}Cr by making the following assumptions, all of which introduce minor uncertainties: 1) the instrumental mass discrimination of Cr isotopes is calculated from $^{57}\text{Fe}/^{56}\text{Fe}$ ratio of samples relative to the certified IRMM-014 value, even though the instrumental mass discrimination might differ between these ratios (Albarède and Beard, 2004), 2) the $^{57}\text{Fe}/^{56}\text{Fe}$ ratio of the sample differs up to 1.5‰ from IRMM-014 and 3) the ratio $^{54}\text{Cr}/^{52}\text{Cr}$ is considered to be constant, although natural mass-dependent fractionation exists (e.g. Schoenberg et al., 2008). An incorrect Cr correction should result in data that does not follow the mass-dependent fractionation line in a $\delta^{56/54}\text{Fe}$ versus $\delta^{57/54}\text{Fe}$ plot, but a minor insufficient ^{54}Cr correction can easily escape notice. In a three isotope plot, under- or over-correction shifts the data along a vector with the slope of 1, whereas the fractionation line has a slope of 1.4881. LA data can be shifted by about $\pm 0.2\%$ in $\delta^{56/54}\text{Fe}$ and still appear within errors to plot along the fractionation line. This correction method has been demonstrated to be sufficient for solution ICP-MS data with low Cr concentrations and $^{54}\text{Cr}/^{54}\text{Fe}$ ratios up to 0.0001, (Schoenberg and von Blanckenburg, 2005). Therefore this correction was adopted with the same Cr limit for LA-ICP-MS in this study. The LA data of the samples fayalite, biotite, hornblende, and Fe-Mn crust reveal $^{54}\text{Cr}/^{54}\text{Fe}$ ratios of 0.0001 or lower, and agree with the solution ICP-MS data within their respective precision (*Table 2.4*). This demonstrates an adequate Cr correction for these samples and excludes other matrix-effects. The SC Olivine (forsterite) exhibits a $^{54}\text{Cr}/^{54}\text{Fe}$ ratio of 0.0011. The $\delta^{56/54}\text{Fe}$ data obtained by LA are on average 0.3‰ lower when compared to solution data giving evidence for under-correction of ^{54}Cr on ^{54}Fe (*Figure 2.1b*). Garnet revealed a similar $^{54}\text{Cr}/^{54}\text{Fe}$ ratio of 0.0010, but the data appear to be less affected on average. The mean LA $\delta^{56/54}\text{Fe}$ value does not differ significantly from the solution ICP-MS value (*Figure 2.1c*). To circumvent this limitation for high Cr concentrations, $\delta^{56/54}\text{Fe}$ can be calculated from the unaffected $\delta^{57/56}\text{Fe}$ value by multiplying with a factor of 1.9944, which corresponds to the mass difference between ^{56}Fe and ^{54}Fe relative to the mass difference between ^{57}Fe and ^{56}Fe and an exponential fractionation law. For the SC Olivine, this approach

reveals an inferred mean $\delta^{56/54}\text{Fe}$ value of $-0.13 \pm 0.30\text{‰}$ (2 SD, n=18) as compared to -0.04‰ in $\delta^{56/54}\text{Fe}$ obtained by solution ICP-MS, which is consistent within its precision. The inferred mean $\delta^{56/54}\text{Fe}$ value for garnet is $-0.17 \pm 0.38\text{‰}$ (2 SD, n=11), which agrees well with -0.18‰ in $\delta^{56/54}\text{Fe}$ revealed by solution ICP-MS.

For sample materials with a $^{54}\text{Cr}/^{54}\text{Fe}$ ratio higher than 0.0001, $\delta^{56/54}\text{Fe}$ values should be inferred from $\delta^{57/56}\text{Fe}$, since Cr correction becomes unreliable. All analysed matrices yield accurate results within their precision after careful evaluation of the Cr correction demonstrating matrix independency.

2.4.2. Variable mass load in the ICP-MS

Variable ion loads in the mass spectrometer may be present if sample and standard material were ablated with different laser repetition rates in order to compensate for variable Fe concentrations of the materials (*Table 2.3*). Mass load induced-matrix effects in the mass spectrometer can result in variable instrumental mass discrimination and potentially occur for both ns and fs laser ablation (e.g. Horn and von Blanckenburg, 2007; Krosiakova and Guenther, 2007). A changing ion load might influence the space charge effect in the ICP, which describes the preferential extraction of heavy ions, and the extraction conditions in the ion optical system of the mass spectrometer. Despite the application of very different repetition rates and therefore highly variable mass loads (*Table 2.3*), this effect appears to be negligible as accuracy is maintained for all analyzed samples.

2.4.3. Precision and accuracy

The external repeatability of Fe isotope analysis for the various matrices have been determined by multiple analyses (n > 10), which have been obtained in one to three measuring sessions within a period of 12 months. For hornblende and the surface of the Fe-Mn crust, a precision of close to 0.10‰ was achieved in $\delta^{56/54}\text{Fe}$ (2 SD), which is identical to the precision obtained for pure iron (Puratronic) (*Table 2.4*) and other homogeneous materials, e.g. iron oxides and iron meteorites (Horn et al., 2006). Fayalite and biotite exhibit slightly increased standard deviations of $\pm 0.15\text{‰}$ (2 SD), respectively. This results from low signal intensities for biotite, e.g. 5 V on mass ^{56}Fe , and from sample heterogeneity in the case of fayalite. Although the fayalite crystallized at high temperatures during contact metamorphism in the Biwabik Iron Formation, it exhibits slightly heterogeneous Fe concentrations (Frost et al., 2007). Because of high Cr

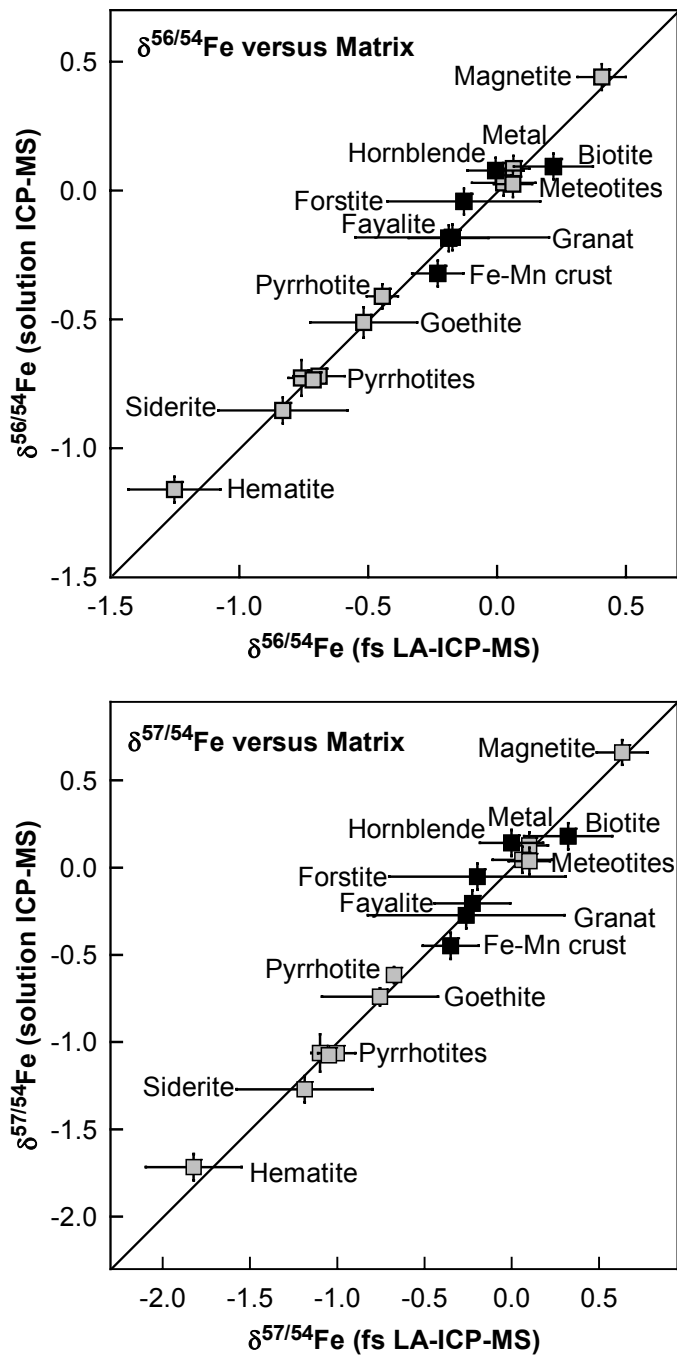


Figure 2.2 Comparison of mean $\delta^{56/54}\text{Fe}$ and $\delta^{57/54}\text{Fe}$ values obtained by *in situ* UV fs LA-ICP-MS with those measured by solution ICP-MS. Gray data points were published in Horn et al. (2006), black data points are from this study. All LA data agree with the data obtained from solution within errors. While maintaining high precision and accuracy, the reliability of matrix-independent calibration is now validated for metals, oxides, hydroxides, carbonates, sulfides, silicates and the complex matrix of Mn-Fe crusts. Large error bars for some of the LA data are caused by heterogeneous sample material. Due to high Cr concentrations in forsterite and garnet, the $\delta^{56/54}\text{Fe}$ and $\delta^{57/54}\text{Fe}$ values are inferred from $\delta^{57/56}\text{Fe}$ values which increases their errors.

concentrations relative to the Fe contents in SC Olivine and garnet, $\delta^{57/56}\text{Fe}$ values are preferred. These values have a slightly increased uncertainty of 0.15‰ (2 SD) for SC Olivine due to the low Fe concentration. For $\delta^{56/54}\text{Fe}$ values inferred from $\delta^{57/56}\text{Fe}$ values, propagation doubles uncertainties. Garnet exhibits a large error in $\delta^{57/56}\text{Fe}$ of $\pm 0.38\%$ (2 SD), which can be explained by a heterogeneous Fe isotope composition of the crystal, although its chemical composition is homogenous. The outer rim of the crystal revealed a mean inferred $\delta^{56/54}\text{Fe}$ values of -0.25% , which differs significantly from 0.07% obtained in 2 cm distance from the rim (two-sample Student's *t*-test, 99% confidence level) (*Table 2.3*). This Fe isotope zonation in garnet indicates different growth stages of the crystal and shows that substantial Fe isotope heterogeneities exist in high-temperature metamorphic minerals.

2.5. Conclusions

These results support the observations of Horn et al. (2006) and demonstrate that UV fs LA coupled to MC-ICP-MS provide highly precise and accurate Fe isotope data at high spatial resolution using non-matrix matched calibration. This applies even for sample materials with complex matrices and low Fe concentrations (< 10wt.% FeO).

- 1) For the analysis of siliceous matrices, continuous ablation of the sample material prior to analysis establishes stable conditions by conditioning the interface region of the ICP-MS.
- 2) Due to the isobaric interference of ^{54}Cr on ^{54}Fe in the ICP-MS, a careful consideration of the Cr correction is necessary for sample materials with high Cr concentrations. $\delta^{57/56}\text{Fe}$ values are preferred for sample materials with a $^{54}\text{Cr}/^{54}\text{Fe}$ ratio higher than 0.0001. Commonly used $\delta^{56/54}\text{Fe}$ and $\delta^{57/54}\text{Fe}$ values can be inferred by multiplying $\delta^{57/56}\text{Fe}$ with the relative mass difference of the desired isotope ratio because of the mass-dependent fractionation behaviour of Fe isotopes, both in nature and during analytical mass discrimination.
- 3) The accuracy and precision of Fe isotope have been verified for following matrices: pure iron, iron meteorites, iron oxides and hydroxides, iron sulfides, iron carbonates, biotite, olivine (forsterite and fayalite), hornblende, garnet and a Fe-Mn crust (this study, Horn et al., 2006). All of which have been measured using non-matrix matched calibration, which demonstrates that matrix effects are absent within the obtainable precision of 0.1‰ (2 SD) in $\delta^{56/54}\text{Fe}$ and 0.2‰ (2 SD) in $\delta^{57/54}\text{Fe}$ independent of the matrix.

fs LA-ICP-MS provides an excellent tool to study Fe isotope variations *in situ* at high spatial resolution independent of the matrix while maintaining precision and accuracy. This capability opens a wide spectrum of applications allowing the investigation of Fe isotope variations in

coexisting mineral phases in order to constrain processes in low and high temperature environments. An example for this type of application is the study of Fe isotopes in Precambrian banded iron formations to reconstruct their genesis (Steinhoefel et al., submitted a, b). Precise Fe isotope analysis of silicate mineral phases is of particular interest when investigating processes in metamorphic and igneous rocks, which exhibit small variation in Fe isotope composition (e.g. Beard and Johnson, 2004; Poitrasson and Freydier, 2005; Schoenberg, 2009; Schuessler et al., 2006; Schuessler et al., 2009). The potential to explore high-temperature processes becomes obvious considering the Fe isotope zonation with differences of 0.3‰ in $\delta^{56/54}\text{Fe}$ discovered in garnet. Many applications using tracer studies in the material sciences now also appear to be possible.

3

Micro-scale tracing of Fe and Si isotope signatures in banded iron formation using femtosecond laser ablation

Abstract

We have detected micrometer-scale differences in Fe and Si stable isotope ratios between coexisting minerals and between layers of banded iron formation (BIF) using a UV femtosecond laser ablation system connected to a MC-ICP-MS. In the magnetite-carbonate-chert BIF from the Archean Old Wanderer Formation in the Shurugwi Greenstone Belt (Zimbabwe), magnetite shows neither intra- nor inter-layer trends giving overall uniform $\delta^{56}\text{Fe}$ values of $\sim 0.9\%$, but exhibits intra-crystal zonation. Bulk iron carbonates are also relatively uniform at near-zero values, however their individual $\delta^{56}\text{Fe}$ value is highly composition-dependent: both siderite and ankerite and mixtures between both are present, and $\delta^{56}\text{Fe}$ end member values are 0.4% for siderite and -0.7% for ankerite. The data suggest either an early diagenetic origin of magnetite and iron carbonates by the reaction of organic matter with ferric oxyhydroxides catalysed by Fe(III)-reducing bacteria; or more likely an abiotic reaction of organic carbon and Fe(III) during low-grade metamorphism. Si isotope composition of the Old Wanderer BIF also shows significant variations with $\delta^{30}\text{Si}$ values that range between -1.0 and -2.6% for bulk layers. These isotope compositions suggest rapid precipitation of the silicate phases from hydrothermal-rich waters. Interestingly, Fe and Si isotope compositions of bulk layers are covariant and are interpreted as largely primary signatures. Moreover, the changes of Fe and Si isotope signatures between bulk layers directly reflect the upwelling dynamics of hydrothermal-rich water which govern the rates of Fe and Si precipitation and therefore also the development of layering. During periods of low hydrothermal activity, precipitation of only small amounts of ferric oxyhydroxide was followed by complete reduction with organic carbon during diagenesis

resulting in carbonate-chert layers. During periods of intensive hydrothermal activity, precipitation rates of ferric oxyhydroxide were high, and subsequent diagenesis triggered only partial reduction, forming magnetite-carbonate-chert layers. We are confident that our micro-analytical technique is able to detect both the solute flux history into the sedimentary BIF precursor, and the BIF's diagenetic history from the comparison between coexisting minerals and their predicted fractionation factors.

3.1. Introduction

Banded iron formations (BIFs) are chemical marine sediments that formed periodically throughout the Precambrian (3.8 to 0.5 Ga) and are usually characterized by alternating Fe- and Si-rich layers. The peak in BIF formation between 2.5 and 2.3 Ga appears to correlate with major changes in the Earth's history such as the rise of atmospheric oxygen and the change from anoxic to oxic conditions in the ocean (Canfield, 2005; Holland, 2006). BIFs are the product of chemical precipitation from seawater and subsequent depositional, diagenetic and metamorphic processes. Because of this extraordinary record of the early Earth, it is of major interest to understand the genetic history of BIFs.

The investigation of light stable isotope systems in BIFs, namely O, C and S isotope ratios, has a long tradition (e.g. Becker and Clayton, 1972, 1976; Perry et al., 1973, 1978; Goodwin et al., 1976; Baur et al., 1985; Beukes et al., 1990; Kaufman et al., 1990; Mojzsis et al., 1996; Fedo et al., 2006). In recent years, advances in analytical techniques have provided the opportunity to study the stable isotope fractionation of the two major elements in BIFs, Fe and Si. The investigation of fractionation mechanisms of stable Fe isotopes is now well-advanced, and shows an overall range of ~ 5 ‰ in $\delta^{56}\text{Fe}$ (for overview see Anbar, 2004; Beard and Johnson, 2004; Dauphas and Rouxel, 2006). The largest variability in the Fe isotope composition in any single type of sample has so far been measured in BIFs (Johnson et al., 2003, 2008; Dauphas et al., 2004, 2007; Rouxel et al., 2005; Frost et al., 2007; Whitehouse and Fedo, 2007; Valaas Hyslop et al., 2008) and ranges from about -2.5 to 1.6‰ in $\delta^{56}\text{Fe}$. It has been shown that Fe isotope heterogeneities in BIFs can be preserved during diagenesis and metamorphism (Frost et al., 2007; Whitehouse and Fedo, 2007). Magnetite, for example, appears to be of diagenetic origin and preserves its Fe isotope signature throughout all but the highest grades of prograde contact metamorphism (Frost et al., 2007). Therefore, Fe isotopes appear to be a powerful tool for the reconstruction of the early history of BIF deposition, and much effort is now being directed at deciphering the underlying processes that have caused their heterogeneous Fe isotope

composition. For example, the appearance of BIFs that are depleted in heavy Fe isotopes have been interpreted as evidence for bacteria-mediated Fe reduction during diagenesis (Johnson and Beard, 2006; Johnson et al., 2008). Dissimilatory Fe reduction appears to be a significant form of metabolism since at least 2.9 Ga (Vargas et al., 1998). In contrast, BIFs which are enriched in heavy Fe are regarded to reflect partial oxidation of Fe in the upper levels of ocean water (Dauphas et al., 2004; 2007; Johnson and Beard, 2006; Johnson et al., 2008).

The variability of stable Si isotope ratios has also been explored in natural systems, with an overall fractionation of ~12‰ in $\delta^{30}\text{Si}$ (for overview see André et al., 2006; van den Boorn et al., 2007). However, experiments on processes and degrees of Si isotope fractionation are yet to be carried out. Chert within BIFs exhibits a largely negative Si isotope signature ranging from about -2.5 to -0.5‰ in $\delta^{30}\text{Si}$ which has been interpreted as a hydrothermal signal (Jiang et al., 1993; Ding et al., 1996; André et al., 2006). Positive $\delta^{30}\text{Si}$ values in Precambrian chert may reflect elevated temperature of the seawater, the influence of a continental source, or precipitation from isotopically heavy seawater (Robert and Chaussidon, 2006; van den Boorn et al., 2007).

The questions posed by these studies generally revolve around the relative impact of variable source isotope compositions as opposed to those caused by diagenesis. In previous studies, these issues are left unresolved, to some extent, by the experimental approach which is mostly based on bulk rock or bulk mineral concentrate analysis and may obscure small-scale fractionation processes within layers of a BIF or temporal developments between layers. These issues may be resolved by an increased spatial resolution of the measurement. In this study, we present the results on the first in situ determination of Fe and Si isotope compositions using an UV femtosecond laser ablation system coupled to a multicollector inductively coupled plasma mass spectrometer (MC-ICP-MS). The advantage of this in situ method is the high spatial resolution while maintaining a high precision of the isotope ratio measurement. This approach provides the opportunity to investigate potential small-scale temporal trends and processes as based on the composition of individual mineral phases. We show that small-scale intra-layer fractionations are of diagenetic origin, while secular trends in the BIF isotope stratigraphy reveal the source of the contributing fluids.

3.2. Investigated BIF

The investigated sample material represents an Algoma-type iron formation from the Wanderer Formation within the late Archean Shurugwi Greenstone Belt in Zimbabwe and was collected

from the Old Wanderer Mine (Figure 3.1). The Shurugwi Greenstone Belt belongs to the Bulawayan Supergroup, a well-preserved greenstone belt sequence in the Zimbabwe craton. Isotope age data of this sequence range from 2.88 to 2.65 Ga (Moorbath et al., 1987; Wilson et al., 1995). The evolution and the tectonic setting of the Bulawayan Greenstone Belt Sequence are still subjects to controversy. It is now generally believed that the belt is associated with a passive continental margin setting and the interaction of mantle plumes during the beginning continental break-up (Prendergast, 2004).

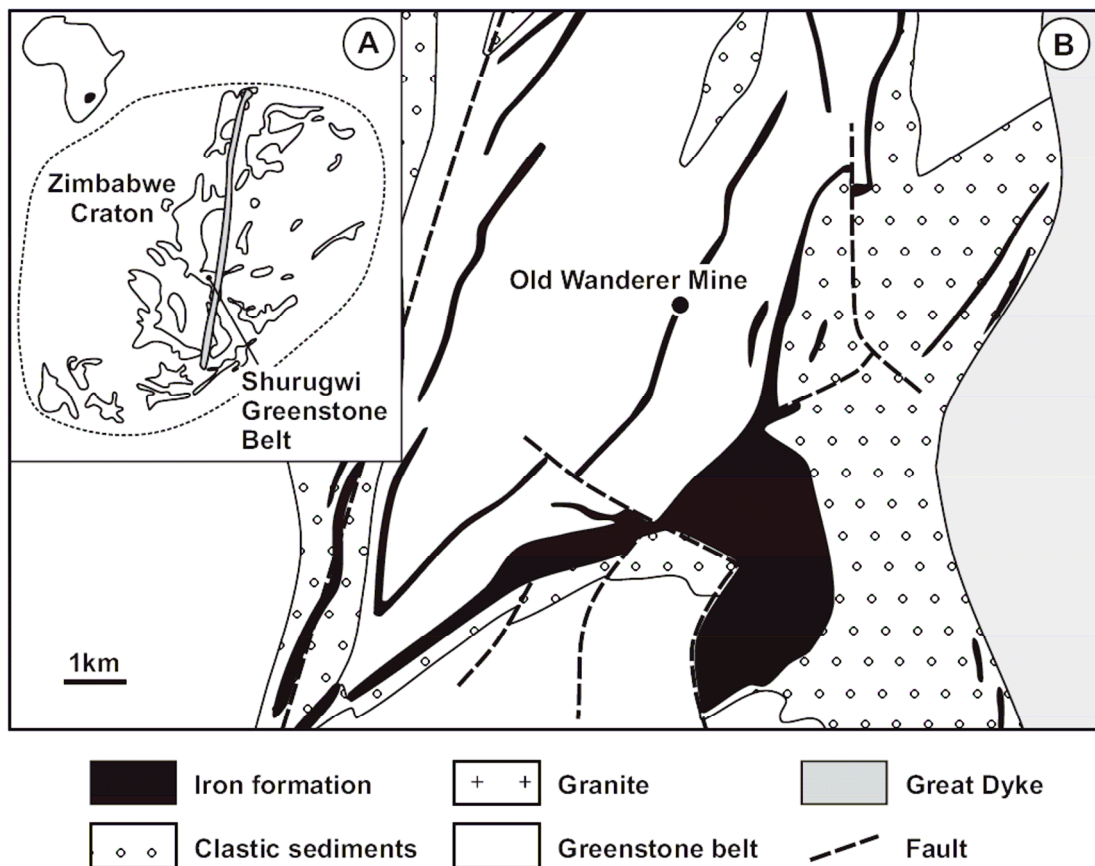


Figure 3.1 Simplified geological map of the Shurugwi Greenstone Belt. **A)** Greenstone belts (white) and Great Dyke (grey) within the Archean Zimbabwe Craton (modified after Oberthuer et al., 1990). **B)** Part of the *ca.* 2.7 Ga old Shurugwi Greenstone Belt (modified after Tyndale-Biscoe, 1949). Rocks of the greenstone belt include epidiorite, basaltic schist and serpentine. The Wanderer Formation consists of banded iron formation and clastic rocks including conglomerate, grit, quartzite and phyllitic schist. The investigated sample was collected in the area of the Old Wanderer Mine.

The Wanderer Formation is a sequence of clastic and chemical sediments with a number of ore bodies of approximately 100 m in thickness, which partly contain gold mineralizations (Tyndale-Biscoe, 1949; Foster and Gilligan, 1987). The iron formation within this succession is described as a mixed silicate carbonate facies. The chondrite-normalized rare earth element (REE) distribution of this iron formation exhibits a flat pattern with a distinct positive Eu-anomaly and depleted absolute concentrations which is typical for Archean Fe-rich sediments (Oberthuer et al., 1990). The presence of positive Eu-anomalies in BIFs indicates a dominant high-temperature hydrothermal source for Fe (Bau and Dulski, 1996). Gold mineralizations occur mainly in phyllite. They are rare in iron formation, where they are associated with high abundance of iron sulphide (Tyndale-Biscoe, 1949; Oberthuer et al., 1990). The metamorphic overprint of this area is at the most greenschist facies as conversion of chlorite to biotite is rare in phyllite (Tyndale-Biscoe, 1949).

The magnetite-carbonate-chert BIF investigated in this study (*Figure 3.2*) is pristine: primary textures and structures are well preserved, replacements of secondary iron sulfides are absent, and quartz occurs in the form of microcrystalline chert. Layers of several millimetres thickness are composed of variable amounts of chert, iron carbonates (siderite and ankerite), magnetite, and minor pyrite and chlorite (*Figure 3.3, Table 3.1*). Greenish layers are magnetite-rich with minor chlorite. Fe concentrations are high with ~35 wt.%. In these layers, the chemical composition of iron carbonates is dominated by siderite; ankerite is a minor constituent. Light layers are dominated by iron carbonate and chert and contain no magnetite. These layers exhibit much lower Fe concentrations of ~10 wt.%, and ankerite and siderite may reach equal proportions. The chemical compositions of magnetite, siderite and ankerite have been investigated by electron microprobe and are presented in *Table 3.2*. The very pure magnetite of stoichiometric composition exhibits grains of 10 to 50 μm in diameter with sub- to euhedral habit and is concentrated within well-defined bedding planes. Iron carbonate occurs as siderite, $(\text{Fe}_{0.75-0.90}, \text{Mg}_{0.10-0.25})\text{CO}_3$, and ankerite, $\text{Ca}(\text{Fe}_{0.60-0.75}, \text{Mg}_{0.25-0.40})(\text{CO}_3)_2$, in variable proportions. Both types of iron carbonates exhibit chemically zoned crystals indicating a complex growth history. In the thin section, cores of irregular shape show distinct transitions to interlocked overgrowths which differ in the relative proportion of Mg and Fe (*Figure 3.2b*). Average chemical compositions of the two siderite and ankerite varieties, respectively, are given in *Table 3.2*. Xenomorphic quartz occurs in form of microcrystalline chert grains with grain-sizes between 5 to 50 μm in diameter. Assuming similar depositional rates as estimated for other BIF deposits (Trendall et al., 2004, Pickard 2002; 3003), the investigated thin section may represent some 10^2 to 10^3 years of deposition.

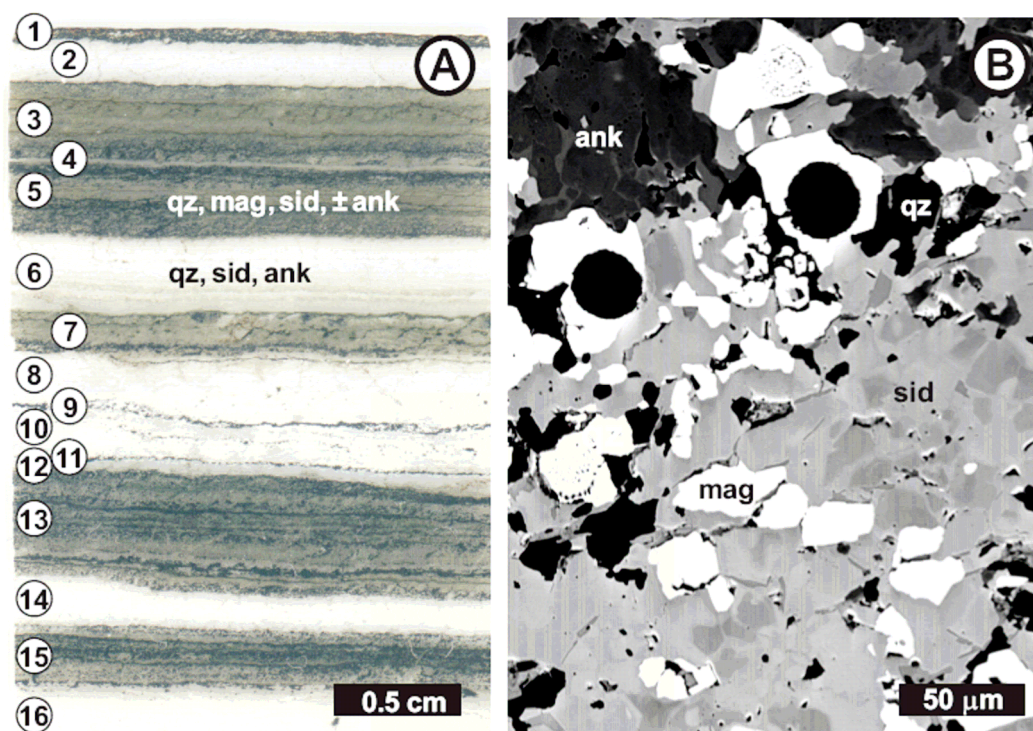


Figure 3.1 Photograph and backscattered electron (BSE) image of the Old Wanderer BIF from the *ca.* 2.7 Ga old Shurugwi Greenstone Belt with mag=magnetite, sid=siderite, ank=ankerite and qz=chert. **A)** The investigated thin section exhibits alternating carbonate-chert and magnetite-carbonate-chert layers. **B)** The BSE image shows laser ablation craters in magnetite crystals. Both types of iron carbonates exhibit chemically zoned crystals indicating a complex growth history. Cores of irregular shape show distinct transitions to interlocked overgrowths which differ in Mg substitution.

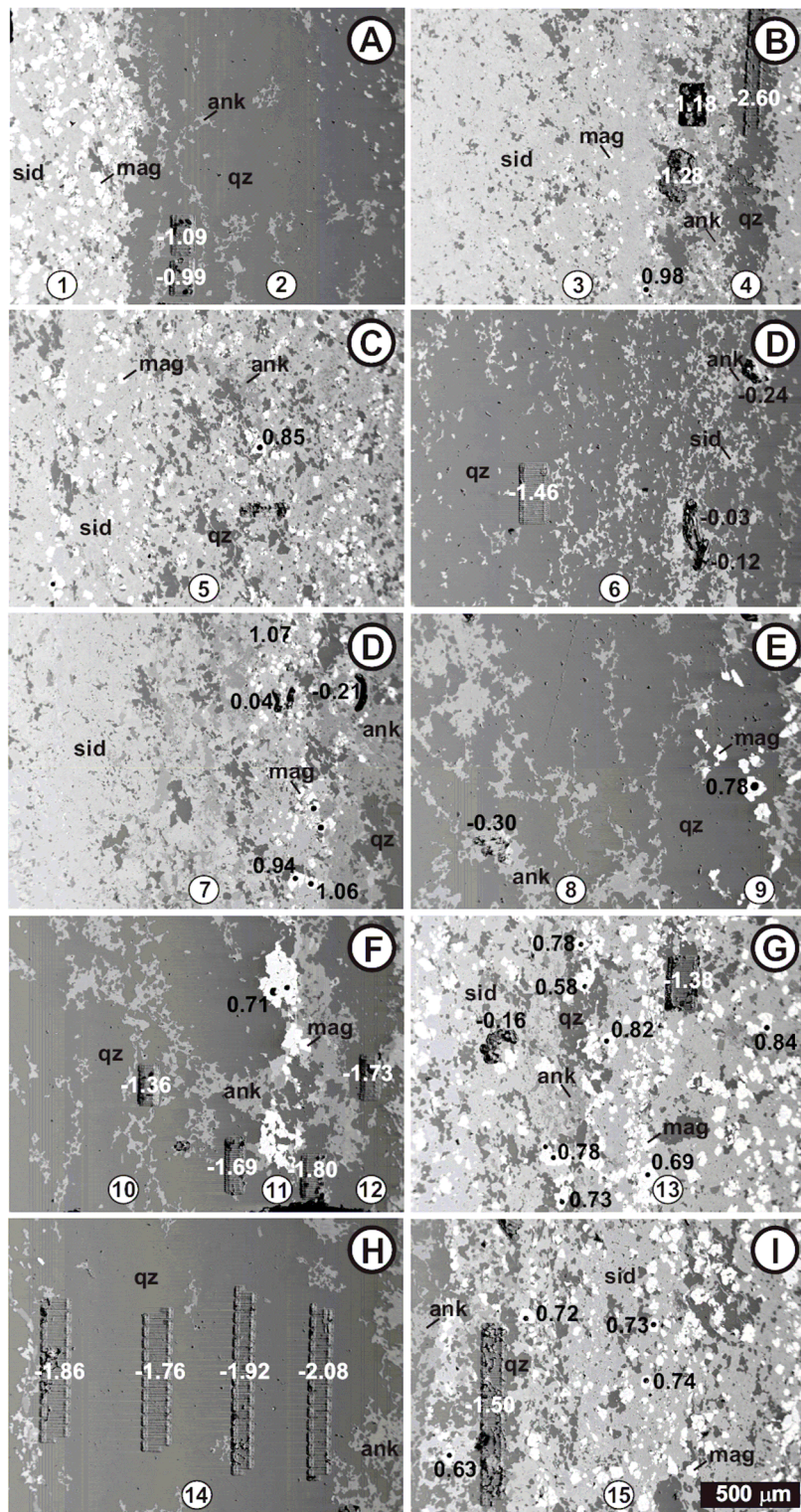


Figure 3.1 BSE images of representative sections of the investigated layers with mag=magnetite, sid=siderite, ank=ankerite and qz=chert. The numbering of the layers corresponds to Figure 3.2a. Fe isotope analyses in magnetite (spots) and in Fe carbonates (short line scans) are labelled with $\delta^{56}\text{Fe}$ values in ‰ (black numbers). Si isotope analyses in chert (rasters) are indicated with $\delta^{30}\text{Si}$ values in ‰ (white numbers).

Table 3.1
Estimated modal abundance and Fe and Si isotope composition of bulk layers

layer	qz	mag	sid	ank	$\delta^{56}\text{Fe}$	$\delta^{30}\text{Si}$
1	15	30	55	0		-1.04
2	90	0	5	5	0.12	-1.48
3	15	10	75	5	0.31	-1.25
4	100	0	0	0		-2.55
5	15	15	65	5	0.36	-1.12
6	70	0	15	15	0.09	-1.45
7	15	10	65	10	0.22	-1.35
8	70	0	0	30	0.25	-1.26
9	0	100	0	0	0.76	
10	70	0	5	25	0.11	-1.41
11	0	100	0	0	0.71	
12	70	0	0	30		-1.79
13	30	25	40	5	0.38	-1.28
14	90	0	5	5	-0.04	-1.84
15	25	25	40	10	0.49	-1.26
16	90	0	5	5	0.18	-1.87

The major mineral phases are qz=quartz, mag=magnetite, sid=siderite, and ank=ankerite. The Fe isotope composition of bulk layers is calculated from Fe isotope data of the major Fe-bearing mineral phases, their estimated modal abundances, and Fe contents. The Si isotope composition of bulk layers is inferred from multiple analyses of chert (see *Table 3.4*). The Fe and Si values of bulk layers are covariant with a correlation factor of 0.71, significant at the confidence level of 95%. Numbering of layers corresponds to *Figure 3.2a*.

Table 3.2

Average chemical composition (in weight % \pm 1 SD) for Fe-bearing mineral phases of the Old Wanderer BIF determined by electron microprobe

Mineral	mag (n=4)	sid 1 (n=6)	sid 2 (n=4)	ank 1 (n=4)	ank 2 (n=5)
SiO ₂	0.87 \pm 0.46	0.04 \pm 0.03	0.04 \pm 0.04	0.04 \pm 0.05	0.04 \pm 0.03
TiO ₂	0.02 \pm 0.02	0	0	0.01 \pm 0.02	0.01 \pm 0.01
Al ₂ O ₃	0.06 \pm 0.03	0	0.01 \pm 0.01	0	0
Fe ₂ O ₃	67.03 \pm 1.24	0	0	0	0
FeO	32.18 \pm 0.55	56.67 \pm 1.45	50.8 \pm 0.94	24.54 \pm 1.71	19.96 \pm 1.11
MnO	0.03 \pm 0.05	0.45 \pm 0.22	1.21 \pm 0.27	0.54 \pm 0.22	0.87 \pm 0.21
MgO	0	3.08 \pm 1.01	7.89 \pm 1.11	5.11 \pm 0.74	8.26 \pm 0.76
CaO	0.03 \pm 0.03	0.4 \pm 0.16	0.35 \pm 0.08	25.65 \pm 0.13	26.07 \pm 0.44
Na ₂ O	0.01 \pm 0.02	0.02 \pm 0.02	0.02 \pm 0.02	0.01 \pm 0.02	0.03 \pm 0.02
K ₂ O	0.01 \pm 0.01	0.01 \pm 0.01	0.01 \pm 0.01	0.01 \pm 0.01	0
Total	100.24 \pm 0.45	60.68 \pm 0.35	60.34 \pm 0.65	55.91 \pm 0.78	55.24 \pm 0.33

Siderite and ankerite appear each in two distinct chemical compositions with variable proportions of Mg and Fe, as indicated by sid1 & sid2 and ank1 & ank2, respectively.

3.3. Methods

The Fe and Si isotope compositions of major Fe-bearing minerals and chert, respectively, were determined by in situ femtosecond laser ablation ICP-MS (LA-ICP-MS) measurements at a high spatial resolution. Fe isotope ratios of bulk mineral separates were also measured by solution ICP-MS. All isotope ratios were determined on a Thermo Finnigan Neptune MC-ICP-MS at the Leibniz University of Hannover and corrected for the instrumental mass discrimination using standard-sample-bracketing. The data are reported as $\delta^{56}\text{Fe}$ and $\delta^{30}\text{Si}$ relative to the reference materials IRMM-014 and NBS28, respectively.

$$\frac{\delta^{56}\text{Fe}}{\text{‰}} = \left(\frac{{}^{56}\text{Fe}/{}^{54}\text{Fe}_{\text{Sample}}}{{}^{56}\text{Fe}/{}^{54}\text{Fe}_{\text{IRMM-014}}} - 1 \right) \quad (3.1)$$

$$\frac{\delta^{30}\text{Si}}{\text{‰}} = \left(\frac{{}^{30}\text{Si}/{}^{28}\text{Si}_{\text{Sample}}}{{}^{30}\text{Si}/{}^{28}\text{Si}_{\text{NBS28}}} - 1 \right) \quad (3.2)$$

3.3.1. *In situ* LA-ICP-MS

The Fe and Si isotope composition of the different mineral phases of the investigated BIF were determined using our in-house built UV femtosecond laser ablation system coupled to a Thermo Finnigan Neptune MC-ICP-MS. The laser ablation system is based on an amplified frequency-quadrupled femtosecond laser (Spectra Physics Hurricane I, USA) operating at a wavelength of 196 nm which avoids laser-induced isotope and elemental fractionation and minimizes the matrix dependency of analyses (Horn and von Blanckenburg, 2007). The accuracy and precision for Fe and Si isotope measurements have been verified for different types of matrices by Horn et al. (2006) and Chmeleff et al. (2008), respectively. Fe isotope ratios were determined by spot analysis with a diameter of 18-35 μm . For an average signal of 10 V for ^{56}Fe on a faraday cup equipped with a $10^{11} \Omega$ resistor, a spot analysis of 2 minutes creates a crater of $\sim 8 \mu\text{m}$ depth at a diameter of 30 μm in pure iron (reference material IRMM-014). A total consumption of $\sim 45 \text{ ng}$ Fe per analysis can be calculated. Because ion beam intensities between standard and sample materials should be matched, the analysis of minerals with lower Fe concentrations demands higher repetition rates resulting in a greater crater depth. The Si isotope ratios were measured in the raster mode using a spot size of $\sim 35 \mu\text{m}$. The raster size was about $50 \mu\text{m} \times 500 \mu\text{m}$. The ablated volume is $\sim 36 \times 10^3 \mu\text{m}^3$ for quartz giving a consumption of $\sim 50 \text{ ng}$ Si per analysis (Chmeleff et al., 2008). The acquisition parameters were set to acquire 30 to 60 cycles per analysis, with a cycle integration time of 2 seconds using the medium mass resolution for the mass spectrometer. The potential tapping of different phases during ablation are identified from shifts in the isotope ratios and/or variations in signal intensity, and such measurements were discarded.

Fe isotope measurements. The Fe isotope composition of magnetite, siderite and ankerite were determined following the analytical procedure of Horn et al. (2006). Previous investigations have shown that the overall reproducibility of different types of matrixes including iron oxides and iron carbonates is better than $\pm 0.1\%$ (2 SD) for $\delta^{56}\text{Fe}$ and that the results are consistent with those obtained by conventional solution ICP-MS measurements (Horn et al., 2006). Over the course of 9 months, replicated spot analyses of the metal standard Puratronic (Johnson Matthey) resulted in mean values of 0.08% for $\delta^{56}\text{Fe}$ and 0.12% for $\delta^{57}\text{Fe}$ relative to IRMM-014, with an external precision of ± 0.08 and $\pm 0.14\%$, respectively (2 SD, $n=101$) (Figure 3.4). This agrees well with the average value of $0.09 \pm 0.05 \%$ for $\delta^{56}\text{Fe}$ (2 SD, $n=4$) and $0.13 \pm$

0.08‰ for $\delta^{57}\text{Fe}$ (2 SD, n=4) obtained by solution ICP-MS measurements in our laboratory. The data show a Gaussian distribution and plot along the theoretical fractionation line for $\delta^{56}\text{Fe}$ versus $\delta^{57}\text{Fe}$ which confirms the long-term accuracy and reproducibility of the LA-ICP-MS measurements.

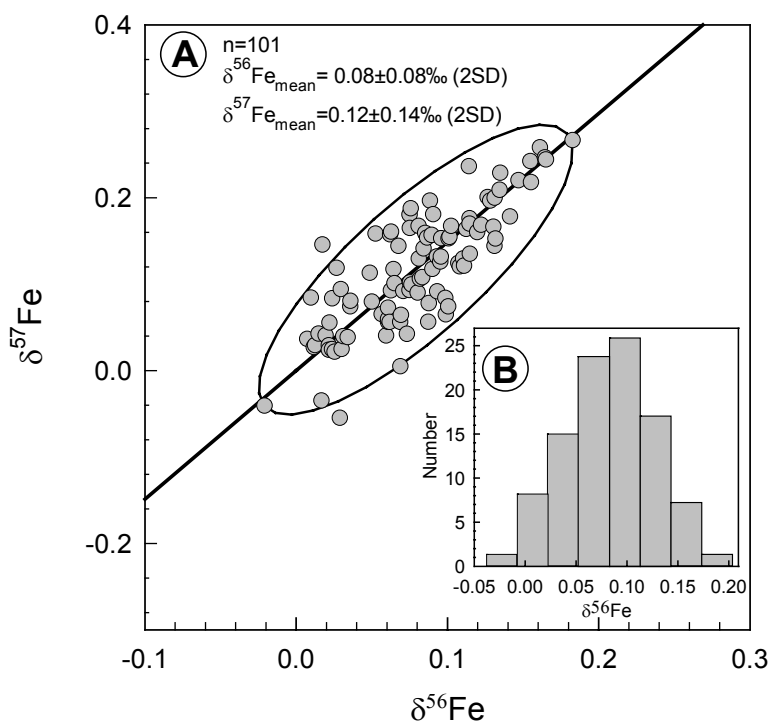


Figure 3.3 Reproducibility of Fe isotope spot analyses by LA-ICP-MS. **A)** The metal standard Puratronic was repeatedly measured against the reference material IRMM-014 over a course of about 9 months and plotted in a three-isotope diagram. The error ellipse indicates the 95% confidence level of the Puratronic data. **B)** Histogram of Puratronic data shows a Gaussian distribution.

The Fe isotope measurements by LA-ICP-MS on the BIF sample were carried out as follows. Magnetite crystals were analysed by spot analyses (Figure 3.2b, 3.3). The size of the crater ranged between 25 and 35 μm in diameter. The analyses were performed preferentially along the boundaries between layers to disclose potential intra-layer isotope trends but a number of analyses were also carried out in the center of the layers. Siderite and ankerite were analysed using the raster mode or short line scans on areas of 50 by 50 to 100 by 100 μm (Figure 3.3).

To detect potential isotope zonation within single magnetite crystals (< 50 μm), we developed a new analytical procedure that involves sequential coring - the core of the mineral phase is determined first using a spot diameter of 18 to 25 μm . In a second step, a spot analysis with a diameter of ~ 35 μm is superimposed onto the same location. This step removes a ring of

material around the pit of the first analysis and determines the Fe isotope composition of the outer part (rim) of the mineral phase for a cubic crystal structure. This procedure was validated prior to the analysis of magnetite using the spatially homogeneous metal standard Puratronic (Johnson Matthey). Figure 5 shows the result of 13 pairs of such core-rim analyses on the metal standard Puratronic in terms of their $\delta^{56}\text{Fe}$ compositions. The mean of $\delta^{56}\text{Fe}_{\text{core}}$ and $\delta^{56}\text{Fe}_{\text{rim}}$ is determined at $0.07 \pm 0.08\text{‰}$ and $0.06 \pm 0.17\text{‰}$, respectively, showing no significant difference of the distributions (two-sample Student's t-test, 95% confidence level). This result indicates that femtosecond laser-induced lateral damages or alterations of the material surrounding an ablation crater are undetectable at a precision level of 0.1‰ (2 SD) with respect to the Fe isotope composition.

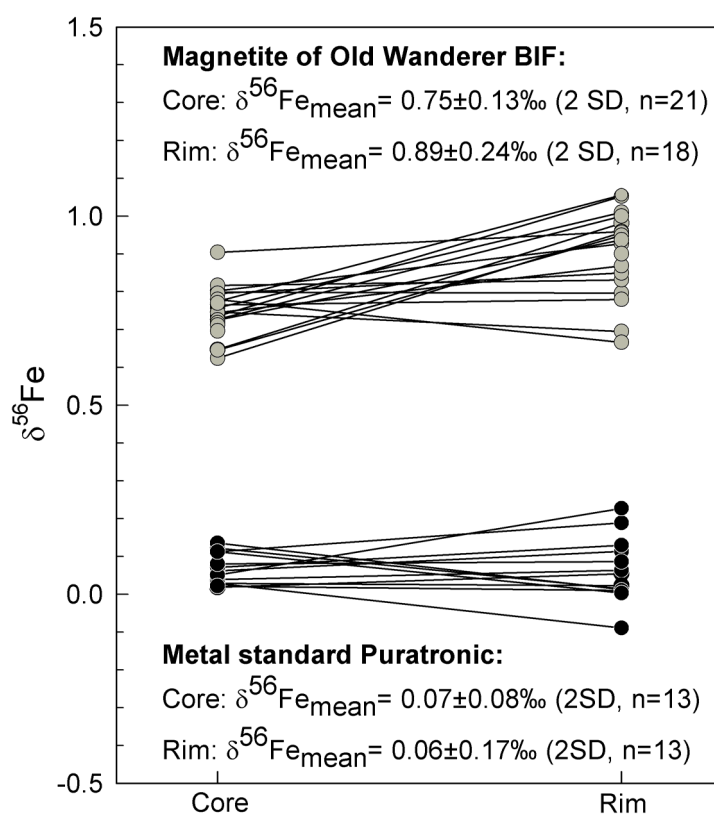


Figure 3.3 Fe isotope zonation in magnetite crystals in the Old Wanderer BIF. Corresponding pairs of core-rim analysis show that magnetite crystals tend to be heavier in their Fe isotope composition towards the rim. Considering all data the relative mean difference between core and rim is 0.14‰ in $\delta^{56}\text{Fe}$. To verify this method, the same experiment was carried out successfully on the homogeneous metal standard Puratronic. Here the inner spot analyses (=core) are identical with the outer spot analyses (=rim) within the analytical precision.

Si isotope measurements. The Si isotope composition were investigated in chert by LA-ICP-MS using the method described in detail by Chmeleff et al. (2008) which is similar to that of Fe isotope analysis. Accuracy and precision have been previously verified for different types of matrices including quartz giving a overall reproducibility of 0.24‰ (2 SD) for $\delta^{30}\text{Si}$ (Chmeleff et al., 2008). Chert was analysed by narrow rasters of about 50 by 500 μm to reach a high spatial resolution perpendicular to the layering (*Figure 3.3*).

3.3.2. Solution ICP-MS

In addition to LA-ICP-MS, the Fe isotope composition of iron carbonate and magnetite was investigated as bulk mineral leachates for several layers by solution ICP-MS. Individual layers were sampled using either a diamond tipped core bit or tungsten carbide micro-drill bits. The extracted material was crushed in an agate mortar if necessary and the different mineral phases were separated and dissolved as follows. The magnetite was removed magnetically and dissolved in aqua regia. Carbonates were leached with 10% acetic acid at 35°C to avoid dissolution of minor iron phases as chlorite, pyrite and any residual magnetite following the procedure of von Blanckenburg et al. (2008). Dissolution tests conducted under the same conditions have shown that 10% acetic acid does not dissolve magnetite, other iron oxides or pyrite. Layer 6 was used to test whether siderite and ankerite, exhibiting widely different isotope composition when analysed in situ (*Table 3.3, Figure 3.6a, b*), are leached in representative proportions. The calculated Fe isotope composition for bulk iron carbonate (based on estimated modal abundances of siderite and ankerite, their average Fe contents and their isotope compositions obtained by LA-ICP-MS) is -0.02‰ – this value shows no significant difference to 0.09‰ determined by solution ICP-MS and the leachates are considered representative. The Fe isotope composition of magnetite and iron carbonate were determined after chemical purification following the procedure described by Schoenberg and von Blanckenburg (2005). The obtained long-term external reproducibility of the solution ICP-MS measurements is better than $\pm 0.05\%$ (2 SD).

3.4. Results

3.4.1. Fe isotope composition

The Fe isotope compositions of the major Fe-bearing mineral phases are presented in *Table 3.3* and *Figures 3.6a, b* and *3.7*. Solution ICP-MS of magnetite exhibits $\delta^{56}\text{Fe}$ values of 0.82 to 1.00‰. LA-ICP-MS reveals significant variation in the magnetite Fe isotope composition in lateral as well as in vertical directions. However, Fe isotope compositions averaged over entire layers are surprisingly uniform (*Figure 6b*). Comparison of the standard deviation of magnetite populations with the standard deviation of a dataset obtained from homogeneous material shows that in most cases the variations exceed the analytical precision. This demonstrates that small-scale variations in magnetite-rich layers exist, and can be measured. The maximal observed range within a stratigraphic level is 0.45 to 0.76‰ in $\delta^{56}\text{Fe}$ giving a mean of $0.66 \pm 0.18\text{‰}$ (2 SD, n=11). Standard deviations of magnetite populations range from ± 0.08 to 0.21‰ (2 SD, n=5 to 17). The means of the layers obtained by LA-ICP-MS range from 0.71 to 1.02‰. Although heterogeneities exist, neither intra- nor inter-layer trends can be observed within layers 9 to 15, in which more than 5 analyses have been performed. Taking all spot analyses obtained in these layers, the dataset shows a Gaussian distribution giving an average of $0.72 \pm 0.17\text{‰}$ (2 SD, n=77) (*Figure 3.7*).

The magnetite crystals are internally heterogeneous in their Fe isotope composition, as revealed in layer 13 by the sequential coring method (*Figure 3.5*). Depending on the cut of the magnetite crystals in the thin section, the cores are up to 0.3‰ lighter in their Fe isotope composition than the rims. The mean $\delta^{56}\text{Fe}_{\text{core}}$ is $0.75 \pm 0.13\text{‰}$ (2 SD, n=21) which presents a resolvable difference from the mean $\delta^{56}\text{Fe}_{\text{rim}}$ of $0.89 \pm 0.24\text{‰}$ (2 SD, n=18) (two-sample Student's *t*-test, 95% confidence level).

Comparing average LA and solution ICP-MS measurements of magnetite in designated layers (*Table 3.3, Figure 3.6b*), the solution data appear to indicate a slightly heavier Fe isotope composition than the corresponding LA data. This discrepancy can be explained by the isotope zonation found in magnetite crystals. Spot analyses are usually placed away from crystal edges to avoid mixing of different phases. Because the outer rim is also the isotopically heaviest part of the crystals, the LA data is biased towards lighter compositions.

The iron carbonates were investigated in several layers via bulk mineral solution ICP-MS. The $\delta^{56}\text{Fe}$ values range from -0.13 to 0.25‰ giving an average of about 0‰. LA-ICP-MS of siderite

and ankerite show significant variations in their Fe isotope composition. Because pure iron carbonate phases are usually smaller than the area required for a LA analysis and cannot easily be distinguished from each other using the optical microscope integrated in the LA system, most analyses are likely to represent mixtures of siderite and ankerite. As expected from their distinct chemical composition with variable degrees of Mg- and Ca-substitution, Fe isotope compositions vary. Ankerite shows values which are always isotopically lighter when compared to siderite within a given layer. If we assume the lowest $\delta^{56}\text{Fe}$ values to represent the best estimate of ankerite compositions, whereas the highest $\delta^{56}\text{Fe}$ corresponds to those of the siderite end member, then ankerite exhibits $\delta^{56}\text{Fe}$ values as low as -0.70‰ , whereas siderite shows consistently positive $\delta^{56}\text{Fe}$ values of up to 0.43‰ . The relative difference of $\delta^{56}\text{Fe}$ observed in layers where both mineral phases were examined is ~ 0.4 to 1.1‰ .

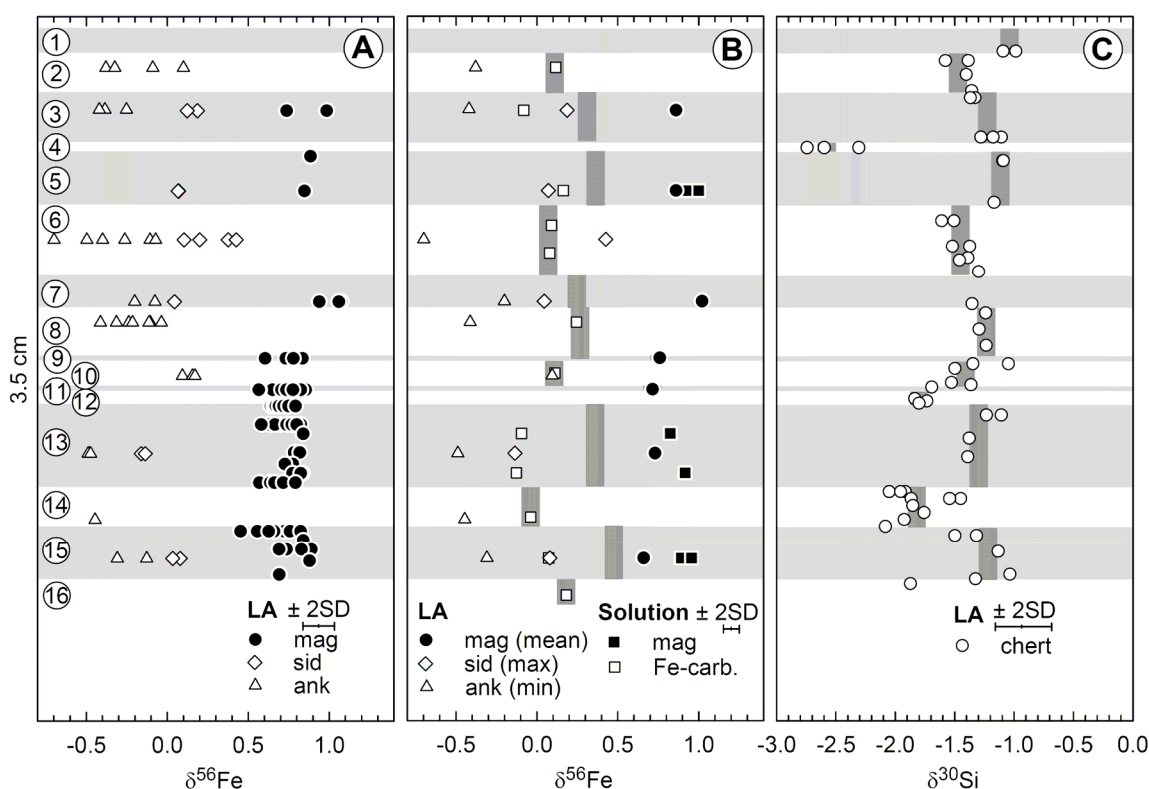


Figure 3.6 Fe and Si isotope variations in the Old Wanderer BIF within a section of 3.5 cm. The numbering of layers corresponds to *Figure 3.2a*. Carbonate layers consists of siderite, ankerite and chert (in white), whereas magnetite-rich layers are mainly composed of magnetite, siderite and chert (in grey). **A)** Fe isotope data for magnetite, siderite and ankerite obtained by LA-ICP-MS. Single magnetite crystals were investigated by LA spot analyses revealing significant variations in the Fe isotope composition. Siderite and ankerite were analysed by LA using the raster procedure. The variation in the Fe isotope composition of siderite and ankerite are largely attributed to variable mixing proportions of these end member minerals. The lowest and the highest $\delta^{56}\text{Fe}$ values represent the best estimates of ankerite and siderite end member

composition, respectively. **B)** Fe isotope composition of bulk mineral separates obtained by solution ICP-MS and summary of Fe isotope data obtained by LA-ICP-MS. The estimated Fe isotope composition of bulk layers is indicated by vertical bars. **C)** Si isotope composition of chert obtained by LA-ICP-MS using raster-mode. Average Si isotope composition of layers is indicated by vertical bars. The Fe and Si isotope compositions of bulk layers show a covariance (correlation factor=0.71).

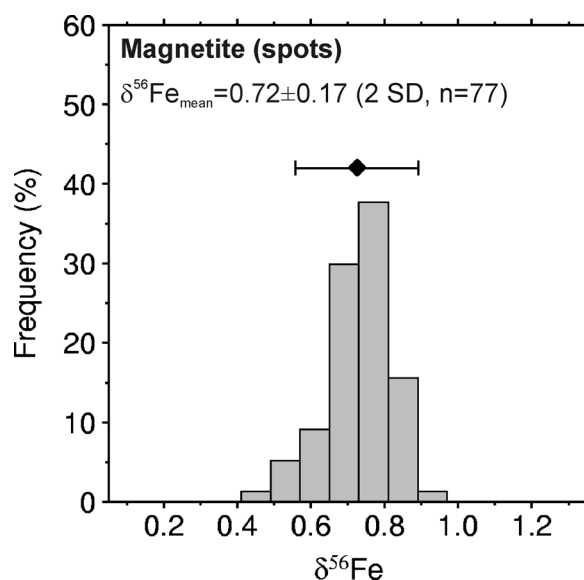


Figure 3.7 Histograms of Fe isotope data of magnetite obtained by LA spot analyses. The population exhibits a Gaussian distribution. The standard deviation differs significantly from the external reproducibility (error bar) indicating true heterogeneity in the Fe isotope composition on a sub-millimeter scale.

3.4.2. Si isotope composition

The Si isotope data are presented in *Table 3.4* and *Figure 3.6c*. Chert in the investigated BIF exhibits strong variations in its Si isotope composition perpendicular to layering giving a mean $\delta^{30}\text{Si}$ value of $-1.56 \pm 0.76\text{‰}$ (2 SD, n=68). The calculated mean composition of the layers ranges between -1.04 to -2.55‰ . Intra-layer variations are minor with ± 0.09 to 0.44‰ (2 SD), which is close to the achievable precision of $\pm 0.24\text{‰}$ (2 SD).

Table 3.3

Fe isotope data obtained by LA-ICP-MS and solution ICP-MS

LA-ICP-MS						Solution ICP-MS							
Layer	Mineral	$\delta^{56}\text{Fe}_{\text{mean}}$	$\delta^{56}\text{Fe}_{\text{em}}$	2 SD	no. of analyses	Layer	Mineral	$\delta^{56}\text{Fe}$					
1	ank	-0.17	-0.38	0.44	4	2	sid+ank	0.12					
3	mag	0.86		0.35	2	3	sid±ank	-0.08					
	ank	-0.35	-0.42	0.18	3	5	mag	1.00					
	sid	0.15	0.19	0.09	2		sid±ank	0.92					
5	mag	0.86		0.05	2	6	sid+ank	0.16					
	sid	0.07	0.07	0.01	2								
6	ank	-0.34	-0.70	0.48	6	6	sid+ank	a	0.09				
	sid	0.28	0.43	0.30	4			b	0.08				
7	mag	1.02		0.15	3	8	sid+ank	0.25					
	ank	-0.14	-0.20	0.18	2	10	sid+ank	0.11					
	sid	0.04			1								
8	ank	-0.20	-0.41	0.26	7	13	mag	a	0.82				
9	mag	0.76		0.15	7			sid±ank	a	-0.10			
						b	-0.13						
10	ank	0.14	0.09	0.08	3	14	sid+ank	-0.04					
11	mag	0.71		0.21	9	15	mag	0.89					
									13	mag	a	0.82	
											b	0.92	
											sid±ank	a	-0.10
											b	-0.13	
14	sid+ank	-0.04											
13	mag	a	0.71	0.08	17	15	mag	0.89					
		b	0.73	0.16	11				sid±ank	0.07			
		c	0.67	0.17	5								
		total	0.73	0.14	41								
16	sid+ank	0.18											
14	ank	-0.48	-0.49	0.02	3	15	mag	0.89					
									15	mag	0.89		
15	mag	a	0.66	0.18	11	15	mag	0.89					
		b	0.77	0.16	5								
		total	0.71	0.22	20								
15	ank	-0.22	-0.31	0.26	2	16	sid+ank	0.18					
									16	sid+ank	0.18		
15	sid	0.06	0.08	0.06	2	16	sid+ank	0.18					
									16	sid+ank	0.18		

The numbering of layers corresponds to *Figure 3.2a*, letters refer to different stratigraphic levels within layers. LA-ICP-MS data are presented as mean values, but all data are plotted in *Figures 3.6 and 3.7*. 2 SD refers to multiple analyses (n). In addition, we provide potential end member ratios ($\delta^{56}\text{Fe}_{\text{em}}$) for ankerite and siderite, respectively. The minimal value represents the endmember composition of ankerite, whereas the maximal value corresponds best to the end member composition of siderite.

Table 3.4
Si isotope data of chert obtained by LA-ICP-MS

Layer	$\delta^{30}\text{Si}$	2 SD	Layer	$\delta^{30}\text{Si}$	2 SD	Layer	$\delta^{30}\text{Si}$	2 SD	Layer	$\delta^{30}\text{Si}$	2 SD
1	-1.09		5	-1.10		10	-1.05		14	-1.45	
	-0.99			-1.09			-1.35			-1.54	
total	-1.04	0.15		-1.17			-1.50			-2.05	
			total	-1.12	0.09		-1.53			-1.92	
2	-1.39						-1.36			-1.96	
	-1.58		6	-1.51			-1.69			-1.87	
	-1.39			-1.61		total	-1.41	0.44		-1.85	
	-1.58			-1.37						-1.76	
total	-1.48	0.22		-1.52		12	-1.84			-1.92	
				-1.39			-1.73			-2.08	
3	-1.33			-1.46			-1.80		total	-1.84	0.41
	-1.37			-1.30		total	-1.79	0.10			
	-1.28		total	-1.45	0.21				15	-1.32	
	-1.11					13	-1.11			-1.50	
	-1.18		7	-1.35			-1.23			-1.13	
total	-1.25	0.22					-1.38			-1.33	
			8	-1.24			-1.39			-1.04	
4	-2.74			-1.29		total	-1.28	0.27	total	-1.26	0.32
	-2.31			-1.24							
	-2.60		total	-1.26	0.07				16	-1.87	
total	-2.55	0.44									

The numbering of layers corresponds to *Figure 3.2a*.

Table 3. 5
Fe isotope fractionation factors

Reactant	Product	Condition	$\Delta^{56}\text{Fe}_{\text{Product-Reactant}}$ (‰)	Reference
Experimental studies				
$\text{Fe(II)}_{\text{aq}}$	$\text{Fe(III)}_{\text{aq}}$	equilibrium	T=22°C +2.8 to +3.0	Johnson et al. (2002), Welch et al. (2003)
Fe(OH)_3	$\text{Fe(II)}_{\text{aq}}$	anaerobic photosynthesis	-1.5 ± 0.2	Croal et al. (2004)
dto.	dto.	abiotic	-1.0	Bullen et al. (2001)
Fe_2O_3 , FeO(OH)	$\text{Fe(II)}_{\text{aq}}$	DIR, equilibrium	-3.0	Crosby et al. (2007)
		equilibrium ¹	+0.1 ± 0.2	Skulan et al. (2002)
$\text{Fe(III)}_{\text{aq}}$	Fe_2O_3	DIR, equilibrium	+1.3 ± 0.1	Johnson et al. (2005)
$\text{Fe(II)}_{\text{aq}}$	Fe_3O_4	magnetotactic bacteria	0	Mandernack et al. (1999)
$\text{Fe(II)}_{\text{aq}}$	FeCO_3	DIR, equilibrium	0	dto.
$\text{Fe(II)}_{\text{aq}}$	FeCO_3	abiotic	-0.5 ± 0.2	Wiesli et al. (2004)
$\text{Fe(II)}_{\text{aq}}$	$\text{Ca}_{0.15}\text{Fe}_{0.85}\text{CO}_3$	DIR, equilibrium	-0.9	Johnson et al. (2005)
Fe_3O_4	FeCO_3	DIR, equilibrium	-1.3	dto.
Fe_3O_4	$\text{Ca}_{0.15}\text{Fe}_{0.85}\text{CO}_3$	DIR, equilibrium	-2.2	dto.
Fe_3O_4	FeCO_3	equilibrium	-1.8	Johnson et al. (2008) based on Johnson et al. (2005) and Wiesli et al. (2004)
Predictions by modeling				
$\text{Fe(II)}_{\text{aq}}$	$\text{Fe(III)}_{\text{aq}}$	equilibrium ²	TT=22°C +2.5 to +3.0	Anbar (2005)
$\text{Fe(II)}_{\text{aq}}$	Fe_3O_4	equilibrium ²	+0.3 to -0.8	based on Polyakov et al. (2007), Mineev et al. (2007) and Anbar (2005)
$\text{Fe(III)}_{\text{aq}}$	Fe_3O_4	equilibrium ²	-2.3 to -3.6	dto.
Fe_2O_3	Fe_3O_4	equilibrium ²	-0.9 to -1.8	based on Polyakov and Mineev (2000), Polyakov et al. (2007) and Mineev et al. (2007)
Fe_3O_4	FeCO_3	equilibrium ²	-1.8 to -2.8	dto.
$\text{Fe(II)}_{\text{aq}}$	FeCO_3	equilibrium ²	-2.5 to -2.6	based on Polyakov and Mineev (2000) and Anbar (2005)
$\text{Fe(II)}_{\text{aq}}$	$\text{CaFe}_{0.5}\text{Mg}_{0.5}(\text{CO}_3)_2$	equilibrium ²	-4.0 to -4.1	dto.
$\text{Fe(II)}_{\text{aq}}$	$\text{Ca}_{1.1}\text{Mg}_{0.5}\text{Fe}_{0.3}\text{Mn}_{0.1}(\text{CO}_3)_2$	equilibrium ²	-3.0 to -3.2	dto.

(1) A kinetic fractionation factor that was lower by 1 to 2‰ was documented for this reaction in the same study.

(2) Range is defined by $\text{Fe(III)}_{\text{aq}}$ and $\text{Fe(II)}_{\text{aq}}$ estimates that are from both DFT-PCM and DFT, while magnetite estimates are from both Mössbauer and INRRXS (see references).

3.5. Discussion

3.5.1. Significance of bulk Fe and Si isotope composition in the Old Wanderer BIF

The overall Fe and Si isotope compositions of the 2.7 Ga Old Wanderer BIF is within the observed range of previously investigated BIFs (see overviews in André et al., 2006; Johnson and Beard, 2006; van den Boorn et al., 2007). Iron carbonates with a bulk Fe isotope composition of $\sim 0\text{‰}$ and magnetite with $\delta^{56}\text{Fe}$ of $\sim 0.9\text{‰}$ reveal an overall enrichment in heavy Fe isotopes. Chert displays an overall depleted Si isotope signature, even though strong inter-layer variations exist ranging from -1.04 to -2.55‰ in $\delta^{30}\text{Si}$.

Although the geochemical cycles of Fe and Si in the Precambrian are still poorly understood it is clear that they differed from that of the Phanerozoic. Under anoxic conditions in Precambrian ocean, the Fe concentration in seawater would have been much higher than today, between 2 and 50 ppm (Ewers, 1983; Sumner, 1997; Canfield, 2005). The abundance of iron oxides requires oxidation in a largely anoxic ocean which is generally explained by a stratified ocean system with an oxidising upper water column (e.g. Klein, 2005). Oxidation and subsequent precipitation of ferric oxyhydroxide was most likely caused by anaerobic photosynthesis (e.g. Konhauser et al., 2002; Kappler et al., 2005) or atmospheric oxygen (e.g. Holland, 1973; Drever, 1974; Ehrenreich and Widdel, 1994; Kaufman et al., 2007). In the absence of silica-secreting organisms, the Si concentration in the Precambrian ocean could have been as high as 110 ppm, the saturation state of amorphous silica (Maliva et al., 2005). Therefore the direct precipitation of silica from seawater in form of siliceous gel is the most likely Si removal process. Sorption of silica on clay minerals, iron oxides, or organic matter may have played a role in the nucleation and/or precipitation (Perry and Lefticariu, 2003; Konhauser et al., 2007). BIFs within greenstone belts, such as the Old Wanderer BIF, are generally regarded to have formed in close vicinity to hydrothermal systems (e.g. Klein, 2005). In this regard, we can assume a predominantly hydrothermal fluid source providing the solutes, from which the sedimentary BIF precursor was precipitated. This is certainly suggested by REE patterns showing a positive Eu-anomaly which is interpreted as hydrothermal signature (Bau and Dulski, 1996; Oberthuer et al., 1990). Si isotopes are also compatible with a hydrothermal origin. Even though vent fluids carry Si with $\delta^{30}\text{Si}$ of -0.2 to -0.4‰ (De La Rocha et al., 2000), silica-rich deposits precipitated around oceanic smokers are even lighter with $\delta^{30}\text{Si}$ of $-1.6 \pm 0.7\text{‰}$ (2 SD, $n=25$) (Ding et al., 1996). This compares well to the mean $\delta^{30}\text{Si}$ measured in the Old Wanderer

BIF which is strongly negative at $-1.56 \pm 0.76\text{‰}$ (2 SD, n=57). Fe isotopes can also be explained by precipitation from a hydrothermal Fe source. $\delta^{56}\text{Fe}$ values measured in hydrothermal fluids typically range between -0.6 and -0.2‰ (Sharma et al., 2001; Beard et al., 2003; Severmann et al., 2004) with higher values corresponding to high Fe concentrations. Together with a presumably higher Precambrian hydrothermal flux, an elevated heat flux (Bau and Möller, 1993) and minimal oxidation rate close to the vent site under anoxic conditions, Johnson et al. (2008) have argued that ancient hydrothermal fluids would have exhibited a Fe isotope composition closer towards bulk oceanic crust, i.e. near-zero. This is roughly the composition of bulk Fe in the Old Wanderer BIF.

However, given that both Fe and Si precipitated simultaneously but with variable intensity as BIFs are characterized by alternating Fe-rich and Si-rich layers, their isotope fractionations must be considered together. The precipitation of amorphous silica favours light Si (De La Rocha et al., 1997; Ziegler et al., 2005; Basile-Doelsch, 2006). Fe precipitation by partial oxidation is dominated by ferric oxyhydroxide which is $\sim 1.5\text{‰}$ heavier than $\text{Fe(II)}_{\text{aq}}$ (Bullen et al., 2001; Skulan et al., 2002; Welch et al., 2003; Croal et al., 2004; Anbar et al., 2005). Potential Fe and Si isotope fractionation of the precipitates is illustrated in Figure 8. Considering the presumably long residence times for both Fe and Si in the order of 10^6 years (Siever, 1992; Trendall, 2002), steady state conditions of the ocean are likely and short-term changes of well-mixed seawater within the deposition time of some 10^2 to 10^3 years for the investigated BIF section are unexpected. In this case, a steady state system must exist between hydrothermal influx and chemical deposition.

In the Old Wanderer BIF, however, steady state conditions have not been attained as bulk layers, which reflect presumably primary signatures (see *section 5.2.*), are variable in their isotope compositions and differ in most cases from the hydrothermal signature. It is more likely that the residence time of both Fe and Si was short relative compared to precipitation time scales, and that pulses of hydrothermal emanations triggered episodic recharge and precipitation events. The result is that the degree of Fe and Si depletion of hydrothermal solutions can be variable, and Rayleigh distillation style modifications becomes visible in the Fe and Si isotope signatures. Therefore, both seawater and sediment composition depend on the fraction of Fe and Si precipitation. Because steady state is never achieved, isotope ratios of the precipitates are between those of the hydrothermal fluid (for complete precipitation) and the fractionation factor $\Delta_{\text{precipitate-solution}}$ (for incomplete precipitation). The data of the Old Wanderer BIF indicate high fractions of Fe precipitation (ca. 85-100%) whereas those of Si are low (ca. 1-40%) (*Figure 3.8*). This is compatible with a situation in which Si is precipitated by saturation from the entire

water column of an episodically discharged hydrothermal plume, whereas Fe is almost entirely precipitated as ferric oxyhydroxide, the precursor of magnetite and iron carbonate (see *section 5.2.*), via $\text{Fe(II)}_{\text{aq}}$ oxidation of the plume in the upper water column.

Surprisingly perhaps, $\delta^{56}\text{Fe}$ and $\delta^{30}\text{Si}$ values of bulk layers are covariant with a correlation factor of 0.71, significant at the confidence level of 95% (*Figures 3.6 and 3.8, Table 3.1*). However, given the opposite precipitation fractionation factors for Fe oxidation and Si precipitation, one may expect an anticorrelation.

The only plausible explanation for this phenomenon is one in which high fractions of Fe precipitation are simultaneous in space and time with low fractions of Si precipitation, and vice versa. An example is shown by the model curve in *Figure 8*, in which the fraction of precipitated Fe is always opposite to that of precipitated Si.

Figure 3.9 shows a possible scenario of an episodically active hydrothermal system. At periods of low plume dispersion (*Figure 3.9a*), silica precipitation occurs from a largely unaffected fluid near the venting site causing strongly negative $\delta^{30}\text{Si}$ values, whereas the low supply of Fe to the oxidizing upper water column promotes complete oxidation resulting in ferric oxyhydroxide with $\delta^{56}\text{Fe}$ values close to the hydrothermal signature, i.e. near-zero. This situation is compatible with the origin of carbonate-chert layers which exhibit low Fe contents together with low $\delta^{56}\text{Fe}$ and $\delta^{30}\text{Si}$ values relative to magnetite-rich layers. An extreme situation might be reflected by pure chert layers of exceptionally low $\delta^{30}\text{Si}$ values, i.e. layer 4 reveals -2.55% . In this case, the hydrothermal plume dispersion might be limited to the lower water column preventing Fe precipitation.

In periods, the upwelling plume reaches the surface of the ocean (*Figure 3.9b*), the fluid is modified by ongoing silica precipitation causing Rayleigh distillation or by mixing with ambient seawater with a strong positive isotope composition. Both shift the isotope signature of the precipitating silica towards heavier values (André et al., 2006; van den Boorn et al., 2007). The supply of large quantities of $\text{Fe(II)}_{\text{aq}}$ into the upper water column triggers partial oxidation as the oxidant becomes the limiting factor resulting in high rates of ferric oxyhydroxide formation with positive $\delta^{56}\text{Fe}$ values. Such a situation might be reflected in magnetite-carbonate-chert layers. They show significantly higher Fe contents together with significantly positive $\delta^{56}\text{Fe}$ and increased $\delta^{30}\text{Si}$ values compared to carbonate-chert-layers. This model of an episodically recharged hydrothermal plume explains the Fe and Si signatures of the Old Wanderer BIF but of course fractionation factors and source compositions that change with time cannot be excluded.

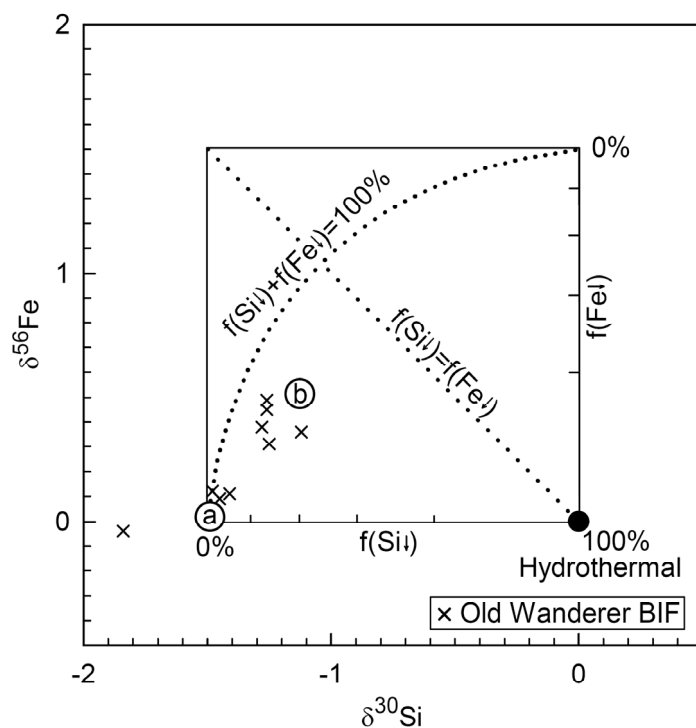


Figure 3.8 Conceptual model of the variability in $\delta^{30}\text{Si}$ and $\delta^{56}\text{Fe}$ for the initial precipitates, silica and ferric oxyhydroxide depending on the precipitated fraction f . A hypothetical hydrothermal solution is emanated with $\delta^{56}\text{Fe}$ and $\delta^{30}\text{Si}$ of 0‰, respectively. Precipitation from this fluid takes place with Fe(III) that is 1.5‰ heavier (through oxidation and ferric oxyhydroxide precipitation, Table 3.5), and SiO_2 (from oversaturation of seawater with Si) that is 1.5‰ lighter. Two opposing scenarios can be envisaged. In the first case, the hydrothermal influx and the depositional output have the same isotope compositions of 0‰ which can be attained either by steady state conditions or 100% precipitation of the dissolved Fe and Si. In the second case, precipitation of small fractions from seawater with a hydrothermal signature results in isotope compositions reflecting the fractionation factors of -1.5‰ in $\delta^{30}\text{Si}$ and 1.5‰ in $\delta^{56}\text{Fe}$. The diagonal line illustrates the isotope evolution by Rayleigh distillation for precipitating equal fractions of dissolved Si and Fe, and the axes of the inset indicate the fractions of Fe and Si precipitated. The data of bulk layers of the Old Wanderer BIF (only $\delta^{30}\text{Si}$ - $\delta^{56}\text{Fe}$ pairs are shown) plot below this line indicating low degrees of Si precipitation (1-40%) at high degrees of Fe precipitation (85-100%) but not steady state conditions. The correlation of the data roughly follows a curve of opposite fractions of cumulative precipitated Si and Fe ($f(\text{Si}\downarrow) + f(\text{Fe}\downarrow) = 100\%$). A possible scenario for the end members of the data indicated by a) and b) is sketched in Figures 3.9a and b, respectively.

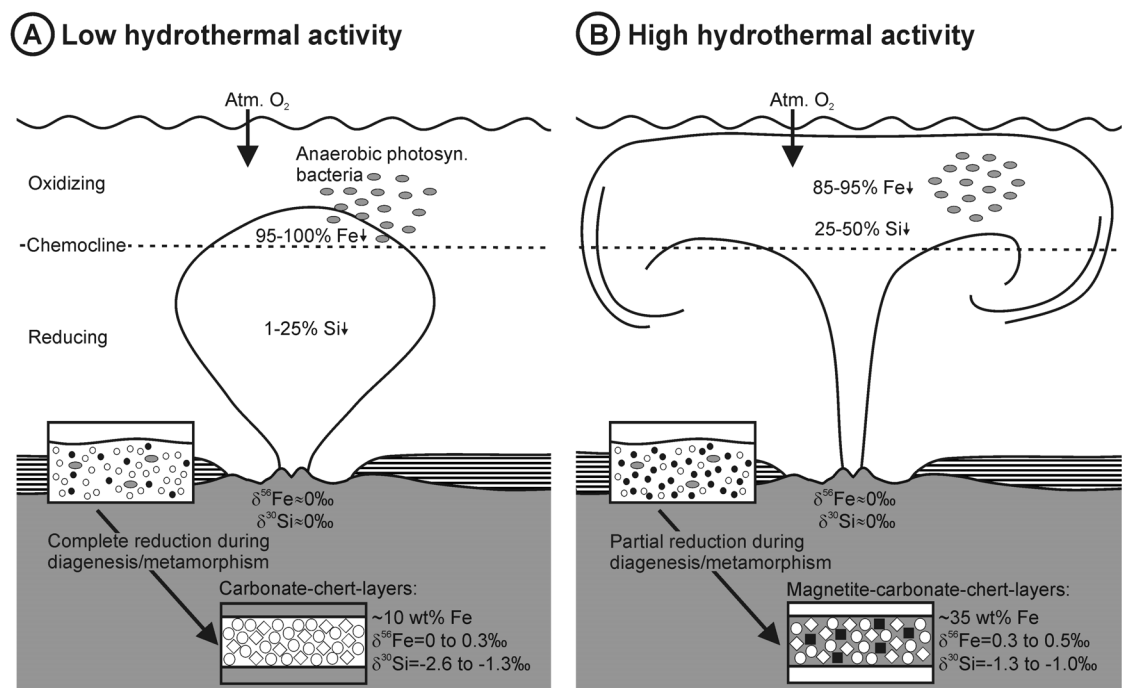


Figure 3.9 Scenario of episodic recharge and precipitation events by pulses of hydrothermal fluids and the origin of BIF layering. Silica (small open circles) is likely to precipitate from the entire water column, whereas the formation of ferric oxyhydroxide (small black circles) is restricted to the oxidizing surface. Magnetite (black squares) and iron carbonate (open diamonds) are diagenetic products of reduction of initial precipitated ferric oxyhydroxide by oxidizing of organic matter (greys ellipsoids); silica consolidates to chert (large open circles).

A) Low spatial expansion of the hydrothermal plume leads to layers which have low $\delta^{30}\text{Si}$ and $\delta^{56}\text{Fe}$ values at low Fe contents corresponding to the data marked with a) in *Figure 3.8*. Silica precipitates from a pristine fluid near the venting site and represents a small fraction of the dissolved Si resulting in strong negative $\delta^{30}\text{Si}$ values. The supply of $\text{Fe(II)}_{\text{aq}}$ into the oxidizing upper water column is limited causing near complete oxidation at low rates of ferric oxyhydroxide precipitation with $\delta^{56}\text{Fe}$ values close to the hydrothermal signature, i.e. 0‰. Subsequently, silica, ferric oxyhydroxide and organic matter are deposited and buried together at the seafloor. The low quantity of ferric oxyhydroxide deposition promotes conditions of organic carbon excess which triggers complete reduction of Fe(III) and conversion to iron carbonate during diagenesis/metamorphism. For example, one mole of organic carbon can reduce eight moles of ferric oxyhydroxide (e.g. Lovley, 1990). These periods are documented by carbonate-chert layers which show low $\delta^{30}\text{Si}$ and $\delta^{56}\text{Fe}$ values at low Fe contents. **B)** Expansion and upwelling of the hydrothermal plume results in layers with higher $\delta^{30}\text{Si}$ and $\delta^{56}\text{Fe}$ values at high Fe contents which is marked with b) in *Figure 3.8*. Now, silica precipitates predominately from a fluid that has previously been modified by ongoing precipitation of isotopically light products with distance to the venting site or by mixing with ambient seawater with a strong positive isotope composition. Both shift the isotope signature towards heavier values (André et al., 2006; van den Boorn et al., 2007). The supply of large quantities of $\text{Fe(II)}_{\text{aq}}$ into the oxidizing zone triggers partial oxidation as the oxidant becomes the limiting factor resulting in high rates of ferric oxyhydroxide precipitation with significant positive $\delta^{56}\text{Fe}$ values. The large quantities of ferric oxyhydroxide deposition triggers partial reduction of Fe(III) as now the organic carbon becomes the limiting factor resulting in the formation of iron carbonate and magnetite. After diagenesis, these periods are represented by magnetite-carbonate-chert layers which exhibit significant positive $\delta^{56}\text{Fe}$ values and moderate negative $\delta^{30}\text{Si}$ values at high Fe contents.

3.6.2. Diagenesis and the formation of magnetite and iron carbonate

The origin of magnetite and iron carbonates in BIFs is controversial and may involve more than one formation pathway (Johnson et al., 2008). Magnetite possibly originates from a primary hydro-magnetite precursor (Klein, 2005) but more likely through biomineralization or diagenetic processes. Nano-particles of magnetite can be precipitated either intra-cellularly by magnetotactic bacteria (e.g. Karlin et al., 1987; Chang et al., 1989; Konhauser, 1998) or, more efficiently, by extracellular processes due to dissimilatory Fe reduction (DIR) of Fe(III) by oxidation of organic matter (e.g. Lovley, 1997; Konhauser et al., 2005). Further pathways involve the abiotic reduction of Fe(III) (e.g. Perry et al., 1973; Morris, 1993). Alternatively, magnetite incorporates hydrothermal Fe(II) (Ohmoto, 2003). Siderite is regarded either as direct precipitate from seawater (Klein and Beukes, 1989; Kaufman et al., 1990; Klein, 2005; Sumner, 1997) or diagenetic product possibly coupled to the formation of magnetite (Ewers and Morris, 1981; Lovley, 1991).

The advantage of Fe isotope analyses of coexisting mineral phases is that they allow one to infer these processes. For example, independent formation pathways of magnetite and siderite result in Fe isotope disequilibrium, whereas coupled diagenetic formation of magnetite and siderite by biotic or abiotic reduction of Fe(III) have to show Fe isotope equilibrium in coexisting mineral phases. The comparison of measured Fe isotope differences of coexisting mineral phases with published fractionation factors (see *Table 3.5*) enables us to identify formation processes.

The direct formation of iron carbonates from seawater appears unlikely in the light of the isotope fractionation factors for Fe(II) incorporation into carbonate. Although the equilibrium fractionation factor is still not well constrained, siderite seems to prefer light Fe(II) relative to Fe(II)_{aq}; an ankeritic component increases the fractionation factor (see *Table 3.5* for references). $\delta^{56}\text{Fe}$ values of bulk iron carbonates (siderite + ankerite) in the Old Wanderer BIF cluster around 0‰ which requires ancient seawater with a heavier $\delta^{56}\text{Fe}$ value than measured for iron carbonates. Taking the equilibrium fractionation factor of Wiesli et al. (2004), the ancient seawater would have had a heavy $\delta^{56}\text{Fe}$ value of at least 0.4 to 0.6‰ which is inconsistent with a strong hydrothermal influence suggesting a Fe isotope signature of the seawater of not more than 0‰.

The most likely scenario is a largely simultaneous diagenetic or metamorphic formation of magnetite and siderite. Both would have formed from a common precursor substrate by the

partial reduction of previously precipitated ferric oxyhydroxides by oxidation of organic matter (Han, 1978; Perry et al., 1973; Ewers and Morris, 1981; Lovley et al., 1991). Given that coexisting magnetite and siderite in the investigated sample show a uniform relative difference of $\sim 0.9\%$ and that this difference agrees with that expected from isotope equilibrium fractionation (see *Table 3.5*), the coupled formation under equilibrium conditions is suggested. The Fe(II) released by reduction reacts either with residual ferric (hydr)oxides to produce magnetite or with bicarbonate to form siderite. Several studies of C isotope compositions in Precambrian BIFs indicate that extensive magnetite and iron carbonate deposition resulted from organic carbon oxidation coupled to Fe(III) reduction (Perry et al., 1973; Walker, 1984; Baur et al., 1985; Kaufman et al., 1990). In this process, layering is of diagenetic origin that is controlled by the relative amount of organic matter to ferric (hydr)oxide in a given layer. This ratio controls the degree of ferric (hydr)oxide dissolution and the pH-Eh conditions and therefore the abundance of siderite and magnetite (*Figure 3.9*).

An early diagenetic pathway involves dissimilatory Fe reducing bacteria which use Fe(III) as electron donor when oxidizing organic matter to produce energy (Lovley et al., 1987; Lovley, 1991; Roden, 2004; Konhauser et al., 2005). In the Old Wanderer BIF, magnetite - siderite pairs show a relative difference of $\sim 0.9\%$. Very similar values have been reported for the Kuruman BIF in the Transvaal Basin, South Africa (Johnson et al., 2003), and the Biwabik BIF (Frost et al., 2007) which have been interpreted as resulting from a coupled diagenetic formation process of siderite and magnetite due to DIR. Experimental work by Johnson et al. (2005) has revealed an equilibrium fractionation factor $\Delta_{\text{siderite-magnetite}}$ of -1.3% for DIR, whereas Johnson et al. (2008) prefer a fractionation factor of -1.8% (see *Table 3.5*). An ankeritic component would increase the fractionation factor (Polyakov and Mineev, 2000; Johnson et al., 2005, see *Table 3.5*). Both fractionation factors are considerable higher than the observed difference which may either indicate that another process is involved or the formation of magnetite and iron carbonates occurred at an elevated temperature.

Alternatively, magnetite and siderite might have formed by abiotic reduction of ferric (hydr)oxides by oxidation of organic matter during late diagenesis or low-grade metamorphism (Perry et al., 1973; Morris, 1993; Frost et al., 2007). Predictions from Mössbauer data (Polyakov and Mineev, 2000; Mineev et al., 2007; Polyakov et al., 2007) give an equilibrium fractionation factor $\Delta_{\text{siderite-magnetite}}$ between -1.8 and -2.8% at 22°C which decreases to -0.8 to -1.2% at 200°C (*Table 3.5*). This elevated-temperature estimate is consistent with the observed difference of -0.9% in magnetite-rich layers.

Ankerite is considered as late diagenetic phase forming at the expense of siderite (e.g. Kaufman et al., 1990). Both experimental and Mössbauer approaches indicate that ankerite incorporates lighter Fe(II) than siderite under equilibrium conditions (see *Table 3.5*). This is also observed in the Old Wanderer BIF, where ankerite is 0.4 to 1.1‰ lighter in its isotope composition than siderite.

Major post-depositional redistribution of Si and Fe, such as recycling to the ocean or equilibration across layering in the course of diagenetic/metamorphic processes, appears unlikely in the Old Wanderer BIF. The significant variations in $\delta^{30}\text{Si}$ for chert on a millimeter-scale supports the notion that Si isotopes are largely unaffected, and that chert preserves the primary isotope signature (André et al., 2006; van den Boorn et al., 2007).

Redistribution of Fe across layering can potentially be caused by different degrees of ferric (hydr)oxide reduction which produces gradients in $\text{Fe(II)}_{\text{aq}}$ activity and pH conditions and drive diffusion of $\text{Fe(II)}_{\text{aq}}$ perpendicular to layers (Ewers, 1983). However, evidence from this sample as well as evidence from other BIFs (Frost et al., 2007; Johnson et al., 2008) suggest that mineral phases from adjacent layers in BIFs did not form in Fe isotope equilibrium and that significant isotope exchange in BIF across layering is absent. In the 1.9 Ga old Biwabik Iron Formation, differences in the oxygen fugacity and in $\delta^{56}\text{Fe}$ of up to 0.8‰ for magnetite in adjacent layers argue for the absence of significant transport of Fe perpendicular to the layering (Frost et al., 2007). The comparison of Fe isotope compositions of magnetite and siderite from adjacent layers in BIFs from the ~2.5 Ga old Hamersley and Transvaal successions exhibit isotope disequilibrium throughout indicating insufficient Fe isotope exchange between layers (Johnson et al., 2003; Johnson et al., 2008). Predominantly layer-parallel fluid flow is also assumed for the sample investigated for the following reasons, although minor Fe redistribution across layering cannot be excluded: 1) There is no obvious reason why the Fe and Si isotope composition of bulk layers should covary if Fe was redistributed between layers. 2) Adjacent greenish and light layers exhibit significant differences in their Fe concentrations with ~35 and ~10 wt%, respectively. 3) The high abundance of chert, especially in carbonate-chert layers (see *Figure 3.3* and *Table 3.1*) have likely prevented major advection and diffusion perpendicular to layering in this sample. Early silica cementation in BIFs limited the permeability and also restricted the exchange between early diagenetic pore fluids and seawater (Beukes and Gutzmer, 2008). 4) Siderite in adjacent layers shows variable Fe isotope composition. For instance, the LA data reveal $\delta^{56}\text{Fe}$ of 0.1‰ for siderite in the magnetite-rich layer 5 which is close to the bulk iron carbonate value as siderite is the dominating iron carbonate phase. In the adjacent carbonate layer 6, siderite exhibits $\delta^{56}\text{Fe}$ of 0.4‰, but the Fe

isotope composition of bulk iron carbonate is very similar due to ankerite with a negative signature. The only other reason for differences in siderite from adjacent layers arises from variable proportions of siderite from different growth generations (see *Figure 3.2*) which carry different Fe isotope values.

Therefore bulk layers in the Old Wanderer BIF are assumed to reflect largely primary Si and Fe isotope signatures. During diagenesis, Fe is partitioned within layers into iron carbonate and magnetite, which each provide diagenetic Fe isotope signatures, whereas primary signatures are preserved in bulk layer compositions.

3.5.3. The significance of zoned magnetite crystals

The fact that magnetite crystals in the Old Wanderer BIF exhibit isotopically heavier rims than cores (*Figure 3.5*) corroborates the diagenetic/metamorphic models discussed above. The observed isotope zonation may also account for the range in $\delta^{56}\text{Fe}$ determined in individual layers. Similar heterogeneities in magnetite have been found in a BIF from the 3.7 Ga old the Isua Greenstone Belt using secondary ion mass spectrometry (SIMS) (Whitehouse and Fedo, 2007). In Isua, the variability is attributed to isotope reservoir effects in pore waters during diagenesis which is also supported by the data presented here.

Ongoing crystallization of magnetite might have changed successively the Fe isotope composition of the pore water by a Rayleigh distillation process, which in turn influences the Fe isotope composition of magnetite. Several processes can change the pore water composition and cause the observed isotope zonation:

- 1) Kinetic isotope effects lead to fractionation at rapid precipitation rates if crystal growth is surface-controlled; or fractionation in the fluid phase if crystal growth is transport-controlled. The first effect can be ruled out as an experimental study has shown for the precipitation of hematite from solution that equilibrium conditions are already attained after some days (Skulan et al., 2002), and recrystallization during diagenesis takes place at a time scale of several thousand years (Berner, 1980). More likely is a kinetic effect during the transport of soluble Fe in a fluid phase if advection is negligible and molecular diffusion dominates. Despite the presence of $\text{Fe(II)}_{\text{aq}}$ as hexaquo complex in aqueous solution which decreases the relative mass differences between isotopes and therefore limits kinetic fractionation effects (Richter et al., 2006), an experimental study of (Rodushkin et al., 2004) postulates a discrimination of dissolved ^{56}Fe relative to ^{54}Fe of -0.3‰ by diffusion.

2) If siderite and magnetite form simultaneously by abiotic reactions and compete for a limited reservoir of $\text{Fe(II)}_{\text{aq}}$ during diagenesis, their isotope composition might affect each other. Both, siderite and magnetite tend to preferentially incorporate light Fe relative to $\text{Fe(II)}_{\text{aq}}$ (*Table 3.5*) but siderite prefers lighter Fe than magnetite under equilibrium conditions. Hence siderite formation enriches the fluid in heavy Fe in the residual $\text{Fe(II)}_{\text{aq}}$. This process could be reflected in the magnetite crystals which contain heavy Fe in the rim.

3) An increasing degree of dissolution of ferric (hydr)oxides can produce a temporal evolution towards a heavy residue. Fe isotope studies of reactive Fe(III) in modern anoxic marine sediments have shown such a process due to DIR (Severmann et al., 2006; Staubwasser et al., 2006). There, ferric (hydr)oxides become successively enriched in heavy Fe as light Fe is preferentially dissolved resulting in a cumulative Fe isotope composition of the pore-water which converges to the initial value of the ferric (hydr)oxides. If magnetite crystallizes from the reaction of ferric (hydr)oxides with $\text{Fe(II)}_{\text{aq}}$ in the pore water, growing magnetite crystals will accumulate successively heavier Fe with preceding reduction of ferric (hydr)oxide which causes the observed isotope zonation.

3.6. Conclusions

The evidence provided here for the Old Wanderer BIF suggests that the isotope variations of bulk layers in Fe and Si isotope are largely of primary origin and post-depositional redistribution across layering or recycling to the ocean was minor. Also, the simultaneous precipitation of light carbonate and a heavy iron oxide from seawater can be discounted. Rather, we suggest that both magnetite and iron carbonate are of secondary origin due to the reaction of organic matter with initially precipitated ferric oxyhydroxide either catalyzed by bacteria during early diagenesis, or more likely abiotically during late diagenesis or low-grade metamorphism at temperatures as high as 200°C. Isotope zonation in magnetite is caused by an evolving fluid and reflects dynamic processes during diagenesis. The heavy bulk Fe composition and the light Si composition suggest rapid precipitation events from an episodically recharged hydrothermal fluid. Steady state of Fe and Si was never achieved. The covariance of Fe and Si isotope signatures of bulk layers reflects the upwelling dynamics of hydrothermal-rich waters. The Fe isotope composition of bulk layers therefore indicates variable degrees of partial oxidation in a stratified ocean. The variability of the Si isotope composition might reflect modifications of hydrothermal fluids with distance to the venting site caused by Rayleigh distillation and/or mixing with ambient seawater. The development of layering depends on the relative proportion

of organic carbon to ferric (hydr)oxide. This proportion might be governed by the rate of ferric oxyhydroxide precipitation, which is determined by the hydrothermal activity. Periods of low hydrothermal activity are documented by layers with low Fe content which represent conditions, in which an excess of organic carbon has led to complete conversion of ferric (hydr)oxide to carbonate. Layers in which the Fe content is high represents intensive hydrothermal activity and organic carbon was the limiting factor resulting in the additional formation of magnetite.

The analysis of BIF mineral isotope compositions by in situ femtosecond laser ablation analysis provides unprecedented insights into the genetic history of these rocks that cannot be achieved by bulk layer or bulk mineral analysis. Future studies of this kind will allow researchers to decipher the factors controlling BIF formation. For example, variations in iron oxide compositions between layers will allow us to infer temporal variations in the Fe source or in genetic processes. The further development of the laser technique to higher sensitivity and higher spatial resolution will facilitate studies aimed at ascertaining the detailed isotope composition and hence genesis of zoned iron carbonates. In situ analysis is the method of choice for the study of Precambrian iron formations.

Deciphering formation processes of banded iron formations from the Transvaal and the Hamersley successions by combined Si and Fe isotope analysis using UV femtosecond laser ablation

Abstract

We determined the Fe and Si isotope composition of coexisting mineral phases in samples from the ~2.5 billion year old Kuruman Iron Formation (Transvaal Supergroup, South Africa) and Dales Gorges Member of the Brockman Iron Formation (Hamersley Group, Australia) by UV femtosecond laser ablation coupled to a MC-ICP-MS. Si in chert yields $\delta^{30}\text{Si}$ values between –1.3 and -0.8‰, but is isotopically homogeneous in each investigated core section. This uniformity suggests that Si precipitated from well-mixed seawater far removed from its sources such as hydrothermal vents or continental drainage. Given that none of these sources releases isotopically light Si, the negative Si isotope signature requires a complementary sink of isotopically heavy Si in order to maintain steady state in the basin. Alternatively, light Si will be precipitated if seawater was temporarily fertilized by extraordinary hydrothermal activity or continental weathering. The Fe isotope composition in Fe-bearing mineral phases is much more heterogeneous than that of Si due to variable degrees of partial Fe(II) oxidation in surface waters and post-depositional Fe redistribution. However, as with Si, the negative bulk isotope composition in the BIF samples investigated have to be balanced either spatially or temporally by deposition of isotopically heavy BIFs. This can be assumed since the overall Fe isotope composition of the Hamersley and Transvaal BIFs of near-zero indicate steady state conditions. We can estimate the ancient seawater composition from presumably primary isotope signatures in hematite and siderite, revealing a minimum range in seawater $\delta^{56}\text{Fe}$ between –0.8 and 0‰.

Magnetite exhibits negative $\delta^{56}\text{Fe}$ values, which can be attributed to a variety of diagenetic pathways: either the light Fe isotope composition was inherited from the ferric (hydr)oxide precursor or heavy Fe was lost by reduction of the ferric Fe precursor, or light Fe(II) was gained from external fluids. We also detected micrometer-scale heterogeneity of $\delta^{56}\text{Fe}$ in Fe oxides that is caused by variable degrees of oxidation and by diagenetic Fe redistribution. Diagenetic Fe(III) reduction caused by oxidation of organic matter and its redistribution is supported by the C isotope composition of a carbonate-rich sample containing primary siderite. These carbonates yield $\delta^{13}\text{C}$ values of $\sim -10\text{‰}$, which hints at a mixed carbon source of both organic and inorganic carbon. These results show that the new ability to determine stable isotope variations of the major chemical constituents of BIFs on the mineral grain scale provides a significant advantage in our effort to reconstruct the temporal evolution of ancient seawater and post-depositional diagenetic processes.

4.1. Introduction

Banded Iron Formations (BIFs) are prominent chemical marine sediments of Precambrian age whose peak of deposition between 2.3 and 2.5 Ga encompasses a period of dramatic change in the form of the evolution of first large scale microbial activity and the associated change in the atmospheric chemistry. Typically, BIFs contain total Fe of 20-40 wt% and SiO_2 of 43-56 wt% (Klein, 2005) and are characterized by alternating Fe-rich and Si-rich layers. Therefore, these sediments represent an extraordinary record of ancient Fe and Si cycles, which are poorly understood but clearly differ from those of the Phanerozoic.

The formation of Fe oxide layers are interpreted to reflect periods of intensive upwelling of Fe(II)-rich deep waters or hydrothermal plumes into the oxidizing surface layers of a largely anoxic ocean, which in turn led to the precipitation of a ferric oxyhydroxide precursor (e.g. Beukes and Gutzmer, 2008; Isley, 1995; Klein and Beukes, 1989). Rare earth element (REE) patterns with positive Eu anomalies and mantle-like Nd isotope signatures reveal a predominately hydrothermal origin for Fe (e.g. Alibert and McCulloch, 1993; Bau and Dulski, 1996; Bau et al., 1997; Jacobsen and Pimentel-Klose, 1988; Klein and Beukes, 1989). It is believed that the chert layers record periods of hydrothermal quiescence and Fe-poor sedimentation (e.g. Morris, 1993). In the absence of silica-secreting organisms in the Precambrian, Si likely precipitated directly from Si-saturated seawater in the form of an amorphous silica gel (e.g. Siever, 1992). The source of Si in the Precambrian seawater is thought to include supply by hydrothermal fluids and/or continental weathering (Hamade et al.,

2003; Maliva et al., 2005). Although Fe and Si have been deposited simultaneously, it is still unclear to what extent they have followed common pathways.

Recent analytical advancements now provide the opportunity to study stable Fe and Si isotopes to decipher the genetic processes of BIFs. Mineral phases formed and altered during different stages of BIF genesis involved processes during primary precipitation from seawater, diagenesis and metamorphism, all of which might be recorded in their Fe or Si isotope signatures. A first combined study of Fe and Si isotopes of the Archean Old Wanderer BIF in the Shurugwi Greenstone Belt (Zimbabwe) has unravelled correlated Fe and Si isotope signatures, which has been interpreted to reflect the upwelling dynamics of hydrothermal-rich waters (see *Chapter 3*). Fe isotope compositions alone have been studied on a number of BIFs of various ages and different grades of metamorphism (Dauphas et al., 2004; Dauphas et al., 2007; Frost et al., 2007; Johnson et al., 2003; Johnson et al., 2008a; Rouxel et al., 2005; Valaas Hyslop et al., 2008; Whitehouse and Fedo, 2007; this study). The relevant fractionation factors are beginning to be established (see *Table 3.4* in *Chapter 3*), which facilitates the exploration of the formation pathways of Fe-bearing mineral phases. Specifically, investigations of the voluminous ~2.5 Ga BIFs of the Hamersley and Transvaal successions have revealed large variations in Fe isotope composition (Johnson et al., 2003; Johnson et al., 2008a). In these studies, positive $\delta^{56}\text{Fe}$ in Fe oxides and carbonates are interpreted as inheritance from a ferric oxyhydroxide precursor formed in the upper water column by partial Fe(II) oxidation, i.e. only part of the reservoir of dissolved Fe(II) was oxidized as the oxidant was the limiting factor. Carbonates with $\delta^{56}\text{Fe}$ values of ~-0.5‰ are suggested to have formed in equilibrium with seawater. In contrast, magnetite and carbonates with strong negative $\delta^{56}\text{Fe}$ values are attributed to the activity of microbial dissimilatory iron reduction (DIR) during diagenesis, which seems to have played an important role in the formation of BIFs. Si isotope variations in chert have been investigated in few BIF samples so far giving a range from -2.6 to -0.5‰ (André et al., 2006; Ding et al., 1996; Jiang et al., 1993). Although the fractionation occurring at silica precipitation still lacks experimental calibration, researchers agree that the light isotopes of Si preferentially precipitate (Basile-Doelsch, 2006; De La Rocha et al., 1997; Ziegler et al., 2005). Precambrian chert deposits appear to have preserved their original isotope signature. Negative $\delta^{30}\text{Si}$ values are considered as hydrothermal signature (André et al., 2006; Ding et al., 1996; Jiang et al., 1993), whereas positive $\delta^{30}\text{Si}$ values may reflect elevated temperature of the seawater, the influence of a continental source or precipitation from isotopically heavy seawater (Robert and Chaussidon, 2006; van den Boorn et al., 2007).

In this study, we present high-spatial resolution Fe and Si isotope data on BIFs of the Transvaal and Hamersley successions determined by femtosecond laser ablation coupled to a multicollector inductively coupled plasma mass spectrometer (MC-ICP-MS). This analytical setup allows us to investigate the relative isotope differences of coexisting mineral phases in distinct BIF layers, an ability that presents a significant advantage in exploring the genetic processes of BIF formation together with temporal changes of these processes as BIFs are deposited.

4.2. Geological Background

The most lateral extensive and best preserved BIFs were deposited within the Transvaal Supergroup, South Africa and the Hamersley Group, Australia (for a recent review see Beukes and Gutzmer (2008)). They represent typical Proterozoic iron formations formed within continental shelf areas. Most of these BIFs have experienced only low-grade metamorphism, which makes them ideally suited for this study. The iron formations exhibit a broad spectrum of textural and mineralogical rock types (e.g. Beukes and Gutzmer, 2008). They range from clastic-textured allochemical to orthochemical microbanded micritic iron formations, which were deposited from high energy environments within shallow-shelf areas to deep water basins. Depending on the major Fe-bearing mineral phases, they are classified as oxide, carbonate and silicate facies with several mixed facies.

The Transvaal Supergroup is mainly preserved within the Transvaal and the correlated Griqualand West Basin in South Africa on the Archean Kaapvaal Craton. The northeastern part is thought to be deposited within small basins that widened to the southwest towards the open ocean (Bau and Dulski, 1992). The Transvaal BIFs are regarded as relatively shallow water shelf deposits extending the basinal facies of a carbonate platform succession and were formed in an back-arc environment (Klein and Beukes, 1989). Our samples have been taken from the Kuruman Iron Formation in the Griqualand West Basin and from the correlated Penge Iron Formation in the Transvaal Basin. The Kuruman Iron Formation consists essentially of alternating siderite-chert-magnetite microbanded macrocycles (Beukes, 1980) and experienced very low-grade metamorphism with temperatures between 110° and 170°C (Miyano and Beukes, 1984). The Penge Iron Formation was affected by contact metamorphism of up to 500°C caused by the 2.06 Ga Bushveld intrusion (Sharpe and Chadwick, 1982; Walraven et al., 1990). Hydrothermal orebodies were formed by hydrothermal oxidative fluids, a late event related to the Bushveld intrusion, and were further improved by deep lateritic weathering

(Gutzmer et al., 2005). SHRIMP U-Pb zircon ages of stilpnomelane-rich tuffaceous mudstones yield an upper age of 2.46 Ga for the Kuruman Iron Formation (Pickard, 2003).

The sediments within the Hamersley Basin were deposited on the Archean Pilbara Craton in Western Australia. The investigated sample material was taken from the 160 m thick Dales Gorge Member, which is the lowermost unit of the Brockman Iron Formation of the Hamersley Group, which is part of the Mount Bruce Supergroup. The Hamersley succession is considered to be formed on a semi-isolated marine platform within backarc basin (Blake and Barley, 1992; Morris, 1993). The unit comprises 33 Fe oxide-rich and carbonate-silicate-rich “macrobands” alternating in a scale of decimeter to meter (Trendall and Blockley, 1970). U-Pb SHRIMP data of zircons from intercalated tuffaceous layers reveal a depositional age between 2.49 and 2.46 Ga for the whole member (Trendall et al., 2004). The unit experienced very low-grade metamorphism with temperatures between 60 and 160°C at the Paraburdoo area, from which the sample material originated (Ewers and Morris, 1981; Kaufman et al., 1990).

The similar depositional ages indicate that the Kuruman Iron Formation and the Brockman Iron Formation were deposited synchronously (Pickard, 2003). Sedimentation rates of consolidated material are in the range of about 33 m per 10⁶ year for both BIFs based on SHRIMP U-Pb ages (Pickard, 2002; Pickard, 2003). REE patterns with positive Eu anomalies and mantle-like Nd isotope signatures of the BIFs reveal a strong influence of a hydrothermal component in the seawater (Alibert and McCulloch, 1993; Bau and Dulski, 1992; Bau and Dulski, 1996; Bau et al., 1997; Klein and Beukes, 1989; Morris, 1993). Similarities in age and stratigraphy between the Transvaal and the Hamersley successions (see review of Beukes and Gutzmer (2008)) give rise to speculations whether these iron formations have been deposited on the same continent within a single restricted ocean basin (e.g. Beukes and Gutzmer, 2008; Cheney, 1996) and might have been the response to widespread magmatic events (e.g. Isley and Abbott, 1999; Nelson et al., 1999).

4.3. Sample Description

Most of the investigated sample material is from pristine orthochemical micritic iron formations belonging to the oxide to carbonate facies and were deposited in rather similar environments. The chemical composition of the various mineral phases in the investigated BIF samples were examined by electron microprobe. Fe oxides exhibit very pure stoichiometric compositions; the variability in Fe carbonate composition is presented in *Table 4.1*.

Table 4.1

Average chemical composition (in weight % \pm 1 SD) determined by electron microprobe and mean Fe isotope composition of iron carbonate phases

mm	Mineral	FeO	MnO	MgO	CaO	n	$\delta^{56}\text{Fe}_{\text{mean}}$
Kuruman Iron Formation 3/59 (Transvaal)							
38.70	ank	18.71 \pm 0.53	1.33 \pm 0.09	7.98 \pm 0.30	27.43 \pm 0.53	7	-0.72
	Mg-sid	39.79 \pm 1.11	1.20 \pm 0.22	17.48 \pm 1.05	0.38 \pm 0.17	19	-0.88
	sid	50.77 \pm 1.77	1.97 \pm 0.37	6.99 \pm 1.87	0.48 \pm 0.21	9	-0.72
38.55	ank	16.95 \pm 3.33	1.02 \pm 0.32	9.49 \pm 3.49	27.92 \pm 0.50	11	-0.66
	Mg-sid	39.79 \pm 0.30	1.13 \pm 0.10	18.09 \pm 0.07	0.33 \pm 0.18	3	-0.90
37.75	ank	17.86 \pm 1.96	1.21 \pm 0.19	8.04 \pm 2.28	27.95 \pm 0.32	6	-0.84
20.80	ank	19.16 \pm 1.20	1.26 \pm 0.24	8.27 \pm 0.76	26.51 \pm 0.40	19	-0.89
	sid	51.98 \pm 1.97	1.72 \pm 0.35	6.50 \pm 1.47	0.49 \pm 0.17	20	-0.65
3.65	sid	52.32 \pm 1.46	1.65 \pm 0.39	5.84 \pm 0.96	0.51 \pm 0.18	8	-0.83
3.45	sid	52.40 \pm 1.28	1.64 \pm 0.32	5.84 \pm 0.74	0.44 \pm 0.18		-0.69
3.00	sid	52.19 \pm 1.49	1.65 \pm 0.34	5.85 \pm 1.00	0.46 \pm 0.39	5	-0.75
0	Mg-sid	45.10 \pm 0.75	2.03 \pm 0.06	11.74 \pm 0.23	0.58 \pm 0.12	2	-1.13
	ank	17.71 \pm 2.32	1.48 \pm 0.16	8.96 \pm 1.82	27.19 \pm 0.28	3	-1.20
Dales Gorge Member DGM-36 (Hamersley)							
35.82	sid	43.07 \pm 4.60	0.64 \pm 0.37	13.56 \pm 4.66	1.26 \pm 0.81	6	-2.18
24.84	sid (rim)	49.08 \pm 1.20	0.74 \pm 0.13	9.65 \pm 0.79	0.34 \pm 0.14	16	-1.97
	sid (core)	51.99 \pm 0.67	0.89 \pm 0.15	6.77 \pm 1.34	0.77 \pm 0.59	4	

The stratigraphic position of each investigated iron carbonate phase is indicated by mm corresponding to *Figure 4.3*. Complete Fe isotope data sets are provided in *Table 4.2*. As visible in *Figure 4.1a*, sample DGM-36 exhibits siderite rhombs with two growth stages indicated by 'sid (rim)' and 'sid (core)'.

Sample TBT represents a BIF altered by iron ore mineralization. It originates from the Penge Iron Formation and was collected in the mining area around Thabazimbi in the northern Transvaal Basin. It consists of alternating micro-layers of hematite and chert, as well as layers of massive chert, which are pigmented by very fine hematite dust. Hydrothermal ore formation in the Thabazimbi area is related to a hydrothermal fluid infiltration event, which caused oxidative carbonate metasomatism (De Kock et al., 2008; Gutzmer et al., 2005). As a consequence, hematite replaced magnetite, grunerite and Fe carbonates. This hematite chert BIF sample might represent a former magnetite chert BIF as other relics than magnetite are absent. The sample is almost completely oxidized as all chert layers appear red and evidence for incomplete martitization processes (= transformation of magnetite into hematite by oxidation of magnetite (e.g. Mücke, 2003) is very rare. Evidence of supergene modifications as leaching of chert are absent. The core sections, 3/79 and 3/59, are from the Kuruman Iron Formation and were sampled at Pomfret located in the north of the Griqualand West Basin. Sample 3/79 represents a magnetite hematite chert BIF consisting of alternating Fe oxide- and chert-rich layers in the scale of millimeter to centimeter. Magnetite is the major Fe oxide phase, which is partly intergrown with hematite. Both minerals occur as anhedral aggregates. Chert layers are

pigmented by fine hematite dust. Core section 3/59 represents a typical laminated magnetite carbonate chert BIF (*Figure 4.1c*). Magnetite crystals are sub- to euhedral of about 30 μm in size. Carbonate phases comprising calcite, siderite and ankerite form either distinct compact layers or occur as finely distributed aggregates. The Fe-bearing varieties are ankerite, $\text{Ca}(\text{Fe}_{0.30-0.60}, \text{Mg}_{0.40-0.70})(\text{CO}_3)_2$, and siderite with variable Mg-substitution, $(\text{Fe}_{0.70-0.80}, \text{Mg}_{0.20-0.30})\text{CO}_3$ and $(\text{Fe}_{0.55}, \text{Mg}_{0.45})\text{CO}_3$. Their chemical compositions of each investigated layer are presented in *Table 4.1* and depicted in *Figure 4.2*. Chert is occasionally red pigmented by hematite dust. The lamination is defined by variable proportions of the constituent minerals.

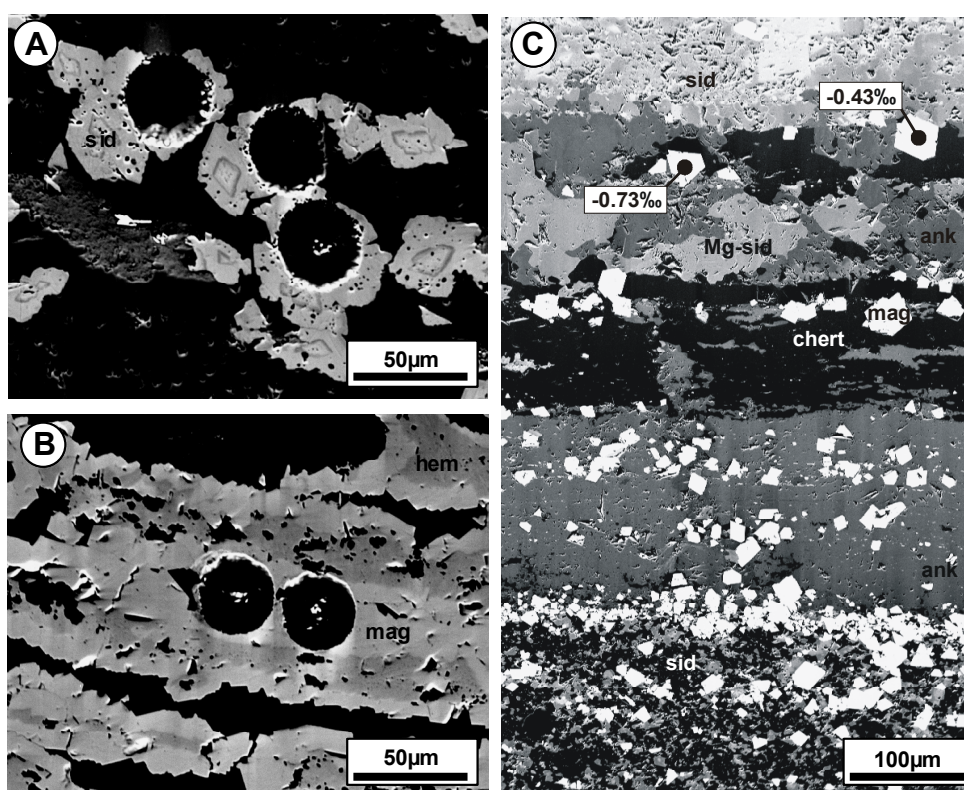


Figure 4.1 Backscattered electron (BSE) images of BIF samples with sid = siderite, Mg-sid = Mg-rich siderite, ank = ankerite, mag = magnetite, hem = hematite and chert = quartz. **A)** and **B)** The images show laser ablation craters in siderite rhomboids and magnetite, respectively in sample DGM-36. **C)** Carbonate magnetite chert layers in sample 3/59. Magnetite exposes abrupt shifts in the Fe isotope signature within few microns as observable between 38.70 and 38.55 mm of the core section.

Core sample DGM-36 represents BIF macroband 16 of the Dales Gorge Member of the Brockman Iron Formation. It originated from drillhole DDH-44 at Paraburdoo sited at the south-west edge of the Hamersley Basin. The sample is a finely laminated hematite magnetite siderite chert BIF. Fe-rich layers consist mainly of hematite, magnetite and minor siderite.

Hematite is texturally variable displaying massive, anhedral to fine platy habits. Subhedral magnetite typically occurs as overgrowths on hematite laminae (*Figure 4.1b*). Siderite, ($\text{Fe}_{0.75}\text{Mg}_{0.25}\text{CO}_3$), appears as very finely distributed phase or in the form of subhedral rhomboids with distinct growth zones (*Figure 4.1a*). Chert is interbedded with Fe-rich layers. Detailed petrographic and geochemical information on this sample are given by Pecoits et al. (in review).

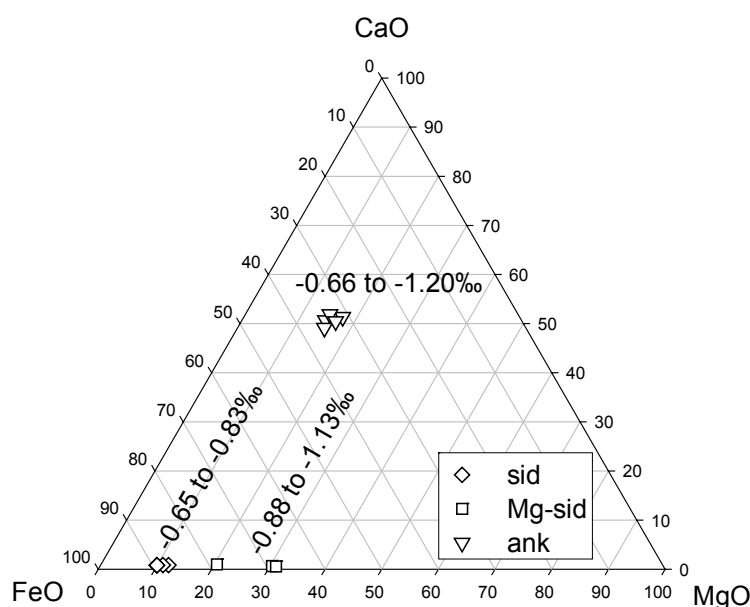


Figure 4.2. Carbonate composition, as mole percent of CaO, MgO and FeO and observed ranges in mean $\delta^{56}\text{Fe}$ values of sample 3/59. The data are listed in *Table 4.1* and *4.2*. The Fe carbonate phases, sid = siderite, Mg-sid = siderite with significant Mg substitution and ank = ankerite each show uniform chemical compositions but differ in the range of their Fe isotope composition. Siderite exhibits a small range in $\delta^{56}\text{Fe}$, whereas siderite with significant Mg substitution and ankerite are depleted in heavy Fe relative to siderite to a range of degrees.

4.4. Methods

High-spatial resolution Fe and Si isotope data of the investigated BIFs were obtained *in situ* from thin sections by laser ablation ICP-MS (LA-ICP-MS). The instrumental setup at the University of Hannover consists of our in-house built UV femtosecond laser ablation system coupled to a ThermoFinnigan Neptune MC-ICP-MS and has been described in detail by Horn and von Blanckenburg (2007). The analytical method followed the procedure of Chmeleff et al. (2008), Horn et al. (2006)) and see *Chapter 3*. The instrumental mass discrimination was corrected by standard-sample-bracketing using the reference materials IRMM-014 and NBS28

for Fe and Si isotope analysis, respectively. The external reproducibilities of $\delta^{56/54}\text{Fe}$ and $\delta^{57/54}\text{Fe}$ are better than 0.1‰ (2 SD) and 0.2‰ (2 SD), respectively, and has been verified for different types of matrices including those investigated herein. Analyses of Si isotopes reveal an overall precision for $\delta^{29/28}\text{Si}$ and $\delta^{30/28}\text{Si}$ of 0.15‰ (2 SD) and 0.24‰ (2 SD), respectively.

We investigated the Fe isotope compositions of all major Fe-bearing mineral phases in selected layers of the sampled BIFs. Fe oxides were analysed by spot analysis with a diameter of 20 to 30 μm . Single magnetite crystals in sample 3/59 were investigated by the experimental procedure described in *Chapter 3* to examine potential intra-mineral isotope zonation. Sequential coring by laser ablation using different spot sizes allows to analysis the Fe isotope composition of the crystal core and the rim, separately in crystals as large as 30 μm . Fe carbonates were investigated prior to Fe isotope analysis by electron microprobe to distinguish distinct phases. Backscattered electron (BSE) images assisted to analyse pure phases using short line scans. Multiple analyses were performed parallel and perpendicular to the lamination to investigate the variability of the Fe isotope composition of the different mineral phases. The Fe isotope data are reported as $\delta^{56/54}\text{Fe}$ and $\delta^{57/54}\text{Fe}$ relative to the reference material IRMM-014. The Si isotope composition was investigated in chert. Analyses using narrow rasters of about 50 μm x 500 μm provide a high-spatial resolution in chert layers. The Si isotope data are presented as $\delta^{29/28}\text{Si}$ and $\delta^{30/28}\text{Si}$ relative to the reference material NBS28.

In addition to Fe and Si isotope ratios, we investigated the C isotope composition in sample 3/59, in which Fe carbonates represents one of the major mineral phases. Micro-sampling of individual layers was performed on a thick section using a 0.5 mm diameter steel drill bit tipped with synthetic diamonds. The analyses were carried out at the Leibniz Institute for Applied Geosciences in Hannover using a fully automated preparation system (ThermoFinnigan Gasbench 2) directly coupled to a ThermoFinnigan Delta Puls XP isotope ratio mass spectrometer following a standard procedure (e.g. Spötl and Vennemann, 2003). All samples were measured in duplicate and reported as mean $\delta^{13}\text{C}$ value relative to the PDB standard. The external reproducibility is better than 0.2‰ (2 SD).

4.5. Results

4.5.1. Fe isotope composition

The Fe isotope compositions of the various Fe-bearing mineral phases in the investigated BIF samples are presented in *Figure 4.3* and in *Table 4.2*. The chemical composition of Fe carbonate

phases and their corresponding mean $\delta^{56}\text{Fe}$ values are summarized in *Table 4.1* and depicted in *Figure 4.2*.

Hematite micro-layers of sample TBT exhibit significant lateral variation in their $\delta^{56}\text{Fe}$ values composition on a sub-millimeter scale, which exceed the analytical error. Average Fe isotope compositions within micro-layers however remain surprisingly uniform (*Figure 4.3a, b*). The maximal observed lateral range is -1.17 to -0.27‰ in $\delta^{56}\text{Fe}$ with an average of $-0.47 \pm 0.52\%$ (2 SD, n=14) at 11.15 mm of the investigated section. Similar variations have been found within other layers with ± 0.11 to 0.44% (2 SD, n=8 to 16). A comparison of the mean values of the boundaries of micro-layers reveals no significant differences in most cases (Student's t-test, 95% confidence level); also inter-layer trends are absent (*Figure 4.3b*). Therefore, the dataset can be considered together showing a Gaussian distribution and a mean of $-0.39 \pm 0.31\%$ (2 SD, n=181). This observation may indicate one dominating process, which has caused the small-scale variation in the Fe isotope composition.

In sample 3/79, magnetite and hematite show homogeneous Fe isotope compositions within several layers, respectively, although differences from layer to layer do exist (*Figure 4.3d, e*). Hematite reveals little variations in $\delta^{56}\text{Fe}$ giving mean values between -0.02 and -0.17‰ for different stratigraphic levels, while magnetite is more variable with mean $\delta^{56}\text{Fe}$ values ranging between -0.59 and -0.14‰. Magnetite shows constantly lower $\delta^{56}\text{Fe}$ than hematite with relative difference between them ranging between 0.08 and 0.50‰.

In sample 3/59, magnetite and the Fe carbonate phases (siderite, Mg-rich siderite and ankerite) were investigated (*Figures 4.2, 4.3g-h, 4.4*). Repeated analyses reveal that all mineral phases are homogeneous in their Fe isotope composition within the lamination. Increased standard deviations of multiple analyses of individual Fe carbonate phases are attributed to slightly variable chemical compositions. Magnetite exhibits significant variations in $\delta^{56}\text{Fe}$ perpendicular to the lamination with abrupt shifts within a few microns giving mean values between -0.02 and -0.86‰ (*Figures 4.1c, 4.3h*). The examination of individual magnetite grains at 39.20 mm of the investigated core section reveals isotopically homogeneous crystals within the analytical precision giving mean $\delta^{56}\text{Fe}$ values of $-0.48 \pm 0.11\%$ (2 SD, n=18) for the crystal core and $-0.44 \pm 0.25\%$ (2 SD, n=12) for the crystal rim (*Figure 4.4*). The Fe isotope composition of Fe carbonate phases show no direct correlation with their chemical composition (see *Table 4.1* and *Figure 4.2*). Mean $\delta^{56}\text{Fe}$ values for siderite are relatively constant ranging between -0.83 and -0.65‰, whereas siderite with significant Mg-substitution is slightly more variable with $\delta^{56}\text{Fe}$ values between -1.13 and -0.88‰. Ankerite is the most variable phase giving mean $\delta^{56}\text{Fe}$ values between -1.20 and -0.66‰. In the sample DGM-36, hematite and magnetite show little inter-

layer variations with mean $\delta^{56}\text{Fe}$ values ranging from -0.90 and -0.76‰ and from -0.94 to -0.82‰, respectively (*Figures 4.3j-k*). Variations of ± 0.13 to 0.41‰ (2 SD, n=6 to 19) for multiple analyses partly differ from the analytical precision indicating slightly heterogeneous Fe isotope compositions within individual layers. When occurring together, hematite and magnetite expose identical Fe isotope compositions within analytical precision. Very fine distributed siderite occurring adjacent to magnetite and hematite could be analysed only once giving a $\delta^{56}\text{Fe}$ value of -2.18‰. Siderite rhombs within a hematite-siderite-rich layer reveal a mean $\delta^{56}\text{Fe}$ value of -1.97‰.

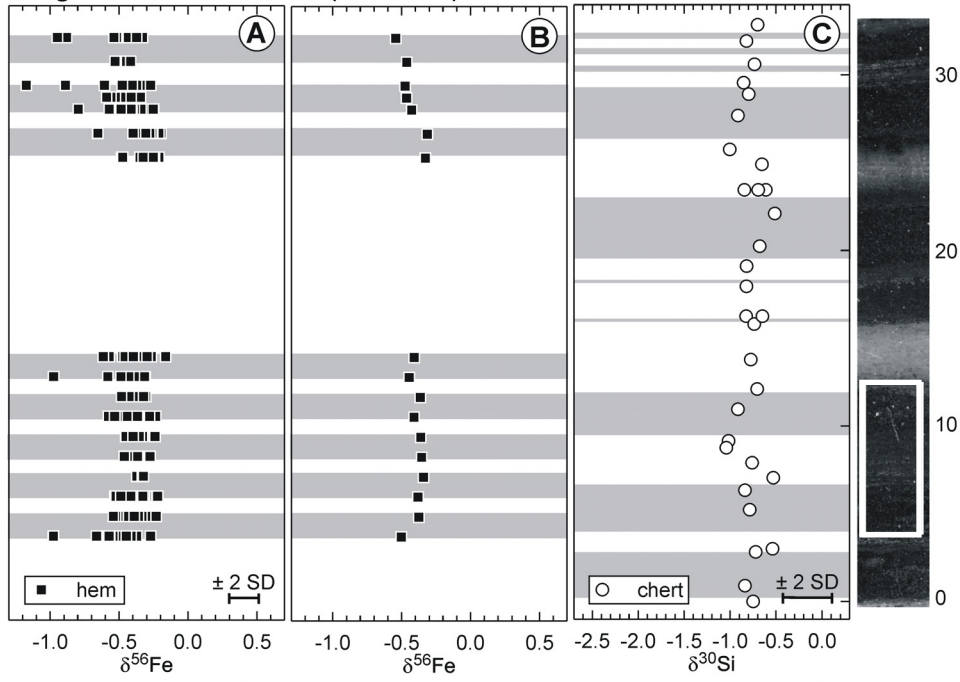
4.5.2. Si isotope composition

The Si isotope data of chert in the investigated BIFs are presented in *Table 4.4* and depicted in *Figure 4.3*. All samples reveal homogeneous Si isotope signatures depleted in isotopically heavy Si as the variability is close to the achievable precision. Samples from the Transvaal succession TBT, 3/59 and 3/79 exhibit mean $\delta^{30}\text{Si}$ values of $-0.82 \pm 0.22\text{‰}$ (2 SD, n=31), $-1.22 \pm 0.31\text{‰}$ (2 SD, n=27) and $-0.77 \pm 0.26\text{‰}$ (2 SD, n=31), respectively. DGM-36 from the Hamersley Basin is slightly more variable giving a mean $\delta^{30}\text{Si}$ values of $-1.25 \pm 0.40\text{‰}$ (2 SD, n=36).

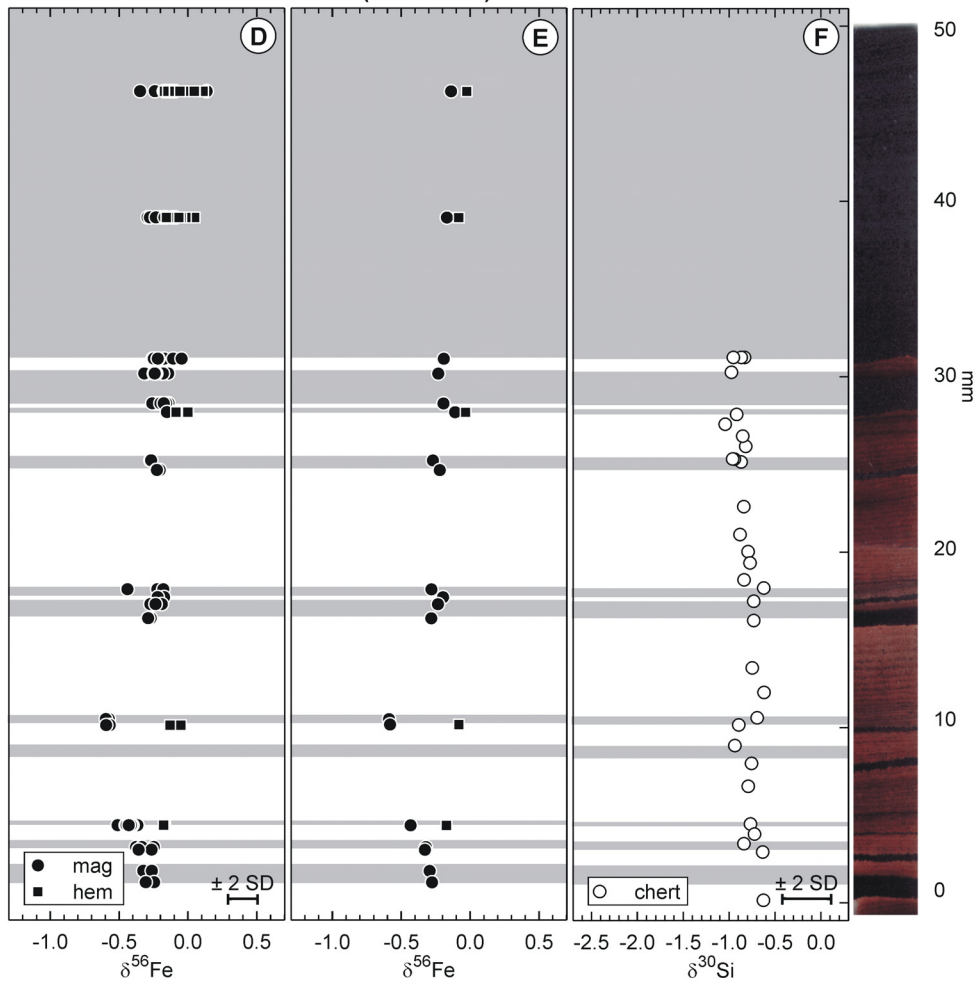
4.5.3. C isotope composition

The C isotope composition was investigated in carbonate-rich layers in sample 3/59. $\delta^{13}\text{C}$ values range between -10.91 and -8.95‰ giving a mean value of $-9.85 \pm 1.26\text{‰}$ (2 SD, n=9) (*Table 4.3, Figure 4.5*).

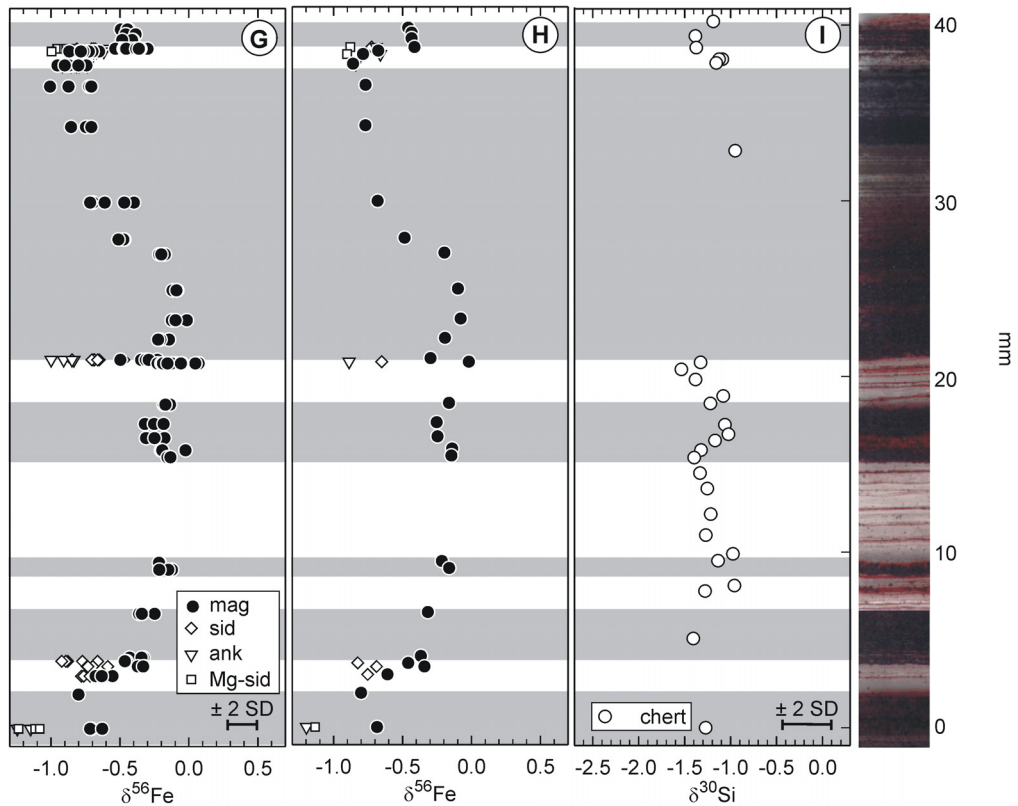
Penge Iron Formation TBT (Transvaal)



Kuruman Iron Formation 3/79 (Transvaal)



Kuruman Iron Formation 3/59 (Transvaal)



Dales Gorge Member DGM-36 (Hamersley)

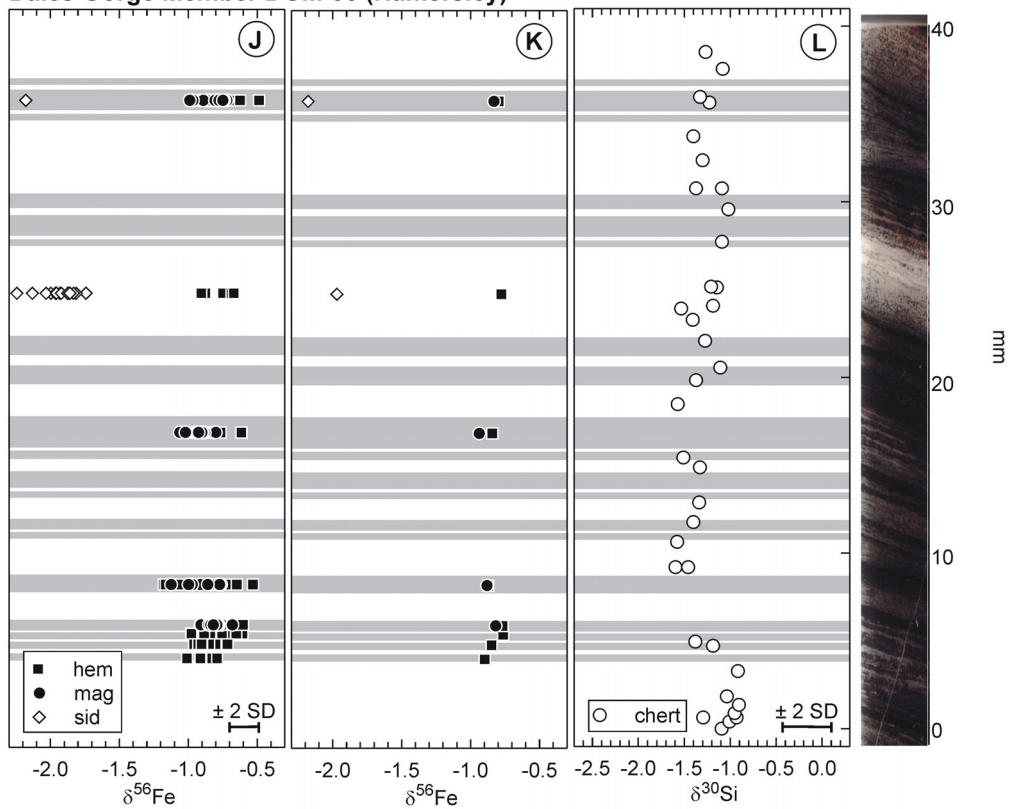


Figure 4.3 Fe and Si isotope variations in the Penge and Kuruman Iron Formation from the Transvaal succession and in the Dales Gorge Member of the Brockman Iron Formation from the Hamersley succession. Mineral phases are presented by hem = hematite, mag = magnetite, sid = siderite, Mg-sid = Mg-rich siderite, ank = ankerite and chert = quartz. **A), D), G)** and **J)** shows all obtained Fe isotope data, whereas **B), E), H)** and **K)** present mean $\delta^{56}\text{Fe}$ values of multiple analyses. Fe isotope data on sample TBT were obtained from the marked section. **C), F), I)** and **L)** display $\delta^{30}\text{Si}$ values of single raster analyses. The investigated core sections represent about 1000 to 1500 years of deposition assuming a deposition rate of 0.033 mm/y (Pickard, 2002; 2003).

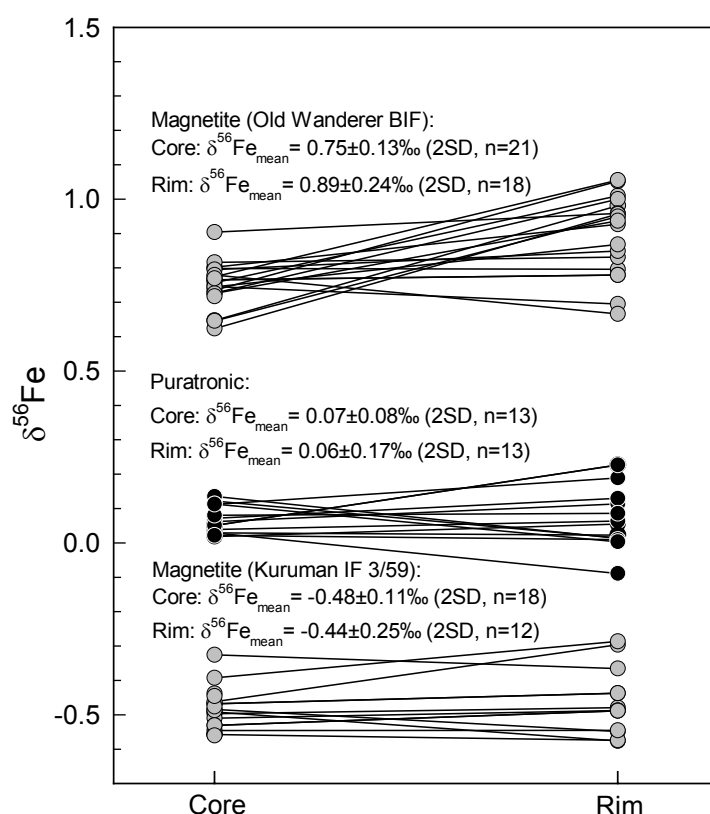


Figure 4.4 Investigation of intra-crystal Fe isotope heterogeneity in magnetite using the method described in *Chapter 3*. Magnetite crystals in the Archean Old Wanderer BIF from the Shurugwi Greenstone Belt (Zimbabwe) show zonation in the Fe isotope composition revealed by corresponding pairs of core-rim analysis (see *Chapter 3*), whereas magnetite in sample 3/59 from the Kuruman Iron Formation exhibits homogeneous crystals. The analytical procedure has been validated on the homogeneous metal standard Puratronic showing that the inner spot analyses (= core) are identical with the outer spot analyses (= rim) within the analytical precision.

Table 4.2 Fe isotope data of investigated BIFs obtained by LA-ICP-MS

Dales Gorge Member DGM-36 (Hammersley)					<i>continued</i>				
mm	Mineral	$\delta^{56}\text{Fe}_{\text{mean}}$	$\delta^{57}\text{Fe}_{\text{mean}}$	n	mm	Mineral	$\delta^{56}\text{Fe}_{\text{mean}}$	$\delta^{57}\text{Fe}_{\text{mean}}$	n
35.82	mag	-0.83 ± 0.16	-1.18 ± 0.19	19	3.00	mag	-0.61 ± 0.11	-0.85 ± 0.22	4
	hem	-0.80 ± 0.29	-1.09 ± 0.34	11		sid	-0.75 ± 0.06	-1.09 ± 0.41	3
	sid	-2.18	-3.02	1	1.95	mag	-0.80	-1.13	1
24.84	hem	-0.78 ± 0.22	-1.05 ± 0.30	5	0.00	mag	-0.69 ± 0.10	-1.00 ± 0.17	3
	sid	-1.97 ± 0.34	-2.74 ± 0.49	15	Mg-sid	-1.13 ± 0.14	-1.68 ± 0.14	4	
16.92	mag	-0.94 ± 0.15	-1.31 ± 0.13	15	ank	-1.20 ± 0.14	-1.66 ± 0.06	2	
	hem	-0.84 ± 0.19	-1.18 ± 0.28	16	Kuruman Iron Formation 3/79 (Transvaal)				
8.26	mag	-0.88 ± 0.24	-1.23 ± 0.29	10	mm	Mineral	$\delta^{56}\text{Fe}_{\text{mean}}$	$\delta^{57}\text{Fe}_{\text{mean}}$	n
	hem	-0.87 ± 0.41	-1.21 ± 0.47	12	46.25	mag	-0.14 ± 0.20	-0.19 ± 0.26	15
5.96	mag	-0.82 ± 0.13	-1.20 ± 0.14	13	hem	-0.02 ± 0.17	-0.03 ± 0.21	14	
	hem	-0.77 ± 0.15	-1.13 ± 0.23	18	39.05	mag	-0.17 ± 0.14	-0.25 ± 0.20	12
5.46	hem	-0.76 ± 0.20	-1.05 ± 0.30	16	hem	-0.08 ± 0.12	-0.11 ± 0.22	14	
4.86	hem	-0.85 ± 0.16	-1.17 ± 0.24	11	31.00	mag	-0.19 ± 0.14	-0.25 ± 0.21	9
4.06	hem	-0.90 ± 0.14	-1.25 ± 0.28	6	30.15	mag	-0.23 ± 0.11	-0.31 ± 0.20	9
	Kuruman Iron Formation 3/59 (Transvaal)					28.45	mag	-0.19 ± 0.07	-0.27 ± 0.17
mm	Mineral	$\delta^{56}\text{Fe}_{\text{mean}}$	$\delta^{57}\text{Fe}_{\text{mean}}$	n	27.95	mag	-0.11 ± 0.08	-0.16 ± 0.12	3
39.80	mag	-0.46 ± 0.06	-0.68 ± 0.08	3	hem	-0.03 ± 0.09	-0.01 ± 0.15	3	
39.52	mag	-0.43 ± 0.08	-0.64 ± 0.11	3	25.20	mag	-0.27 ± 0.01	-0.35 ± 0.04	2
39.20	mag	-0.43 ± 0.09	-0.63 ± 0.13	3	24.65	mag	-0.22 ± 0.03	-0.31 ± 0.05	3
38.70	mag	-0.41 ± 0.13	-0.61 ± 0.15	19	17.85	mag	-0.28 ± 0.28	-0.45 ± 0.41	3
	ank	-0.72 ± 0.14	-1.06 ± 0.23	5	17.40	mag	-0.20 ± 0.07	-0.25 ± 0.17	2
	Mg-sid	-0.88 ± 0.12	-1.28 ± 0.20	12	17.00	mag	-0.23 ± 0.08	-0.33 ± 0.17	3
38.55	sid	-0.72 ± 0.12	-1.03 ± 0.25	4	16.20	mag	-0.28 ± 0.02	-0.39 ± 0.08	3
	mag	-0.75 ± 0.14	-1.09 ± 0.25	8	10.45	mag	-0.59 ± 0.02	-0.87 ± 0.05	3
38.55	ank	-0.66 ± 0.08	-0.95 ± 0.04	3	10.10	mag	-0.58 ± 0.04	-0.85 ± 0.10	2
	Mg-sid	-0.90 ± 0.16	-1.32 ± 0.23	3	hem	-0.08 ± 0.08	-0.12 ± 0.16	3	
37.75	mag	-0.86 ± 0.14	-1.28 ± 0.24	7	4.40	mag	-0.43 ± 0.09	-0.64 ± 0.12	7
	ank	-0.84 ± 0.14	-1.19 ± 0.25	6	4.40	hem	-0.17 ± 0.01	-0.30 ± 0.11	2
36.55	mag	-0.77 ± 0.18	-1.11 ± 0.36	4	4.15	mag	-0.32 ± 0.13	-0.48 ± 0.11	3
34.25	mag	-0.77 ± 0.15	-1.17 ± 0.22	3	3.00	mag	-0.33 ± 0.11	-0.43 ± 0.15	3
29.95	mag	-0.68 ± 0.10	-0.99 ± 0.16	6	1.80	mag	-0.29 ± 0.09	-0.38 ± 0.08	2
26.75	mag	-0.49 ± 0.04	-0.75 ± 0.12	3	1.15	mag	-0.28 ± 0.09	-0.37 ± 0.13	2
25.95	mag	-0.20 ± 0.04	-0.27 ± 0.13	3	Penge Iron Formation TBT (Transvaal)				
23.85	mag	-0.10 ± 0.04	-0.14 ± 0.09	3	mm	Mineral	$\delta^{56}\text{Fe}_{\text{mean}}$	$\delta^{57}\text{Fe}_{\text{mean}}$	n
22.15	mag	-0.08 ± 0.11	-0.09 ± 0.19	3	11.90	hem	-0.54 ± 0.44	-0.63 ± 0.96	9
20.95	mag	-0.19 ± 0.08	-0.25 ± 0.07	3	11.55	hem	-0.46 ± 0.12	-0.62 ± 0.83	3
19.85	mag	-0.30 ± 0.09	-0.45 ± 0.18	6	11.15	hem	-0.47 ± 0.52	-0.60 ± 0.89	14
19.65	mag	-0.02 ± 0.15	-0.03 ± 0.13	14	10.95	hem	-0.46 ± 0.15	-0.59 ± 0.29	8
	ank	-0.89 ± 0.14	-1.26 ± 0.15	5	10.75	hem	-0.43 ± 0.29	-0.59 ± 0.41	14
17.45	sid	-0.65 ± 0.24	-0.92 ± 0.28	8	10.48	hem	-0.31 ± 0.23	-0.40 ± 0.47	13
	mag	-0.16 ± 0.05	-0.21 ± 0.07	3	10.05	hem	-0.33 ± 0.19	-0.42 ± 0.23	9
16.35	mag	-0.25 ± 0.14	-0.36 ± 0.21	3	6.90	hem	-0.41 ± 0.22	-0.51 ± 0.52	16
15.55	mag	-0.25 ± 0.13	-0.34 ± 0.17	4	6.55	hem	-0.45 ± 0.32	-0.60 ± 0.46	15
14.85	mag	-0.14 ± 0.20	-0.18 ± 0.23	4	6.28	hem	-0.36 ± 0.11	-0.45 ± 0.42	10
14.45	mag	-0.15 ± 0.02	-0.19 ± 0.06	4	5.90	hem	-0.41 ± 0.23	-0.54 ± 0.29	8
9.45	mag	-0.21 ± 0.01	-0.33 ± 0.04	2	5.65	hem	-0.36 ± 0.13	-0.47 ± 0.41	9
9.05	mag	-0.16 ± 0.10	-0.20 ± 0.12	3	5.25	hem	-0.36 ± 0.11	-0.53 ± 0.22	9
7.05	mag	-0.32 ± 0.12	-0.49 ± 0.17	3	5.05	hem	-0.34 ± 0.05	-0.44 ± 0.47	3
4.05	mag	-0.37 ± 0.11	-0.50 ± 0.22	3	4.65	hem	-0.38 ± 0.26	-0.45 ± 0.55	9
3.85	mag	-0.46 ± 0.02	-0.60 ± 0.34	2	4.40	hem	-0.37 ± 0.18	-0.53 ± 0.24	16
	sid	-0.83 ± 0.22	-1.16 ± 0.21	5	4.00	hem	-0.50 ± 0.33	-0.71 ± 0.42	16
3.55	mag	-0.34 ± 0.05	-0.41 ± 0.16	3					
	sid	-0.69 ± 0.14	-1.00 ± 0.17	4					

The stratigraphic positions of the analysed mineral phases are indicated by mm corresponding to *Figure 4.3*. Uncertainties given by 2 standard deviations refer to multiple analyses (n).

Table 4.4 Si isotope data of chert in the investigated BIFs obtained by LA-ICP-MS

Dales Gorge Member DGM-36 (Hammersley)			Kuruman Iron Formation 3/69 (Transvaal)			Kuruman Iron Formation 3/79 (Transvaal)			Penge Iron Formation TBT (Transvaal)		
mm	$\delta^{29}\text{Si}$	$\delta^{30}\text{Si}$	mm	$\delta^{29}\text{Si}$	$\delta^{30}\text{Si}$	mm	$\delta^{29}\text{Si}$	$\delta^{30}\text{Si}$	mm	$\delta^{29}\text{Si}$	$\delta^{30}\text{Si}$
38.52	-0.66 ± 0.08	-1.09 ± 0.09	40.20	-0.54 ± 0.07	-1.19 ± 0.14	31.10	-0.40 ± 0.07	-0.83 ± 0.11	32.85	-0.34 ± 0.07	-0.70 ± 0.11
38.12	-0.57 ± 0.05	-1.01 ± 0.07	39.37	-0.62 ± 0.07	-1.38 ± 0.15		-0.35 ± 0.04	-0.87 ± 0.07	31.92	-0.38 ± 0.07	-0.82 ± 0.13
37.88	-0.61 ± 0.08	-1.29 ± 0.12	38.71	-0.76 ± 0.09	-1.37 ± 0.17		-0.47 ± 0.08	-0.96 ± 0.09	30.60	-0.32 ± 0.07	-0.74 ± 0.14
	-0.48 ± 0.08	-0.93 ± 0.10	38.05	-0.55 ± 0.07	-1.09 ± 0.12	30.25	-0.48 ± 0.07	-0.97 ± 0.08	29.55	-0.38 ± 0.07	-0.85 ± 0.13
37.64	-0.43 ± 0.07	-0.95 ± 0.10		-0.61 ± 0.07	-1.13 ± 0.13	27.85	-0.45 ± 0.03	-0.92 ± 0.06	28.90	-0.35 ± 0.06	-0.80 ± 0.13
37.16	-0.48 ± 0.06	-0.91 ± 0.07	37.84	-0.59 ± 0.06	-1.16 ± 0.12	26.03	-0.34 ± 0.08	-0.82 ± 0.12	27.68	-0.38 ± 0.07	-0.92 ± 0.13
36.68	-0.51 ± 0.08	-1.04 ± 0.10	32.84	-0.55 ± 0.11	-0.95 ± 0.19	25.14	-0.35 ± 0.08	-0.87 ± 0.13	25.75	-0.41 ± 0.08	-1.01 ± 0.23
35.24	-0.37 ± 0.09	-0.92 ± 0.11	20.80	-0.66 ± 0.07	-1.33 ± 0.14	25.30	-0.40 ± 0.04	-0.94 ± 0.06	24.90	-0.33 ± 0.07	-0.65 ± 0.18
33.80	-0.50 ± 0.08	-1.19 ± 0.11	20.40	-0.72 ± 0.08	-1.54 ± 0.13	25.31	-0.47 ± 0.07	-0.96 ± 0.12	23.45	-0.22 ± 0.07	-0.61 ± 0.13
33.56	-0.60 ± 0.08	-1.38 ± 0.12	19.82	-0.66 ± 0.06	-1.38 ± 0.13	26.61	-0.40 ± 0.08	-0.85 ± 0.12		-0.29 ± 0.07	-0.70 ± 0.13
29.32	-0.68 ± 0.09	-1.60 ± 0.11	18.88	-0.52 ± 0.07	-1.08 ± 0.11	27.29	-0.46 ± 0.04	-1.04 ± 0.08		-0.42 ± 0.07	-0.85 ± 0.15
	-0.62 ± 0.08	-1.46 ± 0.11	18.46	-0.61 ± 0.03	-1.22 ± 0.06	22.59	-0.41 ± 0.04	-0.84 ± 0.06	22.10	-0.40 ± 0.08	-0.51 ± 0.20
27.88	-0.71 ± 0.09	-1.58 ± 0.11	17.25	-0.56 ± 0.04	-1.06 ± 0.08	21.00	-0.49 ± 0.04	-0.88 ± 0.08	20.24	-0.46 ± 0.07	-0.68 ± 0.17
26.76	-0.67 ± 0.08	-1.40 ± 0.12	16.71	-0.61 ± 0.04	-1.02 ± 0.08	20.03	-0.50 ± 0.07	-0.79 ± 0.14	19.10	-0.37 ± 0.07	-0.82 ± 0.11
25.64	-0.68 ± 0.08	-1.34 ± 0.11	16.35	-0.57 ± 0.03	-1.17 ± 0.06	19.38	-0.45 ± 0.08	-0.77 ± 0.14	17.95	-0.44 ± 0.06	-0.82 ± 0.13
23.64	-0.59 ± 0.08	-1.33 ± 0.11	15.81	-0.65 ± 0.06	-1.32 ± 0.14	18.42	-0.45 ± 0.03	-0.84 ± 0.07	16.25	-0.51 ± 0.06	-0.83 ± 0.12
23.08	-0.75 ± 0.09	-1.51 ± 0.15	15.38	-0.66 ± 0.07	-1.40 ± 0.15	17.95	-0.39 ± 0.07	-0.62 ± 0.13	15.80	-0.37 ± 0.07	-0.74 ± 0.15
20.04	-0.76 ± 0.09	-1.57 ± 0.15	14.50	-0.59 ± 0.04	-1.33 ± 0.04	17.20	-0.35 ± 0.07	-0.73 ± 0.14	16.25	-0.39 ± 0.07	-0.65 ± 0.13
18.68	-0.66 ± 0.06	-1.37 ± 0.09	13.62	-0.55 ± 0.05	-1.25 ± 0.06	16.10	-0.46 ± 0.06	-0.73 ± 0.14	13.78	-0.40 ± 0.07	-0.78 ± 0.14
17.96	-0.58 ± 0.07	-1.11 ± 0.10	12.16	-0.60 ± 0.07	-1.22 ± 0.15	13.40	-0.37 ± 0.08	-0.75 ± 0.17	12.10	-0.31 ± 0.08	-0.71 ± 0.16
16.44	-0.67 ± 0.07	-1.27 ± 0.09	10.97	-0.59 ± 0.07	-1.27 ± 0.15	12.00	-0.35 ± 0.07	-0.62 ± 0.16	10.95	-0.41 ± 0.07	-0.92 ± 0.13
15.24	-0.67 ± 0.07	-1.41 ± 0.11	9.90	-0.44 ± 0.04	-0.98 ± 0.08	10.55	-0.36 ± 0.08	-0.70 ± 0.17	9.15	-0.48 ± 0.08	-1.02 ± 0.14
14.44	-0.62 ± 0.08	-1.19 ± 0.09	9.51	-0.51 ± 0.07	-1.14 ± 0.12	10.15	-0.45 ± 0.07	-0.90 ± 0.21	8.76	-0.49 ± 0.07	-1.04 ± 0.14
14.60	-0.77 ± 0.10	-1.53 ± 0.16	8.10	-0.47 ± 0.03	-0.96 ± 0.05	8.97	-0.50 ± 0.07	-0.94 ± 0.15	7.90	-0.38 ± 0.08	-0.76 ± 0.14
13.40	-0.56 ± 0.07	-1.15 ± 0.09	7.78	-0.69 ± 0.05	-1.28 ± 0.07	6.65	-0.34 ± 0.08	-0.76 ± 0.15	7.05	-0.35 ± 0.07	-0.53 ± 0.14
13.36	-0.68 ± 0.08	-1.21 ± 0.11	5.08	-0.75 ± 0.06	-1.41 ± 0.16	6.55	-0.48 ± 0.08	-0.79 ± 0.17	6.34	-0.35 ± 0.04	-0.84 ± 0.06
10.80	-0.50 ± 0.08	-1.09 ± 0.11	0.00	-0.72 ± 0.08	-1.27 ± 0.16	4.50	-0.42 ± 0.07	-0.77 ± 0.15	5.23	-0.43 ± 0.07	-0.79 ± 0.13
8.96	-0.47 ± 0.08	-1.02 ± 0.11				3.92	-0.46 ± 0.08	-0.72 ± 0.17	3.00	-0.35 ± 0.05	-0.54 ± 0.08
7.76	-0.61 ± 0.09	-1.37 ± 0.13				3.37	-0.40 ± 0.08	-0.84 ± 0.17	2.82	-0.40 ± 0.08	-0.72 ± 0.14
6.16	-0.61 ± 0.08	-1.09 ± 0.10				2.90	-0.35 ± 0.04	-0.64 ± 0.05	0.90	-0.39 ± 0.04	-0.84 ± 0.07
4.80	-0.67 ± 0.07	-1.40 ± 0.11				0.15	-0.33 ± 0.04	-0.63 ± 0.06	0.00	-0.43 ± 0.04	-0.75 ± 0.08
2.88	-0.60 ± 0.07	-1.23 ± 0.12									
2.56	-0.59 ± 0.07	-1.33 ± 0.10									
0.96	-0.50 ± 0.07	-1.08 ± 0.09									
0.00	-0.61 ± 0.07	-1.27 ± 0.10									

The stratigraphic positions of the analyses are indicated by mm (see Figure 4.3) Uncertainties of single analysis are given by 2 SD.

Table 4.5 C isotope data of bulk layers for Kuruman Iron Formation 3/59 (Transvaal)

mm	Carbonate composition of layers	$\delta^{13}\text{C}$
38.35	50% sid, 50% ank	-9.51
34.25	95% calcite, 5% sid	-9.57
29.95	95% calcite, 5% sid	-9.58
27.85	95% calcite, 5% sid	-9.59
20.55	80% ank, 20% sid	-10.29
11.00	60%ank, 40%sid	-10.12
3.45	20% ank, 80% sid	-11.17
1.50	70%ank, 30%sid	-8.95
0.00	70%ank, 30%sid	-10.91

The stratigraphic position of the samples indicated by mm corresponds to *Figure 4.5*. The carbonate composition is inferred from estimated modal abundances.

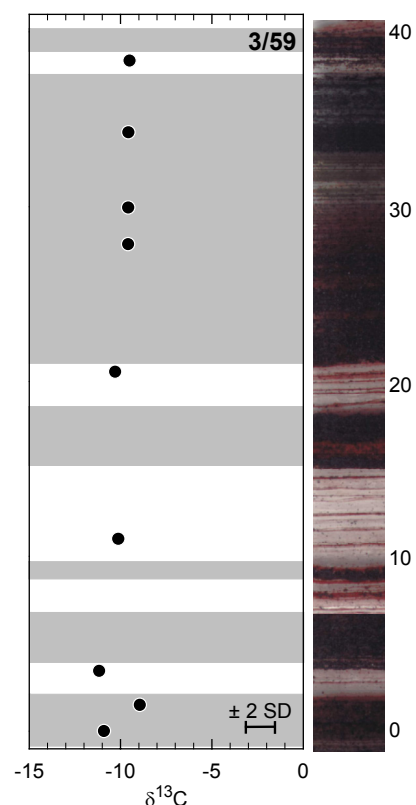


Figure 4.5 C isotope composition of sample 3/59 from the Kuruman Iron Formation, Transvaal (South Africa). Despite variable chemical composition of Fe carbonates, the C isotope composition is largely homogeneous indicating a mixed carbon source of inorganic and organic origin.

4.6. Discussion

4.6.1. Seawater to sediment cycling of Si and Fe

The Fe isotope signatures in the investigated Hamersley and Transvaal BIFs show variations on small spatial scale, whereas the Si isotope signature is uniform in each core section (see *Figure 4.3* and *4.7*). These characteristics imply different pathways for Si and Fe during their formation. In this regard, Proterozoic BIFs may differ from Archean BIFs associated with greenstone belts. For instance, the 2.7 Ga Old Wanderer BIF within the Shurugwi Greenstone Belt (Zimbabwe) shows correlated small-scale variations in both the Si and Fe isotope signatures, which have been interpreted to reflect the dynamics of hydrothermal activity (see *Chapter 3*).

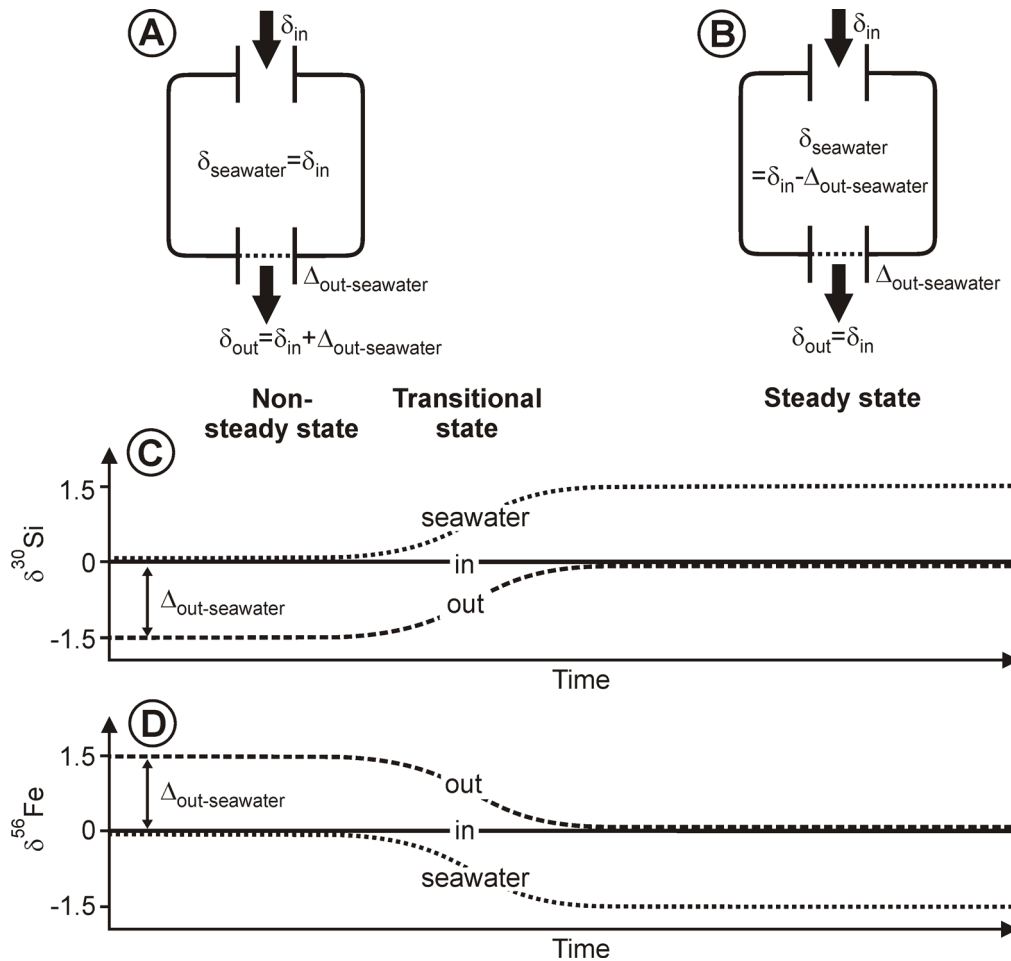


Figure 4.6 Conceptual models for the temporal evolution of the Fe and Si isotope composition in an ocean basin. The ocean basin presents a single compartment with no isotope fractionation at intake, but isotope fractionation at precipitation into sediment with an associated isotope fractionation factor $\Delta_{\text{out-seawater}}$. **A)** At non steady-state, the isotope composition of seawater δ_{seawater} equals that of the influx δ_{in} . The isotope composition of the outflux δ_{out} , i.e. the precipitated Fe and Si, is determined by δ_{seawater} and $\Delta_{\text{out-seawater}}$. **B)** At steady state, the influx equals the outflux in quantity and isotope composition. Hence, δ_{seawater} evolves towards $\delta_{\text{in}} - \Delta_{\text{out-seawater}}$. In **C)** and **D)**, the temporal evolution of Fe and Si isotope signatures of the influx, the seawater and the outflux are delineated as the system evolves from non-steady state to steady state conditions. Here, we assume fractionation factors of -1.5‰ and 1.5‰ for Si and Fe precipitation from solution, respectively, and an isotope composition of 0‰ for both sources, Fe and Si. This temporal evolution is not a Rayleigh type process.

In general, chert in BIFs is considered to result from direct silica precipitation from seawater (e.g. Maliva et al., 2005) and is likely to preserve its original Si isotope signature (André et al., 2006; van den Boorn et al., 2007; and see *Chapter 3*). The homogeneous Si isotope signatures of the investigated core sections suggest continuous silica precipitation from well-mixed seawater with a steady Si isotope composition. The absence of short-term variations is consistent with a presumably long residence time of Si on the order of 10^5 to 10^6 years (Siever, 1992). These conditions are characteristic of the typical depositional setting of Proterozoic BIFs on partially isolated continental shelf platforms. These areas are removed from the direct influence of either hydrothermal venting systems or continental drainage (e.g. Klein, 2005). In contrast, the Fe isotope composition is controlled by many factors including seawater composition, the initially precipitated Fe phases, partial Fe(II) oxidation and diagenetic Fe redistribution, which have caused large variations (see *section 4.6.2*).

Considering the bulk layer Si and Fe isotope composition of the investigated BIFs, both systems exhibit lower values than expected for a steady state ocean model. We can say this because the deposited BIFs did not obtain the assumed composition of the influx, a condition required for the ocean basin to be at steady state (*Figure 4.6*). *Figure 4.7* presents a conceptual isotope model for Si and Fe precipitation and defines two end member scenarios for Precambrian seawater: steady state and non-steady state conditions. In the first case, both quantity and isotope composition of the outflux corresponds to the influx implying that BIFs would carry the Si and the Fe isotope composition of the hydrothermal source (see also *Figure 4.6b*). This source composition is near 0‰ for both systems (Beard et al., 2003; De La Rocha and Bickle, 2005; Severmann et al., 2004; Sharma et al., 2001). A terrigenous component contributing to the Si influx would produce more positive $\delta^{30}\text{Si}$ values (see discussion below). In the non-steady state case, the isotope signatures in BIFs would reflect the equilibrium fractionation factors for Si and Fe precipitation from solution, respectively, which leads to overall negative $\delta^{30}\text{Si}$ and positive $\delta^{56}\text{Fe}$ values (see also *Figure 4.6a*). In the following, we evaluate the Si and Fe isotope mass balance of the Precambrian seawater.

The Si isotope composition of chert in BIFs appears to be in disequilibrium with the Si influx. All BIFs investigated to date including the Hamersley and Transvaal BIFs are depleted in isotopically heavy Si, ranging from -2.6 to -0.5 ‰ in $\delta^{30}\text{Si}$ (André et al., 2006; Ding et al., 1996; Jiang et al., 1993; this study). These values are in marked contrast to the assumed Si influx from hydrothermal fluids, which is at near 0‰ (De La Rocha et al., 2000) and also differ from continental weathering of igneous minerals with ~ 0.8 ‰ (Georg et al., 2006). Nonetheless,

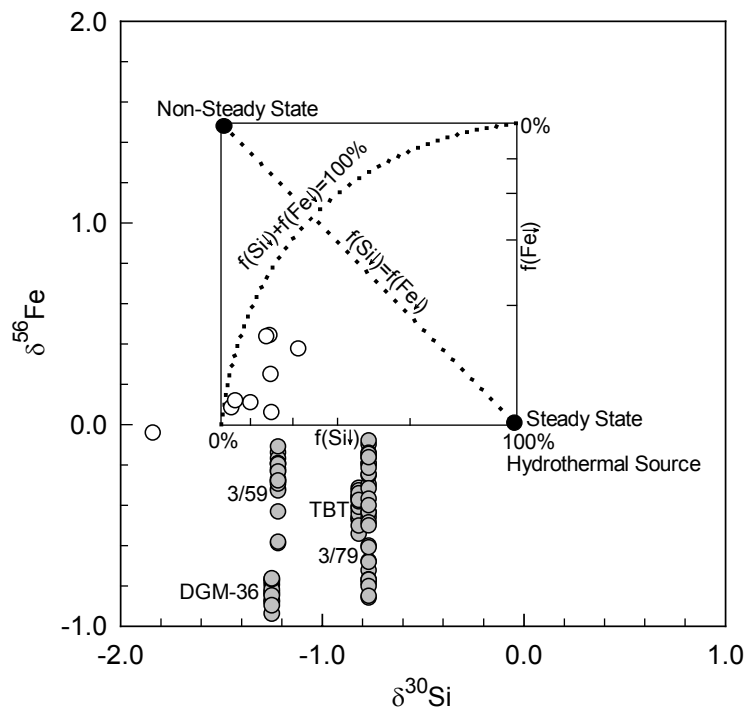


Figure 4.7 Hypothetical model for $\delta^{30}\text{Si}$ and $\delta^{56}\text{Fe}$ of initial precipitates, silica and ferric oxyhydroxide depending on the precipitated fraction f . Precipitation takes place from seawater with a hypothetical hydrothermal signature with $\delta^{56}\text{Fe}$ and $\delta^{30}\text{Si}$ of 0‰, respectively. Ferric oxyhydroxide is 1.5‰ heavier in $\delta^{56}\text{Fe}$, whereas SiO_2 is 1.5‰ lighter compared to seawater. Two end-member scenarios can be defined: 1) The isotope composition of the depositional outflux corresponds to the hydrothermal influx of 0‰, which is realized either by steady state conditions or 100% precipitation of the dissolved Fe and Si. 2) Precipitation of small fractions from seawater with a hydrothermal signature results in isotope compositions reflecting the fractionation factors of -1.5‰ in $\delta^{30}\text{Si}$ and 1.5‰ in $\delta^{56}\text{Fe}$ representing non-steady state conditions. The diagonal dotted line shows the isotope evolution by Rayleigh distillation for precipitating equal fractions of dissolved Si and Fe ($f(\text{Si}\downarrow)=f(\text{Fe}\downarrow)$). The dotted curve illustrates the trend of opposite fractions of cumulative precipitated Si and Fe ($f(\text{Si}\downarrow)+f(\text{Fe}\downarrow)=100\%$). The axes of the inset indicates the removed fractions of Fe and Si.

The Archean Old Wanderer BIF from the 2.7 Ga Shurugwi Greenstone Belt (Zimbabwe) (open cycles) exhibits covariable Si and Fe isotope data for bulk layers, which plot roughly along the curve of opposite fractions of cumulative precipitated Si and Fe. This feature has been interpreted as direct influence on Si and Fe precipitation by hydrothermal activity (for details see *Chapter 3*). In contrast, the estimated bulk layer compositions of the Proterozoic Hamersley Transvaal BIFs (grey cycles) plot below the quadrant of expected Si and Fe isotope composition and show independent Si and Fe isotope signatures. The low but uniform Si isotope signatures suggest precipitation at constant conditions indicating either non-steady state conditions or a complementary sink of isotopically heavy Si. The low $\delta^{56}\text{Fe}$ values imply isotopically light seawater or diagenetic alteration towards lower $\delta^{56}\text{Fe}$ (see discussion for details).

both steady state and non-steady state scenarios in the ocean basins are compatible with the negative Si isotope signature of BIFs. In the steady state case, the seawater would adapt a significantly positive Si isotope signature caused by the preferential precipitation of isotopically light Si (De La Rocha and Bickle, 2005). Assuming that BIFs with negative $\delta^{30}\text{Si}$ values represent the predominant Si deposit in the Precambrian ocean, the source of this Si also had to have carried a significantly negative Si isotope signature. However such a source composition contradicts estimates from modern hydrothermal ($\sim 0\%$) and terrigenous ($\sim -0.8\%$) Si supply rendering this scenario unlikely. Alternatively, chert in BIFs represents the sink of isotopically light Si, whereas the heavy counterpart is deposited elsewhere. Positive $\delta^{30}\text{Si}$ values have been reported for some Archean marine chert deposits, indicating that this complementary sink might exist (Robert and Chaussidon, 2006; van den Boorn et al., 2007). Non-steady state conditions in the ocean basins could have prevailed if BIF formation represents a period of extraordinary hydrothermal activity or continental weathering (see discussion in Maliva et al. (2005)), which increased the Si influx into the basin temporally. In this case, the seawater would have carried the isotope signature of the source, but the deposits would have obtained a negative signature (*Figure 4.6c*) Chert with strongly negative $\delta^{30}\text{Si}$ values, such as found in samples 3/59 and DGM-36 with mean $\delta^{30}\text{Si}$ values of -1.22 and -1.25% , respectively, are close to the Si isotope composition of modern siliceous deposits around oceanic smokers with an average $\delta^{30}\text{Si}$ value of -1.56 ± 0.38 (1 SD, $n=25$) (Ding et al., 1996). Chert with comparatively more heavy $\delta^{30}\text{Si}$ values, i.e. samples TBT and 3/79 with mean $\delta^{30}\text{Si}$ values of -0.82 and -0.77% , respectively, suggest an enhanced terrigenous influence. An alternatively explanation is an ocean basin that is in a transitional stage. Then, strongly negative $\delta^{30}\text{Si}$ values in chert reflect seawater dominated by a hydrothermal influence, while moderately negative values indicate a development away from the hydrothermal signature back to steady state conditions.

Quite differently to the Si isotope signature, the overall Fe isotope composition of the Hamersley and Transvaal BIFs is consistent with a steady state ocean model (Johnson et al., 2008a). Although the major Fe-bearing mineral phases in unmetamorphosed BIFs, magnetite and Fe carbonate, exhibit large variations, the overall bulk BIF Fe isotope signature is close to 0% , which seems to be in balance with the influx composition. $\delta^{56}\text{Fe}$ values of magnetite range from -1.1 to 1.3% with an average of $-0.1 \pm 0.5\%$ (1 SD, $n = 117$), whereas $\delta^{56}\text{Fe}$ values of Fe carbonates vary between -2.2 and 1.1% giving an average of $-0.6 \pm 0.5\%$ (1 SD, $n = 95$) (Johnson et al., 2003; Johnson et al., 2008a; this study) (see *Figure 4.8*). The Fe supply to the seawater by hydrothermal fluids and minor continental drainage (e.g. Canfield, 1998; Jacobsen

and Pimentel-Klose, 1988) has been suggested to have carried a Fe isotope composition between -0.5 and 0‰ (Yamaguchi et al., 2005). However, the investigated samples here are all on the lower end of the Fe isotope range displaying temporal disequilibrium. Several explanations are possible for these negative Fe isotope signatures:

1) Mineralogy-controlled Fe isotope fractionation during precipitation of Fe minerals from seawater can cause a moderately negative Fe isotope signature in sediments. For example, the precipitation of primary siderite would incorporate preferentially isotopically light Fe (Wiesli et al., 2004). However, Fe oxide dominates over siderite in all investigated core sections, which excludes this option.

2) The seawater could have carried a negative Fe isotope signature. Long-term enrichment of the seawater in isotopically light Fe has been suggested to be driven by the preferential deposition of isotopically heavy Fe following partial Fe(II) oxidation in the upper water column (Rouxel et al., 2005). Alternatively, the seawater composition could be dominated by Fe recycled from sediments by DIR analogues to modern shelf environments, which release large quantities of Fe(II)_{aq} with low $\delta^{56}\text{Fe}$ values (Bergquist and Boyle, 2006; Severmann et al., 2006; Severmann et al., 2008; Staubwasser et al., 2006). If the original seawater composition is conserved in bulk BIF throughout diagenesis, the oxide minerals provide an upper limit of the seawater Fe isotope composition due to their preferential incorporation of heavy Fe isotopes, which is likely for sample DGM-36 from the Dales Gorge Member containing hematite with $\delta^{56}\text{Fe}$ values of $\sim -0.8\text{‰}$ (see *section 4.6.2.*).

3) Post-depositional supply of isotopically light Fe(II) or loss of isotopically heavy Fe(II) can shift the overall Fe isotope signature in the sediments to negative values. Large quantities of Fe(II)_{aq} with low $\delta^{56}\text{Fe}$ values might have been released elsewhere by DIR and would have diffused into the consolidating sediments making up the majority of the Fe(II) inventory in BIF (Johnson et al., 2008a). Alternatively, loss of isotopically heavy Fe(II) could have resulted from abiotic Fe(III) reduction in BIFs during late diagenesis or low-grade metamorphism. A diagenetically induced shift to low $\delta^{56}\text{Fe}$ values seems likely for the samples from the Kuruman Iron Formation, 3/59 and 3/79, in which magnetite was formed - usually considered to represent a secondary mineral (see *section 4.6.2.*).

Regardless of the actual cause, the final preservation of isotopically light Fe in these samples requires a balance by deposition of heavy Fe elsewhere if the near 0‰ steady state condition is fulfilled. Recent investigations in the Black Sea and the Baltic Sea have revealed a net transfer of isotopically light Fe released by DIR from oxic to anoxic environments (Fehr et al., 2008; Severmann et al., 2008). A similar redistribution of Fe might also have occurred in Precambrian

ocean basins, which could have promoted the simultaneous formation of both isotopically light and heavy BIF that are separated in space. Alternatively, secular variations in Fe deposition could have led to cyclic deposition of BIF with variable composition.

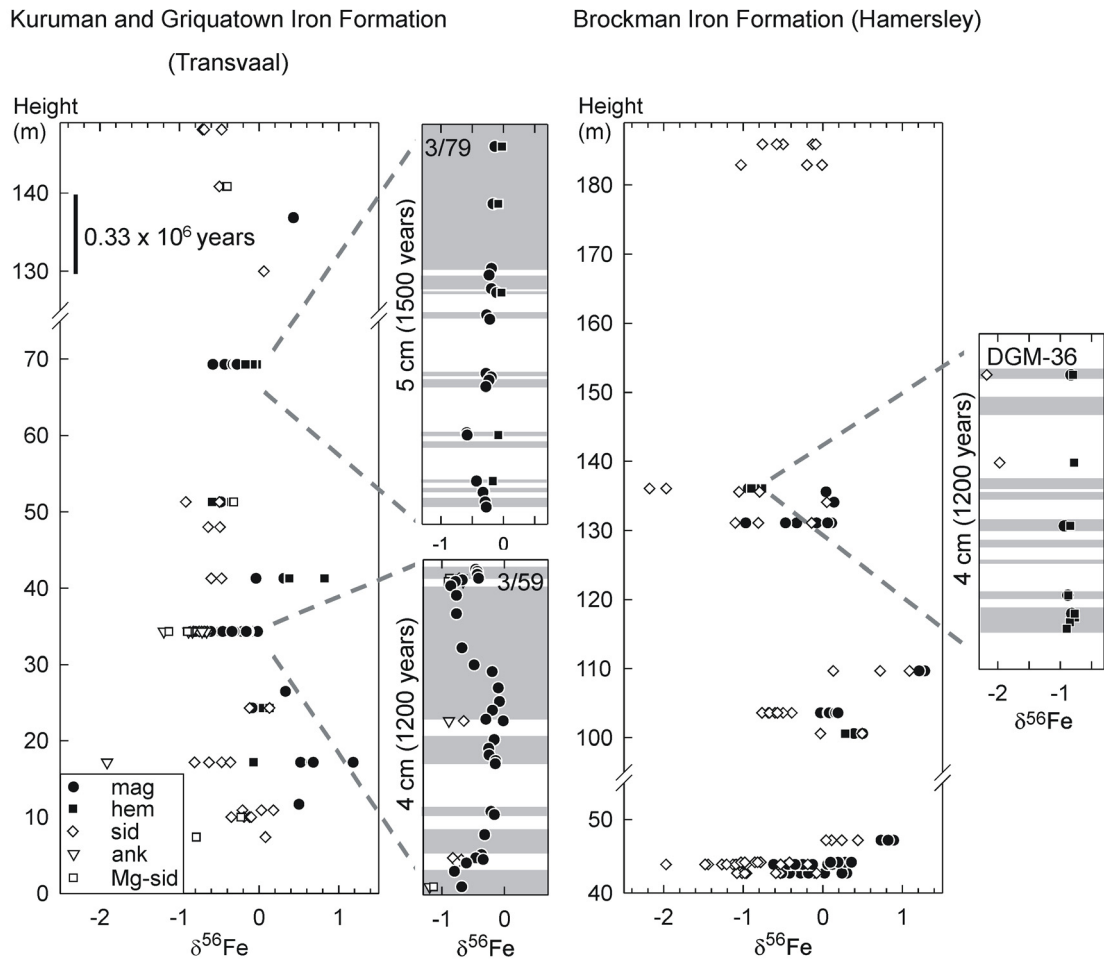


Figure 4.8 Fe isotope data of the Kuruman and Griquatown Iron Formation from the Transvaal succession and the simultaneously deposited Brockman Iron Formation from the Hamersley succession including the data of (Johnson et al., 2003; Johnson et al., 2008a) and this study (modified after Johnson et al. (2008a)). The time scale refers to a depositional rate of consolidated sediment of of $33 \text{ m}/10^6 \text{ years}$ (Pickard, 2002; Pickard, 2003).

4.6.2. Formation of Fe-bearing minerals

Formation of hematite from ferric oxyhydroxide

In virtually unmetamorphosed BIFs, hematite is an early diagenetic product formed by dehydration of the ferric oxyhydroxide precursors (e.g. Klein, 2005). Ferric oxyhydroxide, in turn, is considered to originate from oxidation of Fe(II)_{aq} in surface waters followed by settling of particles through Fe(II)-rich anoxic bottom water. Oxidation of Fe(II)_{aq} was most likely caused by anaerobic photosynthesis (e.g. Kappler et al., 2005; Konhauser et al., 2002; Widdel et al., 1993) or atmospheric oxygen (e.g. Drever, 1974; Ehrenreich and Widdel, 1994; Holland, 1973; Kaufman et al., 2007). UV photo-oxidation has also been considered as possible mechanism (e.g. Cairns-Smith, 1978), but has been recently excluded as cause of efficient iron precipitation (Konhauser et al., 2007). Both mechanisms precipitate ferric hydr(oxide) with a Fe isotope composition that is around 1.5‰ heavier than seawater (Anbar et al., 2005; Croal et al., 2004; Skulan et al., 2002; Welch et al., 2003). Such isotope fractionation is evident when a small quantity of Fe is oxidised, i.e. partial Fe(II) oxidation. In contrast, no fractionation occurs between solution and solid when 100% of the Fe(II) is oxidized. In this case, the isotope signature of the seawater would have been transferred into the precipitate. Hematite preserves this initial isotope composition, unless a diagenetic alteration of this signature has taken place. During diagenesis, biotic or abiotic reduction of ferric (hydr)oxide and the subsequent release of Fe(II)_{aq} into pore fluids can shift the residues isotope signature to higher $\delta^{56}\text{Fe}$ values (Crosby et al., 2005; Crosby et al., 2007; Pedersen et al., 2005; Severmann et al., 2006; Severmann et al., 2008; Staubwasser et al., 2006; Williams and Scherer, 2004).

We suggest that hematite in the core sections 3/79 and DGM-36 reflects a primary Fe isotope composition (*Figure 4.3*). This suggestion is supported by the consistency of Fe isotope composition in these samples. Furthermore, isotope differences to coexisting magnetite, a likely product of DIR, are variable suggesting that hematite or its precursor have conserved the original isotope ratio, while the various fractionation of Fe mobilisation by DIR are recorded in magnetite. Therefore, the Fe isotope composition of hematite appears to be directly related to the degree of partial Fe(II) oxidation in the upper water column. Hematite in samples 3/79 and DGM-36 reveals average $\delta^{56}\text{Fe}$ values of $\sim 0\%$ and $\sim -0.8\%$, respectively, providing upper limits for the seawater composition at the time of deposition.

Primary siderite precipitation

Several authors have suggested primary siderite precipitation during the formation of BIFs (e.g. Kaufman et al., 1990; Klein and Beukes, 1989; Sumner, 1997). The concentration of dissolved Fe(II) may increase with depth in the ocean, which slows calcite precipitation and triggers supersaturation of siderite. Siderite then precipitated directly from the water column or formed at the water-sediment interface, where pore fluids were in equilibrium with seawater providing information on the ancient seawater composition. According to the results of the experimental work of Wiesli et al. (2004), siderite is $\sim 0.5\%$ lighter in its Fe isotope composition than dissolved Fe(II) under equilibrium conditions.

We propose that siderite is primary in sample 3/59 (*Figure 4.3*). The differences in $\delta^{56}\text{Fe}$ amongst coexisting magnetite and Fe carbonate phases in individual layers are variable and also inconsistent with suggested fractionation factors. This observation implies isotopic disequilibrium and decoupled formation pathways for magnetite and Fe carbonates, respectively. Siderite exposes a uniform $\delta^{56}\text{Fe}$ value of $\sim -0.7\%$ in the core section, which is consistent with a steady seawater composition of -0.2% based on the fractionation factor siderite-Fe(II)_{aq} of -0.5% (Wiesli et al., 2004). In contrast, Mg-rich siderite and ankerite are considered as diagenetically altered phases formed at the expense of siderite (Kaufman et al., 1990). They exhibit variably lower $\delta^{56}\text{Fe}$ values compared to siderite ranging from -1.2 to -0.7% .

The C isotope composition of this sample provides additional information (*Figure 4.5, Table 4.3*). Regardless of the chemical composition of carbonates in layers, $\delta^{13}\text{C}$ values are largely constant around -10% , which is in the range of previously investigated BIFs of the Transvaal succession with $\delta^{13}\text{C}$ values between -3 and -14% (Beukes and Klein, 1990; Beukes et al., 1990; Fischer et al., in press; Kaufman, 1996). Relatively high $\delta^{13}\text{C}$ values in carbonates from BIFs have been suggested to reflect a 'mantle-like' seawater composition, whereas carbonates with significant negative $\delta^{13}\text{C}$ values have been interpreted to have incorporated predominately carbon derived from organic matter degradation (Beukes and Klein, 1990; Beukes et al., 1990; Kaufman et al., 1990; Kaufman, 1996). Therefore, carbonates in sample 3/59 with intermediate $\delta^{13}\text{C}$ values have a mixed carbon source of inorganic and organic origin.

Diagenetic siderite and magnetite formation by reduction of ferric (hydr)oxide during organic matter degradation

A likely process in the genesis of BIF is the diagenetic formation of siderite and magnetite due to reduction of ferric (hydr)oxides as organic carbon is oxidized (e.g. Ewers and Morris, 1981; Han, 1978; Lovley, 1991). The $\text{Fe(II)}_{\text{aq}}$ released reacts either with residual ferric oxyhydroxide to form magnetite or with bicarbonate to produce siderite. This conversion is either catalysed by DIR during early diagenesis or is an abiotic spontaneous reaction at late diagenesis or low-grade metamorphism (e.g. Lovley, 1991). Isotope fractionation and the kinetics of isotope exchange in a system involving DIR have been investigated in detail (Crosby et al., 2005; Crosby et al., 2007; Johnson et al., 2005). In contrast, the fractionation in the abiotic system is largely unknown. Coexisting magnetite and siderite, which have formed simultaneously, should reflect the equilibrium magnetite-siderite fractionation factor. This factor is estimated to be 1.8 ‰ for the pathway involving DIR by experimental studies (Johnson et al., 2008a and references therein) and decreases to 1.6 to 0.8‰ for abiotic reduction at temperatures between 120 to 170°C as predicted from Mössbauer data (Mineev et al., 2007; Polyakov and Mineev, 2000; Polyakov et al., 2007).

Coupled diagenetic formation of magnetite and siderite by biotic or abiotic Fe(III) reduction is a likely process in sample DGM-36 (*Figure 4.3*). Even though the magnetite-siderite assemblage could not be measured in direct contact at many locations, both minerals show uniform Fe isotope compositions giving an overall difference of $\sim 1.2\text{‰}$. It might be surprising that the Fe isotope composition of magnetite and hematite are identical in this sample. This isotopic agreement can be explained by the low abundance of siderite. $\text{Fe(II)}_{\text{aq}}$ released by reduction is nearly quantitatively incorporated into magnetite and only to a much lesser extent into the rare occurrences of siderite. Therefore, mass balance dictates that the Fe isotope compositions of magnetite and hematite are virtually indistinguishable. Hence, the low $\delta^{56}\text{Fe}$ values of magnetite are inherited from the ferric(hydr)oxide precursor.

In samples 3/79 and 3/59 diagenetic siderite is absent, hence reductive diagenesis would have only formed magnetite. Since magnetite is lighter than hematite in sample 3/79, diagenetic magnetite formation by an abiotic reductive processes is likely. For these, approaches using Mössbauer data propose 0.1 to -0.5‰ for the equilibrium magnetite- $\text{Fe(II)}_{\text{aq}}$ fractionation factor at ambient temperatures (Anbar et al., 2005; Mineev et al., 2007; Polyakov et al., 2007). Hence, magnetite evolves towards lighter Fe isotope composition than the original Fe(III) substrate, depending on the amount of isotopically heavy $\text{Fe(II)}_{\text{aq}}$ loss. Although hematite is not available for direct comparison with magnetite in sample 3/59, a minimum $\delta^{56}\text{Fe}$ value for a ferric

(hydr)oxide precursor can be inferred from primary siderite as it equals the derived seawater composition of -0.2‰ (see *Primary siderite precipitation*). This inferred $\delta^{56}\text{Fe}$ value for ferric (hydr)oxide is higher than $\delta^{56}\text{Fe}$ values of magnetite ranging between -0.1 and -0.9‰ , therefore abiotic Fe(III) reduction accompanied by loss of isotopically heavy Fe(II) is also likely in this sample.

Alternatively, the lower $\delta^{56}\text{Fe}$ values of magnetite compared to the original Fe(III) substrate in samples 3/59 and 3/79 can also be attributed to the addition of isotopically light $\text{Fe(II)}_{\text{aq}}$ derived from DIR elsewhere. Such addition would represent an alternative mechanism to the loss of isotopically heavy Fe.

Replacement of magnetite by hematite in metamorphosed BIF

Sample TBT from Penge Iron Formation of the Transvaal succession represents an altered BIF, which was effected by contact metamorphism during the Bushveld intrusion and later hydrothermal oxidative fluid infiltrations (Gutzmer et al., 2005). In this sample, hematite has most likely replaced magnetite during hydrothermal iron ore formation. Magnetite preserves its original Fe isotope composition throughout prograde contact metamorphism (Frost et al., 2007). Oxidative metasomatism is unlikely to mobilize Fe. Therefore magnetite is likely to have been quantitatively transformed into hematite without significant Fe redistribution, which preserves the original Fe isotope composition. Hence, the Fe isotope composition in hematite of $\sim -0.4\text{‰}$ in $\delta^{56}\text{Fe}$ reflects the Fe isotope composition of the original magnetite, which likely formed during diagenesis by one of the processes discussed above.

Small-scale heterogeneities

Fe oxide phases exhibit small-scale heterogeneities in the Fe isotope composition including both lateral and vertical variations.

1) In sample 3/79, magnetite exhibits a homogeneous Fe isotope composition within a given Fe oxide-rich layer but is variable between layers. In contrast, its mineralogical precursor, hematite, shows a uniform Fe isotope composition (*Figure 4.3d*). These observations suggest a diagenetic origin of the variability. The inter-layer variability implies that diagenetic fluids have dispersed mainly laterally and supports that significant Fe exchange across layering is absent in BIFs (Frost et al., 2007; Johnson et al., 2008a; and see *Chapter 3*). The homogeneous Fe isotope composition within layers suggests magnetite formation under $\text{Fe(II)}_{\text{aq}}$ excess conditions.

2) Shifts in the Fe isotope composition of magnetite within a few microns as observed in sample 3/59 (*Figures 4.1c* and *4.3h*) suggest a pre-depositional origin as diagenetic fluids would rather

reduce than cause variations on this scale. It is unlikely that these small-scale heterogeneities reflect variable seawater composition as the assumed long residence time of Fe would have prohibited short-term changes (Johnson et al., 2008a). Moreover, the identification of primary siderite in this sample suggests a constant seawater compositions for the period represented by the investigated core section. Hence, most likely this small-scale shifts in magnetite are inherited from its precursor reflecting variable degrees of partial Fe(II) oxidation in the upper water column.

3) Variable Fe isotope composition in both hematite and magnetite within the lamination as observed in sample DGM-36 (*Figure 4.3j*) is thought to be primary, although diagenetic effect on minerals cannot be excluded. Variable oxidation rates within the upper water column could have caused this effect.

4) Lateral heterogeneities in magnetite can also result from Fe(II)_{aq}-limiting conditions during crystallization. Reservoir effects in pore fluids have accounted for isotopically zoned crystals observed in the Archean Old Wanderer BIF (see *Chapter 3* and *Figure 4.4*) and random heterogeneities as found in Isua (Whitehouse and Fedo, 2007). During metamorphism, the heterogeneity of magnetite can be passed on to secondary hematite. For example in sample TBT, hematite formed from magnetite by a oxidative hydrothermal fluid event related to the Bushveld intrusion; its variability might have been inherited from a heterogeneous magnetite precursor.

4.7. Conclusions

The combined analyses of Si and Fe isotope compositions in two major BIF deposits suggests distinct pathways of Si and Fe within Precambrian ocean basins. The uniform Si isotope signatures in chert indicates steady silica precipitation from seawater with a invariant Si isotope composition. Such a scenario is consistent with a depositional setting on a partially isolated platform within continental shelf areas. The long residence time of Si in seawater must have been long. However, the pronounced negative Si isotope signatures in all studied BIF samples stand in marked contrast to the composition of the assumed Si influx to the ocean, which presumably featured a $\delta^{30}\text{Si}$ of between near-zero and moderately positive values depending on the relative proportions of hydrothermal versus terrigenous supply. Therefore, preferential precipitation of light Si was taken place that had to be balanced by a complementary sink for isotopically heavy Si. The only other possibility is transient perturbation of the steady state that would shift the seawater away its assumed heavy composition. An entirely different picture

emerges from the range in Fe isotope compositions. These variations in space and time can be contributed to different mechanisms: 1) different phases initially precipitated into the newly formed sediment, each with their associated fractionation factor; 2) variable degrees of partial Fe(II) oxidation in the upper water column with simultaneous fractionation would have led to variable composition in the precipitates in a Rayleigh-style fashion; 3) variable seawater composition; and 4) diagenetic Fe redistribution by reduction of ferric (hydr)oxide. Reductive diagenetic processes through organic matter oxidation are also indicated by C isotope compositions of BIF layers with primary siderite, which suggests a mixed carbon source of inorganic and organic origin. Nevertheless, the overall Fe isotope record of the Hamersley and Transvaal BIFs of near-zero is consistent with a steady state ocean as suggested by (Johnson et al., 2008). It is noteworthy, however, that our BIF samples contain more negative Fe isotope signatures than bulk samples investigated over a longer stratigraphic section (Johnson et al., 2003; Johnson et al., 2008). This disequilibrium might be balanced temporally or spatially by deposition of isotopically heavy BIFs without disturbing overall steady state conditions in the ocean due to the long residence time of Fe.

We suggest that Proterozoic seawater Fe isotope composition can be inferred from both hematite, if the oxidation of dissolved Fe(II) was quantitative and no diagenetic Fe redistribution occurred, and siderite, that we consider primary if an isotope disequilibrium to other phases exists, thereby excluding diagenetic siderite formation. From this analysis, we conclude that the seawater composition was steady within the depositional period of the individual core sections investigated here. The inferred range of $\delta^{56}\text{Fe}$ is -0.8 to 0‰ . The lower boundary of $\delta^{56}\text{Fe}$ in seawater might be caused either by remobilisation of sedimentary Fe by DIR or by preferential deposition of isotopically heavy Fe elsewhere due to partial Fe(II) oxidation.

The grain to grain isotope analysis identifies distinct diagenetic pathways. Magnetite formed by variably diagenetic processes: 1) It has formed in equilibrium with siderite by biotic or abiotic Fe(III) reduction. In this case, magnetite has inherited its low $\delta^{56}\text{Fe}$ value from a ferric oxyhydroxide precursor precipitated from isotopically light seawater. 2) Magnetite formed independently from siderite by either abiotic Fe(III) reduction accompanied by loss of isotopically heavy $\text{Fe(II)}_{\text{aq}}$ or incorporation of isotopically light $\text{Fe(II)}_{\text{aq}}$ released by DIR elsewhere in the sediment section. Magnetite replacement by hematite due to oxidative hydrothermal ore forming processes likely preserves the original Fe isotope composition. Not all diagenetic Fe carbonates are the product of simultaneous oxidation of organic matter and Fe oxide reduction. Fe carbonate varieties such as ankerite and siderite with significant Mg-

substitution are diagenetic phases, but they are variably depleted in isotopically heavy Fe when compared to the original primary siderite.

This study shows that despite the similar mineralogical composition of BIFs investigated herein, unique formation pathways of the mineral phases do not exist. Although the general Fe isotope composition of the Hamersley and Transvaal BIFs are in equilibrium with those of the Fe sources, the much lighter samples investigated here indicate either post-depositional loss of isotopically heavy Fe or gain of light Fe, or precipitation from isotopically light seawater. These findings pose the questions of whether the complementary heavy Fe is deposited elsewhere or at a different time, and what mechanisms led to these variations. Similarly, at the current state of knowledge of Si sources and isotope fractionation during precipitation, the Si isotope signature in our samples, and apparently in all BIF samples, appears to be too light when compared to the likely input. Here the question arises if the time of BIF deposition represents either steady state in the ocean basin demanding a complementary sink, which needs to be identified or non-steady state conditions caused by increased hydrothermal activity or continental weathering.

References

- Aeschliman D. B., Bajic S. J., Baldwin D. P. and Houk R. S. (2003) High-speed digital photographic study of an inductively coupled plasma during laser ablation: comparison of dried solution aerosols from a microconcentric nebulizer and solid particles from laser ablation. *Journal of Analytical Atomic Spectrometry* **18**, 1008-1014.
- Albarède F. and Beard B. L. (2004) Analytical methods for non-traditional isotopes . In *Geochemistry of Non-Traditional Stable Isotopes* (eds. C. M. Johnson, B. L. Beard and F. Albarède). Reviews in Mineralogy and Geochemistry, Mineralogical Society of America, Washington. pp. 113–152.
- Alexandre A., Meunier J. D., Colin F. and Koud J. M. (1997) Plant impact on the biogeochemical cycle of silicon an related weathering processes. *Geochimica et Cosmochimica Acta* **61**, 677-682.
- Alibert C. and McCulloch M. T. (1993) Rare earth element and neodymium isotopic compositions of the banded iron-formations and associated shales from Hamersley, Western Australia. *Geochimica et Cosmochimica Acta* **57**, 187-204.
- Alleman L. Y., Cardinal D., Cocquyt C., Plisnier P., Descy J., Kimirei I., Sinyinza D. and André L. (2005) Silicon isotopic fractionation in Lake Tanganyika and its main tributaries. *Journal of Great Lakes Research* **31**, 509-519.
- Allenby R. J. (1954) Determination of the isotopic ratios of silicon in rocks. *Geochimica et Cosmochimica Acta* **5**, 40-48.
- Amoruso S., Bruzzese R., Wang X., Nedialkov N. N. and Atanasov P. A. (2007) An analysis of the dependence on photon energy of the process of nanoparticle generation by femtosecond laser ablation in a vacuum. *Nanotechnology* **18**, doi:10.1088/0957-4484/18/14/145612.
- Anbar A. D. (2004) Iron stable isotopes: beyond biosignatures. *Earth and Planetary Science Letters* **217**, 223-236.
- Anbar A. D. and Knoll A. H. (2002) Proterozoic ocean chemistry and evolution: A bioinorganic bridge? *Science* **297**, 1137-1142.
- Anbar A. D., Jarzecki A. A. and Spiro T. G. (2005) Theoretical investigation of iron isotope fractionation between $\text{Fe}(\text{H}_2\text{O})_6^{3+}$ and $\text{Fe}(\text{H}_2\text{O})_6^{2+}$: Implications for iron stable isotope geochemistry. *Geochimica et Cosmochimica Acta* **69**, 825-837.
- Anbar A. and Rouxel O. (2007) Metal stable isotopes in paleoceanography. *Annual Review of Earth and Planetary Sciences* **35**, 717-746.
- André L., Cardinal D., Alleman L. Y. and Moorbath S. (2006) Silicon isotopes in ~3.8 Ga West Greenland rocks as clues to the Eoarchean supracrustal Si cycle. *Earth and Planetary Science Letters* **245**, 162-173.

-
- Archer C. and Vance D. (2006) Coupled Fe and S isotope evidence for Archean microbial Fe(III) and sulfate reduction. *Geology* **34**, 153-156.
- Arrowsmith P. and Hughes S. K. (1988) Entrainment and transport of laser ablated plumes for subsequent elemental analysis. *Applied Spectroscopy* **42**, 1231-1239.
- Basile-Doelsch I. (2006) Si stable isotopes in the Earth's surface: A review. *Journal of Geochemical Exploration* **88**, 252-256.
- Basile-Doelsch I., Meunier J. D. and Parron C. (2005) Another continental pool in the terrestrial silicon cycle. *Nature* **433**, 399-402.
- Bau M. and Dulski P. (1992) Small-scale variations of the rare-earth element distribution in Precambrian iron-formations. *European Journal of Mineralogy* **4**, 1429-1433.
- Bau M. and Dulski P. (1996) Distribution of yttrium and rare-earth elements in the Penge and Kuruman iron-formations, Transvaal Supergroup, South Africa. *Precambrian Research* **79**, 37-55.
- Bau M. and Möller P. (1993) Rare earth element systematics of the chemically precipitated component in early Precambrian iron formations and the evolution of the terrestrial atmosphere-hydrosphere-lithosphere system. *Geochimica et Cosmochimica Acta* **57**, 2239-2249.
- Bau M., Hohndorf A., Dulski P. and Beukes N. J. (1997) Sources of Precambrian rare-earth elements and iron in Paleoproterozoic iron-formations from the Transvaal Supergroup, South Africa - evidence from neodymium isotopes. *Journal of Geology* **105**, 121-129.
- Baur M. E., Hayes J. M., Studley S. A. and Walter M. R. (1985) Millimeter-scale variations of stable isotope abundances in carbonates from Banded Iron-Formations in the Hamersley Group of Western Australia. *Economic Geology* **80**, 270-282.
- Beard B. L. and Johnson C. M. (2004) Fe isotope variations in the modern and ancient earth and other planetary bodies. In *Geochemistry of non-traditional stable isotopes* (eds. C. M. Johnson, B. L. Beard and F. Albarede). Reviews in Mineralogy and Geochemistry, Mineralogical Society America, Washington. pp. 319-357.
- Beard B. L., Johnson C. M., Von Damm K. L. and Poulson R. L. (2003) Iron isotope constraints on Fe cycling and mass balance in oxygenated Earth oceans. *Geology* **31**, 629-632.
- Beard B., Johnson C., Skulan J., Nealson K., Cox L. and Sun H. (2003) Application of Fe isotopes to tracing the geochemical and biological cycling of Fe. *Chemical Geology* **195**, 87-117.
- Becker R. H. and Clayton R. N. (1972) Carbon isotopic evidence for origin of banded iron-formation in Western Australia. *Geochimica et Cosmochimica Acta* **36**, 577-595.
- Becker R. H. and Clayton R. N. (1976) Oxygen isotope study of a Precambrian banded iron-formation, Hamersley Range, Western-Australia. *Geochimica et Cosmochimica Acta* **40**, 1153-1165.
-

-
- Bekker A., Holland H. D., Wang P. L., Rumble D., Stein H. J., Hannah J. L., Coetzee L. L. and Beukes N. J. (2004) Dating the rise of atmospheric oxygen. *Nature* **427**, 117-120.
- Bergquist B. A. and Boyle E. A. (2006) Iron isotopes in the Amazon River system: Weathering and transport signatures. *Earth and Planetary Science Letters* **248**, 39-53.
- Berner R. A. (1997) Paleoclimate - The rise of plants and their effect on weathering and atmospheric CO₂. *Science* **276**, 544-546.
- Berner R. A. (1980) Early diagenesis-A theoretical approach. Princeton University Press, Princeton, New Jersey.
- Beucher C. P., Brzezinski M. A. and Jones J. L. (2008) Sources and biological fractionation of Silicon isotopes in the Eastern Equatorial Pacific. *Geochimica et Cosmochimica Acta* **72**, 3063-3292.
- Beukes N. J. (1980) Lithofacies and stratigraphy of the Kuruman and Griquatown Iron-formations, northern Cape Province, South Africa. *Transactions, Geological Society of South Africa* **83**, 69-86.
- Beukes N. J. and Klein C. (1990) Geochemistry and sedimentology of a facies transition - from microbanded to granular iron-formation - in the Early Proterozoic Transvaal Supergroup, South Africa. *Precambrian Research* **47**, 99-139.
- Beukes N. J., Klein C., Kaufman A. J. and Hayes J. M. (1990) Carbonate petrography, kerogen distribution, and carbon and oxygen isotope variations in an early Proterozoic transition from limestone to iron-formation deposition, Transvaal Supergroup, South Africa. *Economic Geology* **85**, 663-690.
- Beukes N. and Gutzmer J. (2008) Origin and Paleoenvironmental Significance of Major Iron Formations at the Archean-Paleoproterozoic Boundary. In *Banded Iron Formation-Related High-Grade Iron Ore* (eds. S. Hagemann, C. Rosière, J. Gutzmer and N. J. Beukes). Reviews in Economic Geology, Automated Graphic Systems. pp. 5-47.
- Bian Q. Z., Garcia C. C., Koch J. and Niemax K. (2006) Non-matrix matched calibration of major and minor concentrations of Zn and Cu in brass, aluminium and silicate glass using NIR femtosecond laser ablation inductively coupled plasma mass spectrometry. *Journal of Analytical Atomic Spectrometry* **21**, 187-191.
- Bian Q. Z., Koch J., Lindner H., Berndt H., Hergenröder R. and Niemax K. (2005) Non-matrix matched calibration using near-IR femtosecond laser ablation inductively coupled plasma optical emission spectrometry. *Journal of Analytical Atomic Spectrometry* **20**, 736-740.
- Bigeleisen J. (1965) Chemistry of isotopes. *Science* **147**, 463-471.
- Blake T. S. and Barley M. E. (1992) Tectonic evolution of the late Archaean to early Proterozoic Mount Bruce Megasequence set, Western Australia. *Tectonics* **11**, 1415-1425.
- Blankenship, R E, Hartman, H (1998) The origin and evolution of oxygenic photosynthesis. *Trends in Biochemical Sciences* **23**, 94-97.
-

-
- Bleiner, D. and Grasser, P. (2004) Structural features of laser ablation particulate from Si target, as revealed by focused ion beam technology. *Applied Physics A - Materials Science and Processing* **79**, 1019-1022.
- Bouilly D., Perez D. and Lewis L. J. (2007) Damage in materials following ablation by ultrashort laser pulses: A molecular-dynamics study. *Physical Review B - Condensed Matter and Material Physics* **75**, art. no. 075304.
- Brailovsky A. B., Gapanov S. V. and Luchin V. I. (1995) Mechanisms of melt droplets and solid-particle ejection from a target surface by pulsed laser action. *Applied Physics A - Materials Science & Processing* **61**, 81-86.
- Brantley S., Liermann L., Guynn R., Anbar A., Icopini G. and Barling J. (2004) Fe isotopic fractionation during mineral dissolution with and without bacteria. *Geochimica et Cosmochimica Acta* **68**, 3189-3204.
- Brocks J. J., Logan G. A., Buick R. and Summons R. E. (1999) Archean molecular fossils and the early rise of eukaryotes. *Science* **285**, 1033-1036.
- Bruland K. W., Orians K. J. and Cowen J. P. (1994) Reactive trace metals in the stratified central North Pacific. *Geochimica et Cosmochimica Acta* **58**, 3171-3182.
- Brzezinski M. A., Jones J. L., Bidle K. D. and Azam F. (2003) The balance between silica production and silica dissolution in the sea: Insights from Monterey Bay, California, applied to the global data set. *Limnology and Oceanography* **48**, 1846-1854.
- Bullen T. D., White A. F., Childs C. W., Vivit D. V. and Schulz M. S. (2001) Demonstration of significant abiotic iron isotope fractionation in nature. *Geology* **29**, 699-702.
- Bäuerle D. (2000) Laser processing and chemistry. Berlin, Heidelberg, New York: Springer. pp. 605-610.
- Cairns-Smith A. G. (1978) Precambrian solution photochemistry, inverse segregation, and banded-iron formations. *Nature* **276**, 807-808.
- Cameron E. M. (1982) Sulfate and sulfate reduction in early Precambrian oceans. *Nature* **296**, 145-148.
- Canfield D. E. (1998) A new model for Proterozoic ocean chemistry. *Nature* **396**, 450-453.
- Canfield D. E. (2005) The early history of atmospheric oxygen: Homage to Robert M. Garrels. *Annual Review of Earth and Planetary Sciences* **33**, 1-36.
- Canfield D. E., Rosing M. T. and Bjerrum C. (2006) Early anaerobic metabolisms. *Philosophical Transactions of The Royal Society B - Biological Systems* **1474**, 1819-1834.
- Canfield, D. E., Habicht, K. S. and Thamdrup, B. (2000) The Archean sulfur cycle and the early history of atmospheric oxygen. *Science* **288**, 658-661.
-

-
- Cardinal D., Alleman L. Y., Dehairs F., Savoye N., Trull T. W. and André L. (2005) Relevance of silicon isotopes to Si-nutrient utilization and Si-source assessment in Antarctic waters. *Global Biogeochemical Cycles* **19**, 1-13.
- Cardinal D., Alleman L., de Jong J., Ziegler K. and Andre L. (2003) Isotopic composition of silicon measured by multicollector plasma source mass spectrometry in dry plasma mode. *Journal of Analytical Atomic Spectrometry* **18**, 213-218.
- Cardinal D., Savoye N., Trull T. W., Dehairs F., Kopczynska E. E., Fripiat F., Tison J. L. and André L. (2007) Silicon isotopes in spring Southern Ocean diatoms: Large zonal changes despite homogeneity among size fractions. *Marine Chemistry* **106**, 46-62.
- Chacko T., Cole D. R. and Horita J. (2001) Equilibrium oxygen, hydrogen and carbon isotope fractionation factors applicable to geologic systems. In *Stable Isotope Geochemistry, Reviews in Mineralogy and Geochemistry* (eds. J. W. Valley and D. Cole). Mineralogical Society America, Washington. pp. 1-83.
- Chang S. B. R., Stolz J. F., Kirschvink J. L. and Awramik S. M. (1989) Biogenic magnetite in stromatolites. 2. Occurrence in ancient sedimentary environments. *Precambrian Research* **43**, 305-315.
- Cheney E. S. (1996) Sequence stratigraphy and plate tectonic significance of the Transvaal succession of southern Africa and its equivalent in Western Australia. *Precambrian Research* **79**, 3-24.
- Cheng C. and Xu X. (2005) Mechanisms of decomposition of metal during femtosecond laser ablation. *Physical Review B - Condensed Matter and Materials Physics* **72**, 1-15.
- Chmeleff J., Horn I., Steinhoefel G. and von Blanckenburg F. (2008) In situ determination of precise stable Si isotope ratios by UV-femtosecond laser ablation high-resolution multi-collector ICP-MS. *Chemical Geology* **249**, 155-166.
- Chu, N. C., Johnson, C. M., Beard, B. L., German, C. R., Nesbitt, R. W., Frank, M., Bohn, M., Kubik, P. W., Usui, A., Graham, I. (2006) Evidence for hydrothermal venting in Fe isotope compositions of the deep Pacific Ocean through time. *Earth and Planetary Science Letters* **245**, 202-217.
- Clout J. M. F. and Simonson B. M. (2005) Precambrian iron formation and iron formation-hosted iron ore deposits. *Economic Geology* , 643-679.
- Costa F. and Chakraborty S. (2008) The effect of water on Si and O diffusion rates in olivine and implications for transport properties and processes in the upper mantle. *Physics of the Earth and Planetary Interior* **166**, 11-29.
- Croal L. R., Johnson C. M., Beard B. L. and Newman D. K. (2004) Iron isotope fractionation by Fe(II)-oxidizing photoautotrophic bacteria. *Geochimica et Cosmochimica Acta* **68**, 1227-1242.
- Cromwell E. F. and Arrowsmith P. (1995) Semiquantitative analysis with laser ablation inductively coupled plasma mass spectrometry. *Analytical Chemistry* **67**, 131-138.
-

-
- Crosby H. A., Johnson C. M., Roden E. E. and Beard B. L. (2005) Coupled Fe(II)-Fe(III) electron and atom exchange as a mechanism for Fe isotope fractionation during dissimilatory iron oxide reduction. *Environmental Science and Technology* **39**, 6698-6704.
- Crosby H. A., Roden E. E., Johnson C. M. and Beard B. L. (2007) The mechanisms of iron isotope fractionation produced during dissimilatory Fe(III) reduction by *Shewanella putrefaciens* and *Geobacter sulfurreducens*. *Geobiology* **5**, 169-189.
- Dauphas N. and Rouxel O. (2006) Mass spectrometry and natural variations of iron isotopes. *Mass Spectrometry Reviews* **25**, 515-550.
- Dauphas N., Cates N. L., Mojzsis S. J. and Busigny V. (2007) Identification of chemical sedimentary protoliths using iron isotopes in the > 3750 Ma Nuvvuagittuq supracrustal belt, Canada. *Earth and Planetary Science Letters* **254**, 358-376.
- Dauphas N., van Zuilen M., Wadhwa M., Davis A. M., Marty B. and Janney P. E. (2004) Clues from Fe isotope variations on the origin of early Archean BIFs from Greenland. *Science* **306**, 2077-2080.
- De Kock M. O., Evans D. A. D., Gutzmer, J, Beukes, N J and Dorland H. C. (2008) Origin and Timing of Banded Iron Formation-Hosted High-Grade Hard Hematite Deposits—A Paleomagnetic Approach. In *Banded Iron Formation-Related High-Grade Iron Ore* (eds. S. Hagemann, C. Rosière, J. Gutzmer and N. J. Beukes). Reviews in Economic Geology, Automated Graphic Systems. pp. 48-71.
- De Laeter J. R., Böhlke J. K., De Bièvre P., Hidaka H., Peiser H. S., Rosman K. J. R., Taylor P. D. P. (2003) Atomic weight of the elements: review 2000. *International Union of Pure and Applied Chemistry* **75**, 683-800.
- De La Rocha C. (2002) Measurement of silicon stable isotope natural abundances via multicollector inductively coupled plasma mass spectrometry (MC-ICP-MS). *Geochemistry Geophysics Geosystems* **3**, 1-8.
- De La Rocha C. L. and Bickle M. J. (2005) Sensitivity of silicon isotopes to whole-ocean changes in the silica cycle. *Marine Geology* **217**, 267-282.
- De La Rocha C. L., Brzezinski M. A. and DeNiro M. J. (1997) Fractionation of silicon isotopes by marine diatoms during biogenic silica formation. *Geochimica et Cosmochimica Acta* **61**, 5051-5056.
- De La Rocha C. L., Brzezinski M. A. and Deniro M. J. (2000) A first look at the distribution of the stable isotopes of silicon in natural waters. *Geochimica et Cosmochimica Acta* **64**, 2467-2477.
- De La Rocha C. L., Brzezinski M. A., DeNiro M. J. and Shemesh A. (1998) Silicon-isotope composition of diatoms as an indicator of past oceanic change. *Nature* **395**, 680-683.
- De la Rocha C. L. (2003) Silicon isotope fractionation by marine sponges and the reconstruction of the silicon isotope composition of ancient deep water. *Geology* **31**, 423-426.
-

-
- Ding T. P., Ma G. R., Shui M. X., Wan D. F. and Li R. H. (2005) Silicon isotope study on rice plants from the Zhejiang province, China. *Chemical Geology* **218**, 41-50.
- Ding T. P., Ma G. R., Shui M. X., Wan D. F. and Li R. H. (2005) Silicon isotope study on rice plants from the Zhejiang province, China. *Chemical Geology* **218**, 41-50.
- Ding T. P., Zhou J. X., Wan D. F., Chen Z. Y., Wang C. Y. and Zhang F. (2008) Silicon isotope fractionation in bamboo and its significance to the biogeochemical cycle of silicon. *Geochimica et Cosmochimica Acta* **72**, 1381-1395.
- Ding T., Jiange S., Wan D., Li Y., Li J., Song H., Liu Z. and Yao X. (1996) Silicon Isotope Geochemistry. Geological Publishing House, Beijing, China.
- Ding T., Tian S. and Gao J. (2007) Silicon isotope compositions of the underground water, limestone and soil from Karst caves in Guilin City, Guangxi, China. *Geochimica et Cosmochimica Acta* **71**, A225.
- Ding T., Wan D., Wang C. and Zhang F. (2004) Silicon isotope compositions of dissolved silicon and suspended matter in the Yangtze River, China. *Geochimica et Cosmochimica Acta* **68**, 205-216.
- Dixon P. R., Perrin R. E., Rokop D. J., Maeck R., Janecky D. R. and Banar J. P. (1993) Measurements of iron isotopes (Fe-54, Fe-56, Fe-57, and Fe-58) in submicrogram quantities of iron. *Analytical Chemistry* **65**, 2125-2130 .
- Douthitt C. B. (1982) The geochemistry of stable isotopes of silicon. *Geochimica et Cosmochimica* **46**, 1449-1458.
- Drever J. I. (1974) Geochemical model for origin of Precambrian Iron Formations. *Geological Society of American Bulletin* **85**, 1099-1106.
- Eggins S. M., Kinsley L. P. and Shelley J. M. G. (1998) Deposition and element fractionation processes during atmospheric pressure laser sampling for analysis by ICP-MS. *Applied Surface Science* **129**, 278-286.
- Ehrenreich A. and Widdel F. (1994) Anaerobic oxidation of ferrous iron by purple bacteria, a new-type of phototrophic metabolism. *Applied and Environmental Microbiology* **60**, 4517-4526.
- Elderfield H. and Schultz A. (1996) Mid-ocean ridge hydrothermal fluxes and the chemical composition of the ocean. *Annual Review of Earth and Planetary Science* **24**, 191-224.
- Engrand C., McKeegan K. D., Leshin L. A., Herzog G. F., Schnabel C., Nyquist L. E. and Brownlee D. E. (2005) Isotopic compositions of oxygen, iron, chromium, and nickel in cosmic spherules: Toward a better comprehension of atmospheric entry heating effects. *Geochimica et Cosmochimica Acta* **69**, 5365-5385.
- Engström E., Rodushkin I., Baxter D. C. and Öhlander B. (2006) Chromatographic purification for the determination of dissolved silicon isotopic compositions in natural waters by high-resolution multicollector inductively coupled plasma mass spectrometry. *Analytical Chemistry* **78**, 250-257.
-

-
- Ewers W. E. (1983) Chemical factors in the deposition and diagenesis of banded iron-formation. In *Iron-Formation: Facts and Problems* (eds. A. F. Trendall and R. C. Morris). Elsevier. pp. 491-510.
- Ewers W. E. and Morris R. C. (1981) Studies of the Dales Gorge member of the Brockman iron formation, Western Australia. *Economic Geology* **76**, 1929-1953.
- Fantle M. S. and De Paolo D. J. (2004) Iron isotopic fractionation during continental weathering. *Earth and Planetary Science Letters* **228**, 547-562.
- Farquhar J. and Wing B. A. (2003) Multiple sulfur isotopes and the evolution of the atmosphere. *Earth and Planetary Science Letters* **213**, 1-13.
- Farquhar J., Savarino J., Airieau S. and Thiemens M. H. (2001) Observation of wavelength-sensitive mass-dependent sulfur isotopes effects during SO₂ photolysis: implication for the early Earth atmosphere. *Journal of Geophysical Research-Planets* **106**, 32829-32839.
- Fedo C. M., Whitehouse M. J. and Kamber B. S. (2006) Geological constraints on detecting the earliest life on Earth: A perspective from the Early Archaean (older than 3.7 Gyr) of southwest Greenland. *Philosophical Transactions of the Royal Society B: Biological Sciences* **361**, 851-867.
- Fehr M. A., Andersson P. S., Halenius U. and Morth C. M. (2008) Iron isotope variations in Holocene sediments of the Gotland Deep, Baltic Sea. *Geochimica et Cosmochimica Acta* **72**, 807-826.
- Fernández B., Claverie F., Pécheyran C. and Donard O. F. X. (2007) Direct analysis of solid samples by fs-LA-ICP-MS. *Trends in Analytical Chemistry* **26**, 951-966.
- Figg D. J., Cross J. B. and Brink C. (1998) More investigations into elemental fractionation resulting from laser ablation inductively coupled plasma mass spectrometry on glass samples. *Applied Surface Science* **129**, 287-291.
- Fischer W. W., Schroeder S., Lacassie J. P., Beukes N. J., Goldberg T., Strauss H., Horstmann U. E., Schrag D. P. and Knoll A. H. (in press) Isotopic constraints on the Late Archean carbon cycle from the Transvaal Supergroup along the western margin of the Kaapvaal craton, South Africa. *Precambrian Research*.
- Flisch M. (1982) Potassium argon analysis. In *Numerical dating in stratigraphy* (ed. G. S. Odin). John Wiley, Chichester. pp. 151-158.
- Foster R. P. and Gilligan J. M. (1987) Archean iron-formation and gold mineralization in Zimbabwe. In *Precambrian iron-formation* (eds. P. W. Uitterdijk Appel and G. L. Laberge). Theophrastus Publications, Athen. pp. 635-674.
- Freydier R., Candaudap F., Poitrasson F., Arbouet A., Chatel B. and Dupre B. (2008) Evaluation of infrared femtosecond laser ablation for the analysis of geomaterials by ICP-MS. *Journal of Analytical Atomic Spectrometry* **23**, 702-710.
-

-
- Fripiat F., Cardinal D., Tison J. L., Worby A. and André L. (2007) Diatom-induced silicon isotopic fractionation in Antarctic sea ice. *Journal of Geophysical Research - Biogeosciences* **112**, G02001 .
- Frost C. D., von Blanckenburg F., Schoenberg R., Frost B. R. and Swapp S. M. (2007) Preservation of Fe isotope heterogeneities during diagenesis and metamorphism of banded iron formation. *Contribution to Mineralogy and Petrology* **153**, 211-235.
- Galer S. J. G. and O'Nions R. K. (1989) Chemical and Isotopic Studies of Ultramafic Inclusions from the San Carlos Volcanic Field, Arizona: A Bearing on their Petrogenesis. *Journal of Petrology* **30**, 1033-1064.
- Gao S., Liu X. M., Yuan H. L., Hattendorf B., Guenther D., Chen L. and Hu S. H. (2002) Determination of forty two major and trace elements in USGS and NIST SRM glasses by laser ablation-inductively coupled plasma- mass spectrometry. *Geostandards Newsletter- the Journal of Geostandards and Geoanalysis* **26**, 181-196.
- Garcia C. C., Wälle M., Lindner H., Koch J., Niemax K. and Günther D (2008a) Femtosecond laser ablation inductively coupled plasma mass spectrometry: Transport efficiencies of aerosols released under argon atmosphere and the importance of the focus position . *Spectrochimica Acta Part B* **63**, 271–276.
- Garcia C. C., Lindner H., von Bohlen A., Vadla C. and Niemax K. (2008b) Elemental fractionation and stoichiometric sampling in femtosecond laser ablation. *Journal of Analytical Atomic Spectrometry* **23**, 470-478.
- Garrels R. M. (1987) A model for the deposition of the microbanded Precambrian Iron Formations. *American Journal of Science* **287**, 81-106.
- Georg R. B., Halliday A. N., Schauble E. A. and Reynolds B. C. (2007) Silicon in the Earth's core. *Nature* **447**, 1102-1106.
- Georg R. B., Reynolds B. C., Frank M. and Halliday A. N. (2006) Mechanisms controlling the silicon isotopic compositions of river waters. *Earth and Planetary Science Letters* **249**, 290-306.
- Georg R. B., Reynolds B. C., West A. J., Burton K. W. and Halliday A. N. (2007) Silicon isotope variations accompanying basalt weathering in Iceland. *Earth and Planetary Science Letters* **261**, 476-490.
- Georg R., Reynolds B., Frank M. and Halliday A. (2006) New sample preparation techniques for the determination of Si isotopic compositions using MC-ICPMS. *Chemical Geology* **235**, 95-104.
- González J. J., Oropeza D., Mao X. and Russo R. E. (2008) Assessment of the precision and accuracy of thorium (²³²Th) and uranium (²³⁸U) measured by quadrupole based inductively coupled plasma-mass spectrometry using liquid nebulization, nanosecond and femtosecond laser ablation. *Journal of Analytical Atomic Spectrometry* **23**, 229–234.
-

-
- González, J., Dundas, S.H., Liu, C.Y., Mao, X. and Russo, R.E. (2006) UV-femtosecond and nanosecond laser ablation-ICP-MS: internal and external repeatability. *Journal of Analytical Atomic Spectrometry* **21**, 778-784.
- González J., Liu C., Mao X. and Russo R. E. (2004) UV-femtosecond laser ablation-ICP-MS for analysis of alloy samples. *Journal of Analytical Atomic Spectrometry* **19**, 1165-1168.
- Goodwin A. M., Monster J. and Thode H. G. (1976) Carbon and Sulfur isotope abundances in Archean iron-formations and early Precambrian Life. *Economic Geology* **71**, 870-891.
- Graham S., Pearson N., Jackson S., Griffin W. and O'Reilly S. Y. (2004) Tracing Cu and Fe from source to porphyry: in situ determination of Cu and Fe isotope ratios in sulfides from the Grasberg Cu-Au deposit. *Chemical Geology* **207**, 147-169.
- Grassineau N. V., Niset E. G., Bickle M. J., Fowler C. M., Lowry D., Matthey D. P., Abell P. and Martin A. (2001) Antiquity of the biological sulphur cycle: evidence from sulphur and carbon isotopes in 2700 million-year-old rocks of the Belingwe Belt, Zimbabwe. *Proceedings of the Royal Society of London Series B - Biological Sciences* **268**, 113-119.
- Gray A. L. (1985) Solid sample introduction for inductively coupled plasma source-mass spectrometer. *Analyst* **110**, 551-556.
- Gross G. A. (1972) Primary features in cherty iron-formations. *Sedimentary Geology* **7**, 241-261.
- Gross G. A. (1973) The depositional environment of the principal types of Precambrian iron-formations. In *Genesis of Precambrian Iron and Manganese Deposits* (eds.). UNESCO, Paris, Earth Sciences 9. pp. 15-21.
- Guelke M. and von Blanckenburg F. (2007) Fractionation of stable iron isotopes in higher plants. *Environmental Science and Technology* **41**, 1896-1901.
- Guillong M. and Guenther D. (2002) Effect of particle size distribution on ICP-induced elemental fractionation in laser ablation-inductively coupled plasma-mass spectrometry. *Journal of Analytical Atomic Spectrometry* **17**, 831-837.
- Guillong M., Horn I. and Guenther D. (2003) A comparison of 266 nm, 213 nm and 193 nm produced from a single solid state Nd : YAG laser for laser ablation ICP-MS. *Journal of Analytical Atomic Spectrometry* **18**, 1224-1230.
- Guillong M., Kuhn H. R. and Guenther D. (2003) Application of a particle separation device to reduce inductively coupled plasma-enhanced elemental fractionation in laser ablation-inductively coupled plasma-mass spectrometry. *Spectrochimica Acta Part B - Atomic Spectroscopy* **58**, 211-220.
- Gutzmer J., Beukes N. J., de Kock M. O. and Netshiozwi S. T. (2005) Origin of high-grade iron ores at the Thabazimbi deposit, South Africa. *Iron Ore Conference, Freemantle, 19-21 September 2005, Proceedings* , 57-65.
-

-
- Hamade T., Konhauser K., Raiswell R., Goldsmith S. and Morris R. (2003) Using Ge/Si ratios to decouple iron and silica fluxes in Precambrian banded iron formations. *Geology* **31**, 35-38.
- Han T. (1978) Microstructures of magnetite as guide to its origin in some Precambrian iron formations. *Fortschritte der Mineralogie* **56**, 105-142.
- Hergenröder R. (2006a) Laser-generated aerosols in laser ablation for inductively coupled plasma spectrometry. *Spectrochimica Acta B - Atomic Spectroscopy* **61**, 284-300.
- Hergenröder R. (2006b) A model for the generation of small particles in laser ablation ICP-MS. *Journal of Analytical Atomic Spectrometry* **21**, 1026.
- Hergenröder R. (2006d) A model of non-congruent laser ablation as a source of fractionation effects in LA-ICP-MS. *Journal of Analytical Atomic Spectrometry* **21**, 505-516.
- Hergenröder R. (2006c) Hydrodynamic sputtering as a possible source for fractionation in LA-ICP-MS. *Journal of Analytical Atomic Spectrometry* **21**, 517-524.
- Hergenröder R., Samek O. and Hommes V. (2006) Femtosecond laser ablation elemental mass spectrometry. *Mass Spectrometry Reviews* **25**, 551-572.
- Hill P. S. and Schauble E. A. (2008) Modeling the effects of bond environment on equilibrium iron isotope fractionation in ferric aquo-chloro complexes. *Geochimica et Cosmochimica Acta* **72**, 1939-1958.
- Hirata T. (2003) Chemically assisted laser ablation ICP mass spectrometry. *Analytical Chemistry* **75**, 228-233.
- Hirata T. and Kon Y. (2008) Evaluation of the analytical capability of NIR femtosecond laser ablation-inductively coupled plasma mass spectrometry. *Analytical Sciences* **24**, 345-353.
- Hirata T. and Nesbitt R. (1995) U-Pb isotope geochronology of zircon: Evaluation of the laser probe inductively coupled plasma mass spectrometry technique. *Geochimica et Cosmochimica Acta* **59**, 2491-2500.
- Hodson M. J., Parker A. G., Leng M. J. and Sloane H. J. (2008) Silicon, oxygen and carbon isotope composition of wheat (*Triticum aestivum* L.) phytoliths: implications for palaeoecology and archaeology. *Journal of Quaternary Science* **23**, 331-339.
- Hoefs J. (2004) *Stable Isotope Geochemistry*. Springer.
- Holland H. D. (1973) Ocean - possible source of iron in iron-formations. *Economic Geology* **68**, 1169-1172.
- Holland H. D. (1984) *The Chemical Evolution of the Atmosphere and Oceans*. Princeton, NJ, Princeton University Press.
- Holland H. D. (2006) The oxygenation of the atmosphere and oceans. *Philosophical Transactions of the Royal Society B - Biological Science* **361**, 903-915.
-

-
- Holland H. D. (2004) The geological history of seawater. In *Treatise on Geochemistry* (eds. H. D. Holland and K. K. Turekian). Oxford, Elsevier. pp. 583-625.
- Holzheid A. and Grove T. L. (2002) Sulfur saturation limits in silicate melts and their implications for core formation scenarios for terrestrial planets. *American Mineralogist* **87**, 227-237.
- Horn I. (2008) Comparison of femtosecond and nanosecond laser interactions with geological matrices and their influence on accuracy and precision of LA-ICP-MS data. In *Laser Ablation-ICP-MS in the Earth Sciences* (ed. P. J. Sylvester). Mineralogical Association of Canada Short Course Series. pp. 53-65.
- Horn I. and Guenther D. (2003) The influence of ablation carrier gasses Ar, He and Ne on the particle size distribution and transport efficiencies of laser ablation-induced aerosols: implications for LA-ICP-MS. *Applied Surface Science* **207**, 144-157.
- Horn I. and von Blanckenburg F. (2007) Investigation on elemental and isotopic fractionation during 196 nm femtosecond laser ablation multiple collector inductively coupled plasma mass spectrometry. *Spectrochimica Acta - Part B Atomic Spectroscopy* **62**, 410-422.
- Horn I., Guenther D. and Guillong M. (2003) Evaluation and design of a solid-state 193 nm OPO-Nd : YAG laser ablation system. *Spectrochimica Acta Part B-Atomic Spectroscopy* **58**, 1837-1846.
- Horn I., Guillong M. and Guenther D. (2001) Wavelength dependant ablation rates for metals and silicate glasses using homogenized laser beam profiles - implications for LA-ICP-MS. *Applied Surface Science* **182**, 91-102.
- Horn I., Rudnick R. L. and McDonough W. F. (2000) Precise elemental and isotope ratio determination by simultaneous solution nebulization and laser ablation-ICP-MS: application to U-Pb geochronology (vol 164, pg 283, 2000). *Chemical Geology* **167**, 405-425.
- Horn I., von Blanckenburg F., Schoenberg R., Steinhoefel G. and Markl G. (2006) In situ iron isotope ratio determination using UV-femtosecond laser ablation with application to hydrothermal ore formation processes. *Geochimica et Cosmochimica Acta* **70**, 3677-3688.
- Horstwood M. S. A., Foster G. L., Parrish R. R., Noble S. R. and Nowell G. M. (2003) Common-Pb corrected in situ U-Pb accessory mineral geochronology by LA-MC-ICP-MS. *Journal of Analytical Atomic Spectrometry* **18**, 837-846.
- Hua X., Huss G. R., Tachibana S. and Sharp T. G. (2005) Oxygen, silicon, and Mn-Cr isotopes of fayalite in the Kaba oxidized CV3 chondrite: Constraints for its formation history. *Geochimica et Cosmochimica Acta* **69**, 1333-1348.
- Icopini G., Anbar A., Ruebush S., Tien M. and Brantley S. (2004) Iron isotope fractionation during microbial reduction of iron: The importance of adsorption. *Geology* **32**, 205-208.
- Ikehata K., Notsu K. and Hirata T. (2008) In situ determination of Cu isotope ratios in copper-rich materials by NIR femtosecond LA-MC-ICP-MS. *Journal of Analytical Atomic Spectrometry* **23**, 1003-1008.
-

-
- Isley A. E. (1995) Hydrothermal plumes and the delivery of iron to banded iron formation. *Journal of Geology* **103**, 169-185.
- Isley A. E. and Abbott D. H. (1999) Plume-related mafic volcanism and the deposition of banded iron formation. *Journal of Geophysical Research B: Solid Earth* **104**, 15461-15477.
- Jackson S. E. and Guenther D. (2003) The nature and sources of laser induced isotopic fractionation in laser ablation-multicollector-inductively coupled plasma- mass spectrometry. *Journal of Analytical Atomic Spectrometry* **18**, 205-212.
- Jackson S. E., Longerich H. P., Dunning G. R. and Freyer B. J. (1992) The application of laser-ablation microprobe; inductively coupled plasma-mass spectrometry (LA-ICP-MS) to in situ trace-element determinations in minerals. *The Canadian Mineralogist* **30**, 1049-1064.
- Jackson S. E., Pearson N. J., Griffin W. L. and Belousova E. A. (2004) The application of laser ablation-inductively coupled plasma-mass spectrometry to in situ U-Pb zircon geochronology. *Chemical Geology* **211**, 47-69.
- Jacobsen S. B. and Pimentel-Klose M. R. (1988) A Nd isotopic study of the Hamersley and Michipicoten banded iron formations: the source of REE and Fe in Archean oceans. *Earth and Planetary Science Letters* **87**, 29-44.
- Jacobsen S. B. and Pimentel-Klose M. R. (1988) Nd isotopic variations in Precambrian banded iron formations. *Geophysical Research Letters* **15**, 393-396.
- Jarzecki A., Anbar A. and Spiro T. (2004) DFT analysis of $\text{Fe}(\text{H}_2\text{O})_6^{3+}$ and $\text{Fe}(\text{H}_2\text{O})_6^{2+}$ structure and vibrations; implications for isotope fractionation. *Journal of Physical Chemistry A* **108**, 2726-2732.
- Jeong S. H., Borisov O. V., Yoo J. H., Mao X. L. and Russo A. E. (1999) Effects of particle size distribution on inductively coupled plasma mass spectrometry signal intensity during laser ablation of glass samples. *Analytical Chemistry* **71**, 5123-5130.
- Jiang S. Y., Ding T. P., Wan D. F. and Li Y. H. (1993) Silicon isotopic compositions of Archean banded Si-Fe Formation (BIF) in the Gongchangling Ore Deposit, Liaoning-Province, China. *Science in China Series B - Chemistry* **36**, 482-489.
- Jochum, K.P. and Willbold, M. (2006) Reference materials in geoanalytical research. Review for 2004 and 2005. *Geostandards and Geoanalytical Research* **30**, 143-156.
- Jochum, K.P., Stoll, B., Herwig, K. and Willbold, M. (2007) Validation of LA ICP MS trace element analysis of geological glasses using a new solid state 193 nm Nd:YAG laser and matrix matched calibration. *Journal of Analytical Atomic Spectrometry* **22**, 112-121.
- Johnson C. M. and Beard B. L. (2006) Fe isotopes: An emerging technique for understanding modern and ancient biogeochemical cycles. *GSA Today* **16**, 4-10.
-

-
- Johnson C. M., Beard B. L. and Roden E. E. (2008b) The iron isotope fingerprints of redox and biogeochemical cycling in the modern and ancient Earth. *Annual Review of Earth and Planetary Sciences* **36**, 457-493.
- Johnson C. M., Beard B. L., Beukes N. J., Klein C. and O'Leary J. M. (2003) Ancient geochemical cycling in the Earth as inferred from Fe isotope studies of banded iron formations from the Transvaal Craton. *Contributions to Mineralogy and Petrology* **144**, 523-547.
- Johnson C. M., Beard B. L., Klein C., Beukes N. J. and Roden E. E. (2008a) Iron isotopes constrain biologic and abiologic processes in banded iron formation genesis. *Geochimica et Cosmochimica Acta* **72**, 151-169.
- Johnson C. M., Roden E. E., Welch S. A. and Beard B. L. (2005) Experimental constraints on Fe isotope fractionation during magnetite and Fe carbonate formation coupled to dissimilatory hydrous ferric oxide reduction. *Geochimica et Cosmochimica Acta* **69**, 963-993.
- Johnson C. M., Skulan J. L., Beard B. L., Sun H., Neelson K. H. and Braterman P. S. (2002) Isotopic fractionation between Fe(III) and Fe(II) in aqueous solutions. *Earth and Planetary Science Letters* **195**, 141-153.
- Kappler A., Pasquero C., Konhauser K. O. and Newman D. K. (2005) Deposition of banded iron formations by anoxygenic phototrophic Fe(II)-oxidizing bacteria. *Geology* **33**, 865-868.
- Karlin R., Lyle M. and Heath G. R. (1987) Authigenic magnetite formation in suboxic marine sediments. *Nature* **326**, 490-493.
- Kaufman A. J. (1996) Geochemical and mineralogic effects of contact metamorphism on banded iron-formation: An example from the Transvaal Basin, South Africa. *Precambrian Research* **79**, 171-194.
- Kaufman A. J., Hayes J. M. and Klein C. (1990) Primary and diagenetic controls of isotopic compositions of iron-formation carbonates. *Geochimica et Cosmochimica Acta* **54**, 3461-3473.
- Kaufman A. J., Johnston D. T., Farquhar J., Masterson A. L., Lyons T. W., Bates S., Anbar A. D., Arnold G. L., Garvin J. and Buick R. (2007) Late Archean biospheric oxygenation and atmospheric evolution. *Science* **317**, 1900-1903.
- Klein C. (2005) Some Precambrian banded iron-formations (BIFs) from around the world: Their age, geologic setting, mineralogy, metamorphism, geochemistry, and origin. *American Mineralogist* **90**, 1473-1499.
- Klein C. and Beukes N. J. (1989) Geochemistry and sedimentology of a facies transition from limestone to iron-formation deposition in the early Proterozoic Transvaal Supergroup, South Africa. *Economic Geology* **84**, 1733-1774.
- Klein C. and Beukes N. J. (1993) Sedimentology and geochemistry of the glaciogenic late Proterozoic Rapitan iron-formation in Canada. *Economic Geology* **88**, 542-565.
-

-
- Klein C. and Ladeira E. A. (2004) Geochemistry and mineralogy of neoproterozoic banded iron-formations and some selected, siliceous manganese formations from the Urucum district, Mato Grosso Do Sul, Brazil. *Economic Geology* **99**, 1233-1244.
- Koch J. and Guenther D. (2007) Femtosecond laser ablation inductively coupled plasma mass spectrometry: achievements and remaining problems. *Analytical and Bioanalytical Chemistry* **387**, 149-153.
- Koch J., Feldmann I., Jakubowski N. and Niemax K. (2002) Elemental composition of laser ablation aerosol particles deposited in the transport tube to an ICP. *Spectrochimica Acta Part B - Atomic Spectroscopy* **57**, 975-985.
- Koch J., Lindner H., Von Bohlen A., Hergenröder R. and Niemax K. (2005) Elemental fractionation of dielectric aerosols produced by near-infrared femtosecond laser ablation of silicate glasses. *Journal of Analytical Atomic Spectrometry* **20**, 901-906.
- Koch J., Wälle M., Pisonero J. and Guenther D. (2006) Performance characteristics of ultra-violet femtosecond laser ablation inductively coupled plasma mass spectrometry at similar to 265 and similar to 200 nm. *Journal of Analytical Atomic Spectrometry* **21**, 932-940.
- Koch J., Wälle M., Schlamp S., Rösgen T. and Günther D. (2008) Expansion phenomena of aerosols generated by laser ablation under helium and argon atmosphere. *Spectrochimica Acta Part B* **63**, 37-41.
- Koch J., von Bohlen A., Hergenröder R. and Niemax K. (2004) Particle size distributions and compositions of aerosols produced by near-IR femto- and nanosecond laser ablation of brass. *Journal of Analytical Atomic Spectrometry* **19**, 267-272.
- Konhauser K. O. (1998) Diversity of bacterial iron mineralization. *Earth Science Reviews* **43**, 91-121.
- Konhauser K. O., Amskold L., Lalonde S. V., Posth N. R., Kappler A. and Anbar A. (2007) Decoupling photochemical Fe(II) oxidation from shallow-water BIF deposition. *Earth and Planetary Science Letters* **258**, 87-100.
- Konhauser K. O., Hamade T., Raiswell R., Morris R. C., Ferris F. G., Southam G. and Canfield D. E. (2002) Could bacteria have formed the Precambrian banded iron formations? *Geology* **30**, 1079-1082.
- Konhauser K. O., Newman D. K. and Kappler A. (2005) The potential significance of microbial Fe(III) reduction during deposition of Precambrian banded iron formations. *Geobiology* **3**, 167-177.
- Kozlov B., Saint A. and Skroce A. (2003) Elemental fractionation in the formation of particulates, as observed by simultaneous isotopes measurement using laser ablation ICP-oo-TOFMS. *Journal of Analytical Atomic Spectrometry* **18**, 1069-1075.
-

-
- Košler J., Pedersen R. B., Kruber C. and Sylvester P. J. (2005) Analysis of Fe isotopes in sulfides and iron meteorites by laser ablation high-mass resolution multi-collector ICP mass spectrometry. *Journal of Analytical Atomic Spectrometry* **20**, 192-199.
- Košler J., Tubrett M. N. and Sylvester P. J. (2001) Application of laser ablation ICP-MS to U-Th-Pb dating of monazite. *Geostandards Newsletter* **25**, 375-386.
- Košler J., Wiedenbeck M., Wirth R., Hovorka J., Sylvester P. and Míková J. (2005) Chemical and phase composition of particles produced by laser ablation of silicate glass and zircon - Implications for elemental fractionation during ICP-MS analysis. *Journal of Analytical Atomic Spectrometry* **20**, 402-409.
- Kroslakova I. and Guenther D. (2007) Elemental fractionation in laser ablation-inductively coupled plasma-mass spectrometry: Evidence for mass load induced matrix effects in the ICP during ablation of a silicate glass. *Journal of Analytical Atomic Spectrometry* **22**, 51-62.
- Kuhn H. R. and Guenther D. (2003) Elemental fractionation studies in laser ablation inductively coupled plasma mass spectrometry on laser-induced brass aerosols. *Analytical Chemistry* **75**, 747-753.
- Kuhn H. R. and Guenther D. (2004) Laser ablation-ICP-MS: particle size dependent elemental composition studies on filter-collected and online measured aerosols from glass. *Journal of Analytical Atomic Spectrometry* **19**, 1158-1164.
- Kuhn H. R., Guillong M. and Guenther D. (2004) Size-related vaporisation and ionisation of laser-induced glass particles in the inductively coupled plasma. *Analytical and Bioanalytical Chemistry* **378**, 1069-1074.
- Lanier W. P. (1989) Interstitial and pedoidal microfossils from the 2.0 Ga Gunflint Formation: implication for the paleoecology of the Gunflint stromatolites. *Precambrian Research* **45**, 291-318.
- Levasseur S., Frank M., Hein J. and Halliday A. (2004) The global variation in the iron isotope composition of marine hydrogenetic ferromanganese deposits: implications for seawater chemistry? *Earth and Planetary Science Letters* **224**, 91-105.
- Liu C. Y., Mao X. L., Mao S. S., Greif R. and Russo R. E. (2005) Particle size dependent chemistry from laser ablation of brass. *Analytical Chemistry* **77**, 6687-6691.
- Liu C., Mao X. L., Mao S. S., Zeng X., Greif R. and Russo R. E. (2004) Nanosecond and femtosecond laser ablation of Brass: particulate and ICPMS measurements. *Analytical Chemistry* **76**, 379-383.
- Longerich H. P., Guenther D. and Jackson S. E. (1996) Elemental fractionation in laser ablation inductively coupled plasma mass spectrometry. *Fresenius' Journal of Analytical Chemistry* **355**, 538-542.
- Lorazo P., Lewis L. and Meunier M. (2006) Thermodynamic pathways to melting, ablation, and solidification in absorbing solids under pulsed laser irradiation. *Physical Review B - Condensed Matter and Materials Physics* **73**, 1-22.
-

-
- Lovley D. R. (1991) Dissimilatory Fe(III) and Mn(IV) reduction. *Microbiological Reviews* **55**, 259-287.
- Lovley D. R. (1997) Microbial Fe(III) reduction in subsurface environments. *FEMS Microbiology Reviews* **20**, 305-313.
- Lovley D. R., Stolz J. F., Nord Jr G. L. and Phillips E. J. P. (1987) Anaerobic production of magnetite by a dissimilatory iron-reducing microorganism. *Nature* **330**, 252-254.
- Lu Q. M., Mao S. S., Mao X. L. and Russo R. E. (2002) Delayed phase explosion during high-power nanosecond laser ablation of silicon. *Applied Physics Letters* **80**, 3072-3074.
- Lugaro M., Zinner E., Gallino R. and Amari S. (1999) Si isotopic ratios in mainstream presolar SiC grains revisited. *Astrophysical Journal* **527**, 369-394.
- Luk'yanchuk B. S., Marine W. and Anisimov S. I. (1998) Condensation of vapor and nanoclusters formation within the vapor plume, produced by ns-laser ablation of Si. *Laser Physics* **8**, 291-302.
- Ma J. F. (2003) Functions of Silicon in Higher Plants. In *Silicon Biomineralization* (ed. W. E. G. Müller). Springer, Berlin. pp. 127-160.
- Maliva R. G., Knoll A. H. and Simonson B. M. (2005) Secular change in the Precambrian silica cycle: Insights from chert petrology. *Geological Society of America Bulletin* **117**, 835-845.
- Mandernack, K.W., Bazylinski, D.A., Shanks, W.C. and Bullen, T.D. (1999) Oxygen and iron isotope studies of magnetite produced by magnetotactic bacteria. *Science* **285**, 1892-1896
- Mao X. L. and Russo R. E. (1997) Observation of plasma shielding by measuring transmitted and reflected laser pulse temporal profiles. *Applied Physics A - Material Science and Processing* **64**, 1-6.
- Mao X. L., Chan W. T., Caetano M., Shannon M. A. and Russo R. E. (1996) Preferential vaporization and plasma shielding during nanosecond laser ablation. *Applied Surface Science* **96-8**, 126-130.
- Mao X. L., Ciocan A. C. and Russo R. E. (1998) Preferential vaporization during laser ablation inductively coupled plasma atomic emission spectroscopy. *Applied Spectroscopy* **52**, 913-918.
- Margetic V., Niemax K. and Hergenröder R. (2001) A study of non-linear calibration graphs for brass with femtosecond laser-induced breakdown spectroscopy. *Spectrochimica Acta Part B Atomic Spectroscopy* **56**, 1003-1010.
- Margetic V., Pakulev A., Stockhaus A., Bolshov M., Niemax K. and Hergenröder R. (2000) A comparison of nanosecond and femtosecond laser-induced plasma spectroscopy of brass samples. *Spectrochimica Acta Part B Atomic Spectroscopy* **55**, 1771-1785.
-

-
- Markl G., von Blanckenburg F. and Wagner T. (2005) Iron isotope fractionation during hydrothermal ore deposition and alteration. *Geochimica et Cosmochimica Acta* **70**, 3011-3030.
- Matthews A., Morgans-Bell H., Emmanuel S., Jenkyns H., Erel Y. and Halicz L. (2004) Controls on iron-isotope fractionation in organic-rich sediments (Kimmeridge Clay, Upper Jurassic, southern England). *Geochimica et Cosmochimica Acta* **68**, 3107-3123.
- Matthews A., Zhu X. and O'Nions K. (2001) Kinetic iron stable isotope fractionation between iron (-II) and (-III) complexes in solution. *Earth and Planetary Science Letters* **192**, 81-92.
- Milligan A. J., Varela D. E., Brzezinski M. A. and Morel F. M. M. (2004) Dynamics of silicon metabolism and silicon isotopic discrimination in a marine diatom as a function of pCO₂. *Limnology and Oceanography* **49**, 322-329.
- Mineev S. D., Polyakov V. B. and Permyakov Y. V. (2007) Equilibrium iron isotope fractionation factors for magnetite from Mössbauer spectroscopy and inelastic nuclear resonant X-ray scattering data. *Geochimica et Cosmochimica Acta* **71**, A669.
- Miotello A. and Kelly R. (1999) Laser-induced phase explosion: new physical problems when a condensed phase approaches the thermodynamic critical temperature. *Applied Physics A-Materials Science and Processing* **69**, S67-S73.
- Miyano T. and Beukes N. J. (1984) Phase relations of stilpnomelane, ferri-annite and riebeckite in very low-grade metamorphosed iron-formations. *Transactions, Geological Society of South Africa* **87**, 111-124.
- Mojzsis S. J., Arrhenius G., McKeegan K. D., Harrison T. M., Nutman A. P. and Friend C. R. L. (1996) Evidence for life on Earth before 3,800 million years ago. *Nature* **384**, 55-59.
- Molini-Velsko C., Mayeda T. K. and Clayton R. N. (1986) Isotopic composition of silicon in meteorites. *Geochimica et Cosmochimica Acta* **50**, 2719-2726.
- Moorbath S., Taylor P. N., Orpen J. L., Treloar P. and Wilson J. F. (1987) First direct radiometric dating of Archean stromatolitic limestone. *Nature* **326**, 865-867.
- Morris R. C. (1993) Genetic modelling for banded iron-formation of the Hamersley Group, Pilbara Craton, Western Australia. *Precambrian Research* **60**, 243-286.
- Mozna V., Pisonero J., Hola M., Kanicky V. and Guenther D. (2006) Quantitative analysis of Fe-based samples using ultraviolet nanosecond and femtosecond laser ablation-ICP-MS. *Journal of Analytical Atomic Spectrometry* **21**, 1194-1201.
- Méheut M., Lazzeri M., Balan E. and Mauri F. (in press) Structural control over equilibrium silicon and oxygen isotopic fractionation: A first-principles density-functional theory study. *Chemical Geology*, doi:10.1016/j.chemgeo.2008.06.051.
- Mücke A. (2003) General and comparative considerations of whole-rock and mineral compositions of Precambrian iron-formations and their implications. *Neues Jahrbuch für Mineralogie, Abhandlungen* **179**, 175-219.
-

-
- Nelson D. R., Trendall A. F. and Altermann W. (1999) Chronological correlations between the Pilbara and Kaapvaal cratons. *Precambrian Research* **97**, 165-189.
- Nolte S., Momma H., Jacobs H., Tünnermann A., Chichkov B. N., Wellegehausen B. and Welling H. (1997) Ablation of metals by ultrashort laser pulses. *Journal of the Optical Society of America B: Optical Physics* **14**, 2716–2722.
- Norman M. D., McCulloch M. T., O'Neill H. S. C. and Yaxley G. M. (2006) Magnesium isotopic analysis of olivine by laser-ablation multi-collector ICP-MS: Composition dependent matrix effects and a comparison of the Earth and Moon. *Journal of Analytical Atomic Spectrometry* **21**, 50-54.
- Noël S., Hermann J. and Itina T. (2007) Investigation of nanoparticle generation during femtosecond laser ablation of metals. *Applied Surface Science* **253**, 6310-6315.
- Oberthuer T., Saager R. and Tomschi H. (1990) Geological, mineralogical and geochemical aspects of archean banded iron-formation-hosted gold deposits: some examples from southern Africa. *Mineralium Deposita* **25**, 125-135.
- Ohmoto H. (1996) Evidence in pre-2.2 Ga paleosols for the early evolution of atmospheric oxygen and terrestrial biota. *Geology* **24**, 1135-1138.
- Ohmoto H. (2003) Nonredox transformations of magnetite-hematite in hydrothermal systems. *Economic Geology and the Bulletin of the Society of Economic Geologist* **98**, 157-161.
- Olesik J. W. (1997) Investigating the fate of individual sample droplets in inductively coupled plasmas. *Applied Spectroscopy* **51**, 158A-175A.
- Opfergelt S., Cardinal D., Henriët C., André L. and Delvaux B. (2006a) Silicon isotope fractionation between plant parts in banana: In situ vs. in vitro. *Journal of Geochemical Exploration* **88**, 224-227.
- Opfergelt S., Cardinal D., Henriët C., Draye X., André L. and Delvaux B. (2006b) Silicon isotopic fractionation by banana (*Musa* spp.) grown in a continuous nutrient flow device. *Plant and Soil* **285**, 333-345.
- Outridge P. M., Doherty W. and Gregoire D. C. (1996) The formation of trace element enriched particulates during laser ablation of refractory materials. *Spectrochimica Acta Part B Atomic Spectroscopy* **51**, 1451-1462.
- Outridge P. M., Doherty W. and Gregoire D. C. (1997) Ablative and transport fractionation of trace elements during laser sampling of glass and copper. *Spectrochimica Acta Part B Atomic Spectroscopy* **52**, 2093-2102.
- Pan J., Zhang Q., Ma D. and Li C. (2001) Cherts from the Yangla copper deposit, western Yunnan province: Geochemical characteristics and relationship with massive sulfide mineralization. *Science in China, Series D: Earth Sciences* **44**, 237-244.
- Pecoits E., Gingras M. K., Kappler A., Posth N., Barley, M A and Konhauser K. O. (in review) Petrography and trace element geochemistry of Dales Gorge banded iron formation:
-

-
- Paragenetic sequence, source and implications for palaeo-ocean chemistry. *Precambrian Research*.
- Pedersen H. D., Postma D., Jakobsen R. and Larsen O. (2005) Fast transformation of iron oxyhydroxides by the catalytic action of aqueous Fe(II). *Geochimica et Cosmochimica Acta* **69**, 3967-3977.
- Perdian D. C., Bajic S. J., Baldwin D. P. and Houk R. S. (2008) Time-resolved studies of particle effects in laser ablation inductively coupled plasma-mass spectrometry. *Journal of Analytical Atomic Spectrometry* **23**, 325-335.
- Perez D. and Lewis L. J. (2003) Molecular-dynamics study of ablation of solids under femtosecond laser pulses. *Physical Review B - Condensed Matter and Materials Physics* **67**, 1841021-18410215.
- Perry E. C. and Lefticariu L. (2003) Formation and geochemistry of Precambrian cherts. In *Treatise on Geochemistry* (ed. F. T. Mackenzie). Elsevier Amsterdam. pp. 99-113.
- Perry E. C., Ahmad S. N. and Swulius T. M. (1978) Oxygen isotope composition of 3,800 my old metamorphosed chert and iron formation from Isukasia, West-Greenland. *Journal of Geology* **86**, 223-239.
- Perry E. C., Tan F. C. and Morey G. B. (1973) Geology and stable isotope geochemistry of Biwabik iron formation, northern Minnesota. *Economic Geology* **68**, 1110-1125.
- Pickard A. L. (2002) SHRIMP U-Pb zircon ages of tuffaceous mudrocks in the Brockman Iron Formation of Hamersley Range, Western Australia. *Australian Journal of Earth Sciences* **49**, 491-507.
- Pickard A. L. (2003) SHRIMP U-Pb zircon ages for the Palaeoproterozoic Kuruman Iron Formation, Northern Cape Province, South Africa: Evidence for simultaneous BIF deposition on Kaapvaal and Pilbara Cratons. *Precambrian Research* **125**, 275-315.
- Poitrasson F. (2007) Does planetary differentiation really fractionate iron isotopes?. *Earth and Planetary Science Letters* **256**, 484-492.
- Poitrasson F. and Freydier R. (2005) Heavy iron isotope composition of granites determined by high resolution MC-ICP-MS. *Chemical Geology* **222**, 132-147.
- Poitrasson F., Levasseur S. and Teutsch N. (2005) Significance of iron isotope mineral fractionation in pallasites and iron meteorites for the core-mantle differentiation of terrestrial planets. *Earth and Planetary Science Letters* **234**, 151-164.
- Poitrasson F., Mao X. L., Mao S. S., Freydier R. and Russo R. E. (2003) Comparison of ultraviolet femtosecond and nanosecond laser ablation inductively coupled plasma mass spectrometry analysis in glass, monazite, and zircon. *Analytical Chemistry* **75**, 6184-6190.
- Polyakov V. B. (1997) Equilibrium fractionation of the iron isotopes: Estimation from Mössbauer spectroscopy data. *Geochimica et Cosmochimica Acta* **61**, 4217.
-

-
- Polyakov V. B. and Mineev S. D. (2000) The use of Mössbauer spectroscopy in stable isotope geochemistry. *Geochimica et Cosmochimica Acta* **64**, 849-865.
- Polyakov V. B., Clayton R. N., Horita J. and Mineev S. D. (2007) Equilibrium iron isotope fractionation factors of minerals: Reevaluation from the data of nuclear inelastic resonant X-ray scattering and Mössbauer spectroscopy. *Geochimica et Cosmochimica Acta* **71**, 3833-3846.
- Prendergast M. D. (2004) The Bulawayan Supergroup: A late Archaean passive margin-related large igneous province in the Zimbabwe craton. *Journal of the Geological Society* **161**, 431-445.
- Ragueneau O., Treguer P., Leynaert A., Anderson R. F., Brzezinski M. A., DeMaster D. J., Dugdale R. C., Dymond J., Fisher G., Francois R., Heinze C., Maier-Reimer E., Martin-Jezequel V., Nelson D. M. and Queguiner B. (2000) A review of the Si cycle in the modern ocean: recent progress and missing gaps in the application of biogenic opal as a paleoproductivity proxy. *Global and Planetary Change* **26**, 317-365.
- Reynold J. H. and Verhoogen J. (1953) Natural variations in the isotopic constitution of silicon. *Geochimica et Cosmochimica Acta* **3**, 224-234.
- Reynolds B. C., Frank M. and Halliday A. N. (2006) Silicon isotope fractionation during nutrient utilization in the North Pacific. *Earth and Planetary Science Letters* **244**, 431-443.
- Richter F. M., Mendybaev R. A., Christensen J. N., Hutcheon I. D., Williams R. W., Sturchio N. C. and Beloso A. D. (2006) Kinetic isotopic fractionation during diffusion of ionic species in water. *Geochimica et Cosmochimica Acta* **70**, 277-289.
- Robert F. and Chaussidon M. (2006) A palaeotemperature curve for the Precambrian oceans based on silicon isotopes in cherts. *Nature* **443**, 969-972.
- Roden E. E., Sobolev D., Glazer B. and Luther G. W. (2004) Potential for microscale bacterial Fe redox cycling at the aerobic-anaerobic interface. *Geomicrobiology Journal* **21**, 391.
- Rodushkin I., Stenberg A., Andreñ H., Malinovsky D. and Baxter D. C. (2004) Isotopic Fractionation during Diffusion of Transition Metal Ions in Solution. *Analytical Chemistry* **76**, 2148-2151.
- Rouxel O. J., Bekker A. and Edwards K. J. (2005) Iron isotope constraints on the Archean and Paleoproterozoic ocean redox state. *Science* **307**, 1088-1091.
- Rouxel O., Fouquet Y. and Ludden J. (2004) Subsurface processes at the Lucky Strike hydrothermal field, Mid-Atlantic Ridge: Evidence from sulfur, selenium, and iron isotopes. *Geochimica et Cosmochimica Acta* **68**, 2295-2311.
- Russo R. E., Mao X. L., Borisov O. V. and Liu H. C. (2000) Influence of wavelength on fractionation in laser ablation ICP-MS. *Journal of Analytical Atomic Spectrometry* **15**, 1115-1120.
-

-
- Russo R. E., Mao X. L., Gonzalez J. J. and Mao S. S. (2002) Femtosecond laser ablation ICP-MS. *Journal of Analytical Atomic Spectrometry* **17**, 1072-1075.
- Saetveit N. J., Bajic S. J., Baldwin D. P. and Houk R. S. (2008) Influence of particle size on fractionation with nanosecond and femtosecond laser ablation in brass by online differential mobility analysis and inductively coupled plasma mass spectrometry. *Journal of Analytical Atomic Spectrometry* **23**, 54-61.
- Schauble E. A. (2004) Applying stable isotope fractionation theory to new systems. In *Non-traditional stable isotopes* (eds. C. M. Johnson, B. L. Beard and F. Albarède). Reviews in Mineralogy and Geochemistry, Mineralogical Society of America, Washington. pp. 65-111.
- Schauble E. A., Rossman G. R. and Taylor H. P. (2001) Theoretical estimates of equilibrium Fe-isotope fractionations from vibrational spectroscopy. *Geochimica et Cosmochimica Acta* **65**, 2487-2497.
- Schoenberg R. and von Blanckenburg F. (2005) An assessment of the accuracy of stable Fe isotope ratio measurements on samples with organic and inorganic matrices by high-resolution multicollector ICP-MS. *International Journal of Mass Spectrometry* **242**, 257-272.
- Schoenberg R. and von Blanckenburg F. (2006) Modes of planetary-scale Fe isotope fractionation. *Earth and Planetary Science Letters* **252**, 342-359.
- Schoenberg, R., Marks, M A W, Schuessler, J A , von Blanckenburg, F , Markl, G, 2009. Fe isotope systematics of coexisting amphibole and pyroxene in the alkaline igneous rock suite of the Ilímaussaq Complex, South Greenland. *Chem. Geol.* 258 , 65-77.
- Schoenberg, R., Zink, S., Staubwasser, M. and von Blanckenburg, F. (2008) The stable Cr isotope inventory of solid Earth reservoirs determined by double spike MC-ICP-MS. *Chemical Geology* **249**, 294-306.
- Schuessler J. A., Schoenberg R., Sigmarsson O., 2009. Iron and lithium isotope systematics of the Hekla volcano, Iceland - Evidence for Fe isotope fractionation during magma differentiation. *Chem. Geol.* 258, 78-91.
- Schuessler J. A., Schoenberg R., Behrens H. and von Blanckenburg F. (2006) Experimental evidence for high temperature iron isotope fractionation between pyrrhotite and peralkaline rhyolitic melt. *Geochimica et Cosmochimica Acta* **71**, 417-433.
- Severmann S., Johnson C. M., Beard B. L. and McManus J. (2006) The effect of early diagenesis on the Fe isotope compositions of porewaters and authigenic minerals in continental margin sediments. *Geochimica et Cosmochimica Acta* **70**, 2006-2022.
- Severmann S., Johnson C. M., Beard B. L., German C. R., Edmonds H. N., Chiba H. and Green D. R. H. (2004) The effect of plume processes on the Fe isotope composition of hydrothermally derived Fe in the deep ocean as inferred from the Rainbow vent site, Mid-Atlantic Ridge, 36 degrees 14' N. *Earth and Planetary Science Letters* **225**, 63-76.
-

-
- Severmann S., Lyons T. W., Anbar A., McManus J. and Gordon G. (2008) Modern iron isotope perspective on the benthic iron shuttle and the redox evolution of ancient oceans. *Geology* **36**, 487-490.
- Shahar A. and Young E. D. (2007) Astrophysics of CAI formation as revealed by silicon isotope LA-MC-ICPMS of an igneous CAI. *Earth and Planetary Science Letters* **257**, 497-510.
- Sharma M., Polizzotto M. and Anbar A. (2001) Iron isotopes in hot springs along the Juan de Fuca Ridge. *Earth and Planetary Science Letters* **194**, 39-51.
- Sharma M., Polizzotto M. and Anbar A. D. (2001) Iron isotopes in hot springs along the Juan de Fuca Ridge. *Earth and Planetary Science Letters* **194**, 39-51.
- Sharpe M. R. and Chadwick B. (1982) Structures in Transvaal Sequence rocks within and adjacent to the eastern Bushveld Complex. *Transactions of the Geological Society of South Africa* **85**, 29-41.
- Siever R. (1992) The silica cycle in the Precambrian. *Geochimica et Cosmochimica Acta* **56**, 3265-3272.
- Simonetti A., Heaman L. M., Hartlaub R. P., Creaser R. A., MacHattie T. G. and Böhm C. (2005) U-Pb zircon dating by laser ablation-MC-ICP-MS using a new multiple ion counting Faraday collector array. *Journal of Analytical Atomic Spectrometry* **20**, 677-686.
- Simonson B. M. and Hassler S. W. (1996) Was the deposition of large Precambrian iron formations linked to major marine transgressions? *Journal of Geology* **104**, 665-676.
- Skulan J. L., Beard B. L. and Johnson C. M. (2002) Kinetic and equilibrium Fe isotope fractionation between aqueous Fe(III) and hematite. *Geochimica et Cosmochimica Acta* **66**, 2995-3015.
- Sláma, J., Košler, J., Condon D. J., Crowley J. L., Gerdes A., Hanchar J. M., Horstwood M., Morris G. A., Nasdala L., Norberg N., Schaltegger U., Schoene B., Turbett M. N. and Whitehouse M. J. (2008) Plešovice zircon – new natural reference material for U–Pb and Hf isotopic microanalysis. *Chemical Geology* **249**, 1-35.
- Sommer M., Kaczorek D., Kuzyakov Y. and Breuer J. (2006) Silicon pools and fluxes in soils and landscapes - A review. *Journal of Plant Nutrition and Soil Science* **169**, 310-329.
- Spotl C. and Vennemann T. W. (2003) Continuous-flow isotope ratio mass spectrometric analysis of carbonate minerals. *Rapid Communications in Mass Spectrometry* **17**, 1004-1006.
- Staubwasser M., von Blanckenburg F. and Schoenberg R. (2006) Iron isotopes in the early marine diagenetic iron cycle. *Geology* **34**, 629-632.
- Street-Perrott F. A., Barker P. A., Leng M. J., Sloane H. J., Wooller M. J., Ficken K. J. and Swain D. (2008) Towards an understanding of late Quaternary variations in the continental biogeochemical cycle of silicon: multi-isotope and sediment-flux data for
-

-
- Lake Rutundu, Mt Kenya, East Africa, since 38 ka BP. *Journal of Quaternary Science* **23**, 375-387.
- Sumner D. Y. (1997) Carbonate precipitation and oxygen stratification in late Archean seawater as deduced from facies and stratigraphy of the Gamohaam and Frisco formations, Transvaal Supergroup, South Africa. *American Journal of Science* **297**, 455-487.
- Sumner D. Y. and Grotzinger J. P. (2004) Implications for Neoproterozoic ocean chemistry from primary carbonate mineralogy of the Campbellrand-Malmani Platform, South Africa. *Sedimentology* **51**, 1273-1299.
- Sun L., Wu L. H., Ding T. P. and Tian S. H. (2008) Silicon isotope fractionation in rice plants, an experimental study on rice growth under hydroponic conditions. *Plant and Soil* **304**, 291-300.
- Sylvester P. J. (2008) Matrix effects in laser ablation ICP-MS. In *Laser Ablation-ICP-MS in the Earth Sciences* (ed. P. J. Sylvester). Mineralogical Association of Canada Short Course Series. pp. 67-78.
- Telouk P., Rose-Koga E. F. and Albarède F. (2003) Preliminary results from a new 157 nm laser ablation ICP-MS instrument: New opportunities in the analysis of solid samples. *Geostandards Newsletter-the Journal of Geostandards and Geoanalysis* **27**, 5-11.
- Teng F. Z., Dauphas N. and Helz R. T. (2008) Iron isotope fractionation during magmatic differentiation in Kilauea Iki Lava Lake. *Science* **320**, 1620-1622.
- Teutsch N., Halliday A., von Gunten U., Cirpka O. and Porcelli D. (2005) Adsorption as a cause for iron isotope fractionation in reduced groundwater. *Geochimica et Cosmochimica Acta* **69**, 4175-4185.
- Tice M. M. and Lowe D. R. (2004) Photosynthetic microbial mats in the 3,416-Myr-old ocean. *Nature* **431**, 549-552.
- Tilles D. (1961) Natural variations in isotopic abundances of silicon. *Journal of Geophysical Research* **66**, 3003-3014.
- Treguer P., Nelson D. M., van Bennekom A. J., DeMaster D. J., Leynaert A. and Queguiner B. (1995) The silica balance in the world ocean — a reestimate. *Science* **268**, 375-379.
- Trendall A. F. (2002) The significance of iron-formation in the Precambrian stratigraphic record. In *Precambrian Sedimentary Environments: A Modern Approach to Depositional Systems* (eds. W. Altermann and P. L. Corcorane). International Association of Sedimentologists Special Publications . pp. 33-66.
- Trendall A. F. and Blockley J. G. (1970) The Iron-Formation of the the Precambrian Hamersley Group, Western Australia, with special reference to the associated crocidolite. *Geological Survey Western Australia Bulletin* **119**.
- Trendall A. F., Compston W., Nelson D. R., De Laeter J. R. and Bennett V. C. (2004) SHRIMP zircon ages constraining the depositional chronology of the Hamersley Group, Western Australia. *Australian Journal of Earth Sciences* **51**, 621-644.
-

-
- Tripa C. E., Pellin M. J., Savina M. R., Davis A. M., Lewis R. S. and Clayton R. N. (2002) Fe isotopic compositions of presolar SiC mainstream grains. *Lunar Planetary Science*, XXXIII:1975.
- Tyndale-Biscoe M. A. (1949) The Geology of the Country around Gwelo. Southern Rhodesia Geological Survey, Bulletin No. 39. Reprinted by the Government Printer, Salisbury, 1972.
- Urey H. C. (1947) The thermodynamic properties of isotopic substances. *Journal of the Chemical Society*, 562–81.
- Vadillo J. M. and Laserna J. J. (2004) Laser-induced plasma spectrometry: Truly a surface analytical tool. *Spectrochimica Acta B* **59**, 147-161.
- Valaas Hyslop E., Valley J. W., Johnson C. M. and Beard B. L. (2008) The effects of metamorphism on O and Fe isotope compositions in the Biwabik iron-formation, northern Minnesota. *Contributions to Mineralogy and Petrology* **155**, 313-328.
- Varela D. E., Pride C. J. and Brzezinski M. A. (2004) Biological fractionation of silicon isotopes in Southern Ocean surface waters. *Global Biogeochemical Cycles* **18**, GB1047.
- Vargas M., Kashefi K., Blunt-Harris E. L. and Lovley D. R. (1998) Microbiological evidence for Fe(III) reduction on early earth. *Nature* **395**, 65-67.
- Villa I. M. and von Blanckenburg F. (1991) A hornblende ³⁹Ar-⁴⁰Ar age traverse of the Bregaglia tonalite (southwest Central Alps). *Schweizer Mineralogische und Petrologische Mitteilungen* **71**, 73-87.
- Völkening J. and Papanastassiou D. A. (1989) Iron isotope anomalies. *Astrophysical Journal* **347**, L43-L46.
- van den Boorn S. H. J. M., van Bergen M. J., Nijman W. and Vroon P. Z. (2007) Dual role of seawater and hydrothermal fluids in Early Archean chert formation: Evidence from silicon isotopes. *Geology* **35**, 939-942.
- van den Boorn S., Vroon P., van Belle C., van der Wagt B., Johannes Schwieters J. and van Bergen M. (2006) Determination of silicon isotope ratios in silicate materials by high-resolution MC-ICP-MS using a sodium hydroxide sample digestion method. *Journal of Analytical Atomic Spectrometry* **21**, 734 - 742.
- von Blanckenburg F., Mamberti M., Schoenberg R., Kamber B. S. and Webb G. E. (2008) The iron isotope composition of microbial carbonate. *Chemical Geology* **249**, 113-128.
- von Stackelberg U., Kunzendorf H., Marchig V. and Gwozdz R. (1984) Growth History of a Large Ferromanganese Crust from the Equatorial North Pacific Nodule Belt. *Geologisches Jahrbuch* **A75**, 213-235.
- Walczyk T. (1997) Iron isotope ratio measurements by negative thermal ionisation mass spectrometry using FeF₄ - molecular ions. *International Journal of Mass Spectrometry* **161**, 217-227.
-

-
- Walczyk T. and von Blanckenburg F. (2002) Natural iron isotope variations in human blood. *Science* **295**, 2065-2066.
- Walczyk T. and von Blanckenburg F. (2005) Deciphering the iron isotope message of the human body. *International Journal of Mass Spectrometry* **242**, 117-134.
- Walker J. C. G. (1984) Suboxic diagenesis in banded iron formations. *Nature* **309**, 340-342.
- Walraven F., Armstrong R. and Kruger F. (1990) A chronostratigraphic framework for the north-central Kaapvaal craton, the Bushveld Complex and the Vredefort structure. *Tectonophysics* **171**, 23-48.
- Wang Z., Hattendorf B. and Guenther D. (2006) Vaporization and ionization of laser ablation generated aerosols in an inductively coupled plasma mass spectrometer – implications from ion distribution maps. *Journal of Analytical Atomic Spectrometry* **21**, 1143-1151.
- Webb R. L., Dickinson J. T. and Exarhos G. J. (1997) Characterization of particulates accompanying laser ablation of NaNO₃. *Applied Spectroscopy* **51**, 707-717.
- Wedepohl K. H. (1995) The composition of the continental crust. *Geochimica et Cosmochimica Acta* **59**, 1217-1232.
- Welch S. A., Beard B. L., Johnson C. M. and Braterman P. S. (2003) Kinetic and equilibrium Fe isotope fractionation between aqueous Fe(II) and Fe(III). *Geochimica et Cosmochimica Acta* **67**, 4231-4250.
- Whitehouse M. J. and Fedo C. M. (2007) Microscale heterogeneity of Fe isotopes in > 3.71 Ga banded iron formation from the Isua Greenstone Belt, Southwest Greenland. *Geology* **35**, 719-722.
- Widdel F., Schnell S., Heising S., Ehrenreich A., Assmus B. and Schink B. (1993) Ferrous iron oxidation by anoxygenic phototrophic bacteria. *Nature* **362**, 834-836.
- Wiederhold J. G., Kraemer S. M., Teutsch N., Borer P. M., Halliday A. N. and Kretzschmar R. (2006) Iron isotope fractionation during proton-promoted, ligand-controlled, and reductive dissolution of goethite. *Environmental Science and Technology* **40**, 3793-3148.
- Wiesli R. A., Beard B. L. and Johnson C. M. (2004) Experimental determination of Fe isotope fractionation between aqueous Fe(II), siderite and "green rust" in abiotic systems. *Chemical Geology* **211**, 343-362.
- Williams A. G. B. and Scherer M. M. (2004) Spectroscopic evidence for Fe(II)-Fe(III) electron transfer at the iron oxide-water interface. *Environmental Science and Technology* **38**, 4782-4790.
- Wilson J. F., Nesbitt R. W. and Fanning C. M. (1995) Zircon geochronology of Archaean felsic sequences in the Zimbabwe craton: a revision of greenstone stratigraphy and a model for crustal growth. In *Early Precambrian Research* (eds. M. P. Coward and A. C. Reis). Special Publications, Geological Society, London. pp. 109-126.
-

-
- Wu J., Boyle E., Sunda W. and Wen L. S. (2001) Soluble and colloidal iron in the oligotrophic North Atlantic and North Pacific. *Science* **293**, 847-849.
- Wu S. Y., Ding T. P., Meng X. W. and Bai L. M. (1997) Determination and geological implication of O-Si isotope of the sediment core in the CC area, the Pacific Ocean. *Chinese Science Bulletin* **42**, 1462-1465.
- Wälle M., Koch J. and Guenther D. (2008) Analysis of brass and silicate glass by femtosecond laser ablation inductively coupled plasma mass spectrometry using liquid standard calibration. *Journal of Analytical Atomic Spectrometry* **23**, 1285-1289.
- Xu Y. (2001) Silicon isotope study of thermal springs in Jiaodong Region, Shandong Province. *Science in China, Series E: Technological Sciences* **44**, 158-159.
- Yamaguchi K. E. and Ohmoto H. (2006) Comment on "Iron isotope constraints on the Archean and Paleoproterozoic ocean redox state. *Science* **311**, 135-169.
- Yamaguchi K. E., Johnson C. M., Beard B. L. and Ohmoto H. (2005) Biogeochemical cycling of iron in the Archean-Paleoproterozoic Earth: Constraints from iron isotope variations in sedimentary rocks from the Kaapvaal and Pilbara Cratons. *Chemical Geology* **218**, 135-169.
- Young E. D., Ash R. D., Galy A. and Belshaw N. S. (2002) Mg isotope heterogeneity in the Allende meteorite measured by UV laser ablation-MC-ICPMS and comparisons with O isotopes. *Geochimica et Cosmochimica Acta* **66**, 683-698.
- Yuan, H.L., Gao, S., Liu, X.M., Li, H.M., Günther, D. and Wu, F. (2004) Accurate U Pb age and trace element determinations of zircon by laser ablation inductively coupled plasma mass spectrometry. *Geostandards and Geoanalytical Research* **28**, 353-370.
- Zhigilei L. V. (2003) Dynamics of the plume formation and parameters of the ejected clusters in short-pulse laser ablation. *Applied Physics A: Materials Science and Processing* **76**, 339-350.
- Zhigilei L. V. and Garrison B. J. (2000) Microscopic mechanisms of laser ablation of organic solids in the thermal and stress confinement irradiation regimes. *Journal of Applied Physics* **88**, 1281-1298.
- Zhu X., O'Nions R., Guo Y. and Reynolds B. (2000) Secular variation of iron isotopes in North Atlantic Deep Water. *Science* **287**, 2000-2002.
- Ziegler K., Chadwick O. A., Brzezinski M. A. and Kelly E. F. (2005) Natural variations of $\delta^{30}\text{Si}$ ratios during progressive basalt weathering, Hawaiian Islands. *Geochimica et Cosmochimica Acta* **69**, 4597-4610.
- Ziegler K., Chadwick O. A., White A. F. and Brzezinski M. A. (2005) $\delta^{30}\text{Si}$ systematics in a granitic saprolite, Puerto Rico. *Geology* **33**, 817-820.
-

Curriculum Vitae

Grit Steinhöfel

Email: gritstein@gmx.de

Persönliche Angaben

Geboren am 30.09.1977 in München

Nationalität: Deutsch

Familienstand: ledig, eine Tochter

Schulbildung

1984-1988 Grundschule in Germering und Wörthsee

1988-1997 Christoph-Probst-Gymnasium Gilching

07.1997 Abitur

Hochschulbildung

1997-2003 Studium der Geologie/Paläontologie an der Ludwig-Maximilians-Universität München, Technischen Universität München und University of Toronto

12/2003 Diplom in Geologie

11/2004-12/2008 Doktorandin am Institut für Mineralogie,
Gottfried-Wilhelm-Leibniz Universität Hannover

Anstellungen

11/2004-08/2008 Wissenschaftliche Mitarbeiterin am Institut für Mineralogie,
Gottfried-Wilhelm-Leibniz Universität Hannover

ab 12/2008 Wissenschaftliche Mitarbeiterin
am Leibniz-Zentrum für Agrarlandschaftsforschung Müncheberg

Publications

- Steinboefel G., Hegner E. and Oliver G. J. H. (2008) Chemical and Nd isotope constraints on granitoid sources involved in the Caledonian Orogeny in Scotland. *Journal of the Geological Society* **165**, 817-827.
- Chmeleff J., Horn I., Steinboefel G. and von Blanckenburg F. (2008) In situ determination of precise stable Si isotope ratios by UV-femtosecond laser ablation high-resolution multi-collector ICP-MS. *Chemical Geology* **249**, 155-166.
- Horn I., von Blanckenburg F., Schoenberg R., Steinboefel G. and Markl G. (2006) In situ iron isotope ratio determination using UV-femtosecond laser ablation with application to hydrothermal ore formation processes. *Geochimica et Cosmochimica Acta* **70**, 3677-3688.
